MEDICAL COMPTON CAMERAS BASED ON SEMICONDUCTOR DETECTORS: DESIGN AND EXPERIMENTAL DEVELOPMENT

Maria Giulia Scannavini

UNIVERSITY COLLEGE LONDON

Submitted for
The Degree of Doctor of Philosophy
The University of London

February 2001

ProQuest Number: U642138

All rights reserved

INFORMATION TO ALL USERS
The quality of this reproduction is dependent upon the quality of the copy submitted.

In the unlikely event that the author did not send a complete manuscript
and there are missing pages, these will be noted. Also, if material had to be removed,
a note will indicate the deletion.

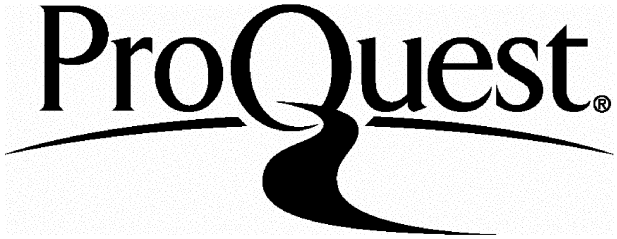

ProQuest U642138

Published by ProQuest LLC(2015). Copyright of the Dissertation is held by the Author.

All rights reserved.
This work is protected against unauthorized copying under Title 17, United States Code.
Microform Edition © ProQuest LLC.

ProQuest LLC
789 East Eisenhower Parkway
P.O. Box 1346
Ann Arbor, MI 48106-1346

Abstract

The work presented in this thesis is aimed at the study of Compton scatter as an alternative method of collimating gamma-rays in nuclear medicine applications. Conventional approaches to radioisotope medical imaging and their current limitations are examined. The theory of electronic collimation based on Compton scatter is introduced and it is shown that in principle its application could provide an advantageous imaging method, with both high spatial resolution and high sensitivity. The current status of research in the field of Compton cameras is assessed and potential niches for applications of clinical interest are suggested. The criteria for the design of a Compton scatter camera are examined. A variety of semiconductors are considered for the construction of an electronic collimator and results from Monte Carlo computer simulations are presented for photon energies of clinical interest. It is concluded that the most viable approach is to design a silicon collimator for the imaging of high-energy (511 ke V) photons.

A computer model of a Compton camera is developed in order to study the phenomena that affect the angular resolution and the sensitivity of the system. This simulation tool is applied to select the optimum characteristics of the silicon scatter detector. Such results are employed to design and initiate the construction of an experimental prototype of Compton camera, based on the use of double-sided silicon microstrip detectors. The development of special readout electronics required for the camera operation is described. Experimental tests are performed for the characterisation of the silicon strip detectors and the results are presented. Predictions are made on the performance of the designed system. Finally, the current stage of system development is assessed and the main areas for future work are identified.

Contents

Appendix I

Appendix II

Figures

Chapter 1

Chapter 2

Chapter 3

Chapter 4

Chapter 5

Appendix I

Appendix II

Tables

Chapter 1

Chapter 2

Chapter 3

Chapter 4

Publications

The following list includes the scientific papers that have resulted from the work presented in this thesis:

1) Scannavini M G, Speller R D, Royle G J, Cullum I, Raymond M, Hall G and Iles G: A possible role for Silicon Microstrip Detectors in Nuclear Medicine: Compton Imaging of Positron Emitters, submitted for publication in *Nuclear Instruments and Methods in Physics & Research.*

2) Scannavini M G, Speller R D, Royle G J, Cullum I, Raymond M, Hall G and Iles G: Design of a Small Laboratory Compton Camera for the Imaging of Positron Emitters, *IEEE Transactions on Nuclear Science*, **47**, no.3, pt.3 (2000), 1155-62

3) Speller R, Royle G, Scannavini M G and Horrocks J: Impact of new digital X- and gamma ray imaging systems upon patient doses, *Applied Radiation and Isotopes* **50** (1999) 153-163. This paper is also a chapter in the book "Subject Dose in Radiological Imaging", edited by Kwan-Hoong Ng, D.A. Bradley and H.M. Warren-Forward, published by Elsevier, 1998.

Acknowledgements

I would like to thank Prof. Robert Speller for supervising this project and for all his helpful advice during the duration of my PhD. I am extremely grateful to Dr. Ian Cullum of the Institute of Nuclear Medicine, Middlesex Hospital, for the invaluable help he gave me over the last few years and for the fundamental contribution he made to the project. I would also like to thank Dr. Gary Royle. Thank you also to many present and past members of the Radiation Physics Group at UCL for their friendship and support over the years.

I wish to thank Prof. Geoff Hall of the High Energy Physics Group at Blackett Laboratory, Imperial College for generously making the APV6 chip available for this project, and for allowing me to use many of their laboratory resources. I would like to thank everybody that made my time at Imperial College so interesting and enjoyable. Many thanks are due to Dr. Mark Raymond for the great help and guidance that he was willing to provide. I am especially indebted to Dr. Greg Iles for his kind contribution and support. Thank you also to Dr. Alex Howard for all his help and useful suggestions. I would also like to thank Sarah Greenwood, Maria Khaleeq and John Reilly at Imperial College and Jeff Bizzell at the Rutherford Appleton Laboratory for the technical support provided.

Finally, I would like to thank the European Commission, who sponsored my PhD studies through a Marie-Curie Fellowship awarded under the T.M.R. scheme, and the Blanceflor-Boncompagni Swedish Foundation, who provided additional funding during my final year. I also wish to thank the Royal Society, who funded the development of the experimental prototype through a grant awarded to Prof. Speller by the Paul Instrument Fund Committee.

Introduction

The idea of applying Compton scatter to the electronic collimation of γ-rays for the formation of clinical images was suggested for the first time in the early 1970s, as an alternative to mechanical collimation [Todd *et al.*, 1974]. In conventional cameras for emission imaging, the use of absorptive collimators to select photon direction dramatically reduces the photon flux at the detector. Mechanical collimators also suffer from an inverse relationship between geometric efficiency and spatial resolution. In contrast, the process of electronic collimation by Compton scatter can in principle achieve high geometric efficiency without compromising spatial resolution.

The physics of Compton scatter favours the use of this imaging technique with photons of relatively high energy. Compton telescopes have been successfully employed for many years in astronomy, in order to observe celestial sources of radiation in the 1 - 30 MeV energy range [Zych *et al.*, 1979], [Schönfelder *et al.*, 1993]. Portable Compton cameras have also been researched for industrial use in the 0.5 - 3 MeV energy range [Martin *et al.*, 1993], [Royle and Speller, 1994]. A radiation environment in a nuclear industry site was successfully imaged using a prototype system [Royle and Speller, 1997].

Compton telescopes currently remain the only application of Compton imaging that has translated into a well-established technology for mapping distributions of radioactive sources. In near-field applications, such as medical and industrial imaging, reconstruction is a more complex problem, due to the three-dimensional geometry of the radiating objects. System sensitivity is a more problematic issue in medical rather than industrial applications, due to the constraints on the levels of activity that can be administered to a patient. Finally, severe requirements on the energy and spatial resolution capabilities of the detectors make the use of Compton cameras as medical imaging devices a particularly challenging objective.

Feasibility studies in order to build a Compton camera prototype for medical imaging were extensively carried out in the 1980s at both theoretical and

experimental level by Singh and co-workers [Singh, 1983], [Singh and Doria, 1983], [Singh and Brechner, 1990]. However, these results did not show an improvement in the image quality over conventional systems. This was due to the lack of suitable detectors that could meet the stringent requirements in terms of energy and spatial resolution.

The prospects for the development of a clinical Compton camera have much improved during the last decade, thanks to the availability of new position sensitive devices and to the introduction of high-energy physics technology in medical diagnostic instrumentation. Over the last few years, a renewed interest has been shown by various authors in the development of medical Compton cameras. Prototype systems have been developed, based on the use of either solid-state [LeBlanc *et al.*, 1998], [Tümer *et al.*, 1997] or gaseous detectors [Bolozdynya *et al.*, 1996].

However, the scientific community have almost exclusively been focused on producing a Compton camera that will operate with low-energy γ-rays, due to the widespread application of ^{99m}Tc (140 keV) in nuclear medicine examinations. By contrast, this work aims to develop a prototype Compton camera to image high-energy (511 keV) photons from the annihilation of positron emitters. No electronic collimators based on Compton scatter have yet been optimised for this specific application. This thesis presents the initial results on the design and experimental development of a laboratory Compton camera prototype, based on the use of double-sided silicon microstrip detectors.

The work, which includes both computational and experimental aspects, is organised in the thesis as follows:

- *Chapter One* introduces the basic principles of γ-ray emission medical imaging and reviews the different existing approaches to photon collimation in nuclear medicine. The clinical utility of imaging positron emitters is highlighted. The performance of the various systems currently available for clinical imaging at 511 keV is discussed. The chapter includes a literature

review on Compton scatter imaging in astronomy, industry and medicine. General advantages in the medical use of Compton cameras are described and potential clinical applications are identified.

- *Chapter Two* focuses on the selection of the physical and geometrical characteristics of a position sensitive, energy resolving detector, designed to perform Compton scatter collimation of 511 keV γ-rays. The chapter includes the description of a computer model, based on Monte Carlo techniques, which was specifically developed as a design tool for a Compton camera prototype. Simulation results are presented to select the optimal detector material, geometry, spatial resolution and energy resolution. Such results are applied to identify suitable commercially available detectors and integrated readout electronics.

- *Chapter Three* contains the description and results of various experimental tests that were carried out for the characterisation of the detectors prior to the bonding of the electronics. In particular, experiments are reported for the measurement of leakage current and strip capacitance, which strongly affect the noise performance of the detectors. The measurements of strip capacitance required the application of equivalent circuit models that showed the consistency of the results with the geometrical and physical characteristics of the detector design.

- *Chapter Four* presents a series of experimental measurements designed to evaluate the noise performance of the bonded silicon strip detectors and test their operation as charged particle detectors. The electrical parameters obtained from the experiments described in chapter 3 are applied to a noise model of the detector-chip system, so as to formulate an estimate of the expected noise level. The noise pattern across the strips is characterised experimentally and the typical noise level is compared to the theoretical estimate. Observations on the effects of temperature and pulse shape on noise performance are presented. This chapter also includes a discussion of the

energy loss of charged particles in silicon and describes a procedure for a preliminary energy calibration of the detectors.

- *Chapter Five* proposes a laboratory Compton camera prototype, based on a stack of silicon microstrip detectors operating in a double Compton configuration and externally triggered. The development and testing of special-purpose interface electronics are described, along with an overview of the data acquisition system. The Monte Carlo simulation model is applied to evaluate the imaging performance of the proposed collimator. The effects of patient scatter on collimator angular resolution are discussed.

- *Chapter Six* is a summary of the conclusions drawn from this work, followed by suggested areas for future work.

This project was carried out in collaboration with the Institute of Nuclear Medicine of Middlesex Hospital and the High Energy Physics Group at Imperial College. It is therefore necessary to identify the different contributions to this work.

The Monte Carlo simulation model, which produced all the results in chapters 2 and 5 for the design and evaluation of the prototype system, was developed entirely by myself and is based on original EGS4[1] user codes. In the simulation of point source images, all the necessary data were produced using these codes but the image reconstruction was performed by applying an independent source code, which was previously developed at UCL [Royle and Speller, 1994].

Although the Monte Carlo model identified specific geometrical and physical characteristics that were desirable for the silicon microstrip sensors, the detectors that were actually selected for this project were commercially available[2]. Therefore the design work of this thesis does not account for the particular details of the strip layout, such as width and thickness of implant and metal strips, choice of coupling oxides, method of strip bias, etc.

[1]The EGS4 code system [Nelson *et al.*, 1985]

[2] Detectors manufactured by Eurisys Mesures, Tanneries CEDEX, France

All measurements in chapter 3 for the characterisation of unbonded silicon strip detectors were carried out by myself at the Blackett Laboratory, Imperial College with the support of the High Energy Physics Group. The modelling approach for the capacitance measurements is based on models previously formulated in the literature[3], which I have adapted and applied to this specific design of strip detectors.

The APV6 readout chip was designed and developed by Imperial College and the Rutherford Appleton Laboratory (RAL) for the Compact Muon Solenoid (CMS) tracker experiments at the CERN[4] Large Hadron Collider (LHC) [Raymond *et al.*, 1997]. The mount board for the support and readout of the detectors was designed and produced for this project at Imperial College. Technical support was provided by RAL for detector bonding.

All of the performance measurements on bonded detectors in chapter 4 were also carried out by myself at the Blackett Laboratory, Imperial College. These experiments were conducted using a data acquisition system for strip detectors, developed by the High Energy Physics Group, who also provided support. The theoretical estimates of the strip noise are an application of elements of electronic noise theory from the literature[5]. The simulations of energy loss distribution from charged particles in silicon were carried out at Imperial College by Dr. A. Howard.

Dr. I. Cullum of the Institute of Nuclear Medicine, Middlesex Hospital designed the data acquisition and control system for the Compton camera prototype, including the interface electronics and controlling software. The general design and assembly of the mechanical components of the prototype, the experimental development and testing of the interface electronics were done at the Radiation Physics Laboratory of UCL by myself and Dr. Cullum.

[3] [Barberis et al., 1994], [Bacchetta *et al.*, 1995], [Frautschi *et al.*, 1996], [MacEvoy, 1997] etc.

[4] The European Laboratory for Particle Physics

[5] [Nicholson, 1982], [Nygård, 1991], [Dubbs *et al.*, 1996], etc.

Chapter 1

Collimation Approaches in Medical γ-ray Imaging

1.1 Principles of radionuclide imaging in medicine

Techniques for the imaging of radionuclides are employed in nuclear medicine in order to obtain information on morphology and functionality of organs within the human body. Radioactively labelled unsealed substances (radiopharmaceuticals) are introduced in the patient by the parenteral route, usually by simple intravenous injection. These substances are specifically localised in the organ of interest via a variety of physiological and metabolic mechanisms. The organ is imaged by placing around the patient one or more external radiation detectors, assembled in imaging systems.

Radiopharmaceuticals generally consist of single photon emitters that are incorporated in chemical compounds with favourable biological properties. The energy of the emitted photons is usually in the 80-400 keV range. An example of a pure gamma emitter is ^{99m}Tc (140 keV), the isotope most widely utilised in medical investigations. Annihilation photons (511 keV) from positron (β^+) emitters are also used, as they offer the advantage of tracing the pharmacodynamics of substances naturally present in the human metabolism. Positron emitters such as ^{11}C, ^{15}O, ^{13}N and ^{18}F are in fact isotopes of elements that are normal components in many biological molecules and potential natural carriers.

Mapping of gamma emitters is most frequently undertaken with the Anger camera, which traditionally consists of a scintillation detector coupled to a lead collimator. There are however several limitations with this approach, especially at high energies. Electronic collimation is much more efficient and can be found in many clinical investigations that make use of positron emitters. In Positron Emission Tomography (PET) two co-linear photons created from the positron-electron annihilation process are detected in coincidence. As PET scanners are very complex and expensive devices, dual-head cameras of the Anger type may also be manufactured with suitable coincidence electronics so as to allow the removal of the collimators when positron emitters are imaged. Finally, the Compton camera is an alternative type of gamma camera where the physical laws of Compton scattering are employed to electronically collimate single photons.

The imaging principles, upon which all these methods are based, are described in this chapter. Problems regarding the design and the use of mechanical collimators with high energy radioisotopes are also addressed. As the Compton camera was the subject of study in this thesis, advantages of this approach over conventional systems are highlighted. The chapter also includes a review of the theoretical and experimental work available in the literature on Compton cameras. Finally, possible clinical applications are suggested for the use of a Compton scatter imager.

1.2 Mechanically collimated cameras: the Anger camera

1.2.1 Principles of operation

The Anger camera was originally developed in the 1950s [Anger, 1958] and has been subsequently adapted to become the standard imaging instrument in nuclear medicine investigations. This imaging device makes use of a single, large-area scintillation crystal, which is usually made of NaI(Tl) and is relatively thin (approximately 1 cm). The shape of the crystal may be either circular (with a diameter of approximately 40 cm) or rectangular (with a typical size of 55 cm x 40 cm). The crystal is optically

coupled to an array of photomultiplier tubes (PMTs) that are used to view its back plane.

In order to establish a one-to-one spatial correlation between points of emission and detection, a mechanical collimator is placed at the front surface of the scintillation crystal. It usually consists of a block of lead in which parallel holes have been made. The absorptive collimator selects the direction of the photon momentum and restricts it to a very small solid angle.

Figure 1.1 illustrates the principle of operation of a scintillation camera. The PMTs output are weighted by means of analogue electronics and combined to produce a set of (x, y) co-ordinate signals locating the gamma ray interaction in the crystal. An energy signal (z) is also computed by summing the output signals of the PMTs. A pulse-height analyser prevents the recording of scattered and background radiation pulses by discarding those z signals that do not fall within a pre-set energy window.

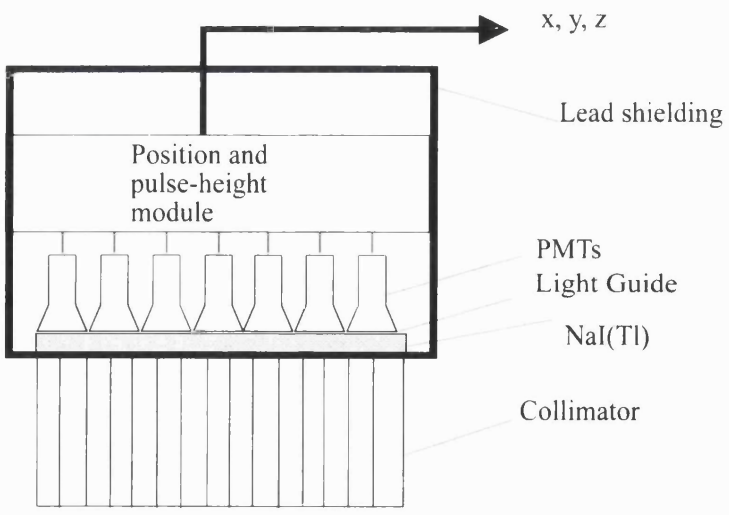

Fig. 1.1: Schematic diagram of the Anger camera.

Single view images obtained with the Anger camera are planar projections of three-dimensional source distributions. In Single Photon Emission Computed Tomography

(SPECT) the camera is rotated around the patient and multiple views can be acquired and combined to reconstruct images of cross sectional slices of the organ of interest. Transaxial, sagittal and coronal sectional images may be reconstructed to obtain information on three-dimensional anatomical structures.

1.2.2 Basic parameters in collimator design

The collimator is the most critical component determining the quality of the images obtained with the Anger camera. The collimator performs the essential function of establish a geometrical relationship between the photons and the detector. The first characteristic of any collimator is the material selected for its construction. As the collimation process relies on the absorption of the photons travelling along certain directions, high-density materials with high atomic number (Z) are employed, such as lead and tungsten, in order to maximise the probability of photoelectric interactions.

The first Anger camera had a simple *pinhole* collimator, which is a small aperture at the apex of a cone located more than 20 cm away from the detector plane. Other designs have since been developed in order to increase efficiency. The most common collimator employed in nuclear medicine imaging is of the *parallel-hole* type, in which all the holes are arranged with their axes perpendicular to the collimator face. The orientation of the hole axes may follow a different pattern (*converging* or *diverging* collimators) when specific applications require magnifying or minifying properties.

Geometrical considerations in hole size and septa thickness are another fundamental aspect in collimator design (see for example [Moore *et al.*, 1992], [Gunter, 1996]). The thickness of the septa is a function of the gamma-ray energy and it is designed to reduce penetration effects. A maximum septum penetration of 5% is usually accepted as reasonable criteria, thus resulting in a *septum thickness t* given by the following expression [Sorenson and Phelps, 1987]:

$$t \geq \frac{6d\,\mu^{-1}}{l - 3\mu^{-1}} \tag{1.1}$$

where d is the hole diameter, l is the physical length of the collimator holes and μ is the total linear attenuation coefficient of the collimator material at the energy of interest.

The physical dimensions of the holes play a major role in determining the system spatial resolution. The *collimator spatial resolution* is usually quantified by means of the width of its point spread function (PSF), which is the radiation profile obtained on the detector from a point source placed in front of the collimator. If the simple and most encountered case of a parallel hole collimator is considered and the thickness of the detector crystal is neglected, the following expression may be used for an approximate evaluation of the collimator resolution R_c, defined as the full width at half-maximum (FWHM) of the collimator PSF [Sorenson and Phelps, 1987]:

$$R_c \approx d\left(l_e + b\right) / l_e \tag{1.2}$$

where d is again the hole diameter, b is the distance between the source and the collimator and l_e is the collimator "effective length" or "effective thickness". The quantity l_e is related to the physical thickness l of the collimator by the equation $l_e = l - 2\mu^{-1}$, where μ is the total linear attenuation coefficient of the collimator material at the given energy. The collimator effective thickness is introduced to account for the effect of penetration. As can be seen from equation (1.2), small values of the ratio (d/l_e) provide better image quality.

The collimator *geometric efficiency g,* defined as the fraction of photons passing through the collimator per photon emitted by the source, can also be expressed in terms of the geometrical dimensions characteristic of the collimator (for a point source in air) [Sorenson and Phelps, 1987]:

$$g \approx K^2 \left(d / l_e\right)^2 \left[d^2 / (d+t)^2\right] \tag{1.3}$$

where d and l_e indicate the same physical quantities as in equation (1.2), t is the septal thickness and K is an adimensional constant that is a function of the hole shape (e.g. K~0.24 for round holes in a hexagonal array). This equation shows that g increases as the quantity $(d/l_e)^2$ is increased.

The *sensitivity* of an imaging system is the fraction of photons counted by the system per photon emitted by the source. The sensitivity S_{MCS} of a mechanically collimated system (MCS) can therefore be defined as the product of the geometric efficiency (equation (1.3)) and the photopeak detection efficiency ε_{det} of the scintillator crystal in the camera:

$$S_{MCS} = g\varepsilon_{\text{det}} \tag{1.4}$$

The photopeak detection efficiency is a function of the source energy: for photon energies up to 100 keV, the Anger camera is over 90% efficient, but at 511 keV it has an efficiency of about 15%. In case of radioactive distributions different than a point source in air, corrections are required to account for the attenuation losses within the object. The sensitivity of a γ-camera with a parallel hole collimator for ^{99m}Tc is typically between 100 and 200 cps/MBq.

Relationships (1.2) and (1.3) indicate that if the collimator is designed so as to increase spatial resolution (i.e. R_c is decreased) then efficiency (or sensitivity) is necessarily decreased and vice versa, according to the approximate relationship $g \propto R_c^2$. The appropriate geometric trade-off between efficiency and resolution is usually tailored to specific applications by collimator manufacturers. Collimators for low-energy photons are therefore typically available in the following designs: high efficiency (low resolution), high resolution (low efficiency) or general-purpose with

intermediate efficiency and resolution. Table 1.1 summarises the typical performance characteristics of commercially manufactured parallel-hole collimators with different properties.

Table 1.1: Performance characteristics of some typical commercially manufactured parallel-hole collimators [Sorenson and Phelps, 1987].

Collimator type	**Maximum energy of operation** (keV)	**Geometric efficiency g**	**Resolution R_c** (FWHM in mm at 10 cm collimator-source distance)
Low Energy, High Resolution	150	1.84×10^{-4}	7.4
Low Energy, General Purpose	150	2.68×10^{-4}	9.1
Low Energy, High Sensitivity	150	5.74×10^{-4}	13.2
Medium Energy, High-Sensitivity	400	1.72×10^{-4}	13.4

The total spatial resolution R_s of a gamma camera system is determined by the combination of the collimator resolution R_c with the intrinsic resolution R_i of the scintillation camera. The intrinsic resolution R_i is a measure of the precision with which interaction points can be localised in the uncollimated crystal. It is a function

of the crystal quality and geometry, of the optical readout system and it also depends on the photon energy. If the collimator and intrinsic PSFs are represented by Gaussian functions, the overall system resolution can be expressed as follows:

$$R_s = \sqrt{R_c^2 + R_i^2} \tag{1.5}$$

As the intrinsic resolution of modern cameras is in the order of 3 - 4 mm, it can be seen from the values reported in Table 1.1 that the collimator resolution is the dominant factor in determining the overall system resolution.

1.2.3 Problems associated with mechanical collimation

As described in the previous paragraphs, most of the radiation potentially useful to construct an image is actually absorbed in the collimator itself. Typically only 1 photon in 10^4 is transmitted by the collimator. The first problem associated with mechanical collimation is the inherent low efficiency of the process. This drawback is particularly evident in clinical applications, where statistical noise cannot be reduced by increasing the number of photons emitted by the source, as the dose to the patient is obviously of primary concern and must be kept to a minimum. Increasing the counting time is not a viable option either. The maximum time allowed for image acquisition is dependent upon the number of patients that can be examined per day. But more importantly it depends on the physical and biological time characteristics of the radiotracer, as well as on the need to perform fast dynamic studies; for example, cardiac imaging may require acquisition of up to 32 images during a single heart beat [Webb, 1988].

The energy of the radionuclide selected for imaging studies is another problematic aspect. Mechanical collimators cannot be optimised for radionuclides that emit multiple photons of different energies, such as ^{67}Ga (94 keV, 184 keV and 296 keV) and ^{127}Xe (172 keV, 202 keV and 375 keV), which are isotopes used in oncology studies and pulmonary ventilation imaging respectively. But the shortcomings of

mechanical collimation become more noticeable as the energy of the photons increases. SPECT imaging techniques with high-energy photons (at 511 keV in particular) offer great potential in clinical applications. Unfortunately, collimator performances in the high-energy range (over 300 keV) are not as satisfactory as in the case of low and medium energies. Typical values of resolution and sensitivity for high-energy collimators are reported in Table 1.2 and the performance of each collimator is shown at both high and low energy. It can be seen that their sensitivity is less than 50 cps/MBq, which is lower by a factor of 2 or 4 than the typical sensitivity of a low-energy collimator.

Table 1.2: Spatial resolution and efficiency of systems making use of Ultra High Energy (UHE) collimators at 511 and 140 keV. The values are obtained from measurements carried out by J. A. Patton et al. [Patton *et al.*, 1996].

Collimator type	**Energy of operation (keV)**	**System Sensitivity (cps/Bq)**	**Resolution R_s (FWHM in mm at 10 cm collimator-source distance)**
UHE parallel beam	511	4.19×10^{-5}	14.1
UHE parallel beam	140	4.82×10^{-5}	10.8
UHE fan beam	511	4.50×10^{-5}	7.4
UHE fan beam	140	5.09×10^{-5}	6.4

Septal penetration presents a major problem and dramatically affects image quality. Thick septa (2 - 4 mm) can prevent these effects, but they also increase the distance between adjacent holes, thus ultimately introducing further artefacts as the hole pattern become visible when the hole spacing ($d + t$) becomes comparable with the intrinsic resolution of the camera. This may be solved by introducing collimator rotation [Brunsden, 1975] so as to average out the hole pattern by motion. Such a solution however introduces the disadvantage of additional mechanical components, required for moving the collimator. Because of their absorption characteristics, high-energy collimators are also extremely heavy (100-200 Kg) and their weight may not be supported by the gantry of a standard gamma camera.

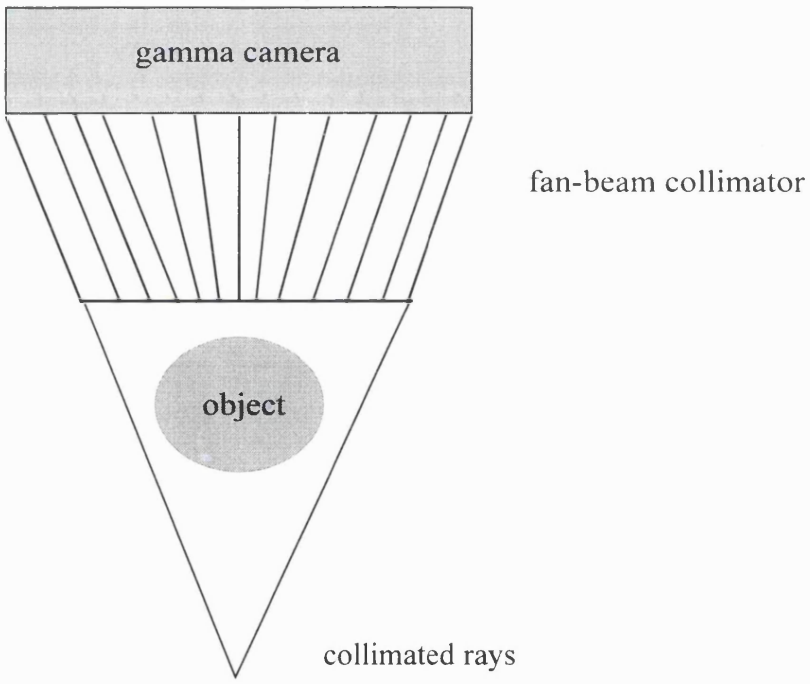

Fig. 1.2: Diagram illustrating the use of a fan beam collimator (see for example [Fahey and Harkness, 1996]). The collimator focuses the photons in the transversal direction, whereas in the axial direction these are collimated as parallel rays.

The use of UHE fan beam collimators (see Fig. 1.2) substantially improves the spatial resolution attainable at 511 keV and images of acceptable quality for clinical use may be produced [Patton *et al.*, 1996]. However, the sensitivity is still rather low (even if approximately 7% higher in comparison with parallel-hole collimators) and obtaining adequate counting statistics remains a problem for many clinical imaging situations. The clinical utility of fan beam collimators, the design and analysis of which is rather complicated, appears therefore to be limited by the maximum imaging time allowed for specific examinations.

In order to increase the sensitivity of high-energy medical SPECT systems, the use of coded aperture techniques has also been suggested as an alternative to conventional collimators [Zhang *et al.*, 1998]. This approach to collimation, which is normally employed in astronomy, was adapted to a near field γ-ray imager. Coded apertures are masks with spatially varying opacity, the pattern of which is designed according to a mathematical algorithm. The spatial distribution of a radiation source can be reconstructed by decoding the shadow that the rays project on the detector through the mask. Experiments conducted at 511 keV on a commercial gamma camera showed that the designed coded aperture provided higher sensitivity over parallel-hole collimators but poorer spatial resolution. Future work is aimed at optimising aperture size and system geometry so as to achieve high sensitivity whilst retaining spatial resolution.

1.3 Dual-photon electronically collimated cameras

1.3.1 Positron emitters for clinical use

The clinical utility of imaging positron emitters (PE) is well recognised. Some positron emitters are isotopes of elements of natural metabolites (such as glucose, ammonia and water) and it is therefore possible to label biological carriers without altering their biochemical structure and behaviour. The main advantage of positron emitters is the associated *in vivo* production of annihilation photon pairs, which can

be "electronically collimated" by means of sophisticated coincidence counting techniques. This method of detection makes it possible to achieve higher sensitivity and superior image quality in comparison with mechanically collimated cameras. Some of the physical characteristics and general properties of the four most commonly used β^+-emitting radionuclides are reported in Table 1.3.

Table 1.3: Characteristics of the positron emitter nuclides that are most commonly used [Gatley, 1996], [Hichwa, 1996].

Nuclide	Half-life (min)	β^+decay (%)	E_{max} (MeV)	Max β^+ range in tissue (mm)	Nuclear reaction
^{11}C	20.4	99.8	0.96	4.1	$^{14}N(p,\alpha)^{11}C$ $^{10}B(d,n)^{11}C$
^{13}N	10	100	1.2	5.1	$^{3}C(p,n)^{13}N$ $^{16}O(p,\alpha)^{13}N$
^{15}O	2.1	99.9	1.7	7.3	$^{14}N(d,n)^{15}O$ $^{15}N(p,n)^{15}O$
^{18}F	110	96.9	0.63	2.4	$^{18}O(p,n)^{18}F$ $^{20}Ne(d,\alpha)^{18}F$

PE nuclides are almost exclusively produced in cyclotron targets by a variety of nuclear reactions. The resulting nuclei are neutron-deficient and can therefore decay by positron emission. The positrons travel a short distance (in the order of a few mm in tissue) before annihilating with an electron of the surrounding medium. It is the detection of the two 511 keV annihilation photons that is the fundamental principle of PE imaging. The photons are emitted in diametrically opposed directions in the centre of mass of the system. In the laboratory system the decay is not exactly collinear, due to the residual kinetic energy of the annihilating positron. Because of their short half-life, the use of positron emitters normally requires a nearby nuclear accelerator. This on one hand has the disadvantage of making imaging examinations expensive and of limiting the routine availability of PE-labelled radiopharmaceuticals. On the other hand, the short half-life of these radionuclides has the advantage of resulting in a low absorbed dose to the patient and of allowing several studies to be made on the same subject on the same day.

Specific areas for the clinical application of PE include [Cook and Maisey, 1996]: cardiology (e.g. detection of coronary artery disease, detection of viable myocardium and evaluation of cardiac innervation); neurology (e.g. studies of cerebral metabolism and neurotransmission, investigation of neurological disorders such as Alzheimer's and Parkinson's diseases, schizophrenia and epilepsy); oncology (e.g. imaging of brain tumours, carcinoma of the lung, breast, head and neck, colorectal and pancreatic carcinoma). Some selected PE radiopharmaceutical agents and their use are shown in Table 1.4.

Table 1.4: Applications of selected positron-emitting radiopharmaceuticals [Gatley, 1996].

Radiopharmaceutical	**Use**
^{11}C-carbon monoxide	Labelling of haemoglobin in blood volume studies
^{11}C-hydroxyephedrine	Used as false neurotransmitter in assessing nerve terminal function
^{11}C-L-methionine	Incorporated into proteins for brain tumour metabolism studies
^{11}C-thymidine	Incorporated into DNA for tumour metabolism studies
^{13}N-ammonia	Diffuses as tissue amino acids (applications in myocardial perfusion)
^{15}O-water	Inert diffusible indicator (applications in brain/heart perfusion)
^{18}F-2-fluoro-2-deoxy-D-glucose (^{18}F - FDG)	Glucose utilisation in a variety of applications (brain scanning, myocardial metabolism, tumour scanning)
^{18}F-6-fluoroDOPA	Specificity for the striatum (applications in diseases with nigro-striatal degeneration, such as parkinsonism)
^{18}F-16-fluoro-17b-estradiol	Specificity for estrogen receptors that are over expressed in breast tumours
^{18}F-fluoromethane	Inert diffusible indicator (studies of cerebral blood flow)

1.3.2 PET scanners

The first positron emission tomography (PET) system that was developed for clinical use consisted of 48 cylindrical NaI(Tl) detectors in a hexagonal array [Hoffman *et al*, 1976]. Modern PET scanners have since evolved into very complex devices that are comprised of thousands of detectors. Typical PET systems now make use of 2.5- to 3.0-cm-thick bismuth germanate (BGO) scintillating crystals, which are approximately 75% efficient to 511-keV photons. The detectors are arranged into circular arrays or rings. The elements in one ring form the so called "direct detection planes". Coincidence counting (with a time window of 10-20 ns) is generally enabled between one detector and a number of opposite detectors in the ring, so as to cover the transverse field of view (FOV) that is required, as shown in Fig. 1.3. Rings of detectors are stacked one upon another so as to increase the solid angle of detection and the axial field of view of the tomograph. Detectors belonging to a given ring can participate in coincidence detection with elements of other rings, thus defining additional cross detection planes. The number of allowed cross planes can be limited by introducing absorptive collimators (septa) between rings (Fig. 1.4). To increase sensitivity, the inter-plane septa can be removed so as to make use of all ring combinations and operate the scanner in 3-D. A summary of the design parameters and performance characteristics of different modern PET scanners is presented in Table 1.5.

The spatial resolution in PET is high (typically in the range of 4-6 mm). The spatial resolution of a PET scanner depends primarily on the physical size and the geometrical configuration of the detector elements. However, as the resolution of the instrumentation is further improved, the finite range of the positron and the non-collinear decay pose an intrinsic limitation to this imaging technique, as it becomes difficult to determine the position of annihilation with respect to the point of emission of the positron. The ultimate limit on spatial resolution in PET may therefore be established as approximately 2 mm FWHM [Jarritt and Acton, 1996]. The absence of mechanical collimators and the ring design allow the PET detectors to cover a wider

field of view than gamma cameras. Sensitivities of PET scanners at the centre of the field of view in 2D-mode are in the order of 500 cps/MBq, which is approximately one order of magnitude greater than the sensitivities attainable in high-energy SPECT.

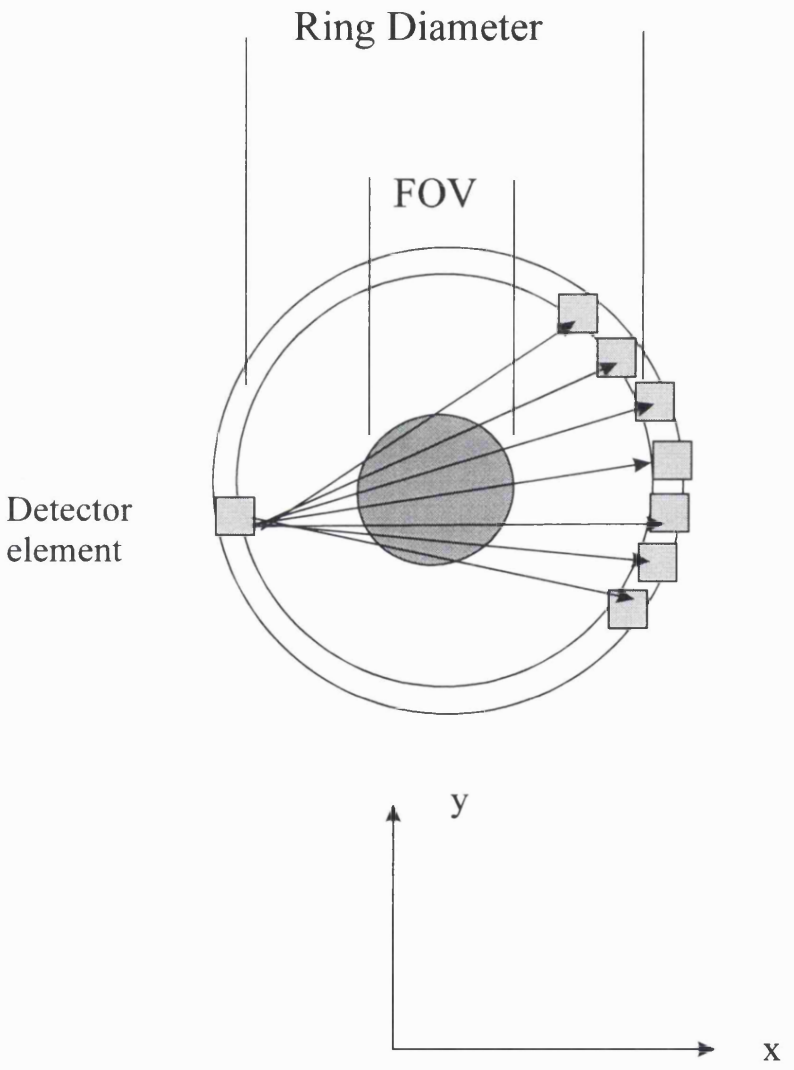

Fig. 1.3: Schematic diagram of a PET system. The diagram shows only the ring elements that take part in coincidence counting. Coincidence counting is enabled between the detector elements opposite a single detector if the coincidence rays intersect the transverse FOV in the (x, y) plane [Hichwa, 1996].

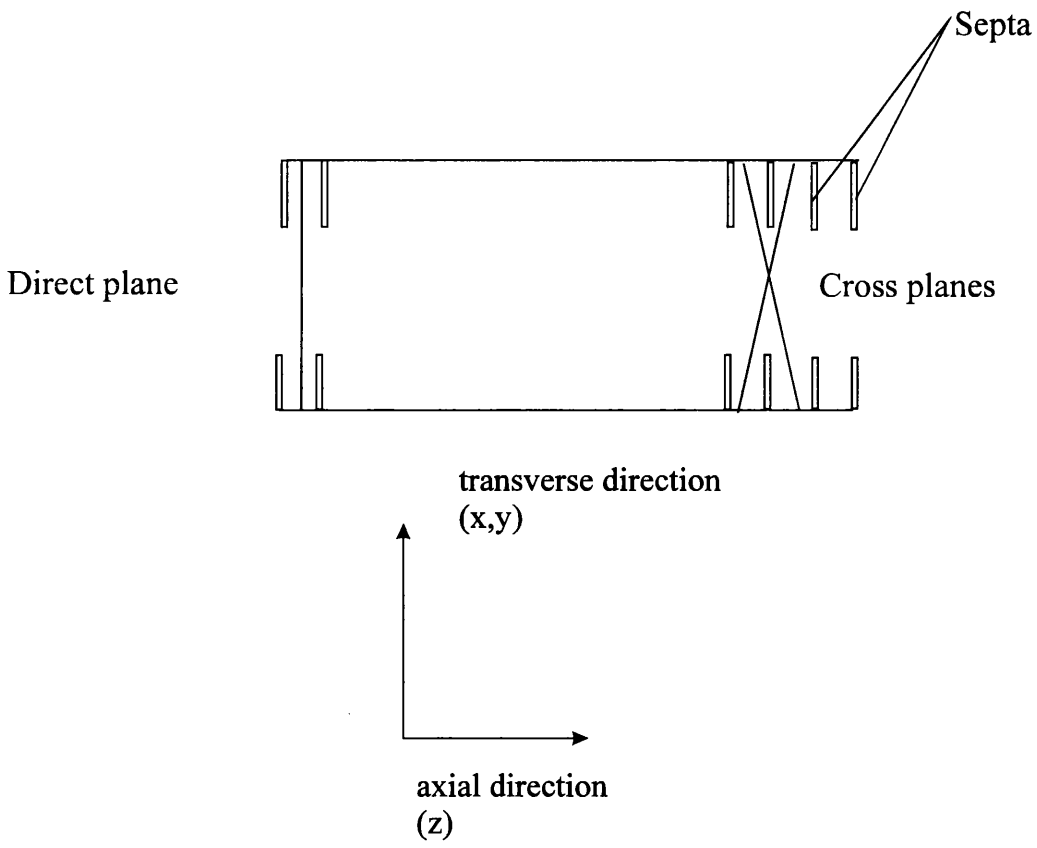

Fig. 1.4: Side view of a PET scanner with multiple rings. Detector elements in the same ring form a so-called *direct plane*. By enabling coincidence counting between elements of different rings, additional detection planes (*cross planes*) are introduced. Collimator septa can be placed between rings in order to limit the number of cross detection planes.

Table 1.5: Characteristics of some modern PET scanners [Erlandsson and Ohlsson, 1998].

Scanner	PC384-7B	ECAT III	Donner-600	ECAT 953B
Crystal type	BGO	BGO	BGO	BGO
Crystal size (mm x mm x mm)	12 x 20 x 30	5.6 x 30 x 30	3 x 10 x 23-30	5.16 x 6.15 x 30
Number of rings	4	2	1	16
Number of crystals/ring	96	512	600	384
Ring diameter (cm)	48	100	60	76.5
In-plane spatial resolution (FWHM in mm)	7.6	4.4	2.6	4.6
Sensitivity cps/(kBq ml^{-1}) per slice of a 20-cm-diameter cylindrical phantom	595	405	216	128

1.3.3 Dual-head coincidence gamma cameras

Although Positron Emission Tomography remains the gold standard technique for the clinical imaging of 511 keV photons, the high cost of PET scanners (typically from 1 to 3 million dollars) has prevented their implementation on a large scale. As a consequence, in recent years substantial effort has been invested in the development of high-energy imaging with γ-cameras of the Anger type.

The advantages of this approach include not only the widespread availability and lower cost (300-600 thousand dollars) of SPECT systems, but also the possibility of performing dual-isotope imaging in a single session. As mentioned in the previous sections, a variety of high-energy collimators have been designed to enable conventional gamma cameras to perform single-photon PE imaging [Patton *et al.*, 1996], [Bax *et al.*, 1995], [Drane *et al.*, 1994], [Van Lingen *et al.*, 1992].

Attention has focussed on the use of ^{18}F-2-[fluorine-18]fluoro-2-deoxy-D-glucose (FDG) (see Table 1.4), a well-established radio-pharmaceutical employed in a number of clinical applications, such as measurement of brain metabolism, myocardial viability assessment and tumour imaging. Because of the relatively long half-life of ^{18}F (110 minutes - see Table 1.3), ^{18}F-FDG can be produced remotely and delivered to medical facilities that do not have access to an on-site cyclotron. However, although the use of mechanical collimators for 511 keV photons has been proved to be feasible, inadequate counting statistics and low resolution seem to limit their applicability to cardiac studies.

In order to overcome these shortcomings, a more promising route has recently been followed with the development of dual-headed coincidence imaging (DHCI) [Wollenweber *et al.*, 1998], [Lewellen *et al.*, 1997], [Miyaoka *et al.*, 1996], [Miyaoka *et al.*, 1995]. In order to perform DHCI, the mechanical collimators of a dual-head gamma camera are removed and the system is provided with custom electronics for coincidence detection (see Fig. 1.5). All current DHCI systems are based on NaI(Tl)

detector technology, but with thicker crystals (up to 1.9 cm) than in conventional gamma cameras. For such detectors the photo-peak efficiency at 511 keV is approximately 20%, which is almost double the efficiency of a standard 9.5-mm-crystal (~ 11%). This is still, however, almost four times less efficient than a standard 3-cm BGO crystal of a PET scanner.

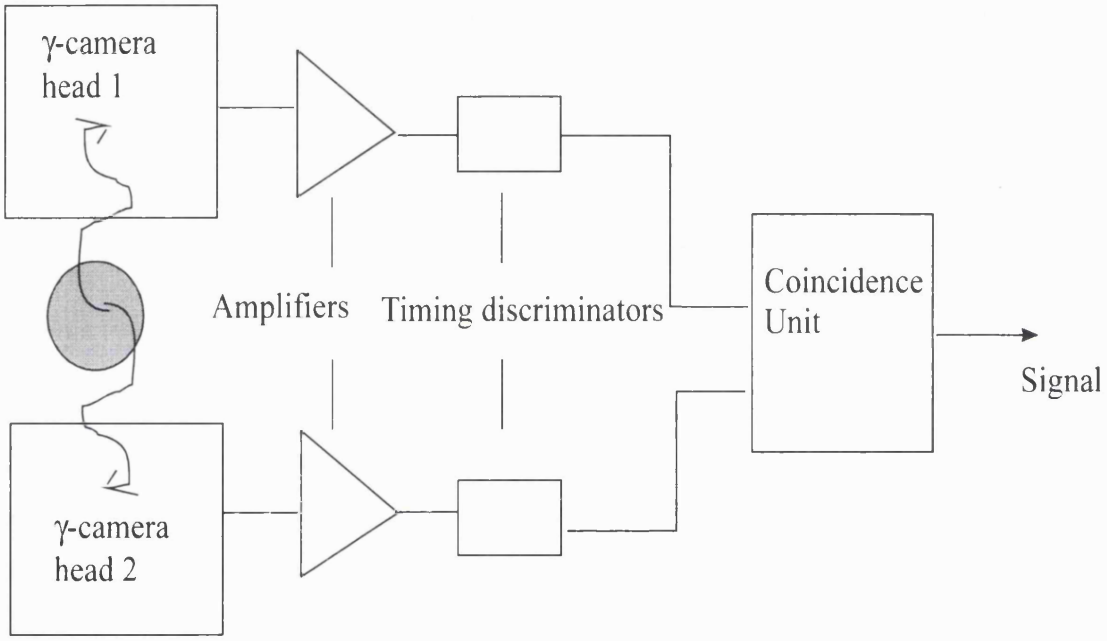

Fig. 1.5: Schematic diagram of the basic components of a dual-head coincidence gamma camera (see for example [Lewellen *et al.*, 1999]).

Several studies [Hasegawa *et al.*, 1999], [Wollenweber *et al.*, 1998], [Lewellen *et al.*, 1999] have shown that DHCI provides superior sensitivity and resolution than high-energy, mechanically collimated SPECT. The spatial resolution at the centre of the field of view of a 20-cm diameter cylinder phantom is in the order of 4-5 mm FWHM, thus comparable to PET. The DHCI sensitivity, however, is lower than PET and is limited by the high rate of single events. The authors of a recent study [Hasegawa *et al.*, 1999] have compared directly ^{18}F-FDG PET, ^{18}F-FDG SPECT with ultra-high-energy general purpose collimators (UHGPs) and ^{18}F-FDG DHCI for the assessment of myocardial viability. The specifications of the three imaging systems are reported in Table 1.6.

Table 1.6: Characteristics of the three imaging systems employed in a recent study that compared DHCI and UHGP-SPECT to PET in ^{18}F-FDG-imaging for the detection of viable myocardium [Hasegawa *et al.*, 1999].

Imaging system	**PET**	**DHCI**	**UHGP-SPECT**
In-plane resolution (FWHM in mm)	3.7	4.8	9.2
Sensitivity (in cpm/MBq/ml)	440	160	15

The system sensitivity of the DHCI system was approximately one order of magnitude higher than UHGP-SPECT and approximately a factor of 3 lower than PET. The FWHM spatial resolution of the DHCI system was also better than UHGP-SPECT. The results on the diagnostic accuracy of DHCI and UHGP-SPECT for the assessment of viable myocardium are summarised in Table 1.7, where the findings of PET are considered the gold standard. Image quality, which was expressed as target-to-background ratios, proved to be better in DHCI than in collimated SPECT. However, diagnostic agreement between coincidence imaging and PET (expressed in

terms of the technique sensitivity[6]) was surprisingly low. The sensitivity of DHCI improved with the application of attenuation correction, although the results were still more accurate with UHGP-SPECT rather than with DHCI.

Table 1.7: Results of the study for the comparison of collimated SPECT and dual-head coincidence cameras in ^{18}F-FDG imaging for the detection of myocardial viability [Hasegawa *et al.*, 1999]. The sensitivity[6] and specificity of SPECT and DHCI were evaluated in this study by using the PET findings as the gold standard.

Index	**DHCI** *without* attenuation correction (%)	**DHCI** *with* attenuation correction (%)	**UHGP-SPECT** (%)
Sensitivity[6]	18.8	48.4	67.2
Specificity	92.6	94.6	91.6

The development of attenuation correction techniques is therefore a major area of interest for the future progress of DHCI. The count rate capability of DHCI systems is in the order of 3,000-10,000 cps (true events), which is higher than collimated SPECT (~1,000 cps per detector) but is lower than most PET scanners in 2D-mode imaging by at least a factor of 10 [Lewellen *et al.*, 1999]. Because of its high spatial resolution capability, the most promising clinical niche for DHCI is in oncology, as a relatively low-cost ^{18}F-FDG-imaging tool. However, the count rate capability and sensitivity of DHCI systems may not improve sufficiently so as to fulfil the requirements of studies with short-lived emitters, such as ^{11}C and ^{15}O.

[6] Please note that in this context the term "sensitivity" has a completely different meaning than in Table 1.6, where it is used to represent the efficiency of an imaging system. The "sensitivity" is here a statistical index, which measures how frequently a technique or clinical test is positive in the population with a disease. The "specificity" measures how frequently the test is negative in the population without the disease.

1.4. Single-photon electronically collimated gamma cameras: the Compton camera

1.4.1 The principle of Compton scatter imaging

The Compton camera is a type of gamma-camera that makes use of the kinematics of Compton scatter to construct the image of a radioactive distribution without the aid of mechanical collimators. The principle of a gamma camera based on the Compton effect was initially proposed by Todd et al. [Todd *et al.*, 1974]. In the Compton camera the conventional absorptive collimator is replaced with a second detector, which electronically collimates the photons by recording the Compton scatter information.

The basic camera design consists of two planar detectors with position sensitive and energy resolving capabilities, placed in a known location with respect to each other and operating in coincidence (Fig. 1.6). The location of a point source is defined by the back projection and intersection of conic surfaces in the image space. Each cone corresponds to a single source emission, which is followed by a single Compton interaction in the front detector and a second interaction of the scattered photon in the back detector volume.

The cone semi-aperture θ is the Compton scatter angle and can be determined from the recoil electron energy E_{re} measured in the front detector, if the source energy E_γ is known:

$$\cos\vartheta = 1 - m_0 c^2 \left(\frac{1}{E_\gamma - E_{re}} - \frac{1}{E_\gamma} \right) \tag{1.6}$$

where $m_0 c^2$ is the electron rest-mass energy ($m_0 c^2$ = 0.511 MeV).

The cone axis is defined by the line joining the points of interaction in the two sensors. If an image plane is defined to intersect the cones, the point source will be imaged as the overlap of curves, which are generally ellipses but can be in some cases parabolas or hyperbolae.

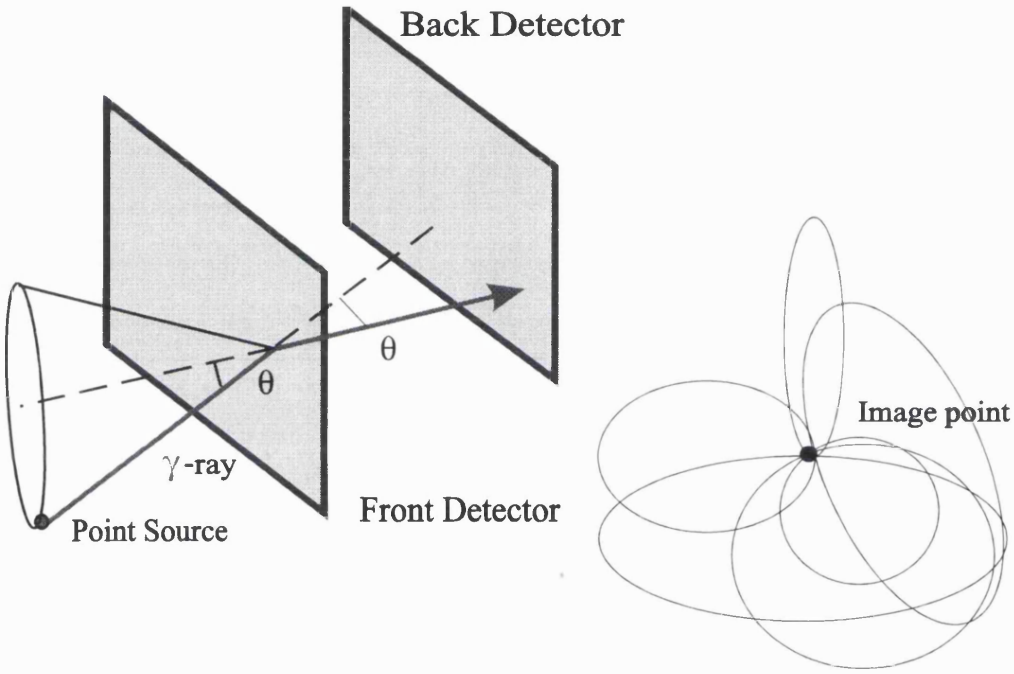

Fig. 1.6: Illustration of the principle of functioning of the Compton camera.

If the source is not placed in air or void, the events produced by the photons that have scattered in the medium before reaching the first detector should be rejected. This is done by selecting Compton scattered photons that are photo-electrically absorbed in the back detector and by ensuring that the sum of the energies deposited in the two detectors matches the energy of the source within a set window.

The tracking of the original direction of the emitted photons is strongly dependent on the accuracy with which the parameters of the conic surfaces are determined. The energy resolution and position resolution of the detectors therefore play a major role in locating the point source and in ultimately determining the quality of the image.

The imaging principle is described here for a simple point source. An extended radiating object may be thought of as a distribution of point sources. The depth and the inclination of the image plane are arbitrary variables. Thus, one can back-project the cones onto a multitude of planes and obtain a variety of sections through the object (from the same set of experimental data) that can be combined to obtain images in three dimensions.

A Compton scatter camera offers many potential advantages over other imaging systems. In comparison to lead-collimated cameras, its principle of operation could provide higher efficiency and a wider field of view. Unlike conventional SPECT systems, Compton cameras do not require to view the object at different angles around its axis in order to reconstruct 3-D images. The absence of heavy components would also allow the construction of a more compact and lightweight system, which could be built as a portable unit for many imaging applications.

Compton cameras have been proposed in the scientific literature for a variety of applications including gamma-ray astronomy, high-energy imaging in the nuclear industry and medical imaging. Few experimental prototypes have, however, been constructed. In the following paragraphs, the most interesting achievements and recent results in the design and experimental development of Compton cameras are reviewed for these three main areas of application.

1.4.2 Compton telescopes

Gamma ray telescopes using Compton scatter techniques have been employed as an efficient method to observe low fluxes of cosmic radiation sources in the 0.3 - 30 MeV energy range. The astrophysical observations are aimed at objectives such as mapping the nuclear line emissions across the Galaxy, studying the diffuse gamma-ray background, the occurrence of supernovae, etc. The emissions from the sources of interest consist of both discrete spectral lines and continuum radiation. The sensitivity of a Compton telescope is a measure of how intense these sources need to be in order to be imaged. The point-source sensitivity of a Compton γ-ray telescope can be expressed as a function of the background and source counts, the detection area and the observation time [Schönfelder *et al*, 1993]. The sensitivity limit (photons cm^{-2} s^{1}) is usually employed to characterise the performance of a Compton telescope.

One of the first designs of a Compton telescope [Zych *et al.*, 1979] utilised two large-area (1 m^2) arrays of scintillators separated by a distance of 1.25 m. This design is since known as the "double Compton telescope". The first array consisted of ten linear plastic scintillation detectors (1-m long), with cross-sections of 10 cm x 10 cm. The second array was made of ten linear NaI(Tl) detectors of the same size and configuration as the first array. This telescope was specifically designed for satellite observations in the medium energy range (1-30 MeV). The angular resolution of the system was approximately 5.5° HWHM (Half Width at Half Maximum) at 1 MeV and 3° HWHM at 6.1 MeV. The estimated sensitivity for discrete sources of line emission (1 MeV) was 3 x 10^{-5} γ cm^{-2} s^{-1}. A more recent version of this telescope (flown by balloon in 1989) was developed at UCR (University of California at Riverside) [Ait-Ouamer *et al.*, 1990] by combining two planes made up of bars of plastic scintillator (16 units, each having a size of 6.35 x 7.62 x 103 cm^2) and NaI(Tl) (16 units, each having a size of 4.83 x 4.83 x 102 cm^3) respectively.

The Compton telescope COMPTEL [Schönfelder *et al*, 1984] was until recently the observation instrument available in gamma-ray astrophysics with the best angular

resolution properties. The instrument, which was the result of an international collaboration including the Max Planck Institute for Extraterrestrial Physics, the University of New Hampshire, the Space Research Organisation of Netherlands and ESA[7], was launched in 1991 on board the NASA[8]'s COMPTON Gamma Ray Observatory (CGRO). The Observatory mission ended in June 2000 via a controlled re-entry following technical failure of one of its gyroscopes. COMPTEL consisted of an open array of seven upper cells filled with a liquid scintillator (each one was 28 cm in diameter and 8.5 cm deep) and fourteen lower NaI scintillation units (each one was 28 cm in diameter by 7.5 cm in depth). An angular resolution (1 σ width of the point spread function) of 2° and 1.3° was obtained respectively at 1.2 and 2.75 MeV. The telescope was able to cover the γ-ray energy range from 0.75 MeV to 30 MeV. The sensitivity of the instrument to line emissions at 1 MeV was down to approximately 2 x 10^{-5} γ/(cm^2s) [Schönfelder *et al.*, 1993].

The next generation of Compton telescopes aims to advance the level of observation beyond the current standard set by COMPTEL. The requirements on the performance of a new instrument include: the capability of operating in the 300 keV - 30 MeV γ–ray energy range; an angular resolution better than 0.5° at 1 MeV; sensitivities approaching 10^{-7} γ/(cm^2s) in the low-energy range (511 keV – 2 MeV) [Kurfess, 1998]. These goals pose very stringent requirements on the energy resolution (~ a few keV) and spatial resolution (~ 1 mm) of the detectors. Different configurations, based on state-of-the-art position sensitive detectors, have been proposed. All the proposed designs involve the use of solid-state detectors, with the exception of one telescope that consists of a liquid gas detection chamber.

A new Compton telescope design has been developed within the Tracking and Imaging Gamma-ray Experiment (TIGRE) [O'Neill *et al.*, 1992]. This telescope configuration aims to improve the COMPTEL sensitivity by one order of magnitude.

[7] *European Space Agency*
[8] *National Aeronautic and Space Administration*

It is estimated that at 2 MeV of energy a telescope sensitivity could be achieved down to 1.6 x 10^{-6} γ/(cm^2s). A small laboratory prototype was constructed with 7 double sided silicon strip detectors (3.2 cm x 3.2 cm x 300 μm with 1 mm pitch in both the x and y directions), which were used to track the recoil electron from the Compton interaction and measure its energy [O'Neill *et al.*, 1995]. The energy and the position of interaction of the scattered photon were determined using 36 CsI(Tl) photodiode detectors (1 cm x 1 cm x 1.7 cm). The silicon detectors were separated by a distance of 6.5 mm. The 36 scintillation crystals were grouped into four arrays of nine units each and were placed at a distance of 26 cm from the silicon detectors. The innovative feature of tracking scattered electrons would allow easy discrimination between upward and downward photons. Tests carried out with a point source at 511 keV and 900 keV showed an angular resolution of 11° and 10° (FWHM) respectively.

A similar approach has been recently adopted by the Max Planck Institute with the design of the MEGA telescope (Medium Energy Gamma-ray Astronomy telescope), a successor for COMPTEL that aims to extend the energy range of observable γ-rays from 0.5 MeV to 50 MeV [Schopper *et al.*, 1999]. The design consists of a stack of double-sided silicon strip detectors, which act as the Compton scatter unit and allow the recoil electron to be tracked, so as to determine the orientation of the incident photon. The scattered photon is absorbed in a calorimeter that consists of small CsI(Tl) scintillation bars coupled to silicon PIN photodiodes and low-noise electronics. The silicon detectors in the tracker have a sensitive area of 6 cm x 6 cm, a thickness of 0.5 mm and a pitch of 0.47 mm on both sides. The calorimeter is highly segmented. It is made up of several blocks that surround the side and the bottom of the tracker. Each block is a monolithic array of 10 x12 CsI(Tl) bars, with pixel size of 5 mm x 5 mm. Bars of different depths (2 cm and 8 cm) have been tested with single-side and double-side readout respectively [Schopper *et al.*, 2000]. A small prototype is currently being developed with 11 silicon layers, where each layer is a matrix of 3x3 strip detectors. The design of the future telescope will include 4 adjacent towers,

each being made up of 32 layers. The high spatial resolution of the detectors should allow the tracker to be as close as possible to the calorimeter, thus making the telescope more compact and efficient. Simulations of the prototype design indicate that at 2 MeV an angular resolution of approximately 1° FWHM may be obtained. The telescope is expected to achieve an approximate sensitivity gain of one order of magnitude over COMPTEL in the 0.5-50 MeV energy range.

Another concept being investigated is the feasibility of building a large-area, high-resolution Compton telescope (ATHENA, Advanced Telescope for High Energy Nuclear Astrophysics) based on position sensitive germanium detectors [Johnson *et al.*, 1995]. The telescope has been designed to cover the energy range from ~ 300 keV to above 10 MeV. An initial study was carried out using a 25 x 25 strip (2 mm pitch, 11 mm thick) Ge detector in combination with a 5 x 5 strip (9 mm pitch, 11 mm thick) Ge detector [Phlips *et al.*, 1996]. The two sensors were separated by a 45 cm distance. The imaging capabilities of the detectors as a near-field Compton telescope were tested with a ^{137}Cs (662 keV) point source, located at a distance of 8 cm from the front plane. An angular resolution of approximately 1° FWHM was obtained. The design of the actual astronomic telescope should consist of two 1-cm thick germanium detector layers acting as the front scatter component and six germanium detector layers placed behind for the detection of the Compton scattered photons. The back six layers would be separated from the first two by a distance of 1 metre. It is estimated that a 1-m^2 Ge telescope would achieve a line sensitivity down to ~ 7 x 10^{-7} $\gamma/(cm^2 s)$ at 1 MeV.

Finally, a Liquid-Xenon Gamma-Ray Imaging Telescope (LXeGRIT) is under development at the Astrophysics Laboratory of Columbia University with NASA support and with the collaboration of other universities and space centres [Aprile *et al.*, 1996]. The design is based on the use of two liquid-gas time-projection chambers (TPCs) in coincidence. The upper chamber is filled with liquid argon (LAr-TPC) and operates as a scatter detector. The lower chamber is filled with liquid xenon (LXe-

TPC) and acts as an absorption detector for the scattered photons, although it can also work as an independent Compton telescope for those photons that fail to scatter in the upper chamber (the double detector configuration is preferred as it improves the angular resolution of the telescope). In order to demonstrate the feasibility of the LXeGRIT design, a small LXeTPC prototype has been developed and operated as a Compton telescope. After successful laboratory testing, the same prototype was successfully flown by balloon for the first time in 1997 [Aprile *et al.*, 1998].

In this specific design of Compton camera, the primary scatter event and subsequent photon interactions (multiple Compton and/or photo-absorption) are recorded within a homogeneous detector. The chamber has a total volume of 10 litres and a sensitive area of 400 cm^2. The cathode is at the top of the chamber and the anode is at the bottom. An X-Y mesh (consisting of two planes of 62 parallel wires each, in orthogonal direction) separates the active volume into a 7-cm drift gap (between the mesh and the cathode) and a narrow collection region between the mesh and the anode. Both the ionisation and the primary scintillation light produced by the electrons are detected. The scintillation photons are detected by four UV sensitive photo-multipliers, coupled to the anode by quartz windows. The scintillation light provides the event time zero, so as to infer the Z co-ordinate of the event. The ionisation electrons drift across the chamber gap in a uniform electric field towards the mesh, where they induce signals that are used to obtain the X-Y co-ordinate information. The collection signal on the anode is used to determine the energy deposition associated with the event. Amplitude and timing analysis allows differentiation between subsequent interactions, so as to make use of Compton kinematics to reconstruct the direction of the incoming γ-ray.

The angular resolution of the 10-litre LXeTPC prototype at 1 MeV is ~ 2° (1 σ width of the point spread function), with a line sensitivity down to 5.7 x 10^{-5} γ/(cm^2s). The two detectors proposed for the LXeGRIT design will have a sensitive area of ~ 4000 cm^2, a ten-fold increase over the LXe-TPC prototype. It is estimated

that, assuming a separation distance $\geq$ 50 cm, the combined operation of the two chambers will achieve an angular resolution $\leq$ 0.14° (1 σ width of the point spread function at 10 MeV). The line sensitivity of LXeGRIT is expected to be down to 1.6 x 10^{-6} $\gamma/(cm^2 s)$ at 1 MeV and 2.8 x 10^{-7} $\gamma/(cm^2 s)$ at 10 MeV.

A summary of the characteristics of the Compton telescopes described in this section is given in Table 1.8.

Table 1.8: Summary of properties of the designed and/or constructed Compton telescopes that are described in the text.

Detector Configuration	**Energy**	**Angular resolution (FWHM)**	**Sensitivity** (γ cm^{-2} s^{-1})	**Type of system**
Linear array of plastic scintillators + NaI(Tl) crystal array	1 MeV 6 MeV	~ 11° ~ 6°	3 x 10^{-5} -	Double Compton telescope [Zych *et al.*, 1979]
Array of liquid scintillator cells + NaI(Tl) crystal array	1 MeV 3 MeV	~ 5° ~ 3°	2 x 10^{-5} -	COMPTEL [Schönfelder *et al.*, 1993]
Stack of Si microstrip detectors + CsI(Tl) modules	2 MeV 511 keV 900 keV	- ~ 11° ~ 10°	1.6 x 10^{-6} - -	TIGRE telescope [O'Neill *et al.*, 1995]
Stack of Si microstrip detectors + CsI(Tl) modules	0.5 – 50 MeV 2 MeV	- ~ 1°	0.1 x COMPTEL -	MEGA telescope [Schopper *et al.*, 1999]
2 x Ge strip detectors	662 keV 1 MeV	~ 1° -	- 7 x 10^{-7}	ATHENA [Johnson *et al.*, 1995]
2 x Time Projection Chambers (LArTPC + LXeTPC) in coincidence	1 MeV 10 MeV	- $\leq$0.3 °	1.6 x 10^{-6} 2.8 x 10^{-7}	LXeGRIT [Aprile *et al.*, 1996]

1.4.3 Compton cameras for applications in the nuclear industry

The interest in Compton cameras for imaging applications in the nuclear industry is mainly associated with the potential portability of such devices. Possible applications include environmental monitoring and radioactive waste management at industrial sites. Accurate non-destructive analysis of radioactive waste containers requires the source distribution to be localised within the container. This makes it possible to suitably correct for attenuating materials when estimating the activity in the container, thus reducing the costs of handling and storage that may be associated with overestimation of activity.

A new Compton camera design, the Ring Compton Scatter Camera, was proposed by Martin and Singh in order to image radio-nuclides of industrial interest in the medium energy range (from 0.5 to 3.0 MeV) [Martin *et al.*, 1993]. It consisted of a 4 x 4 planar array of HPGe detectors (5 mm x 5 mm x 6 mm) surrounded by a ring array of 8 cylindrical NaI(Tl) crystals (19.1 mm in diameter and 50.8 mm in length). The scintillators were equally spaced in the azimuthal angle around the ring, with the same central scattering angle and centre-to-centre distance from the germanium array. The camera geometry allowed the central scatter angle to be varied between 15° and 60°. The distance of the scintillator modules from the Ge collimator could be varied between 15 cm and 70 cm. The ring shape for the second detector was designed to reduce the fraction of recorded events from small-angle scatter and from unscattered photons. However, as the ring subtended a smaller range of Compton scattering angles, such design showed lower efficiency in comparison with the use of a planar back detector. Point sources of ^{137}Cs were imaged with an angular resolution of 9.1°. The absolute efficiency of the camera (defined as the number of events contributing to the image per photon emitted by the source) was measured to be approximately 4.5×10^{-7} (assuming a scatter angle of 45°, a separation distance between front and back detectors of 30 cm and a distance of 10 cm between the source and the electronic collimator).

A second prototype was later developed with 16 NaI(Tl) crystals [Martin *et al.*, 1994]. This work was aimed at investigating the capability of the camera to image multi-energy gamma-ray fields, as such fields are often of interest in the nuclear industry. Photons with different energy were discriminated on the basis of the sum of the energy signals deposited in the two detectors. The spectral imaging capability of the system was demonstrated by acquiring images of a phantom containing simultaneously the isotopes ^{64}Cu (0.511 keV) and ^{65}Zn (1.116 MeV). The same authors have more recently proposed the replacement of the germanium collimator with a room-temperature operating Si(Li) detector, so as to improve the system portability [Evans and Martin, 1996].

A prototype camera for gamma ray imaging within industrial sites was constructed by Royle and Speller [Royle and Speller, 1994]. The system was based on the use of germanium and NaI(Tl) detectors. Three different configurations were tested with ^{137}Cs point sources. An angular resolution of approximately 11° was achieved with a camera made of two large-element (5 cm x 5 cm) NaI(Tl) detectors. A combination of two small-element (1.6 cm x 1.6 cm) HPGe detectors provided an angular resolution of ~ 7°. An angular resolution of approximately 9° was obtained with a "mixed" configuration featuring both HPGe and NaI(Tl) as front and back detector respectively. The same authors have more recently suggested a modular structure for a flexible, low-cost Compton camera to be used in industrial radiation environments with restricted access [Royle and Speller, 1996]. The work was carried out on behalf of British Nuclear Fuels for applications in their reprocessing plant in Sellafield, UK. A prototype camera was built with three 1 x 1 x 1 mm^3 NaI(Tl) detectors arranged in a small cluster and operating in coincidence. The camera was evaluated in a laboratory simulation of a limited-access industrial site; a point spread function of 17 cm at 1-m distance was measured for ^{137}Cs point sources. After the laboratory evaluation, the system was used to image a real decommissioning environment at the Sellafield plant [Royle and Speller, 1997]. It produced the world's first land based images within an actual, highly active decommissioning site. Simulation studies

suggested the possibility of replacing the scintillators with CdZnTe semiconductor detectors. It is predicted that such a system would achieve an angular resolution of approximately 6-7°.

The capability of generating non-tomographic three-dimensional images with an all-germanium Compton camera was demonstrated by McKisson *et al.* [McKisson *et al.*, 1994]. A Compton camera prototype was built with eight HPGe coaxial detectors (each 4 cm in diameter and 4 cm long) configured in two planes of four detectors each. The point source FWHM resolution for a ^{137}Cs source varied from 0.5 to 1 cm depending on the source-camera distance ranging from 25 cm to 1m. The system was tested to prove the feasibility of Compton imaging as a non-destructive testing technique for the evaluation of mixed waste containers [King *et al.*, 1994]. Separation of multiple lines with different intensities was reported using ^{137}Cs, ^{60}Co and ^{133}Ba sources. Experiments with sources placed in water-filled drums were also carried out in order to investigate the effects of surrounding media in a high scattering environment. A point spread function of 6.6 cm (FWHM) was obtained at 662 keV of energy and at a distance of 1 m between the camera front detector plane and the drum centre.

A novel approach has been recently proposed with a design that combines mechanical collimation (based on the use of coded-apertures) with electronic collimation (based on Compton scatter) [Smith *et al.*, 1998]. This hybrid camera was specifically designed as an industrial γ-ray imaging system, with the aim of providing good angular resolution and efficiency over a broad energy range (50 keV - 3 MeV). The system comprises a coded aperture placed at 20 cm distance in front of a first scintillation detector, consisting of a 100 x 100 x 10 mm^3 NaI(Tl) crystal with a four-phototube Anger logic readout. A second detector is placed at a 30° central scatter angle and at a 35-cm distance angle with respect to the first one. The second detector is a CsI(Na) crystal of 7x7 pixels (the size of each pixel is 9 x 9 x 30 mm^3), coupled to a position sensitive photomultiplier tube (PSPMT). The hybrid camera was

designed with the aim of optimising the characteristics of the imaging system as a function of the photon energy. The basic idea is that at low energies (< 300 keV) the photons are mechanically collimated onto the first detector, where they are photo-electrically absorbed as in a conventional gamma camera. For higher-energy photons (> 600 keV) the system can operate in a Compton camera mode. At such energies the coded mask will not be a significant attenuator and many photons will Compton scatter in the first scintillator before being absorbed in the second detector. At intermediate energies (300-600 keV), complementary data sets from both mechanically and electronically collimated photons can be combined to reconstruct the source image. Monte Carlo modelling of the hybrid camera predicts an intrinsic efficiency (defined as the probability that a photon incident on the front detector will result in a useful imaging event) ranging from approximately 0.5 to 1 $x10^{-4}$. An angular resolution of 3-5° is predicted over the 50 keV – 3 MeV sensitive energy range.

The characteristics of the industrial Compton cameras described in this section are summarised in Table 1.9.

Table 1.9: Summary of properties of the designed and/or constructed industrial Compton cameras that are described in the text.

Detector Configuration	**Energy**	**Angular resolution** [9] (FWHM)	**Type of system**
Small-element planar HPGe array + ring array of NaI(Tl) crystals	662 keV	~ 9°	Laboratory prototype for industrial use in the 0.5 – 3 MeV energy range [Martin *et al.*, 1993]
a) 2 x Large-element NaI(Tl) b) 2 x Small-element HPGe c) HPGe + NaI(Tl) d) triangular cluster of NaI elements	662 keV	~ 11° ~ 7° ~ 9° ~ 9.6°	Industrial prototype for imaging applications within limited access industrial sites [Royle and Speller, 1997]
2 x planes of 4 HPGe coaxial detectors	662 keV (in air) (in a water-filled drum)	~ 1° ~ 4 °	Prototype for applications in nuclear waste imaging [McKisson *et al.*, 1994]
Coded aperture + NaI crystal + CsI(Na) crystal	50 keV-3 MeV	3-5°	Hybrid portable Gamma camera [Smith *et al.*, 1998]

[9] The FWHM angular resolution, when not explicitly reported by the authors, has been evaluated as $\Delta\vartheta_{FWHM}$ from the following relationship [Singh, 1983] (equation 2.5 in section 2.5.1 of Chapter 2): $\Delta S_{FWHM} = D \tan(\Delta\vartheta_{FWHM})$, where ΔS_{FWHM} is the FWHM spatial resolution and D is the source-electronic collimator distance.

1.4.4 Compton cameras for medical imaging

The idea of a Compton camera aimed at clinical applications was initially proposed by Todd *et al.* [Todd *et al.*, 1974]. The authors suggested the use of a single three-dimensional lattice consisting of orthogonal arrays of 0.5 mm silicon cubic elements. The tracking of photons would be achieved by measuring the (x, y, z) co-ordinates of the first two consecutive events in multiple Compton interactions. Practical problems were however highlighted in the hypothetical construction of an actual camera, particularly in association with the difficult task of determining the sequential order of interactions. A subsequent study by the same authors proposed a different camera design, which employed a stack of 50 5-cm diameter discs, each forming a two-dimensional array of silicon diodes [Everett *et al.*, 1977]. Suggestions were also made in order to initially build a simple two-layer prototype, where the sequential order of interactions would be more easily determined.

The theoretical work of Todd and Everett was followed in the early eighties by the pioneering experimental work of Singh and Doria [Singh and Doria, 1983], who built the first working prototype of a Compton camera for medical use. Since then, a growing interest has been reported on the design and experimental development of Compton cameras for nuclear medicine applications, due to the rapid advances in the technology of position sensitive detectors. The following paragraphs describe the most important contributions made to this specific field during the last twenty years. State-of-the–art developments include collimator designs based on the use of both semiconductors and gaseous scintillators.

I) Germanium collimators

As previously introduced, the first experimental device ever constructed for medical imaging was designed by Singh and Doria in 1983. It consisted of a single 6-mm-diameter x 6-mm-thick germanium element coupled to a conventional uncollimated scintillation camera in a coincidence detection mode. The separation between the Ge detector and the γ–camera was 5 cm. Images of ^{99m}Tc and ^{137}Cs point sources were

obtained, thus demonstrating for the first time the feasibility of electronically collimating single photon emitters. A spatial resolution of approximately 0.7 cm was obtained for a ^{99m}Tc (140 keV) point source located on the central axis at a distance of 4.3 cm from the detector. A ^{137}Cs (662 keV) point source, located at a 2.6 cm distance, produced a spatial resolution in the order of 0.5 cm. The measured sensitivity of this first prototype was 77 cps, obtained with a 78.5 MBq point source of ^{99m}Tc, which was located 5.9 cm from the germanium detector. An extrapolation of this value was used to determine the sensitivity of larger arrays of germanium detector elements. The predicted sensitivity of the system was ten times greater than a conventional collimator; this could be achieved by optimising the system geometry and increasing the size of the electronic collimator.

Further developments were carried out in the construction of a new version of the electronic collimator consisting of a 4 x 4 germanium detector array [Singh and Doria, 1985]. This detector prototype was obtained from a single high-purity germanium slab, segmented into 16 independent 5 mm x 5 mm x 6 mm elements. The Ge detector was located 5 cm from the uncollimated gamma camera. Each Ge element was independently interfaced to its own circuitry providing amplification, energy discrimination and analogue-to-digital conversion. Detection of valid coincidences between one element of the Ge detector and the scintillation camera enabled the process of digitising the interaction position signals in the scintillator, identifying the Ge element in which the hit was produced and digitising its energy signal so as to allow the computation of the scatter angle. The energy signal from the scintillation camera was also digitised and added to the energy signal from the germanium detector. Pulse height discrimination was applied to reject radiation scattered from the object and to reduce the fraction of random coincident counts. Events were rejected in the case where simultaneous signals were produced from more than one germanium channel.

Three-dimensional images of cylindrical test-objects were acquired [Singh and Brechner, 1990]. The phantoms imaged contained either ^{99m}Tc or ^{137}Cs and were located at 12 cm and 14.5 cm distance respectively from the germanium detector. Conventional SPECT data were also acquired from the same test-objects for comparison, by removing the Ge detector and mounting on the camera a conventional high-resolution parallel-hole collimator for ^{99m}Tc and a pin-hole collimator for ^{137}Cs. The SPECT images obtained with mechanical collimators showed slightly better spatial resolution (1.3 $\pm$ 0.5 cm at 140 keV, 1.5 $\pm$ 0.5 cm at 662 keV) when compared to the images produced by electronic collimation (1.5 $\pm$ 0.5 cm at 140 keV, 1.7 $\pm$ 0.5 cm at 662 keV). Experimental results on the camera count rate, however, made it possible to confirm that electronic collimation would provide much higher sensitivity. Extrapolation of such results confirmed that if objects were placed at a 1-cm distance from the Compton scatter collimator and if the size of the germanium array was extended to 33x33 elements, the sensitivity gain over mechanical collimation at 140 keV would be approximately one order of magnitude.

The sensitivity gain was expected to increase with higher energy gamma rays: thick septa reduce sensitivity in high energy mechanical collimators, whereas electronic collimation sensitivity improves with increasing energy due to both an increase in the Compton/photoelectric ratio and to more forward scattering. Such an increase could not be observed on the basis of the experimental results obtained for the ^{137}Cs source, due to the low absorption efficiency of the scintillation camera at 662 keV. It was estimated, however, that the use of a more efficient scintillator material such as BGO would approximately double the sensitivity at 662 keV compared to 140 keV.

II) Compound semiconductor collimators

In recent years, the feasibility of using room-temperature operating Cadmium-Zinc-Telluride (CdZnTe) detectors as the front detector in electronically collimated SPECT has been investigated as an alternative to cryogenically cooled Ge detectors [Singh *et al.*, 1995]. A theoretical study was carried out in order to compare CdZnTe and Ge

electronic collimators in terms of their Compton Aperture Efficiency (CAE). The CAE is defined as the probability that a photon incident on the collimator undergoes a single Compton interaction in the first detector, followed by an escape of the scattered photon within the solid angle subtended by the back detector. The study showed that at 140 keV the CAE of a CdZnTe-based system would be a factor of 2.5 lower in comparison to Ge and the spatial resolution attainable would also be worse by approximately a factor of 2. However, preliminary experimental measurements with a ^{137}Cs point source showed that at higher energies the performances of the two types of detectors become comparable, thus encouraging the application of CdZnTe detectors with their practical advantages to the imaging of radioisotopes at energies above 500 keV. The use of CdZnTe position sensitive detectors replacing the scintillation camera in the back has also been proposed in conjunction with the use of an electronic collimator made of silicon [Rohe and Valentine, 1996], [Tümer *et al.*, 1997] or gallium arsenide [Kramer *et al.*, 1998]. The development of a prototype Compton camera based on two 3-D position sensitive CdZnTe detectors has also been recently proposed [Du *et al.*, 1999]. Computer simulations predicted that an angular resolution of 2-3° could be expected from such a system in the 0.511-1 MeV energy range. It is estimated that the intrinsic efficiency for a point source at 10-cm distance would range from $1.5x10^{-4}$ at 500 keV to $8.8x10^{-6}$ at 3 MeV.

III) Single-scatter silicon collimators

Silicon detectors have been suggested by various authors for the construction of the electronic collimator as an alternative to germanium, by virtue of their advantage of room temperature operation, low cost and wide availability. A 3 x 3 array of silicon drift detectors (2.75 x 2.75 mm^2 elements) was built and proposed for use in imaging 140 keV photons [Kuykens and Audet, 1988]. Because of its practical advantages, the use of a 5 cm x 5 cm silicon microstrip detector was also suggested in order to perform medical studies with radionuclides in the 100 keV to 1 MeV energy range, even if silicon has a lower probability of Compton interaction than germanium [Solomon and Ott, 1988]. It was estimated that a Compton device consisting of a 2-

mm thick silicon detector in coincidence with a standard NaI γ-camera would achieve an intrinsic efficiency of 1.7% for photons of 140 keV of energy (the intrinsic efficiency was defined as the likelihood of a detected coincidence given that the photon is incident on the face of the scattering detector).

A feasibility study was also more recently carried out in order to test silicon microstrip detectors for Compton imaging [Tümer *et al.*, 1997]. This system was based on the design of the TIGRE telescope that was previously described. A small desktop prototype system was built, in which a stack of three double sided silicon detectors with 1 mm pitch (size of 40 x 40 x 1 mm^3) acted as scatter components (the detectors were separated by 2 cm). The back detector comprised of three CsI(Tl) scintillation modules, each one consisting of an array of 3 x 3 crystals of size 1 x 1 x 2.5 cm^3 coupled to silicon photodiodes. Events were selected for image reconstruction if one and only one of the silicon detector planes would generate a signal in coincidence with one of the scintillation modules and if the sum of the two energy signals detected would fall within a pre-set window centred around the source energy value. Images of a ^{22}Na point source (511 keV) were reconstructed using approximately 400 events, due to the low efficiency of the prototype. A spatial resolution of approximately 1.5 cm was obtained for a distance of 10.5 cm between the source and the central strip detector. In order to increase efficiency, the use of 15-25 silicon planes was recommended for future developments of the prototype. The authors also suggested that replacing the scintillation modules with higher-resolution CdZnTe detectors would substantially improve the system performance, achieving a 3-10 sensitivity gain.

A prototype Compton camera (C-SPRINT, Compton-Single Photon RINg Tomograph) based on a silicon collimator is currently being developed at the University of Michigan for low energy (140 keV) γ-ray imaging [LeBlanc *et al.*, 1998]. The system comprises a single 3 x 3 x 0.1 cm^3 silicon pad detector (pixellated into a 22 x 22 array of 1.2 x 1.2 mm^2 elements), which is operated in coincidence

with the pre-existing Michigan SPECT system (SPRINT) with its lead collimators removed. SPRINT consists of a ring of eleven scintillator modules, where each module is an array of 1.27-cm thick NaI bars viewed by 20 PMTs. The scintillator modules are arranged so as to form a 50-cm-diameter, 10-cm long cylinder, at the front face of which is located the silicon collimator. Monte Carlo simulations of the set-up predict absolute Compton efficiency in the order of 2.7×10^{-5} (the absolute Compton efficiency is defined as the fraction of all source photons that are first incident on the silicon detector, then single Compton scatter in the silicon detector, then escape into the solid angle subtended by SPRINT, in which finally undergo full energy deposition). The authors claim that this efficiency could be improved by two orders of magnitude by using a stack of five detectors with larger area (9×9 cm^2) and by re-designing the geometry of the scintillator ring so as to accept a wider range of scatter angles. It is predicted that at 140 keV the system could achieve a sensitivity gain of ~ 20 over mechanical collimators, with an angular resolution of approximately 4° FWHM.

Experimental results from the system were recently reported making use of a single scintillation module, with a ^{99m}Tc source placed on the SPRINT centreline axis at a 2.5-cm distance from the silicon pad detector, which was set 8 cm inside the ring [LeBlanc *et al.*, IEEE 1999]. The silicon pad detector had 3.5 keV FWHM energy resolution at 60 keV of energy. The image performance of the system was rather poor, with an angular resolution of approximately 40° FWHM, obtained with a simple backprojection algorithm. The authors claim that the resolution would improve to ~ 25° if an iterative method was used for reconstruction. A second set of experiments were performed by making use of all eleven modules and by replacing the original collimator with a 300-μm thick silicon pad detector with better energy resolution (2.2 keV FWHM at 60 keV). The source was placed at 10 cm from the silicon detector. The spatial resolution was calculated to be 1.5 cm. This corresponds to more than a factor of four improvement in the angular resolution (8.6° FWHM). If the iterative algorithm was used on this second data run, the resolution would

improve to 7 mm (i.e. ~ 4° FWHM). However, such a resolution recovery was obtained at the expense of increased noise in the image.

Compton cameras have improved performance with high-energy photons, as will be discussed in the next chapter. Therefore, although C-SPRINT was specifically designed for low-energy imaging, the authors are now considering the application of C-SPRINT at higher energies. Their interest is currently in the medical applications of the high-energy line (393 keV) of the isotope ^{113m}In [Le Blanc *et al.*, NIM 1999]. It is estimated that the sensitivity gain of the C-SPRINT system at this energy would be a factor of 3 to 5 when compared to ^{99m}Tc imaging.

IV) Multiple-scatter silicon collimators

Multiple layers of silicon detectors have been proposed in order to extend the Compton scatter imaging principle to multiple scatter events [Kamae *et al.*, 1987]. This method was devised to enhance the efficiency of the events used in image reconstruction. Another potential advantage of this approach is the polarisation dependence of multiple Compton scattering. The use of the polarisation induced by scattering has in fact been suggested as a method to resolve the azimuthal ambiguity that characterises single Compton scatter [Dogan *et al.*, 1992]. The system design of Kamae *et al.* is based on a stack of independent large area, energy resolving and position sensitive silicon microstrip detectors. The thickness of each layer must be adequately small so as to minimise the probability of multiple scatter but at the same time must be sufficient to contain the recoil electron range. The stack is surrounded by a scintillation counter in order to increase detection efficiency. In order to reconstruct the direction of the incoming photons, the characteristics of the first two interactions are needed. This requires the identification of the exact sequence of events in the stack, which can be achieved through the known kinematics of Compton scattering.

Simulation work was carried out to optimise the design for gamma rays in the 150-600 keV energy range [Kamae *et al.*, 1988]. Each detecting silicon layer was

simulated with a sensitive area of 6 x 6 cm^2 and a thickness of 500 μm, with 500 μm pitch both in the x and y co-ordinates. The minimum detectable energy was set to 10 keV and the electronic noise contribution to the detector energy resolution was assumed to be 1 keV. The side counter was designed as a CsI(Tl) cylindrical detector of 10 cm inner radius, 18 cm height and 2 cm thickness. The system angular resolution was estimated to be in the 3° - 5° range (FWHM) when using 50 layers. Further work was carried out extending the photon energy up to 1 MeV and stacks of germanium detectors were also taken into consideration [Dogan *et al.*, 1990]. The "reconstruction efficiency" (defined as the fraction of incident photons the incident direction and energy of which are correctly reconstructed) was estimated to be 7-14% for Si and 16-28% for Ge, depending on the photon energy (in both cases the layer thickness was 5 mm).

More recent work aimed at optimising the layer thickness of silicon detectors for operation at specific energies [Dogan and Wehe, 1994]. Optimal values were found to be less than 0.5 mm at 150 keV, 2 mm at 511 keV and 5 mm at 1 MeV. The construction of a 20-layer prototype (each layer being 1 mm thick) was also proposed. Multiple Compton cameras have however never been constructed, mainly because of the high cost of the large number of detectors required and the complex electronics associated.

V) Gas detector-based collimators

Finally, among other type of detectors, gas scintillators have also been considered in order to build a Compton camera for medical use. An electronically collimated gamma camera was proposed, where a gas scintillation position-sensitive detector was employed as the scatter component, coupled to a multi-layer and multi-wire proportional chamber (MPWC) as the back detector [Fujieda and Perez-Mendez, 1986]. The authors acknowledged the superior energy resolution of germanium detectors with respect to gas scintillators, but suggested that such disadvantage may be offset by the higher spatial resolution and large field of view of gaseous detectors.

Theoretical calculations were carried out in order to evaluate the system performance at 140 keV, considering xenon as the filling gas. The front detector was assumed to have 1 mm x 1 mm x 1 mm intrinsic spatial resolution. The back detector spatial resolution was assumed to be 1 mm FWHM. It was estimated that a point spread function with 5.7 mm FWHM at a 5 cm distance may be obtained, but the probability of events undergoing single Compton interactions in the front detector and reaching the back detector would be less than 1.2%. The proposed system showed low efficiency in comparison with germanium-based cameras.

The idea of realising a xenon-filled detector for a Compton camera has been recently reinterpreted with a novel approach [Bolozdynya *et al.*, 1996]. A prototype for γ-ray imaging has been constructed, which consists of a single high-pressure xenon scintillation drift chamber with a large active area (30 cm in diameter). The field of view of the camera is comparable to the conditions encountered in clinical examinations. It contains a low-field drift region (37 mm deep) followed by a high-field light emitting gap (6-mm deep). The radiation is absorbed in the drift region with low electric field and produces both primary scintillation light and ionisation clusters. The electron clusters drift to the high-field gap where a secondary scintillation process (electro-luminescence) is activated. Light originated from both scintillation and electro-luminescence is detected by 19 PMTs. The (x, y) position of each electron cluster is measured from the distribution of the electro-luminescence signals over the PMT array, whilst the z co-ordinate is obtained from the delay time between the primary scintillation signal (the trigger) and the electro-luminescence signal.

In order to recognise those events where the incoming photon undergoes single Compton scatter followed by photoelectric absorption, after the scintillation trigger three vertices must be present in the drift region, each one producing a separate electro-luminescence signal: the Compton vertex of the recoil electron, the vertex of the scattered and photo-absorbed photon and the vertex of the photo-absorbed

fluorescent photon. The energy of the fluorescent photon is approximately 30 keV, whereas the energies corresponding to the other two vertices should lie within ranges allowed by the Compton kinematics. The sum of the three signals must be equal to the energy of the incident photon. Preliminary tests were carried out with the camera operating in Compton mode and a spatial resolution of 25 mm FWHM at a 10.5 cm distance was obtained for a ^{99m}Tc point source. The authors suggested that the performance may be noticeably improved by replacing the 80-mm diameter PMTs with a fibre optic readout system. The camera efficiency to Compton scatter (2.2 % at 9 atm) may also be increased by filling the camera with high pressure (30 atm) argon.

The same authors have more recently proposed a cylindrical geometry for a two-detector Compton camera for low-energy γ-ray imaging based on gaseous position sensitive detectors [Bolozdynya *et al*,.1997]. The proposed design consists of an inner scatter cylinder (surrounding the object to be imaged) filled with pressurised argon, in conjunction with an outer concentric absorption cylinder filled with pressurised xenon. The authors suggested the concept of a Multi-layer Electro-Luminescence Camera (MELC) [Bolozdynya and Morgunov, 1998] to be used for both the scatter and the absorption detectors. It is estimated that the proposed configuration for a Compton camera would achieve a sensitivity gain of one order of magnitude over conventional SPECT systems whilst maintaining comparable spatial resolution.

In order to summarise the state-of-the-art in the field of Compton cameras for medical applications, the characteristics of the few systems that have actually been constructed are shown in Table 1.10.

Table 1.10: Summary of properties of the Compton camera prototypes that have been constructed for medical applications.

Detector Configuration	**Energy**	**Angular resolution[10] (FWHM)**	**Potential sensitivity gain over mechanical collimators**	**Type of system**
Planar HPGe array + single NaI(Tl) module	140 keV	~ 7°	~10	Planar geometry SPECT prototype [Singh and Brechner, 1990]
Double-sided Si microstrip detectors + CsI(Tl) modules	511 keV	~ 8°	3-10	Small desktop prototype based on the design of the TIGRE telescope [Tümer *et al.*, 1997]
Silicon pad detector + ring of NaI(Tl) modules	140 keV	~ 25°(*) ~ 4°(**)	~20	Ring geometry SPECT prototype (C-SPRINT) [LeBlanc *et al.*, 1999]
High-pressure Xe scintillation drift chamber	140 keV	~ 13°	~10	Electroluminescent camera operated in Compton mode for feasibility study [Bolozdynya *et al.*, 1997]

(*) 3x3x0.1 cm^3 Si detector with 3.5 keV FWHM energy resolution (measured at 60 keV).

(**) 3x3x0.03 cm^3 Si detector with 2.2 keV FWHM energy resolution (measured at 60 keV).

[10] See note 9 of Table 1.9.

1.4.5 Potential advantages of a Compton scatter camera for clinical use

The Compton camera offers many attractive features for γ-ray imaging applications in medicine. Potentially, Compton cameras can achieve both high spatial resolution and high sensitivity, thus fulfilling the two main requirements of emission medical imaging.

Typical values of administered activity for imaging studies are in the order of 100 MBq and acquisition times are normally between 10 and 30 minutes (the total examination time is actually much longer as scans are often performed from 15 minutes to a few hours after the injection of the radio-pharmaceutical). The use of Compton cameras in medical investigations could imply a reduction of both the administered activity (thus lowering the dose delivered to the patient) and the time allowed for the imaging procedure (thus achieving increased patient comfort and diminishing image artefacts due to patient motion).

Another important feature of the Compton camera is its capability to perform 3-D imaging with no need for detector motion, as opposed to rotating SPECT systems. This characteristic would simplify the mechanical design of the system. It would also allow the camera to be positioned as close as possible to the organ of interest; physical limitations often require a large radius of rotation for conventional gamma cameras (e.g. 25 cm in abdominal SPECT with circular orbit), with a consequent degradation in spatial resolution. The absence of heavy collimators would also make the camera portable and therefore mobile, allowing clinical investigations to be carried out in a varied environment.

As will be discussed later, the principle of Compton camera imaging is most advantageous for medical applications with high-energy radioisotopes, where the performance of mechanical collimators is degraded by radiation scatter and penetration and the performance of electronic collimators improves. A variety of high-energy applications are of possible interest. The emission spectrum of ^{131}I, for

example, which consists of a 364 keV primary photon with accompanying gamma rays of even higher energy (637 keV and 723 keV), is not favourable with conventional collimators. The ^{123}I isotope is currently considered a better agent than ^{131}I for thyroid gland imaging because of its lower energy emission (160 keV) that is more suited to the collimation characteristics of gamma cameras. ^{131}I however is low-cost, readily available and can be used not only for diagnostic purposes, but also for therapy (typically for thyroid cancer treatment) as it is both a gamma and a beta emitter. A portable lightweight Compton camera would be ideal for imaging patients undergoing therapy.

Another possible isotope for use with a Compton camera is ^{113m}In (gamma emission at 393 keV). ^{113m}In could substitute in some applications the more commonly used ^{111}In (173 and 274 keV), which is employed, for example, in labelled leukocytes scintigraphy (a technique employed to localise infections and inflammatory sites) and platelet radiolabelling (a technique used to identify clots in the vasculature). Finally, Compton scatter may be considered as a potentially successful approach to positron emitter imaging, as suggested in the next chapter.

Chapter 2

Design and Selection of a Compton Scatter Detector for Positron Emitter Imaging

In this chapter, considerations are made to justify the optimisation of a Compton collimator for application at 511 keV of energy. Monte Carlo simulations are carried out in order to evaluate the Compton scatter efficiency of a group of semiconductor detectors. The potential sensitivity gain over mechanical parallel-hole collimators is discussed for all considered materials.

The fundamental physical and geometric parameters for the design of an electronically collimated camera are presented. As the scatter detector is the most critical component in determining the overall angular resolution of the camera, its properties are selected using a specifically developed computer model, based on Monte Carlo techniques. The computer code, which fully simulates the operation of a two-element Compton camera, is applied to produce images of point sources. The simulations are carried out for a range of values of spatial and energy resolution in the scatter detector. Results are presented for the optimum design of a silicon sensor to perform Compton collimation of annihilation γ-rays.

The principle of operation of double-sided silicon microstrip detectors is briefly described. Considerations are made on the optimum strip configuration for the detection of recoil electrons resulting from Compton scatter of 511 keV photons. Finally, the results obtained from the modelling work are applied to identify suitable commercially available detectors and integrated readout electronics.

2.1 A Compton camera for PE imaging: motivations

For Compton cameras operating in the energy range of clinical interest (~ 100-500 keV), angular uncertainties decrease as photon energy increases, whilst the fraction of Compton interactions in the electronic collimator increases. The use of Compton scatter cameras with 511 keV photons is therefore likely to provide both higher spatial resolution and higher signal to noise ratio than with low-energy γ-rays. Another advantage of using high-energy gammas in medical applications is that the amount of scattered photons in soft tissue is less than at lower energies. Moreover, scatter rejection is more easily performed at higher energies, due to the greater value of deposited energy for a given scatter angle (see Figures 2.1 and 2.2).

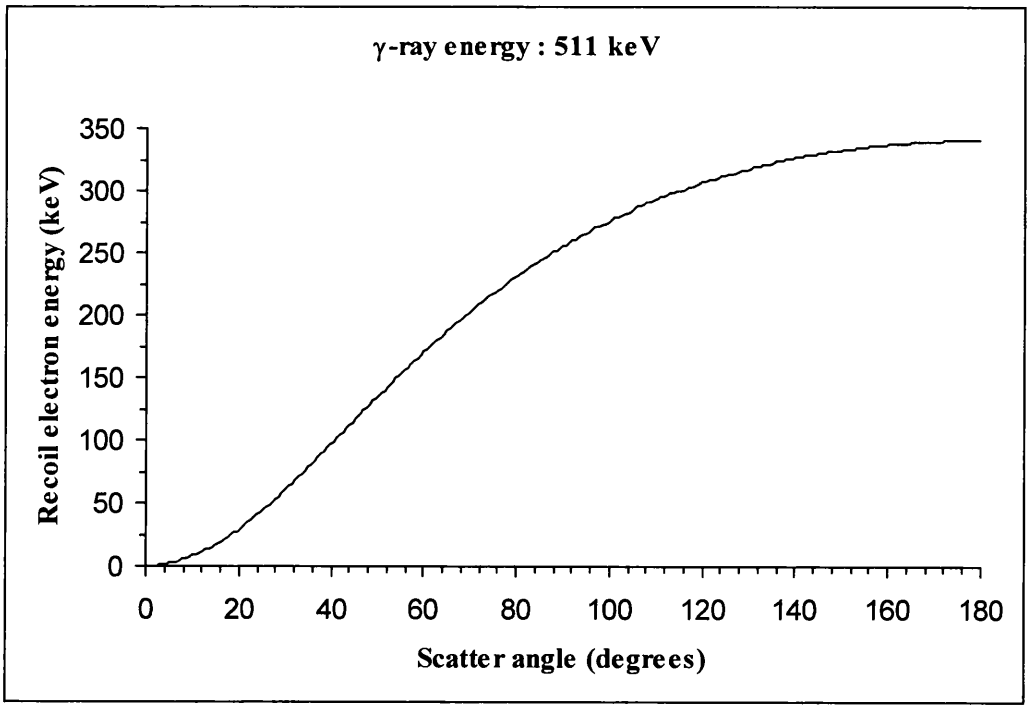

Fig. 2.1: Energy of recoil electrons in a Compton interaction with 511 keV photons, plotted as a function of scatter angle.

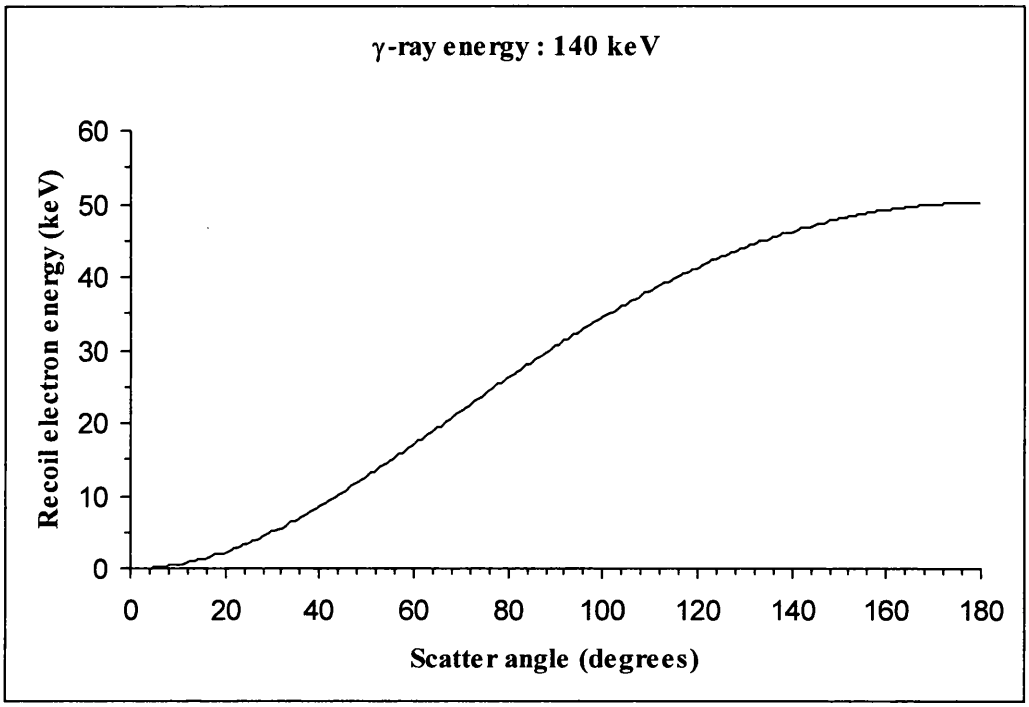

Fig. 2.2: Energy of recoil electrons in a Compton interaction with 140 keV photons, plotted as a function of scatter angle.

At a depth of 10 cm, the percentage of photons attenuated in tissue by scatter is approximately 60% at 511 keV of energy and it approaches almost 80% at 140 keV. If one assumed that scattered photons could be rejected if the energy loss in tissue was above a threshold of 10 keV, only approximately 6% of the scattered photons would then fail to be discriminated at 511 keV, against approximately 20% at 140 keV.

Although the use of positron emitters in nuclear medicine is traditionally more limited than single-photon, low-energy isotopes, a growing niche is appearing for PE imaging methods other than PET scanners. A three-month study was recently conducted in the UK in order to determine the most important cost-effective research priorities for the National Health Service in relation to positron emitter imaging [Robert and Milne, 1999]. The survey, which incorporated the views of 22 national experts, concluded that the key questions for the cost-effectiveness of PET techniques

were in the areas of lung cancer, breast cancer and the assessment of myocardial viability. To this regard, relatively inexpensive collimation approaches such as dual-head coincidence cameras were identified as imaging devices that need urgent assessment in terms of their clinical role.

These results confirm the current interest in imaging modalities that would allow positron emitters to be employed more extensively and at a lower cost than using complex and expensive PET scanners. Compton cameras could be considered within this context as an attractive approach, as they have the potential to improve significantly the spatial resolution over ultra-high energy mechanical collimators and could be built as more efficient systems than current dual-head gamma cameras. Compton devices may therefore, in theory, fill a specific technological niche in the practice of ^{18}F-FDG-SPECT imaging in oncology and cardiology studies. In particular, a specific design for the 100-500 keV range of energy would provide the ideal device for heart studies, as it would make it possible to perform simultaneous dual-isotope acquisition with ^{99m}Tc-MIBI and ^{18}F-FDG in myocardial perfusion/metabolism imaging.

Economically viable applications of a positron Compton camera would also extend to radio-pharmaceuticals other than ^{18}F-FDG, such as compounds labelled with ^{82}Rb or ^{68}Ga. These are cyclotron-independent positron-emitting isotopes that can be obtained as generator eluates in a standard radiopharmacy laboratory. The isotope ^{82}Rb, which is mainly used in myocardial perfusion studies, can be obtained in the form of rubidium chloride from ^{82}Sr/^{82}Rb generators that have been made commercially available in recent years. Because of its very short half-life (75 seconds), repeat PET studies can be performed with this emitter on the same patient in a single session. The isotope ^{68}Ga has a half-life of 68 minutes and can be produced from a ^{68}Ge/^{68}Ga generator. Because the reactivity of gallium is similar to technetium, it can be employed in a wide range of radio-pharmaceuticals that are used in perfusion studies and scanning of many organs.

2.2 Selection of collimator material

The efficiency requirements of a camera for 511 keV photon imaging indicated that solid state detectors were more suitable as scatter elements than gaseous detection systems. The need for a detector with high spatial resolution combined with high spectrometric performance made semiconductors the preferred choice over scintillating crystals. The ideal detector would combine the advantages of room temperature operation, high Compton efficiency and good energy and spatial resolutions. A group of semiconductors, the technology of which makes it possible to build radiation sensors in the form of pixel arrays or other position sensitive devices, were investigated as possible candidates for the construction of an electronic collimator. These materials and their physical properties of interest for radiation detection are listed in Table 2.1.

2.2.1 Monte Carlo simulations of Compton scatter in semiconductor detectors

A variety of simulations were carried out for the considered materials, by making use of a computer code based on radiation-transport routines of the general-purpose EGS4 Monte-Carlo system. A description of the main features of EGS4 is given in [Nelson *et al.*, 1985]. In the simulated problem, a 511 keV γ-ray point source was located at the origin of a three-dimensional frame of reference, at a fixed distance from the centre of a semiconductor detector with a square face (see Fig. 2.3). The photons emitted by the source were generated with suitable direction cosines, so that the points of incidence would be uniformly distributed over the detector surface. The output of the code produced the number and type of interactions occurring during the 'history' of each primary photon.

The single Compton efficiency was defined as the fraction of photons impinging on the detector that undergo single Compton scatter. It was calculated for each considered material as a function of detector thickness. These simulated data also allowed the computation of the ratio of single Compton events to the total number of

interactions. Simulations were carried out for detector thickness values up to a maximum of 0.4 cm. The use of thicker detectors was not taken into consideration, in order to limit the uncertainty of the co-ordinates of interaction within a small pixel volume (this aspect will be discussed later in more detail).

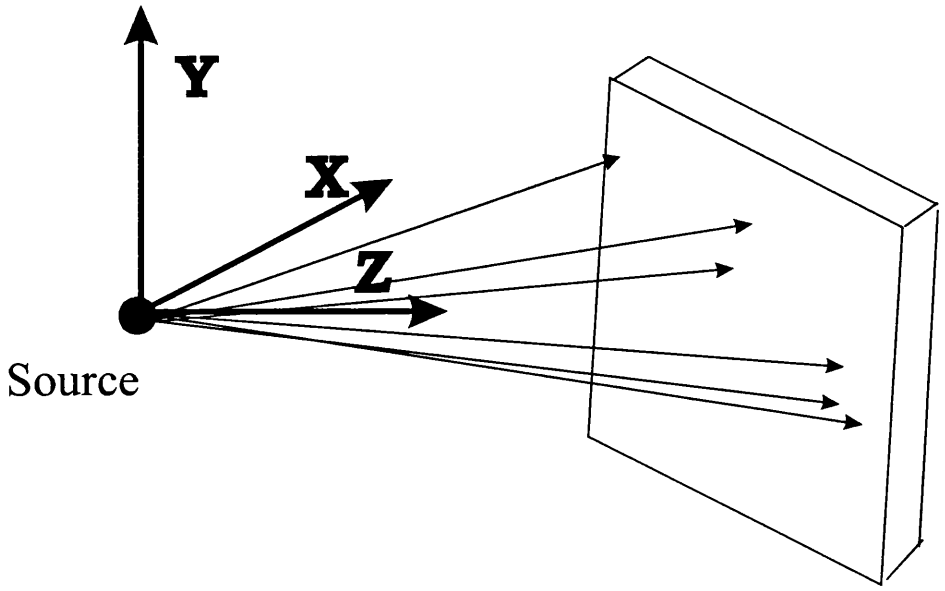

Fig. 2.3: Diagram showing the geometry employed in the simulations of Compton scatter at 511 keV, assuming different semiconductor detectors of varying thickness in the 0-4 mm range. The point source is located at a 5-cm distance from the centre of the detector surface. The detector sensitive area is 6 cm x 6 cm. The points of incidence on the detector surface are randomly generated according to a uniform distribution. The direction cosines of the emitted photons are obtained by back-projecting the rays to the origin of the frame of reference, where the point source is located.

The results of the EGS4 simulations on the efficiency and the proportion of Compton interactions are shown in Fig. 2.4 and Fig. 2.5 for all the materials considered as possible candidates to be used for the construction of a photon scatter collimator at 511 keV. The Monte Carlo simulations were also extended to the case of 140 keV γ-rays for comparison (see Fig. 2.6 and Fig. 2.7).

Table 2.1: Properties of semiconductor materials evaluated for electronic collimation. Data obtained from [Squillante and Shah, 1995].

Semiconductor	**Si**	**Ge**	**GaAs**	**CdTe/CdZnTe**	**HgI_2**
Z	14	32	31-33	48-52 / 48-30-52	80-53
Density ρ (g/cm^3)	2.33	5.32	5.35	6.06 / 5.8	6.30
Bandgap E_G (eV) *@ 300 K*	1.12	0.67	1.43	1.45 / 1.6	2.13
Ionisation Energy w (eV)	3.61	2.96[11]	4.27	4.43/5.00	4.15
Electron Mobility *($cm^2V^{-1}s^{-1}$) @ 300 K*	1500	3900	8500	1000 / 1350	100
Hole Mobility *($cm^2V^{-1}s^{-1}$) @ 300 K*	600	1800	420	80 / 120	4
Electron Lifetime (s)	3×10^{-3}	10^{-3}	10^{-7}	10^{-6}	10^{-7}
Hole Lifetime (s)	3×10^{-3}	10^{-3}	10^{-7}	10^{-6}	10^{-8}
Intrinsic Resistivity *(Ω cm) @ 300 K*	235×10^3	50	10^8	10^9 / 10^{11}	10^{13}

[11] Value for T= 90 K. All other values refer to T= 300 K.

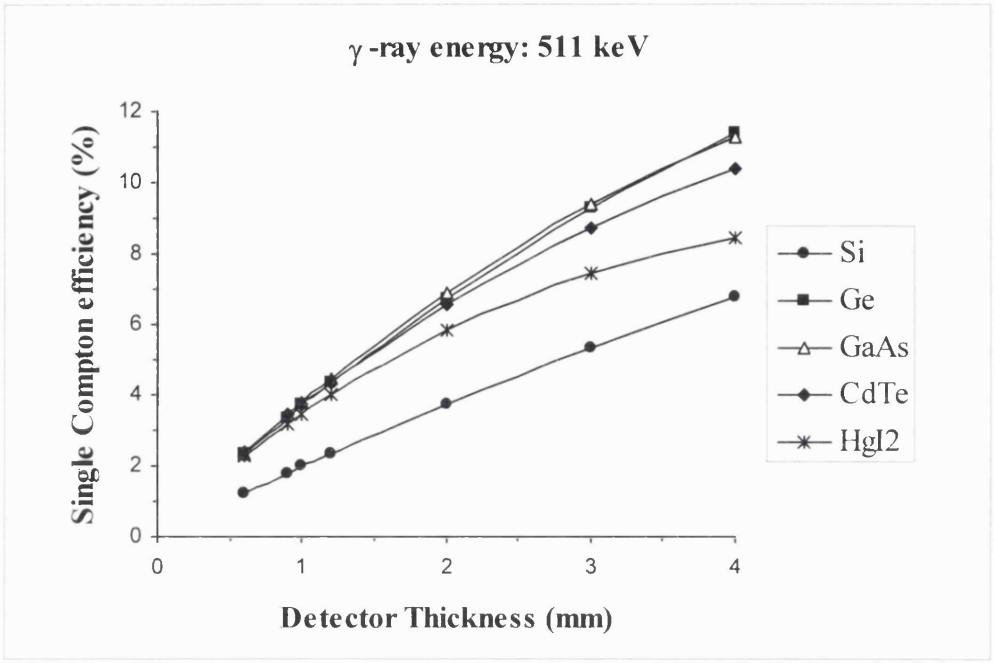

Fig. 2.4: Efficiency of single Compton scatter events as a function of material thickness for photons of 511 keV of energy (values obtained from EGS4 Monte Carlo simulations).

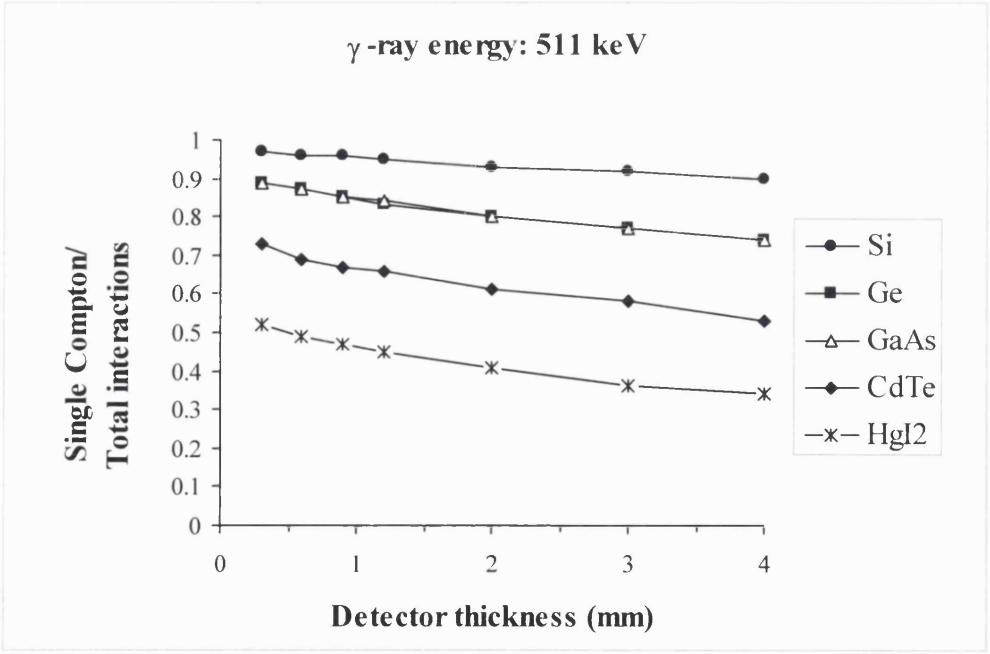

Fig. 2.5: Ratio of single Compton scatter events to total number of interactions as a function of material thickness for photons of 511 keV of energy (values obtained from EGS4 Monte Carlo simulations).

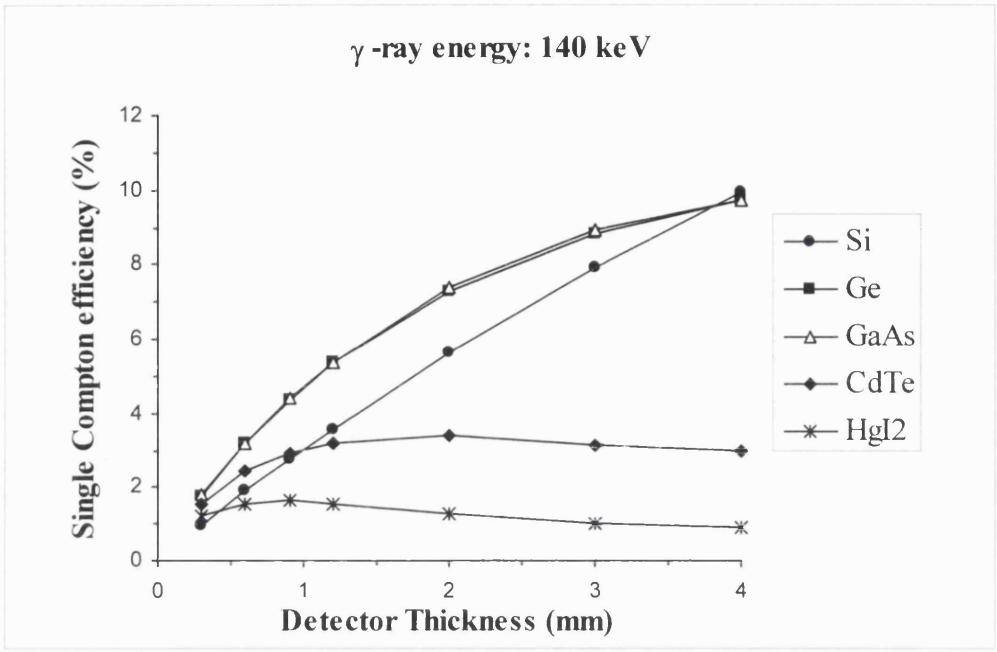

Fig. 2.6: Efficiency of single Compton scatter events as a function of material thickness for 140 keV photons (values obtained from EGS4 Monte Carlo simulations).

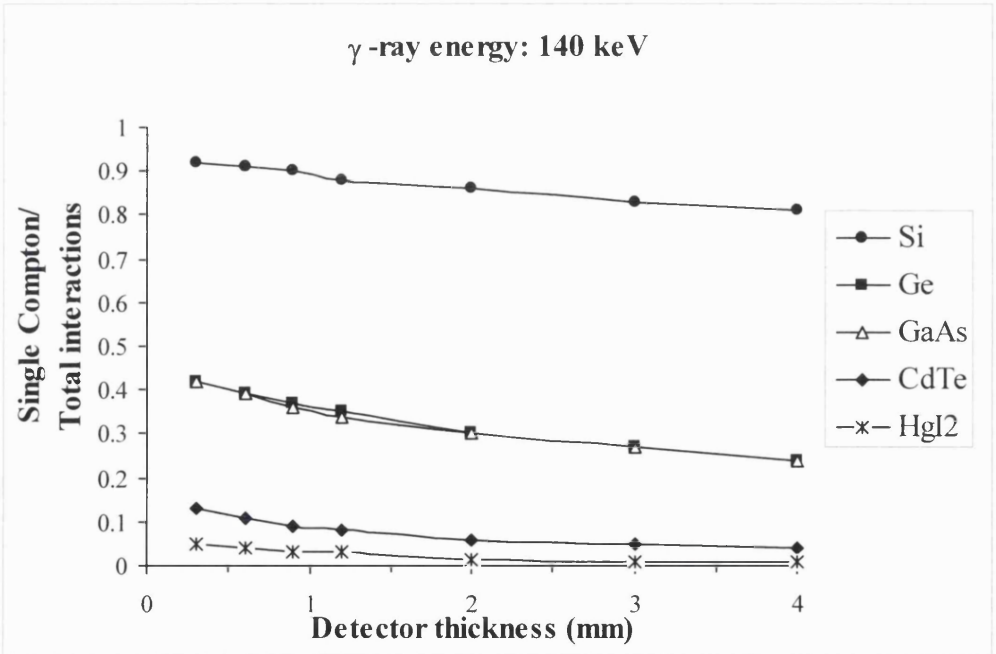

Fig. 2.7: Ratio of single Compton scatter events to total number of interactions as a function of material thickness for 140 keV photons (values obtained from EGS4 Monte Carlo simulations).

2.2.2 Sensitivity of a Compton scatter collimator

The efficiency ε_{ECS} of an electronically collimated system (ECS) based on Compton scatter can be defined as in the case of a conventional imaging camera. The efficiency is the fraction of incident photons that are actually counted by the system and may be calculated as the product of the following factors [Fujieda and Perez-Mendez, 1986]:

$$\varepsilon_{ECS} = P_C \varepsilon_2 \tag{2.1}$$

where ε_2 is the back detector efficiency to photo-absorption of the scattered photons and P_C is the probability of a single Compton scatter in the first detector followed by an escape of the scattered gamma ray with its direction incident on the back detector.

For a point source in air, assuming that there is no scatter between source and front detector, the efficiency can be related to the *sensitivity* S_{ECS} of the system (defined as the fraction of photons emitted isotropically by the source that are actually counted by the system) through the following relationship:

$$S_{ECS} = \Omega_{ECS} \varepsilon_{ECS} \tag{2.2}$$

where Ω_{ECS} is the fraction of solid angle subtended by the front detector with respect to the source.

For the simple case of a point source located on the axis of a detector with circular sensitive area, Ω_{ECS} can be expressed as follows:

$$\Omega_{ECS} = \frac{1}{2}\left(1 - \frac{b}{\sqrt{b^2 + a^2}}\right) \tag{2.3}$$

where a is the detector radius and b is the detector-source distance.

2.2.3 Electronic collimation with semiconductor detectors versus mechanical collimation

The sensitivity S_{MCS} of a mechanically collimated system (MCS) was defined in equation (1.4) of chapter one as the product of the geometric efficiency g of the absorptive collimator and the photopeak detection efficiency of the scintillator crystal in the camera. If the following approximations are made:

1) all the photons scattered in the Compton scatter collimator are intercepted by the back detector;

2) both the back detector in the Compton camera and the scintillator of a conventional gamma camera have 100% detection efficiency to the photons that are incident on their surface;

the sensitivity ratio between an ECS and a MCS will therefore be expressed by:

$$R = \frac{S_{ECS}}{S_{MCS}} = \frac{\Omega_{ECS}}{g} P_C \tag{2.4}$$

where P_C is now simply the probability of occurrence of a single Compton scatter event in the electronic collimator.

Assumptions 1) and 2) are necessary so as to evaluate the sensitivity gain obtained with a Compton collimator made of a specific material irrespective of other design factors, such as the geometry or the detection efficiency of the back elements in both types of camera. This, however, implies some limitations in the calculations that follow. The degree to which the first and second assumptions are achieved in an experimental ECS will strongly depend on the geometrical configuration of the system. Such a condition may be approximated, for example, by a design consisting of annular detectors or of large arrays surrounding the front detector. This analysis

also assumes that the energy deposited by all scattered photons (including the events with small Compton scatter angle) can be detected in the electronic collimator. This assumption would be approximated with the use of an ultra low-noise detection system (e.g. in silicon position sensitive detectors it is possible to achieve a noise level between 1 and 2 keV FWHM [Rönnqvist *et al.*, 1994], [P.Weilhammer *et al.*, 1996]). The second assumption made for a MCS may be considered realistic for 140 keV photons, but correction factors will be required in the case of positron emitters.

The performance of an ECS and of a conventional MCS were compared for a 511 keV point source in air, by applying equation (2.4) to each of the semiconductor detectors considered in section 2.2.1. These calculations were also performed for 140 keV γ-rays for comparison. A typical general-purpose, low-energy lead collimator with a spatial resolution of 9 mm FWHM at 10-cm distance was considered for the 140 keV γ-rays. A high-energy collimator made of the same material and with the same spatial resolution was assumed for the 511 keV case. The geometrical parameters used for both collimators are given in Table 2.2. The septal thickness was evaluated on the basis of equation (1.1) of chapter one, thus assuming a maximum septal penetration of 5%. The geometric efficiency of the mechanical collimators was calculated using equation (1.3) of chapter one. The probability term in equation (2.4) was estimated for all materials as a function of thickness, by making use of the simulation results on Compton scatter efficiency that were presented in section 2.2.1.

Computations of the sensitivity ratios R are shown in Fig. 2.8 and Fig. 2.9 for the two energies of interest. The calculations were performed considering typical detection areas associated with a gamma camera (A_{MCS}) of 40 cm diameter and a solid state electronic collimator (A_{ECS}) of 6 cm diameter. In Fig. 2.10 and Fig. 2.11 the same curves are plotted, now multiplied by a normalisation factor that accounts for the magnitude of the respective detection areas (i.e. the plotted quantity is the ratio R_n of sensitivities per cm^2). All the calculations shown in Fig. 2.8 to 2.11 were performed assuming a distance of 10 cm between the electronic collimator and the

radiation source, as this is the standard distance for the performance assessment of conventional gamma cameras. A small area electronic collimator, however, could be placed much closer to the patient than conventional imaging systems. The sensitivity of the ECS is proportional to the solid angle viewed by the camera; if the source-collimator distance was reduced to 5 cm, the sensitivity gain would increase by a factor of approximately 3.5.

Table 2.2. Parameters and properties used for the mechanical collimators in the evaluation of the sensitivity ratios.

Type of collimator:	***Low-Energy (140 keV)***	***High Energy (511 keV)***
Material	Pb	Pb
Hole shape constant K	0.24	0.24
Collimator length l (cm)	4	9.2
Hole diameter d (cm)	0.25	0.4
Septal thickness t (cm)	0.02	0.2
Resolution (cm) @ 10 cm	0.9	0.9
Geometric efficiency g	2.02×10^{-4}	6.04×10^{-5}

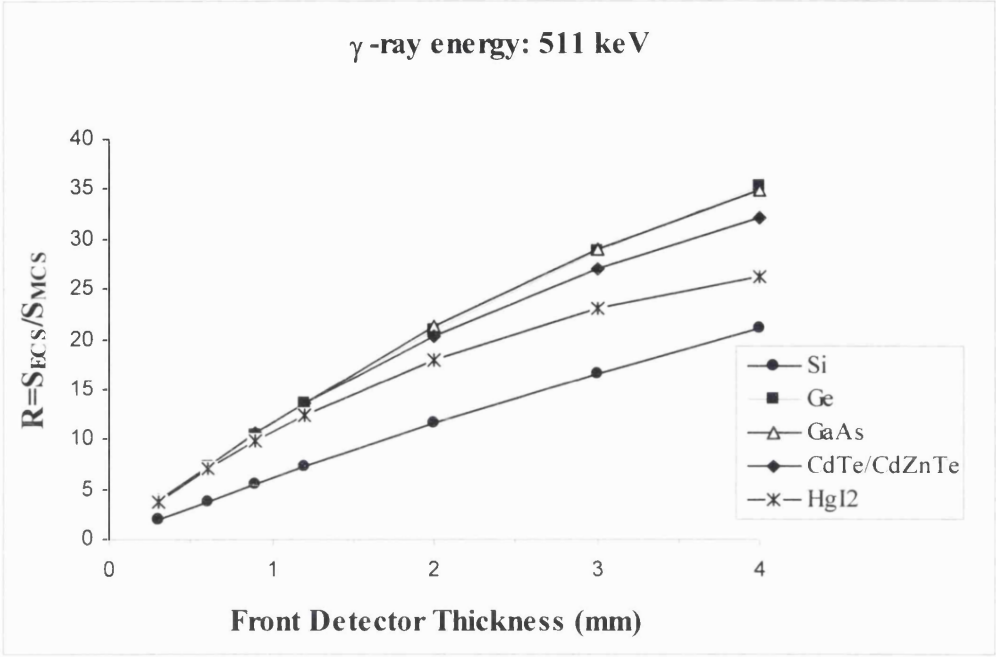

Fig. 2.8: Ratio of sensitivities S_{ECS}/S_{MCS} when using different semiconductors (sensitivity area of 3 cm in radius) to electronically collimate 511 keV photons.

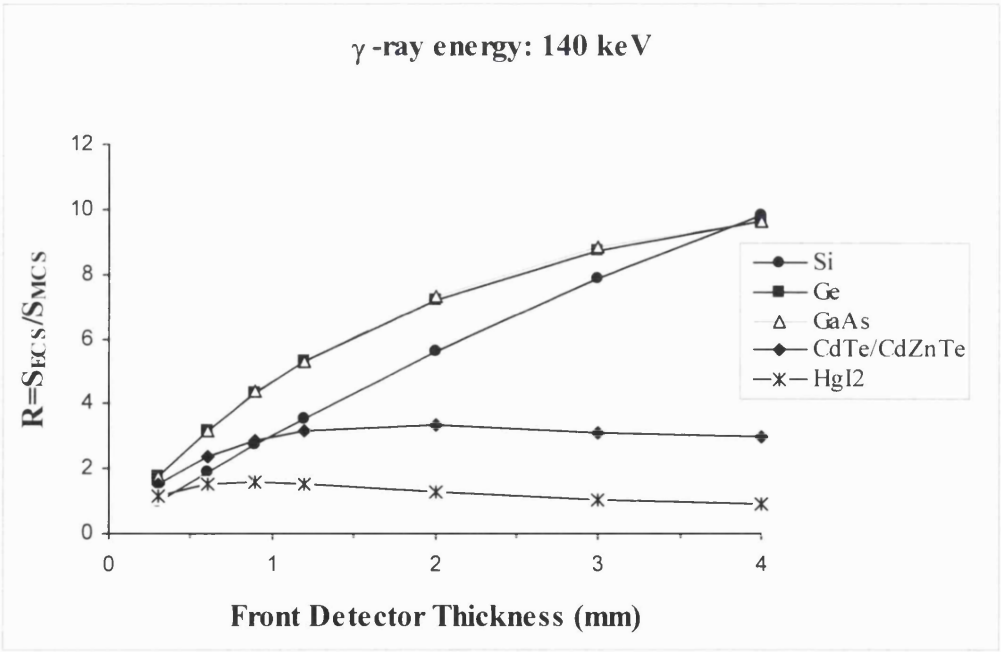

Fig. 2.9: Ratio of sensitivities S_{ECS}/S_{MCS} when using different semiconductors (sensitivity area of 3 cm in radius) to electronically collimate 140 keV photons.

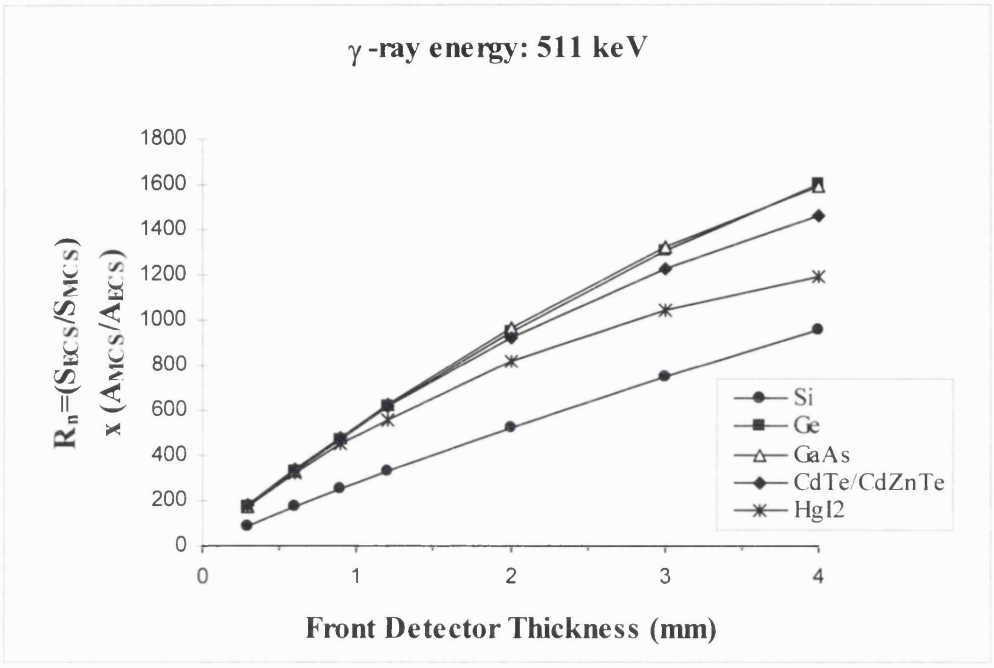

Fig. 2.10: Ratio of the sensitivities normalised to detector surface for 511 keV photons.

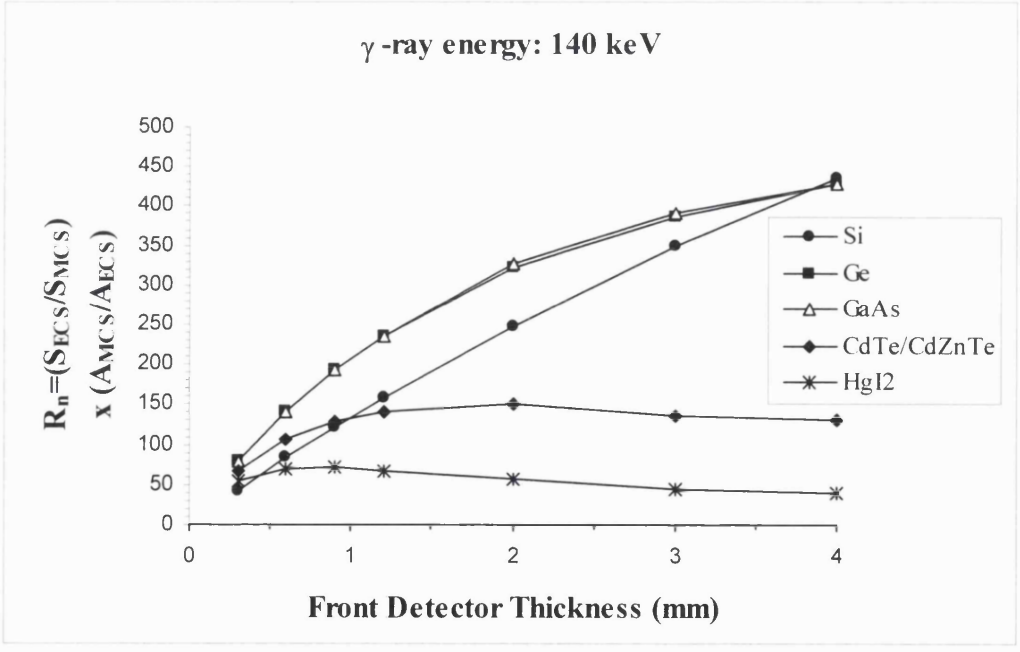

Fig. 2.11: Ratio of the sensitivities normalised to detector surface for 140 keV photons.

2.2.4 Discussion of results

The main purpose of the work presented in this section was to obtain a quantitative estimate of the efficiency of a class of semiconductors (as a function of thickness) and to relate it to the performance of a parallel-hole collimator. The results in Fig. 2.8 to Fig. 2.11 show that Compton scatter could provide a sensitivity gain of between one and three orders of magnitude over mechanical collimation in the 140-511 keV energy range, depending on the size and the material of the Compton collimator.

This study confirms that Compton scatter is a potentially more advantageous form of SPECT collimation than ultra-high energy mechanical collimators. The sensitivity gain is reduced at lower energies because of the improved performance of conventional collimators and the higher probability of photoelectric interactions in the scatter detector. The simplifying assumptions made in this study must be accounted for in order to extrapolate these results to experimental conditions. It has also been shown that the sensitivity gain can be reduced by a factor of 3 to 10 in the image reconstruction process [Bolozdynya *et al.*, 1997], [Singh *et al.*, 1988]. Nevertheless, even allowing for the above limitations, this comparative analysis provides a simple and useful method to obtain an indicative estimate of the relative gain that can be obtained when different semiconductors are used for electronic collimation based on Compton scatter.

The results presented in this section were produced for a simple design where the collimator consists of a single detection element. The design could be made more complex by stacking independent silicon planes to realise a multiple Compton camera (see section 1.4.4 *IV*). For such a design, the considerations made here for the sensitivity gain cannot be directly applied, as the probability of single Compton interactions in separate layers has to be accounted for. However, the characteristics required for each layer would be similar to the case of a single collimating element and the reported results therefore contain useful information to this regard.

At present, silicon and germanium are the most suitable materials for the construction of a Compton collimator for high-energy photons. Germanium is the material that would provide the most efficient electronic collimator (its Compton efficiency is approximately 4% for 1 mm of thickness at 511 keV of energy, see Fig. 2.4). However, the need for cryogenic cooling precludes the design of a compact and lightweight system. An equivalent performance in terms of efficiency would be obtained with the use of gallium arsenide, as its average atomic number and density are approximately the same as those of germanium. However, as good charge transport properties are required for optimum spectrometric performance, elemental semiconductors are currently preferred over compound materials (see Table 2.1). Considerable effort is being directed at improving the energy resolution of detectors made of compound semiconductors and the indications are that such materials (CdZnTe in particular) could be employed in the near future.

Pulse processing techniques for trapping compensation have been developed in recent years for CdTe/CdZnTe detectors and better spectrometric performances can now be obtained, with FWHM energy resolution values of 1.2 keV at 122 keV and 2.4 keV at 662 keV [Niemela *et al.*, 1996], [Ivanov *et al.*, 1998]. Although the current work aims to optimise the scatter collimator for PE imaging, it is desirable to construct a device that could also operate at 140 keV. In this regard the simulation results in Fig. 2.6 and Fig. 2.7 showed that the use of high-Z semiconductors (such as CdZnTe and HgI_2) would not be suited to low-energy photons because of the high number of photoelectric interactions. Germanium and silicon are therefore also a more flexible choice of material.

Room-temperature operation, relatively low-cost and well-established technology for the fabrication of position sensitive devices currently make silicon detectors the most viable option. Although its quantum efficiency at 511 keV is relatively low (~ 2% for 1 mm of thickness, see Fig. 2.4), silicon has the great advantage of the highest Compton/photoelectric ratio and therefore the highest relative efficiency of single

Compton events (approximately 97% of all photon interactions in 1 mm of silicon are single Compton scatter interactions, see Fig. 2.5). Finally, the use of high-energy photons combined with a relatively low-Z material such as silicon minimises the degradation effects of Doppler broadening, which has been recently reported to affect angular resolution in Compton cameras [Ordonez *et al.*, 1997] (this effect and other noise sources will be discussed in more detail in the following sections).

2.3 Analysis of Compton camera angular resolution

In the analysis of Compton scatter cameras, the *angular resolution* is defined as the uncertainty associated with the measurement of the incident direction of the incoming photons. If D is the distance between a point source located at S and the position of the first Compton scatter at (x_1, y_1, z_1) (see Fig. 2.12), the measurement of the scatter angle θ will be contaminated by a number of noise and uncertainty sources, as will be discussed in the following sections.

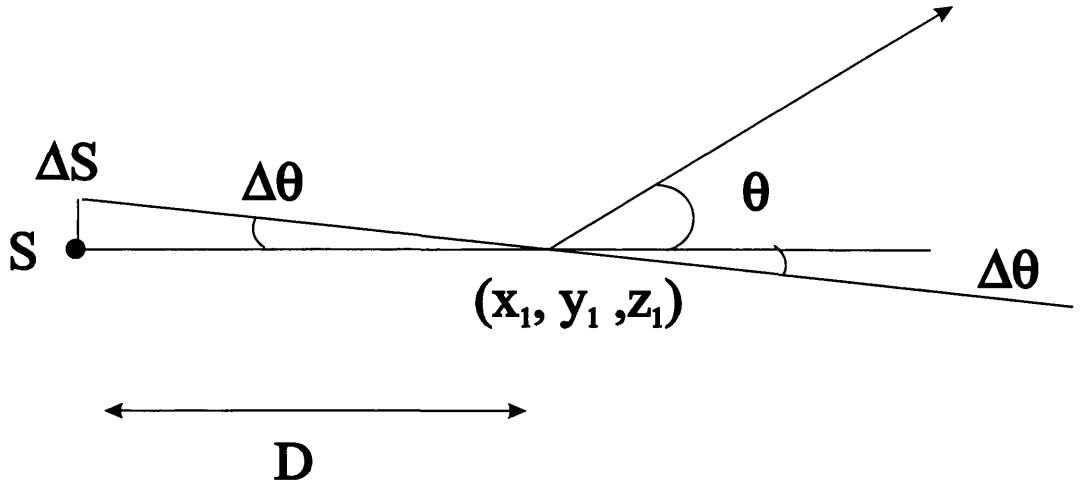

Fig. 2.12: Diagram illustrating the relationship between angular resolution and spatial resolution in a Compton scatter camera.

The precision in the measurement of the scatter angle is represented by the parameter $\Delta\theta$, which will follow a statistical distribution as a result of the fluctuations

in the measurement process of the scatter angle. The statistical distribution of $\Delta\theta$ may be characterised by its FWHM value, which is usually employed to represent the angular resolution of the Compton camera. The precision in determining the position of the source is represented by the spatial parameter ΔS; the fluctuations of $\Delta\theta$ will result in fluctuations of ΔS. The distribution function of ΔS is usually interpreted as the point spread function (PSF) of the system, and its FWHM value is used to characterise the spatial resolution of a Compton camera. The FWHM angular resolution $\Delta\theta_{FWHM}$ is related to the FWHM spatial resolution ΔS_{FWHM} via the source-to-scatter distance D [Singh, 1983]:

$$\Delta S_{FWHM} = D\tan(\Delta\vartheta_{FWHM}) \tag{2.5}$$

An approach to estimating the overall FWHM angular resolution of a Compton camera has been considered by Singh [Singh, 1983], who has identified four independent sources of uncertainty that affect the measurement of the scatter angle. These can be grouped into a geometrical component and a component related to the energy resolution of the scatter detector, so that:

$$\tan^2\left(\Delta\vartheta_{FWHM}^{Tot}\right) = \tan^2\left(\Delta\vartheta_{FWHM}^{Geometry}\right) + \tan^2\left(\Delta\vartheta_{FWHM}^{Energy\ Resolution}\right) \tag{2.6}$$

A detailed description of both terms is given in the following sections.

2.3.1 Geometrical effects

The spatial resolution of both the scatter and the absorption detector is of paramount importance in determining the overall angular resolution of the Compton camera. The angular spread associated with geometric effects was computed by Singh on the basis of his camera design by adding in quadrature the uncertainties due to the pixel width and thickness of the germanium scatter detector and the finite spatial resolution of the back detector, which consisted of an uncollimated γ-camera.

If this analysis is followed [Singh, 1983] and the effect of radiation that is scattered before reaching the front detector is ignored, the combined angular resolution value $\Delta\vartheta_{FWHM}^{Geometry}$ can be obtained from the following expression (see Fig. 2.13, Fig. 2.14 and 2.15):

$$\tan^2\left(\Delta\vartheta_{FWHM}^{Geometry}\right)=\tan^2\left(\Delta\vartheta_{FWHM}^{I}\right)+4\tan^2\left(\Delta\vartheta_{FWHM}^{II}\right)+\tan^2\left(\Delta\vartheta_{FWHM}^{III}\right) \tag{2.7}$$

where the quantities $\Delta\vartheta^{I}$, $\Delta\vartheta^{II}$ and $\Delta\vartheta^{III}$ are evaluated as follows:

$$s\tan(\vartheta+\Delta\vartheta^{I})=\frac{d}{2}+s\tan(\vartheta+\Phi) \tag{2.7 a}$$

$$s\tan(\vartheta+\Delta\vartheta^{II})=\left(s+\frac{l}{2}\right)\tan(\vartheta) \tag{2.7 b}$$

$$s\tan(\vartheta+\Delta\vartheta^{III})=s\tan(\vartheta)+r \tag{2.7 c}$$

and where s is the separation between the two detectors, θ is a given scatter angle, d and l are the front detector pixel width and thickness respectively, Φ is the half-angle subtended by a pixel of the front detector at the source position ($\Phi=\frac{d}{2D}$, where D is the source-electronic collimator distance) and $r=r_0\cos\vartheta$, with r_0 equal to the intrinsic resolution of the back detector. Assuming a typical source-collimator distance of at least 5 cm and a pixel width in the order of a few mm, the implicit dependence on the source-collimator distance D is of the second order and its geometric effect on the overall angular resolution can be neglected.

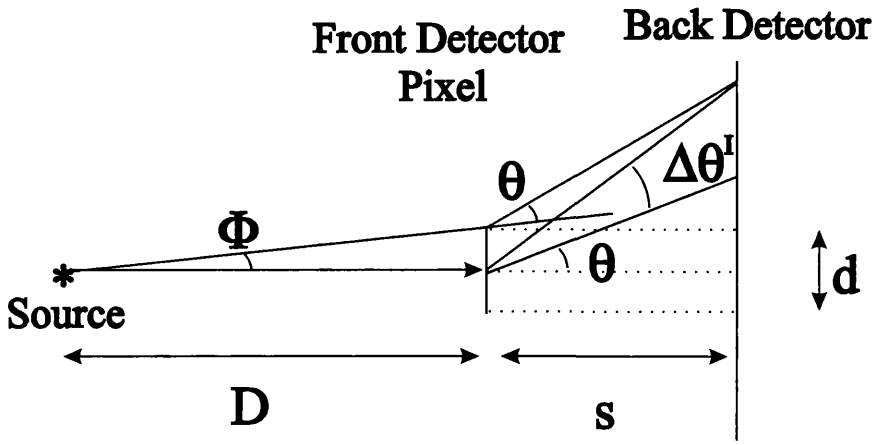

Fig. 2.13: Diagram illustrating the geometric contribution to the angular resolution associated with the width of the front detector pixel (term $\Delta\vartheta^{I}$ in equation 2.7 a).

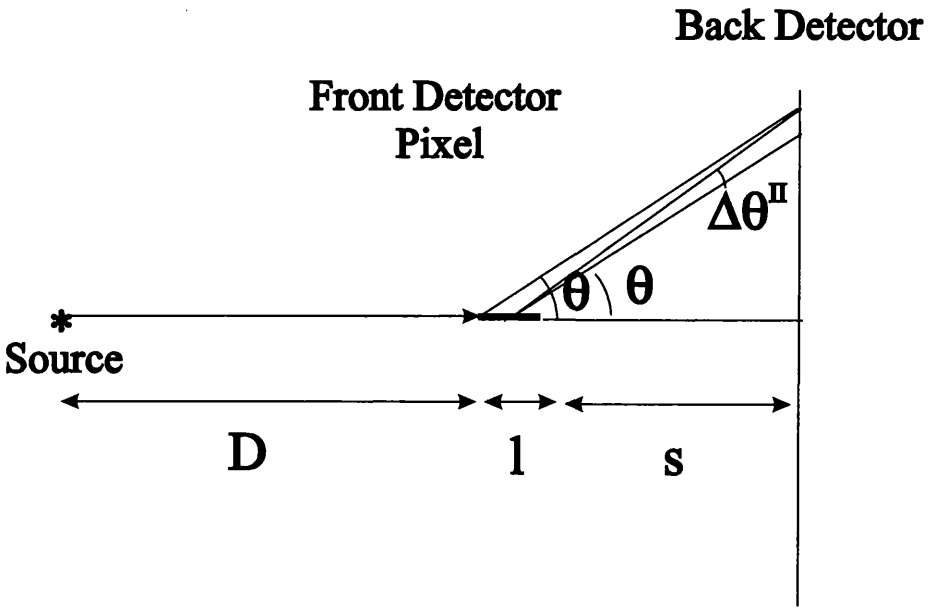

Fig. 2.14: Diagram illustrating the geometric contribution to the angular resolution associated with the thickness of the front detector pixel (term $\Delta\vartheta^{II}$ in equation 2.7 b).

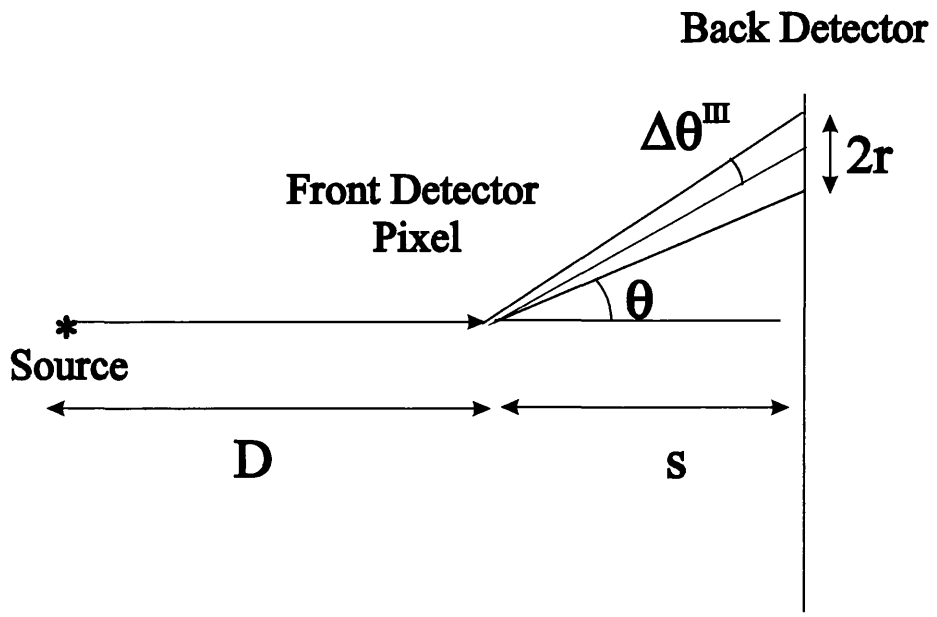

Fig. 2.15: Diagram illustrating the geometric contribution to the angular resolution associated with the finite spatial resolution of the back detector (term $\Delta\vartheta^{III}$ in equation 2.7 c).

From the set of equations (2.7 *a*), (2.7 *b*) and (2.7 *c*) it can be seen that an increase in the separation distance *s* leads to a better spatial resolution of the system. However, this diminishes the sensitivity as it reduces the solid angle subtended by the back detector thus decreasing the probability factor P_C of equation (2.1). An increase in *s* should therefore be compensated by a larger back detector area in order to obtain an equally efficient system. The variation of $\Delta\vartheta^{I}$, $\Delta\vartheta^{II}$ and $\Delta\vartheta^{III}$ as a function of the separation distance (in the range 1-30 cm) is plotted in Fig. 2.16 for a typical detector geometry and an intermediate scatter angle of 45°. Fig. 2.17 shows the geometrical contribution to the total angular resolution that is associated with the width and thickness of the front detector pixel, assuming a separation distance of 1 cm and a scatter angle of 45°.

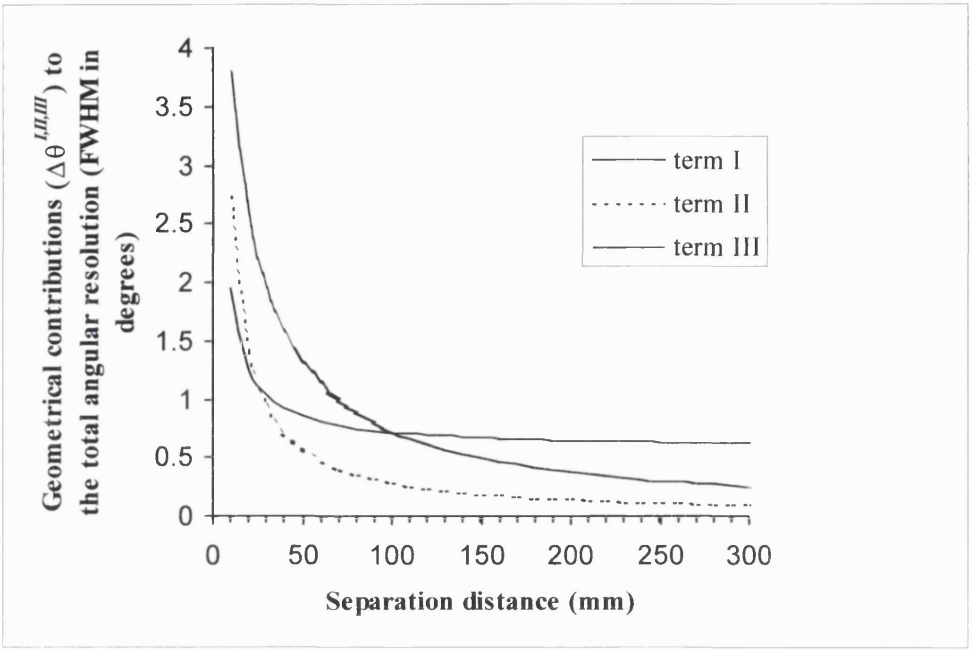

Fig. 2.16: Variation of the geometrical components of the angular resolution in a Compton camera as a function of the distance separating the front and the back detector. The values of $\Delta\vartheta^{I}$, $\Delta\vartheta^{II}$ and $\Delta\vartheta^{III}$ were calculated assuming d = 1 mm, l = 2 mm, r = 4 mm and D =10 cm and θ = 45°.

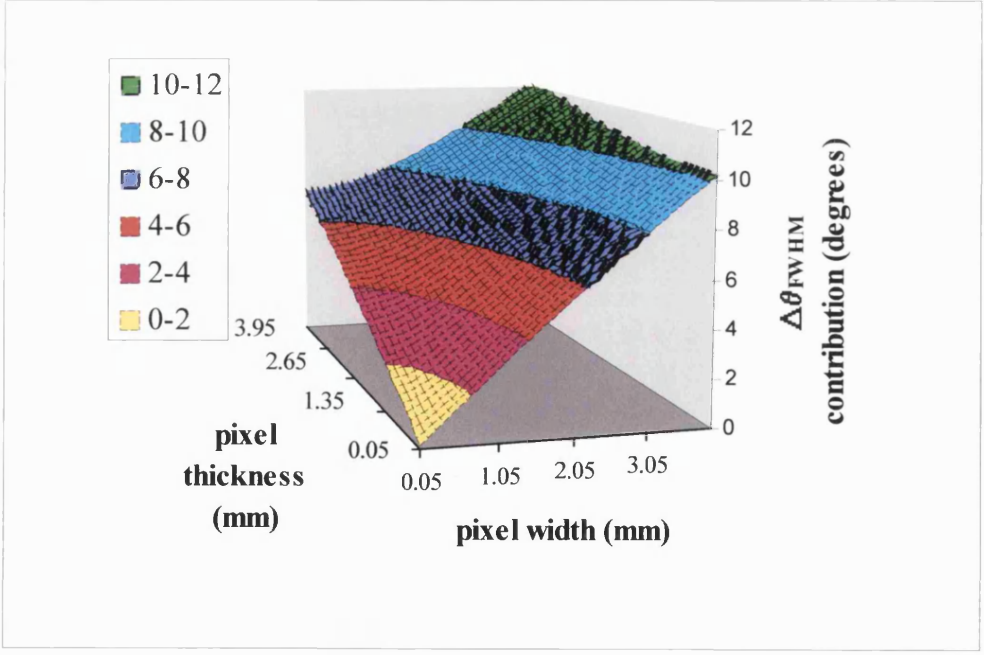

Fig. 2.17: Component of the angular uncertainty (FWHM in degrees) associated with the front detector pixel volume, plotted as a function of pixel width and thickness and calculated for an intermediate scatter angle (45°). The values are calculated assuming s = 1 cm and D = 5 cm.

The contribution of the back detector, considering an intrinsic resolution of 4 mm for the scintillator, is approximately 7°. Assuming that the back detector is used in combination with a relatively thick front detector (4 mm) with equal position sensitivity (i.e. ~ 4 mm in-plane spatial resolution), the total geometric component of the angular resolution will add up to approximately 14° FWHM. If the intrinsic resolution of the back detector is improved by a factor of four (i.e. ~ 1 mm FWHM), the contribution of the geometry to the total angular resolution will decrease only to approximately 12° FWHM. However, if the pixel size and thickness of the front detector are also reduced by a factor of four, the geometric term of the angular resolution will improve dramatically (~ 4° FWHM). These estimates show the critical role played by the spatial resolution of the electronic collimator in determining the overall angular resolution of the camera. The importance of the physical design of the front detector is enhanced further by the effects of its energy resolution over the performance of the camera, as will be shown in the next section.

2.3.2 Energy resolution effects

i) Statistical and electronic noise

The component $\Delta\vartheta_{FWHM}^{Energy\ Resolution}$ in equation (2.6) is related to the uncertainty $\Delta E_{re\ FWHM}$ associated with the measurement of the recoil electron energy in the front detector. This contribution to the total angular spread is therefore a function of the energy resolution of the scatter collimator and can be obtained by differentiating the Compton scatter relationship (1.6) of chapter 1:

$$\Delta\vartheta_{FWHM}^{Energy\ Resolution} = \frac{m_0 c^2}{\sin\vartheta\left(E_\gamma - E_{re}\right)^2}\Delta E_{re\ FWHM} \tag{2.8}$$

The energy measurement uncertainty ΔE_{re} can be interpreted in terms of two physical noise sources that affect the energy resolution in the front detector. These are

the statistical fluctuations in the number of the charge carriers produced by radiation interactions in the semiconductor and the detector electronic noise. As such noise sources are independent and symmetric, their Gaussian distributions allow the total ΔE_{FWHM} energy resolution of a semiconductor detector to be computed as follows [Knoll, 1989]:

$$\Delta E^2_{FWHM} = \Delta E^2_{Stat\ FWHM} + \Delta E^2_{Elec\ FWHM} \tag{2.9}$$

where

$$\Delta E^2_{Stat\ FWHM} + \Delta E^2_{Elec\ FWHM} = 2.35^2\, FwE + (ELN)^2 \tag{2.10}$$

and where F is the Fano factor, w is the mean ionisation energy and ELN is the electronic noise expressed in energy units. The above expression can be computed for $E = E_{re}$ over the whole energy range of the recoil electron for a given energy of the incoming photons, thus allowing relationship (2.8) to be computed at any scatter angle.

The spectrometric contribution of the front detector to the total angular resolution of the Compton camera is plotted in Fig. 2.18 as a function of scatter angle and for a range of values of energy resolutions, assuming that the photon energy is 511 keV and that the front detector is made of silicon. These curves show how the energy resolution of the front detector affects not only the angular resolution of the camera, but also the range of scatter angles that can be used for image reconstruction. It is important to observe that relationship (2.8) is non-linear with energy. The quadratic term in the denominator causes the angular uncertainty to decrease when the gamma-ray energy is increased. This is the major reason why Compton cameras exhibit better performance at high energy. Fig. 2.19 shows for comparison a plot of equation (2.8) at 140 keV and 511 keV, assuming a silicon detector with 1 keV of energy resolution

at 100 keV of measured energy (which represents a typical energy deposition value, corresponding to a scatter angle of approximately 40° for 511 keV γ-rays).

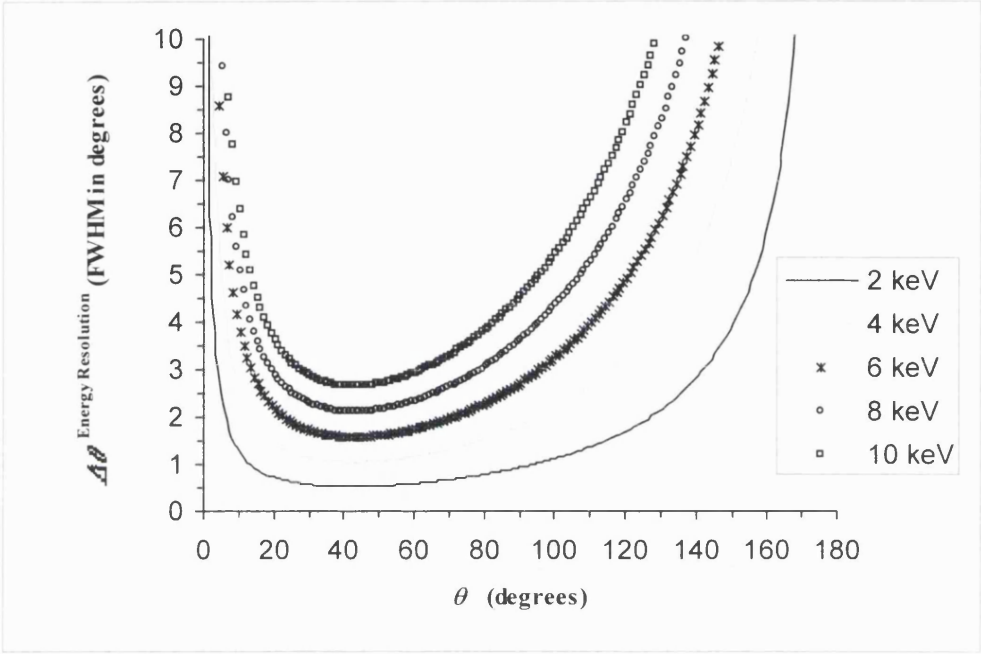

Fig. 2.18: Plots of equation (2.8). The curves are plotted for a silicon detector as a function of the scatter angle and for different values of energy resolution at 100 keV, assuming a 511 keV source.

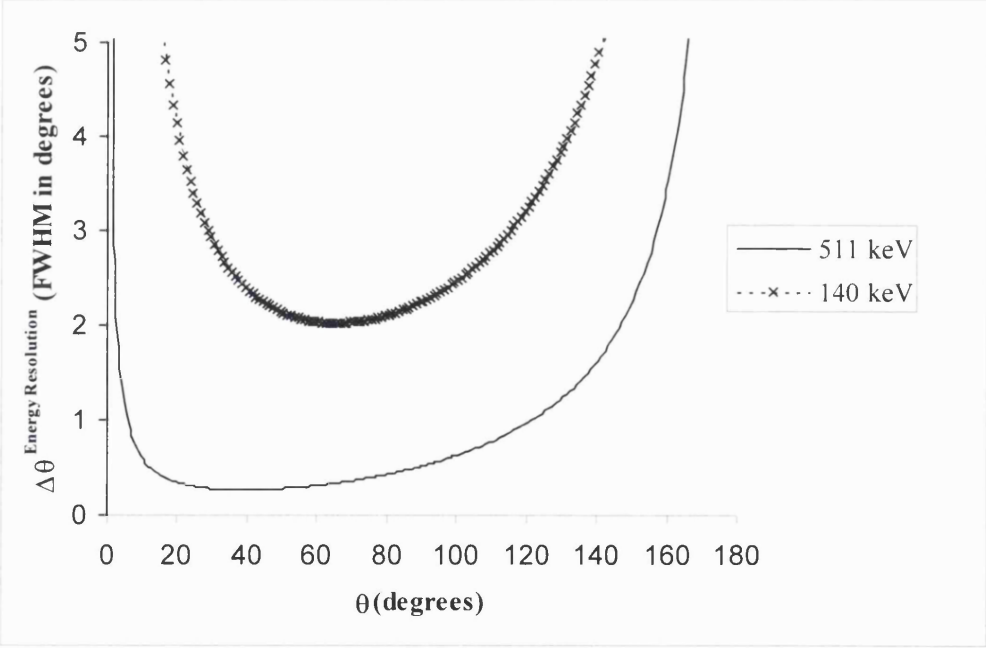

Fig. 2.19: Plots of equation (2.8). The curves are plotted for a silicon detector as a function of the scatter angle and two different values of energy of the incident photons.

By combining the information contained in Fig. 2.17 and Fig. 2.18 it is possible to obtain indications of the angular resolution at a specific scatter angle, when a front detector with given energy resolution and geometry is used. For example, a silicon collimator with 1 x 1 x 1 mm^3 pixel size and 2 keV energy resolution would resolve a 45° scatter angle by 3.4° FWHM. This corresponds to a total camera resolution of 8.5 ° FWHM if the back detector is placed at a distance of 1 cm and its intrinsic spatial resolution is 4 mm.

ii) Doppler broadening

The theoretical analysis of Compton cameras performed by Singh is based on the classical assumption that the Compton interaction in the front detector occurs between a γ-ray and a *free* electron *at rest*. This assumption implies that a one-to-one correspondence is established between the scatter angle θ and the energy E_γ' of the scattered photon, according to the following relationship:

$$E_\gamma' = \frac{E_\gamma}{1 + \frac{E_\gamma}{m_0 c^2}(1 - \cos\theta)} \tag{2.11}$$

where E_γ is the energy of the incident photon. Under these conditions, a one-to-one correlation is therefore assumed also between the kinetic energy of the recoil electron energy E_{re} and the scatter angle θ, considering that it is simply:

$$E_{re} = E_\gamma - E_\gamma' \tag{2.12}$$

From the above relationship one obtains equation (1.6) of chapter 1, which in turn provides expression (2.8) for the angular uncertainty associated with the measurement of the recoil electron energy. In reality, the electrons are *bound* to the atoms of the interacting medium and are *in motion*. An accurate discussion of the energy uncertainty in Compton cameras should therefore consider the binding and pre-

collision motion effects, as was recently observed by Ordonez *et al.* [Ordonez *et al.*, 1997]. The electron momentum before the Compton interaction is described by a distribution or "Compton profile", which is characteristic of the atom and the sub-shell to which the electron belongs. The momentum distribution of the electrons before the collision causes a distribution of possible scattered photon and recoil electron energies for the same scatter angle. As the one-to-one correspondence between energy and scatter angle is lost, the same amount of energy deposited in the detector can also correspond to a range of possible scatter angles.

The energy broadening of Compton-scattered photons (or *Doppler broadening*), which is associated with the momentum of the bound electrons prior to the scatter interaction, is a well-known phenomenon [Stuewer and Cooper, 1977]. However, until very recently the conventional treatment of the angular uncertainties in Compton cameras has always identified the finite energy resolution of the detector as the only source of uncertainty when measuring the energy deposited by the scattered photon in the front detector. Indications are that this effect cannot be neglected, especially in low-energy γ-ray imaging. The effects of Doppler broadening should be considered when the motion and binding energy of the target electrons become important, i.e. at low photon energy and/or high atomic numbers.

Simulation work conducted by Ordonez *et al.* [Ordonez *et al.*, 1997] has suggested that this effect cannot be neglected when designing a camera for ^{99m}Tc imaging. Assuming an incident energy of 140 keV, the simulated distribution of the energy lost by the gamma-rays after Compton scatter at 90° (~ 30 keV) showed a FWHM of approximately 2.1 keV in germanium (Z = 32) and 1.3 keV in silicon (Z=14). These values are not negligible when compared to the typical energy resolutions of elemental semiconductor detectors (e.g. 1 keV or less for a HPGe detector). Further simulation work has estimated that the angular resolution of the C-SPRINT Compton camera at 140 keV is degraded by a as much as 50% because of the effects of Doppler broadening in silicon [Wilderman *et al.*, 1998]. It is worthwhile mentioning,

however, that no *ad hoc* experiments have yet been carried out so as to provide supporting evidence that Doppler broadening has such a dramatic effect on the performance of Compton cameras. This is certainly an aspect of Compton imaging that requires future in-depth investigation.

2.4 Optimisation of the scatter detector characteristics

Although the theory developed by Singh offers a very straightforward method for estimating the angular resolution of a Compton camera, it is mainly based on geometric considerations and is therefore limited to the description of simple designs. The model requires the radiation source to be located on the central axis of the front detector and allows the calculation of the estimated angular resolution only at a specific scatter angle. An adaptation of this model for a ring array used as the back detector predicted angular resolutions only within 25% of the measured values, although the source was located on the symmetry axis of the camera [Martin *et al.*, 1993].

Other aspects of the model may also limit a full description of a system design. The contribution of the back detector, which is represented by equation (2.7 c), is specifically relevant to Singh's camera design, as it is expressed in terms of the intrinsic position resolution of a γ-camera without collimator. The model lacks generality in this sense also because it is limited to a planar view of the interaction sites in the camera. A more general approach should consider the thickness of the pixel in the back detector, which affects the estimate of the interaction co-ordinate in the transverse direction. The energy resolution component in Singh's model is made independent of the front detector thickness, which is a reasonable assumption for low-energy applications. For high-energy photons and relatively thin detectors, however, equation (2.8) should account for possible escapes of high-energy recoil electrons. In addition, as was previously mentioned, current indications are that a realistic procedure for estimating the angular resolution should also include the

effects of Doppler broadening. Finally, the described method neglects the inherent degradation of the PSF due to the ellipse overlap (see section 1.4.1) in the image reconstruction process.

In order to overcome these limitations, a specific-purpose simulation tool was developed for this study. The design tool was applied in order to determine the energy and spatial resolution requirements for a silicon scatter collimator tailored to 511 keV photons.

2.4.1 Development of a computer model

The computer model for a Compton camera was implemented making use of EGS4 [Nelson *et al.*, 1985], which is the same simulation code that was employed for the work described in section 2.2. Other Monte Carlo codes in widespread use for the simulation of radiation transport (e.g. the Integrated TIGER Series (ITS) [Halblieb *et al.*, 1984]) were initially considered for this task. The EGS4 package was chosen to model the problem of interest because of its particularly flexible programming structure, which allows the user to track individual particles and extract the information required to construct the source image. The model, which simulates the operation of a camera consisting of two planar detectors, was initially set up with a scatter detector made of silicon in combination with a scintillation crystal (NaI) as the rear absorption detector (see Fig. 2.20).

In order to maximise the efficiency of Compton scatter, the silicon thickness was set to 1 mm, as this is approximately the technological limit in the growth of crystalline silicon. A sensitive area of 6 x 6 cm^2 was assumed for the silicon scatter detector, as such a size would allow relatively large organs (e.g. the heart) to be imaged. For simplicity of simulation geometry, the sensitive area and thickness of the back detector was assumed to be the same as in the front detector. The silicon wafer was placed at a distance of 5 cm from a point source, located in air, emitting 511 keV γ-rays isotropically. In order to maximise the solid angle viewed by the NaI

detector, the separation distance between the two camera elements was set to a minimum (1 cm).

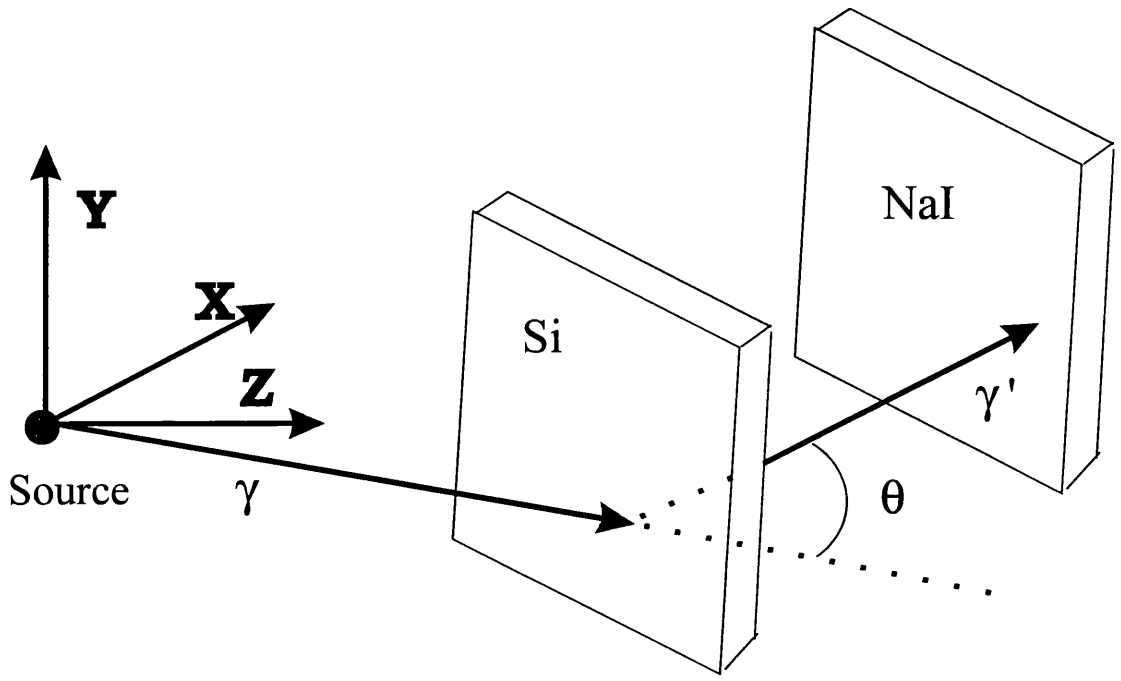

Fig. 2.20: Diagram showing the operation of the two-plane Compton camera that was simulated in the computer model. The events that were tracked in the simulation consisted of a Compton scatter interaction in the Si detector, followed by photoelectric absorption in the scintillation crystal. For each event of interest, the positions of interaction in the two detectors and the energy deposited in the silicon detector were recorded. The simulations were aimed at optimising the spatial resolution and energy resolution of the silicon detector.

Information on the position of interaction and the amount of deposited energy was recorded for all 'useful events', i.e. for those events that consisted of a single Compton interaction occurring in the Si detector, followed by photo-electric absorption in the scintillator. The noise-free pulse height spectrum that was recorded in the scatter detector for such events is shown in Fig. 2.21.

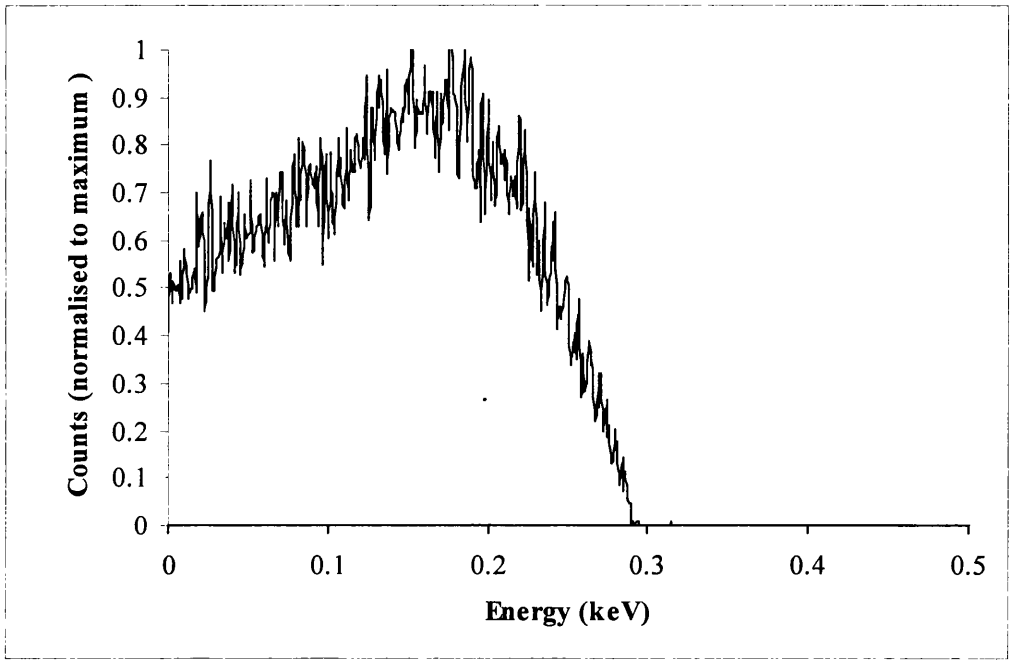

Fig. 2.21: Simulation of the energy spectrum recorded by the silicon detector for those 511 keV photons that undergo single Compton scatter in the front detector and are fully absorbed in the back detector.

In order to simulate the pulse measurement process in the scatter detector, fluctuations were introduced in the energy signals generated by the EGS4-based code. The statistical and electronic noise sources were simulated by using equations (2.9) and (2.10), where for silicon it was assumed that F=0.1 and w = 3.61 eV . The "measured" energy value was sampled from a Gaussian distribution characterised by a variance $\sigma^2 = \frac{\Delta E_{FWHM}^2}{2.35^2}$ and a mean value $\mu = E_{re}$ (with the important difference that here the value E_{re} is not the kinetic energy *transferred* to the recoil electron, but is the energy *deposited* by the recoil electron in the front detector). Doppler broadening effects were accounted for by making use of the LSCAT package developed for EGS4 [Namito *et al.*, 1994]. Realistic detector position signals were also generated. This was done by transforming the interaction co-ordinates into discrete elements of a position matrix associated with the detector pixels.

2.4.2 Results from the simulation of point source images

The simulated measurements of energy and position were used to reconstruct the image of a point source. The image reconstruction was carried out by applying a simple algorithm, which had been previously developed by the UCL Radiation Physics Group and applied to experimental data in the course of their research work on industrial Compton cameras [Royle and Speller, 1994]. The reconstruction programme was based on a pixel matrix on the image plane. The counts (or grey levels) in all the matrix pixels were initialised to zero. The co-ordinates of each pixel were assumed in turn as the initial guess for the source position and were employed to compute the corresponding scatter angle (the direction cosines of the scattered photon were calculated from the recorded positions of the interactions in the two detectors). The computed scatter angle was then used to calculate the corresponding energy value of the recoil electron. When this matched the value of energy that was recorded in the Compton interaction, one count was added in the relevant pixel. The grey level of the pixel map was displayed on a 0-255 scale and was normalised to the maximum value of intensity (i.e. the maximum value of counts).

In this section, results from the Compton camera model are presented, where the Point Spread Function (PSF) of a Compton scatter camera was evaluated as a function of the spatial and energy resolutions of the silicon collimator. In analogy with the definition of the PSF given in section 1.2.2 for a mechanical collimator, the point spread function of the Compton camera was evaluated as the radiation profile obtained from a point source placed in front of the scatter collimator. A number of simulations were carried out by combining different values of pixel size and energy resolution in the front detector. As the aim was to optimise these two physical parameters in the collimator design, the characteristics of the back detector (thickness, area and pixel size) were kept constant in most of the simulations. Some examples of the simulated images of a 511 keV point source are shown in Fig. 2.22 *a* to 2.22 *d*. The corresponding image profiles are shown in Fig. 2.23 *a* to 2.23 *d*. The

PSF widths (at half maximum) that were estimated for the simulated images are presented in Table 2.3.

Table 2.3: Evaluation of Point Spread Function from simulated images of a 511 keV γ-ray point source, placed at a 5 cm distance from the front detector plane. The separation between detectors is 1 cm.

Pixel size x thickness in Front Detector	**Pixel size x thickness in Back Detector**	**Front Detector energy resolution (FWHM in keV) @ 100 keV**	**Estimated Spatial Resolution (FWHM of the PSF in mm) @ 5 cm**	**Corresponding angular resolution (FWHM in °)**
300 μm x 1 mm	1 mm x 1 mm	2	3.4	3.9 °
500 μm x 1 mm	1 mm x 1 mm	2	3.5	4.0 °
1 mm x 1 mm	1 mm x 1 mm	2	4.0	4.6 °
1 mm x 1 mm	4 mm x 1 cm	2	22	24°
300 μm x 1 mm	1 mm x 1 mm	6	4.5	5.1 °
500 μm x 1 mm	1 mm x 1 mm	6	4.8	5.5 °
1 mm x 1 mm	1 mm x 1 mm	6	5.1	5.8 °
300 μm x 1 mm	1 mm x 1 mm	10	5.6	6.4 °
500 μm x 1 mm	1 mm x 1 mm	10	5.8	6.6 °
1 mm x 1 mm	1 mm x 1 mm	10	6.0	6.8 °
---- (*)	---- (*)	---- (*)	0.5 (*)	0.6 ° (*)

(*) "Perfect detectors" case: energy and position are measured in the detectors with infinite accuracy.

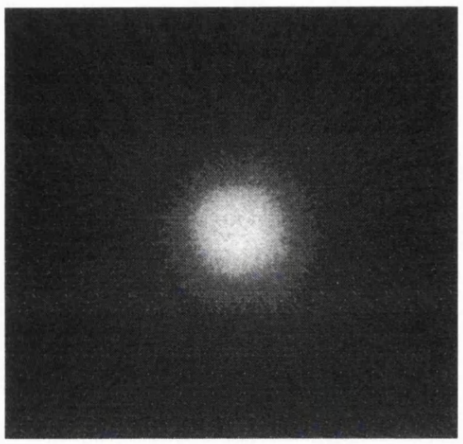

a) *F.D.* pixel size: 1mm x 1mm
F.D. thickness: 1mm
F.D. energy resolution: 2 keV
B.D. pixel size: 4 mm x 4 mm
B.D. thickness: 1 cm

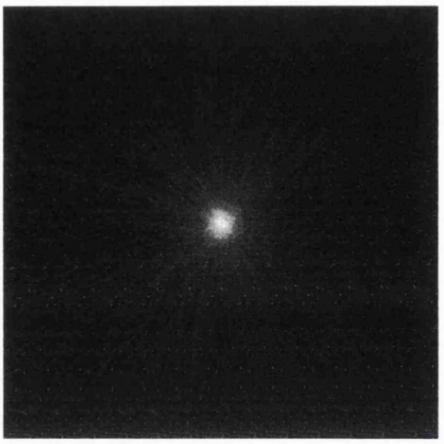

b) *F.D.* pixel size: 1mm x 1mm
F.D. thickness: 1mm
F.D. energy resolution: 10 keV
B.D. pixel size: 1 mm x 1 mm
B.D. thickness: 1 mm

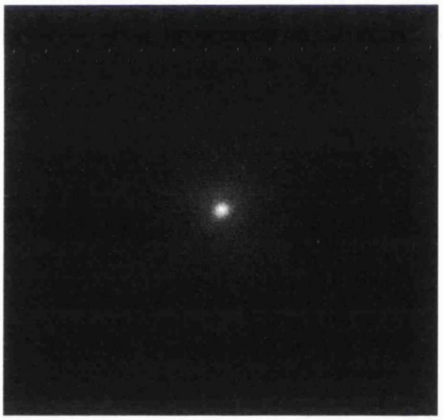

c) *F.D.* pixel size: 0.3 mm x 0.3 mm
F.D. thickness: 1mm
F.D. energy resolution: 2 keV
B.D. pixel size: 1 mm x 1 mm
B.D. thickness: 1 mm

d) Energy and position are here measured with perfect accuracy in both Front and Back Detector (case of 'perfect detectors')

Fig. 2.22: Simulated images of a 511 keV point source, assuming different values of energy resolution (FWHM at 100 keV) and pixel size in the *Front* and *Back Detectors*. The separation distance between detectors is set to 1 cm.

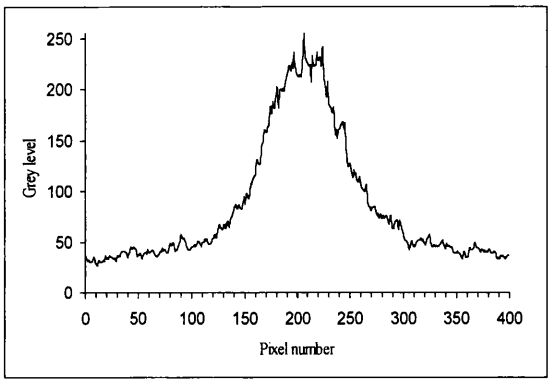

a) *F.D.* pixel size: 1mm x 1mm
F.D. thickness: 1mm
F.D. energy resolution: 2 keV
B.D. pixel size: 4 mm x 4 mm
B.D. thickness: 1 cm

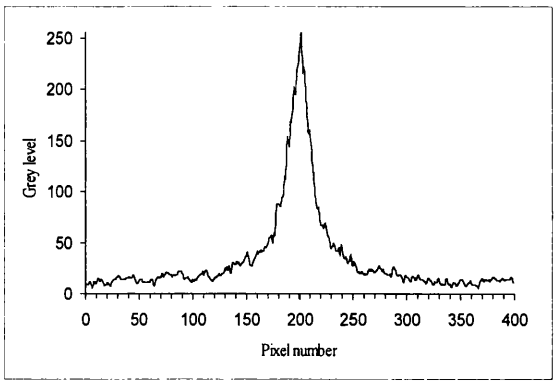

b) *F.D.* pixel size: 1mm x 1mm
F.D. thickness: 1mm
F.D. energy resolution: 10 keV
B.D. pixel size: 1 mm x 1 mm
B.D. thickness: 1 mm

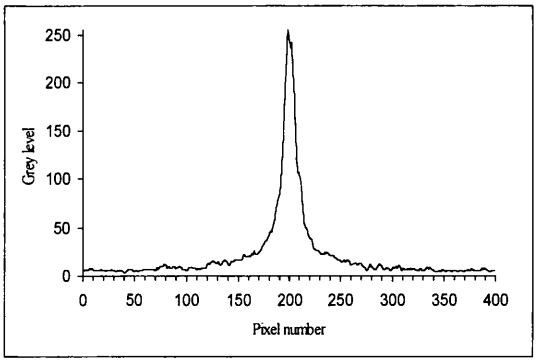

c) *F.D.* pixel size: 0.3 mm x 0.3 mm
F.D. thickness: 1mm
F.D. energy resolution: 2 keV
B.D. pixel size: 1 mm x 1 mm
B.D. thickness: 1 mm

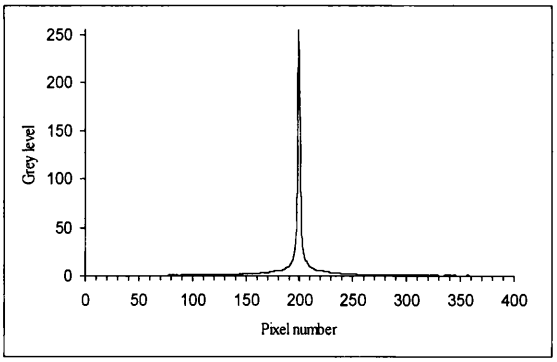

d) Energy and position are here measured with perfect accuracy in both Front and Back Detector (case of 'perfect detectors')

Fig. 2.23: Profiles (or Point Spread Functions) of the images shown in Fig. 2.22 *a)* to Fig. 2.22 *d)*. The spatial resolution of the modelled systems was evaluated in each case as the FWHM of the relevant image profile. Images are 400 x400 pixels in size, with a pixel width of 0.25 mm.

2.4.3 Conclusions on fundamental detector requirements

The performance of existing positron imaging systems may be expressed in terms of their angular resolution by making use of a relationship analogous to (2.5), where the FWHM spatial resolution values are obtained from Tables 1.2, 1.5 and 1.6 and where D equals 10 cm. Following this definition, it results that the angular resolution of PET scanners and DHCI systems ranges from 2° to 4°, whereas for SPECT cameras that make use of parallel-hole mechanical collimators the typical performance at 511 keV of energy is in the order of 7°-8°. As the project aimed to design a Compton camera as a feasible alternative to other collimation methods, the performance of mechanical collimators was set as the minimum requirement for the angular resolution of the first prototype.

The simulations showed that superior angular resolution (less than 4°) would be achieved with a 1-mm thick silicon detector with a pixel size of 300 μm and 2% energy resolution. A Compton camera with good angular resolution (~ 4.6°) could be designed whilst allowing for a larger pixel size (1 mm x 1 mm). In position sensitive detectors made of silicon, the energy resolution is mainly determined by the electronic noise introduced by detector readout. Unfortunately, a noise level as low as 2 keV is rather difficult to achieve in silicon under experimental conditions, even with the use of sophisticated readout integrated electronics. However, the results of the above simulations showed that it is possible to trade off energy resolution for spatial resolution. In particular, the performance obtained by combining 6 keV FWHM energy resolution with a pixel width of 300 μm is almost as good as the one obtained by combining 2 keV energy resolution with 1 mm^2 pixel size. The angular resolution in both cases is approximately equal to 5°, which is well within the upper limit set for the angular spread.

This design study made it possible to define the "ideal" basic characteristics of a silicon scatter detector so as to set up a desktop laboratory prototype, aimed at carrying out tests on the Compton collimation of 511 keV γ-rays. Such a detector

should be 1 mm thick, have a sensitive area of at least 2.5 x 2.5 cm^2 (so as to image objects of size comparable to small organs such as the thyroid) or possibly larger (~ 6 x 6 cm^2), have a spatial resolution in the order of 300 μm (in both the x and y directions) and have an energy resolution of 6 % or better for 100 keV of energy deposition.

2.5 A Compton collimator based on silicon microstrip detectors

2.5.1 Selection of a position sensitive silicon detector

The requirement for a silicon detector with high spatial resolution and two-dimensional position information is fulfilled by different design options. The technology of position sensitive silicon devices has seen enormous developments in the last twenty years. Such progress is associated with the evolution of High-Energy Physics (HEP) instrumentation and in particular of silicon tracking microscopes, which are used to probe a variety of particles of physical interest. The position sensitive silicon sensors employed in HEP experiments include microstrip detectors, pixel detectors and drift detectors.

Microstrip devices [Peisert, 1993], [Damerell, 1995] are the silicon detectors most traditionally employed in HEP experiments. Their technology is therefore well established and they are widely available as commercial products in a variety of geometrical designs and readout configurations. This is the main reason why they were chosen for the realisation of the Compton collimator. Another advantage of silicon microstrip detectors is that the readout electronics is located to the side of the sensitive area and therefore does not interfere with the trajectory of Compton scattered photons. Two-dimensional position information is obtained with double-sided devices [Batignani *et al.*, 1991], [Welhammer, 1994], which are described in the following section.

Pixel detectors [Damerell, 1995], [Weilhammer, 1996] are fabricated in a similar way to microstrip detectors, but with a different segmentation approach: the implant strips on the detector surface are replaced with a 2-D array of pixels or small-area "pads". Pixel detectors are currently of great interest to the HEP international community, as one of their main advantages over strip devices is that they allow multiple hits to be unambiguously located. However, such a capability is obtained at the expense of a much larger number of readout channels (assuming a N x N position grid, the number of channels is N^2 versus 2N as in the case of a double-sided microstrip detector). In pixel detectors the channel readout is usually based on a hybrid approach, where the integrated electronics is implemented on a separate chip that is 'sandwiched' to the back of the detector via a technological process known as 'bump bonding'. Unfortunately, this configuration does not favour the use of pixel devices in a Compton camera, due to the fact that the readout electronics would be positioned right behind the scatter plane. Therefore, pixel devices were not considered a viable option for this project.

Silicon drift detectors [Gatti and Rehak, 1984], on the other hand, have already been suggested for the construction of a Compton camera [Solomon and Ott, 1988]. These devices are based on the measurement of the transport time of the charge carriers produced by the incoming radiation and can be designed so as to provide 2-D information [Chen *et al.*, 1992]. Owing to their low-noise characteristics, these detectors could be suitably applied to the construction of a Compton collimator. However, their production in industry is not as established as for microstrip detectors and their use in this project would have required customised design and production. Such an option was not taken into consideration because of the high associated costs.

2.5.2 Double-sided silicon strip detectors: operation and general characteristics

A microstrip detector is basically a position sensitive *p-i-n* diode, consisting of a wafer of high-purity *n*-type silicon where parallel strips of highly doped p^+ silicon are implanted on one side (*junction or p-side*) and a layer of highly doped n^+ silicon is

implanted on the other (*ohmic or n-side*). The n^+ layer is segmented into strips in the orthogonal direction with respect to the p^+ strips on the opposite side, so as to achieve two-dimensional position sensitivity. Between adjacent strips, on both planes a layer of silicon dioxide (SiO_2) or *passivation layer* is maintained so as to protect the wafer surface. The oxide passivation process introduces a positive fixed oxide charge, which produces an electron accumulation layer at the Si-SiO_2 interface. This phenomenon affects the operation of the *n*-side of the detector, as it causes a short-circuit of all the n^+ strips. In most double-sided detectors this problem is solved by implanting blocking p^+ strips between adjacent n^+ strips [Kemmer and Lutz, 1988].

The p^+- *n* junction can be reverse polarised by applying a positive voltage to the n^+ strips with the p^+ strips grounded. The reverse polarisation produces in the silicon bulk a depletion region, which extends with increasing bias into the *n* side of the wafer until it reaches the n^+ strip back plane. The depletion region is the sensitive volume of the detector and achieves its maximum thickness when the device is fully depleted. The passage of ionising radiation through the depleted silicon produces electron-hole pairs, which migrate in opposite directions and induce a charge signal on the respective collection electrodes.

The reverse voltage can be applied to the detector according to different biasing schemes. The most common approach is the use of integrated polysilicon resistors [Caccia *et al.*, 1987] that join the strips to a common bias line, which traces the perimeter of the implant strips on both sides. Another biasing scheme is the 'reach-through' or 'punch through' [Holl *et al.*, 1989], where a p^+-type DC contact (the 'bias ring') is implanted in an orthogonal direction and at a small distance ($\leq$ 10 μm) with respect to the detector p^+ strips. If a reverse bias is applied between the bias ring and the back plane, a 'reach through current' will be observed, consisting of holes flowing between the floating strips and the bias ring. A state of equilibrium is eventually attained, where the potential of the floating strips follow the bias voltage with a constant difference. A more elaborate version of this method is the FOXFET biasing

approach [Allport *et al.*, 1991], which makes use of a gate electrode on top of the oxide between bias ring and floating strips; the gate voltage allows tuning of the potential difference between the bias ring and the floating strips. Both sides of a silicon strip detector have one or more extra implants, the *guard rings*, which surround the sensitive area of the detector; they are held at the same potential as the bias ring and have the function of collecting edge currents and shaping the periphery of the electric field.

Every p^+ and n^+ implant strip is metallized so as it can be bonded to the readout electronics. The detector strips may be coupled to the preamplifier channels of the readout electronics according to two configurations: AC or DC coupling. In DC-coupled detectors, the strip metal layer is in direct contact with the implanted strips. In AC-coupled detectors, the metal readout strips are isolated from the implanted strips by means of a thin layer of dielectric. This is usually silicon dioxide, although a layer of silicon nitride (Si_3N_4) can also be added. This is done in order to minimise the probability of having simultaneously a 'pinhole' in both the oxide and the nitride layers (see section 3.9 of chapter three regarding detector testing for this type of defect). Figures 2.24 and 2.25 show a schematic diagram of the *p*-side and *n*-side of an AC-coupled double sided strip detector. The use of AC coupling prevents the DC component of the leakage current from being sensed by the amplifier, thus avoiding large pedestal variations across the detector readout channels.

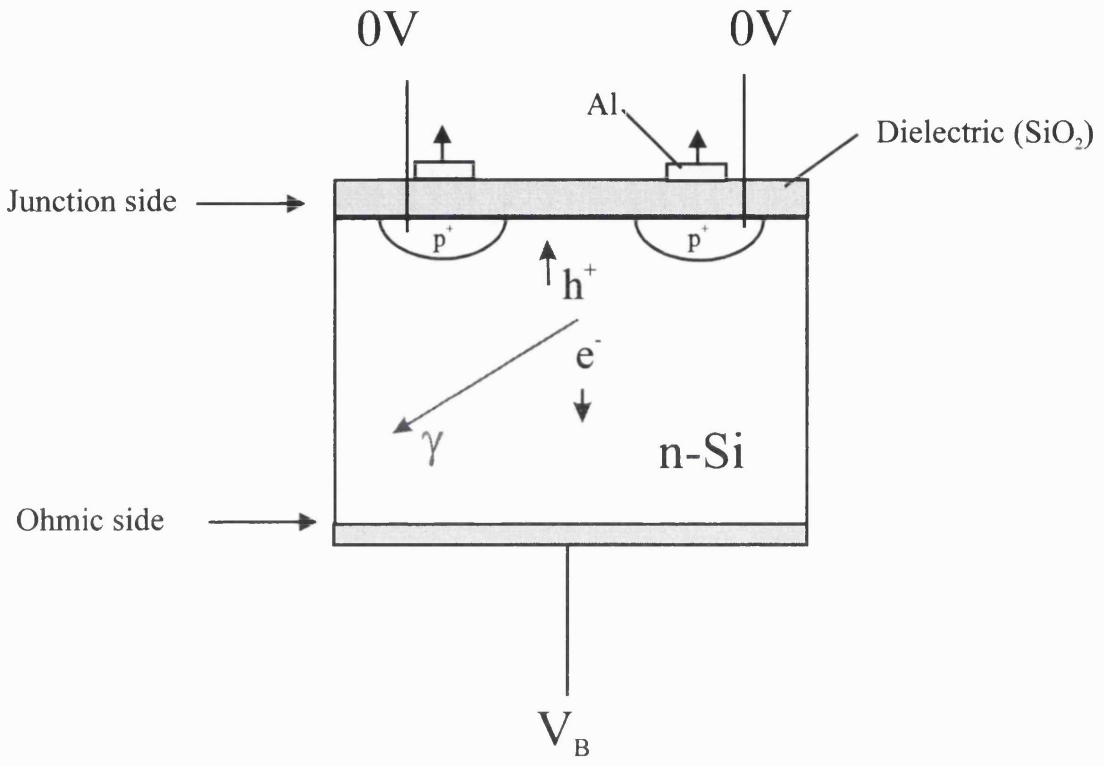

Fig. 2.24: Schematic diagram of a double sided AC-coupled silicon microstrip detector, *p*-side.

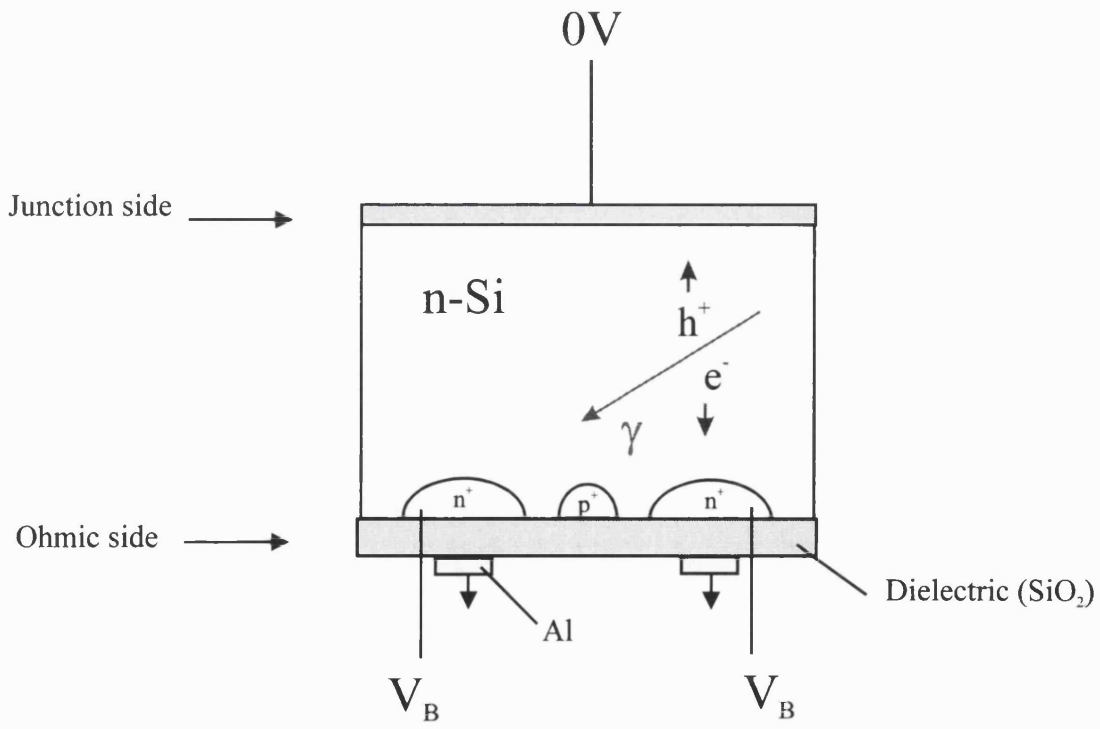

Fig. 2.25: Schematic diagram of a double sided AC-coupled silicon microstrip detector, *n*-side.

2.5.3 Selection of a specific design of strip detector and associated readout electronics

The requirements of an 'ideal' silicon scatter detector for a Compton camera application were summarised in section 2.4.3, where it was stated that a similar performance would be achieved by either combining a pixel size of 1 mm with 2 keV FWHM energy resolution or a pixel size of 300 μm with 6 keV FWHM energy resolution. Such general results are now applied to the specific case of a strip detector design.

In silicon strip detectors, the energy resolution is dominated by the electronic noise, which can be expressed as a function of various components, as will be discussed in more detail in chapter four. The most important components of the noise are associated with the detector leakage current (typically in the order of 5-10 nA per strip) and the VLSI readout electronics. The noise of an integrated preamplifier may be expressed as the standard deviation (σ) of the noise spectrum in keV and as a function of the input capacitance (see chapter four, section 4.4). Assuming 10 pF of input capacitance, examples of noise (σ values) of integrated preamplifier channels are 0.8 keV (Viking chip [Toker, 1994]), 2.3 keV (APV6 chip [Raymond, 1997]) and 4.2 keV (MX3 chip [Schwarz, 1994]). One may therefore assume that a FWHM energy resolution value between 5 and 7 keV (at 100 keV energy deposition) could be achieved by selecting good quality silicon wafers and by making use of a low-noise chip such as the APV6, which was employed in this project. As the APV6 had been designed for use with AC coupled detectors, this type of coupling became an additional requirement on the detector characteristics for this project.

In a strip detector, the requirements on 'pixel size' have to be translated in terms of the *strip pitch*, which is the characteristic distance that separates adjacent implants. If one assumes that the hit position is given by the strip with the highest signal, the FWHM spatial resolution of a strip detector has an inherent geometrical limit, which can be expressed in terms of the pitch p as follows [Weilhammer, 1994]:

$$\Delta x_{FWHM} = 2.35\frac{p}{\sqrt{12}} \tag{2.13}$$

However, if the strip pitch is comparable to or smaller than the width of the charge packet created by the recoil electron at interaction, better precision can be obtained by applying centre of gravity (COG) algorithms (the limit on the achievable resolution is in this case dependent on the signal to noise ratio). The current limitation on the readout pitch of the existing front-end electronics is 50 μm. If sampling of narrow distributions is required, the detector may be designed with a strip pitch that is smaller than the readout pitch (i.e. the separation between the strips that are actually wire-bonded to the electronics). In such applications, intermediate strips are left floating, with the pre-amplifier channels connected every *n*-th strip; the principle of capacitive charge division is employed for the detector read-out [England *et al.*, 1981]. Typical values of spatial precision obtained in HEP experiments are in the order of 5 –10 μm, considering detectors with a strip pitch $\leq$ 50 μm and a readout pitch $\leq$150 μm [Damerell, 1995].

A Monte Carlo study was carried out in order to determine the profile of the recoil electron range following Compton scatter of 511 keV photons in silicon (see Fig. 2.26). It was shown that the FWHM value of the spatial distribution is approximately 280 μm. Although this estimate does not account for diffusion effects and for the presence of an electric field, it suggests the need for a relatively large strip pitch (in the order of a few hundred μm) so as to prevent the produced charge being shared by a large number of strips, resulting in a poor signal/noise ratio. On the other hand, charge sharing may improve spatial resolution by applying the COG position finding method to two or three strips. It was concluded that the optimum strip pitch was approximately 500 μm. According to equation (2.13), such a value would provide a FWHM spatial resolution of 340 μm or better, thus fulfilling the position sensitivity requirements established for the Compton scatter detector.

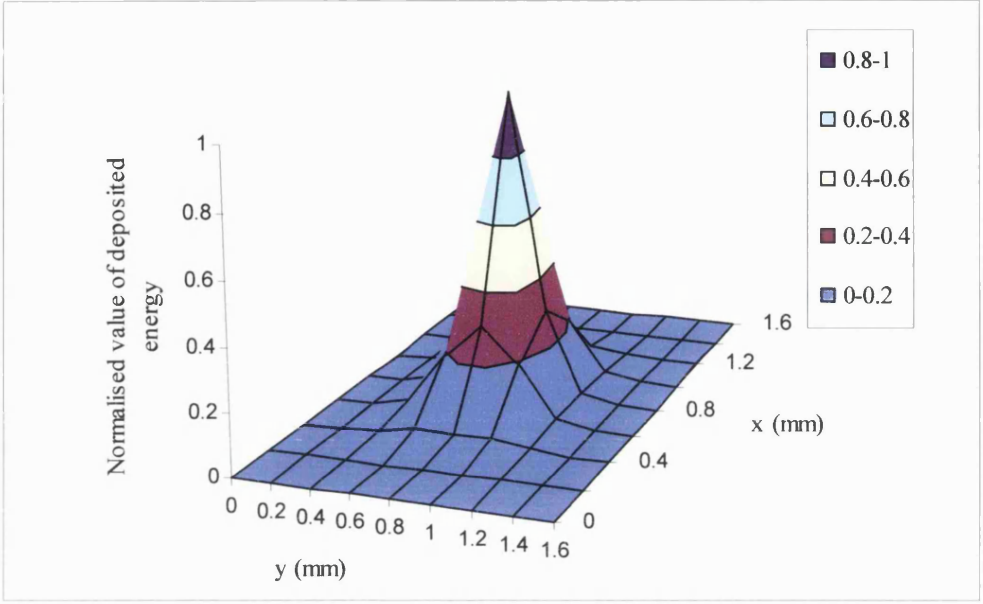

Fig. 2.26: Monte Carlo simulation of the spatial distribution of the energy deposited in silicon by the recoil electrons, following Compton scatter of 511 keV photons.

In section 2.4.3 it was also stated that the desirable thickness of the scatter detector was 1 mm, in order to maximise single Compton efficiency. Satisfying such a requirement posed some difficulties; the standard silicon wafers used in detector manufacture are only 300 μm thick, since they are usually designed for the detection of charged particles or low-energy X-rays. A compromise solution was found in the choice of the IPS 60x60–500 NX-NY128 double-sided silicon microstrip detector, which is manufactured by the French company Eurisys[12]. The detector is AC coupled, punch-through biased, with a sensitive area of 6 x 6 cm^2, a thickness of 500 μm and a strip pitch of 470 μm in both planes (128 channels/side). A detailed description of the strip configuration and the technical specifications of the detector is given in the next chapter. The detector area, strip pitch and type of coupling of this detector design were a perfect match of the required characteristics, which were selected on the basis of the computer model. However, the detector thickness was half the value stated as 'ideal', causing the absolute efficiency of single Compton scatter at 511 keV to

diminish from approximately 2% to 1%. The decrease in efficiency did not pose a serious problem, as the construction of the laboratory prototype was aimed, in its initial phase, to study the spatial resolution of the system rather than its efficiency. A more critical aspect related to the decrease in sensitive thickness was whether this would affect the energy resolution, owing to possible escape of recoil electrons with relatively high energy. To investigate this, the computer model for the simulation of a point source image was applied to a silicon front detector of 500 μm in thickness and the results were compared to the case of a 1-mm thick detector.

A simple study of the electron escapes was also carried out by evaluating the attenuation effects associated with the wafer thickness. No consideration was made regarding the presence of an electric field. It was shown that, although at 511 keV the overall percentage of electron escapes increased from approximately 10% in 1 mm of silicon to 18% in 500 μm of silicon, the percentage of escapes in the group of events used for image reconstruction increased only by 2% (from approximately 6% to 8 %). This was due to the scatter geometry of the modelled camera, for which the maximum central scatter angle was 72° (corresponding to 208 keV of energy deposition). This geometrical constraint prevented those photons that scattered at large angles (for which the recoil electrons were more likely to escape) from reaching the back plane. On the other hand, a thinner detector provided the advantage of higher position sensitivity along the z-axis. The simulations showed that the overall angular resolution was improved by approximately 1.2° when the active thickness was diminished from 1 mm to 0.5 mm (assuming a detector spatial resolution of 1 mm and an energy resolution of 6%). The computer model for the simulation of a point source image was also applied to the case of the standard thickness of a silicon wafer (300 μm), for which the efficiency of single Compton scatter at 511 keV is approximately 0.6%. It was found that in this case the simulated PSF improved by only 0.7° with respect to the case of the 1-mm thick detector, as the gain in spatial resolution along the detector axis was counterbalanced by the loss in energy

[12] Detectors manufactured by Eurisys Mesures, Tanneries CEDEX, France.

resolution, due to the increase of electron escapes in the events contributing to the image (approximately 12%, while the overall electron escapes were 30%).

In conclusion, a double-sided silicon detector manufactured according to the IPS 60x60–500 NX-NY128 design was found to fit the requirements for a scatter detector tailored to the Compton collimation of 511 keV photons. As already suggested in section 2.2.4, the design results for both strip pitch and wafer thickness could also be extended to the case of the design of each silicon layer in a multiple Compton camera, where the collimator would consist of a stack of strip detectors.

Chapter 3

Tests of Electrical Characteristics of Unbonded Silicon Strip Detectors

3.1 Introduction

A good characterisation of the strip detectors was essential to the development of the silicon collimator. Two sets of experimental measurements were carried out for this purpose at the Blackett Laboratory, Imperial College. The first set of tests were performed on the bare silicon wafers, i.e. prior to the bonding of the electronics. Such tests were carried out in order to measure some important electrical properties of the detectors and compare them to the relevant manufacturer specifications. These tests measured parameters, such as the total strip capacitance and the leakage current, which affect the noise level in the detectors. The measurements of strip capacitance required the application of equivalent circuit models, which allowed the experimental results to be related to the geometrical and physical characteristics of the detector design. All measurements on unbonded detectors are presented in this chapter. The second set of experimental tests were performed on the bonded detectors. Such tests were principally aimed at characterising the noise pattern across the strips, as well as performing a preliminary energy calibration of the detectors. The experiments on the bonded detectors are described in chapter four.

As described in the previous chapter, the silicon strip detectors were manufactured by Eurisys Mesures, France with AC coupling and punch-through biasing. A photograph of an unbonded detector is shown in Fig. 3.1. The detector design (type IPS 60x60 – 500 NX-NY128) can be seen in Figures 3.2 to 3.5, which show details of

the technical drawings supplied by the company and indicate the configuration of the strips and the location of the bonding pads. The silicon wafers were realised in planar technology with high-purity, *n*-type (phosphor doped) silicon. The float zone process [Sze, 1985] was used to grow the silicon. The ingots were sliced into wafers with <111> lattice orientation. The strips were created on both sides of each wafer by ion implantation. Two batches of two detectors each were delivered (serial numbers: B2578-1, B2578-2, B2578-3, B2578-4). The nominal characteristics of the detectors, as specified by the manufacturer, are summarised in Tables 3.1 and 3.2.

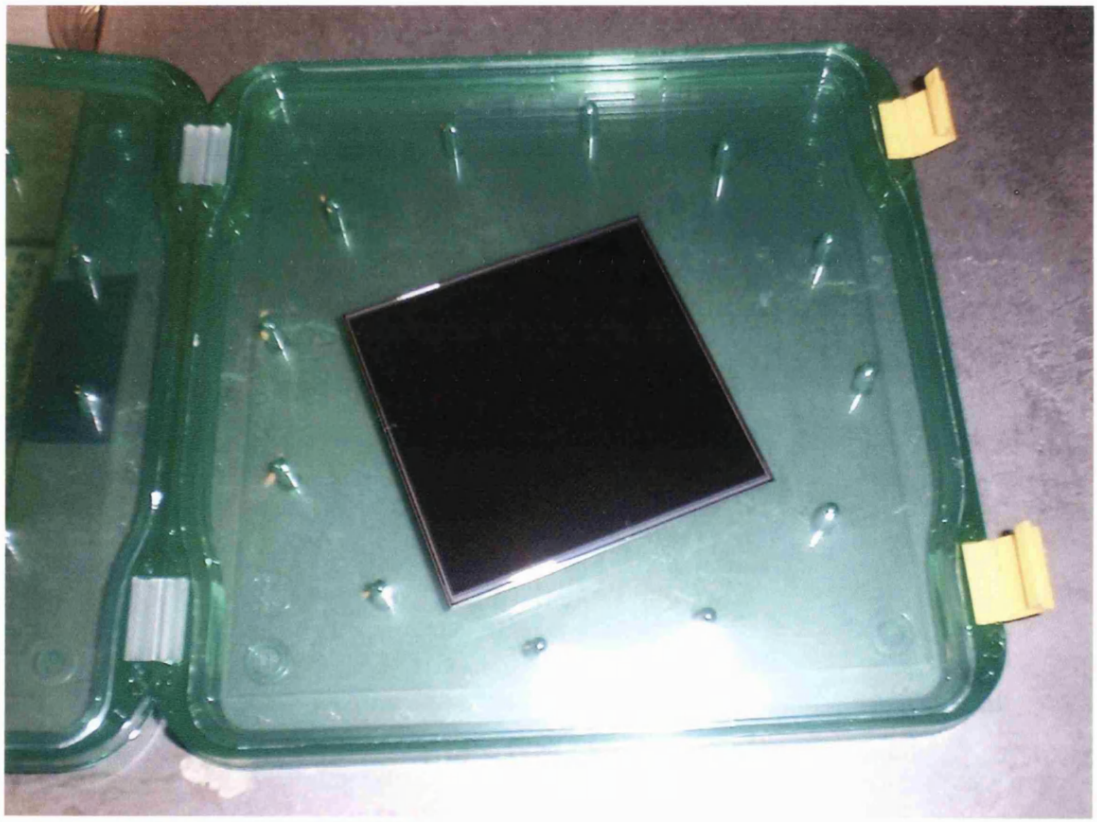

Fig. 3.1: Image showing one of the detectors prior to the bonding of the electronics.

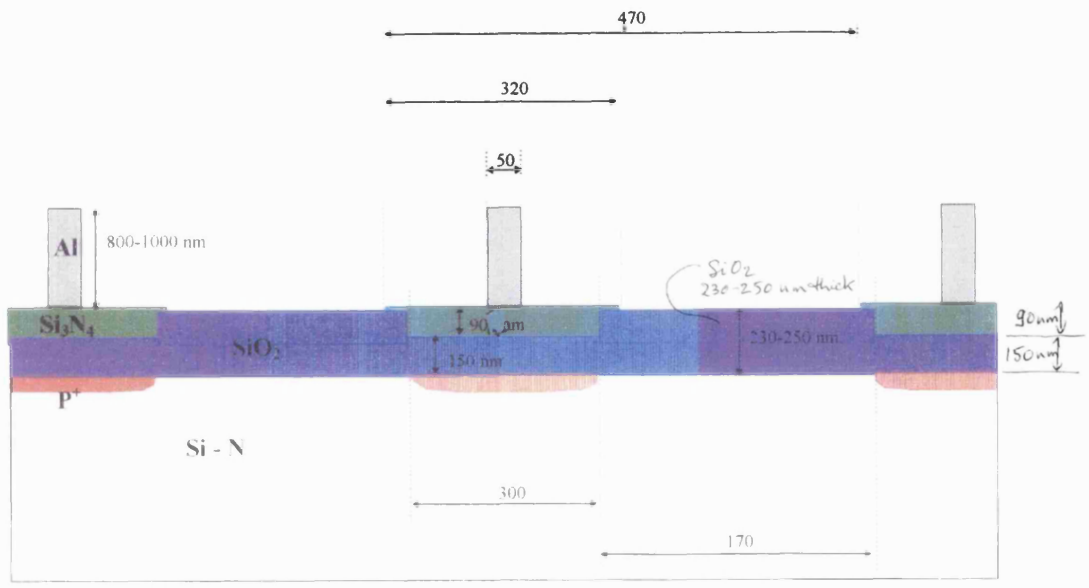

Fig. 3.2: Cross-sectional diagram showing the strip configuration on the *p*-side of the detector (drawing supplied by Eurisys Mesures).

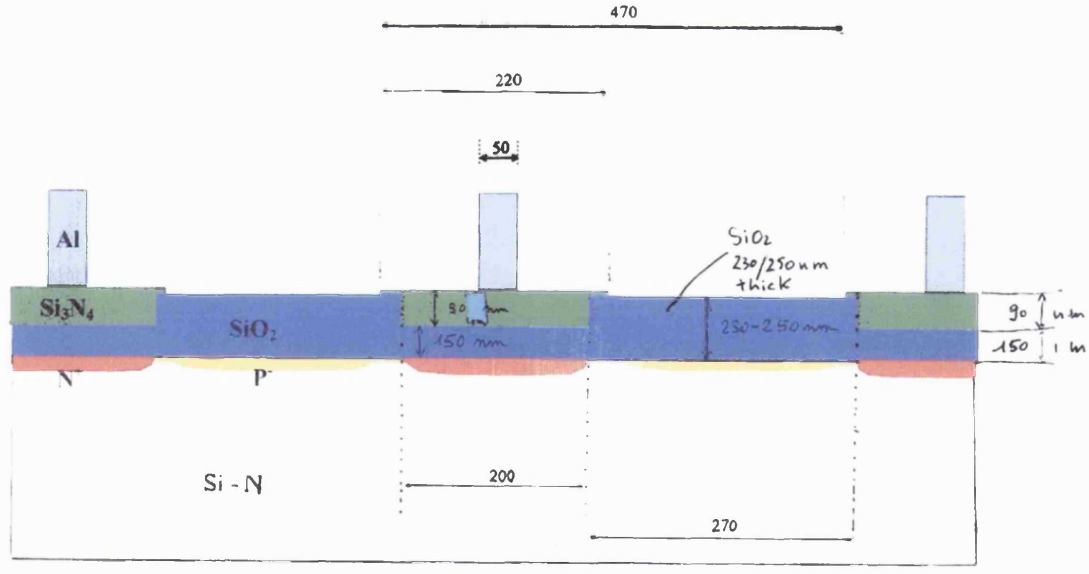

Fig. 3.3: Cross-sectional diagram showing the strip configuration on the *n*-side of the detector (drawing supplied by Eurisys Mesures).

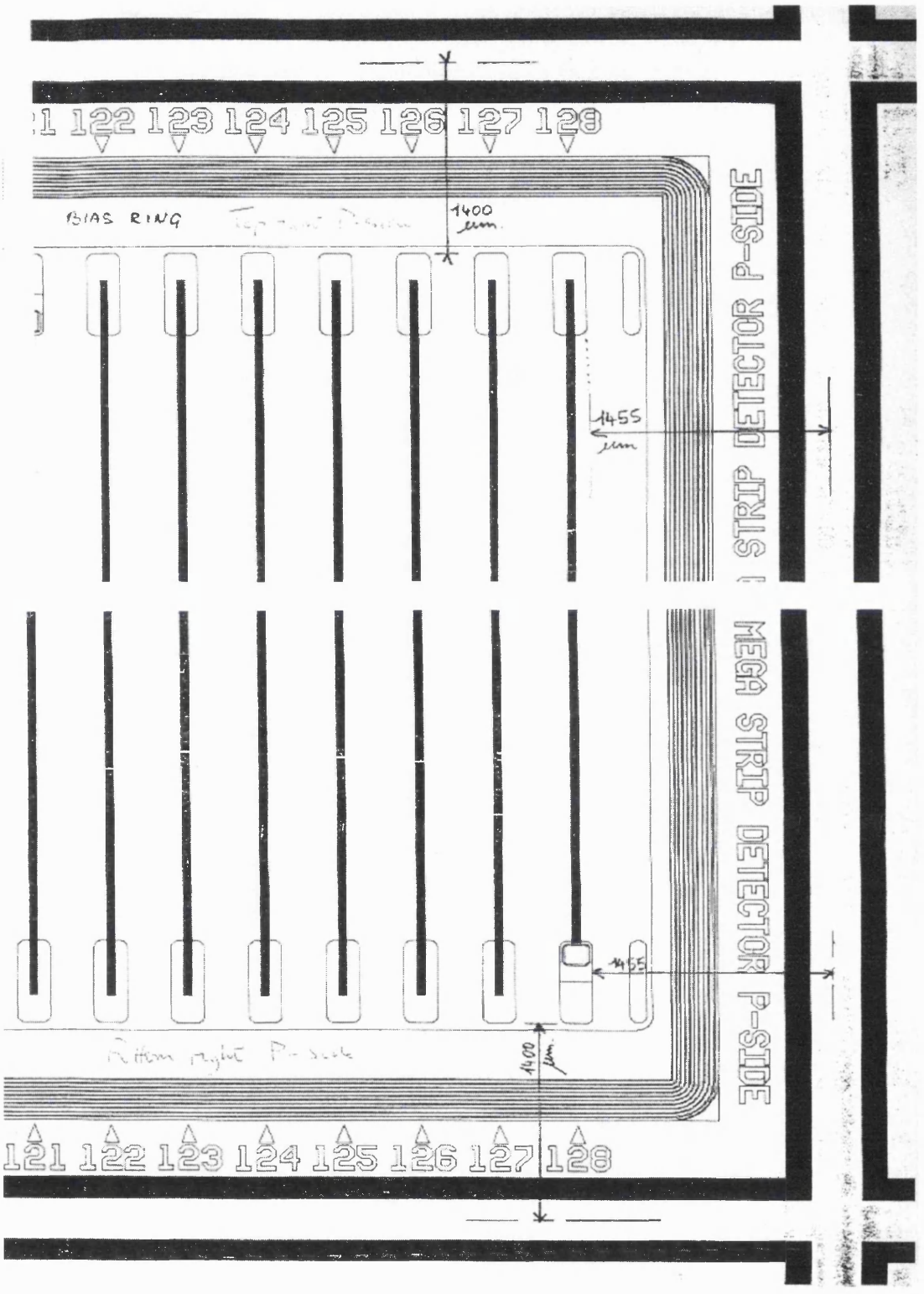

Fig. 3.4: Details of the strip configuration on the *p*-side of the detector (technical drawing supplied by Eurisys Mesures).

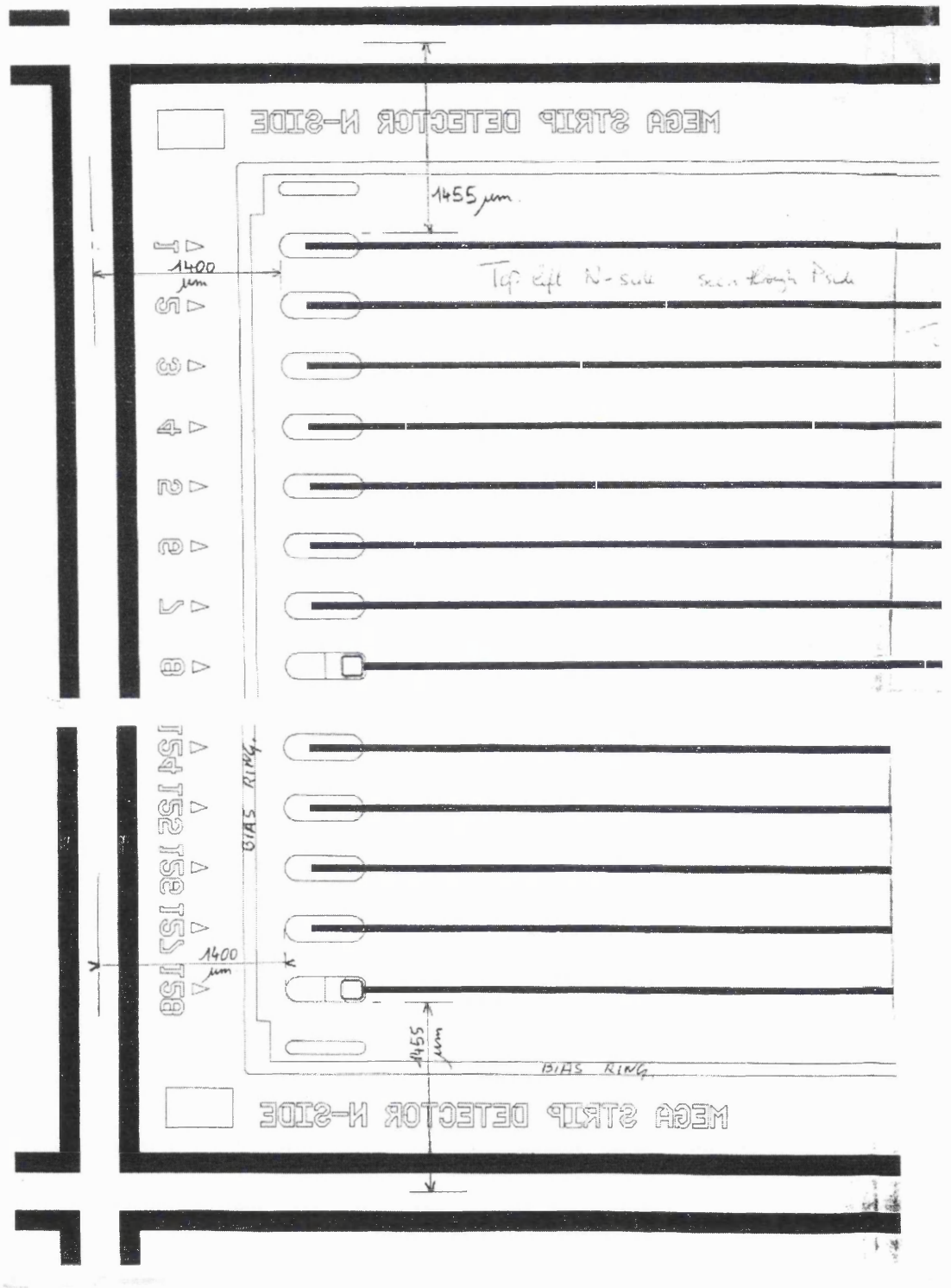

Fig. 3.5: Details of the strip configuration on the *n*-side of the detector (technical drawing supplied by Eurisys Mesures).

Table 3.1: Characteristics of the IPS 60x60 – 500 NX-NY128 detector design (Eurisys Mesures).

Silicon Resistivity	> 14kΩcm
Active area (approx.) / Total area	60x60 mm2 / 63x63 mm^2
Thickness	(500±15) μm
Strip pitch (*p*- and *n*- sides)	470 μm
Strip implantation width *(p- side)*	300 μm
Strip implantation width *(n- side)*	200 μm
Metallisation (Al) thickness	1000 nm
Metallisation (Al) width	50 μm
Polarity on bias ring	negative
Dynamic biasing resistors	> 100 MΩ (punch-through)
Depletion voltage	50 V
Operating voltage (max)	70-80 V

Table 3.2: Detector characteristics @ 20°C (IPS 60x60 – 500 NX-NY128 design by Eurisys Mesures).

Detector serial number	**B2578-1**	**B2578-2**	**B2578-3**	**B2578-4**
Total leakage current (at depletion)	< 2μA	< 1μA	< 2μA	< 2μA
Number of defective strips ("pinholes")	1	2	4	4
Strip to back plane capacitance (theoretical value)	≤ 6 pF	≤ 6 pF	≤ 6 pF	≤ 6 pF
Coupling capacitance	> 120 $pFmm^{-2}$	> 120 $pFmm^{-2}$	> 120 $pFmm^{-2}$	> 120 $pFmm^{-2}$

3.2 Instrumentation used for tests on bare detectors

The tests of the basic electrical properties of the silicon microstrip detectors were carried out using a light-tight probe station (Fig. 3.6) that is routinely dedicated to this type of measurements. The probe station is essentially a micrometric table enclosed in a grounded metallic box, which not only ensures darkness but also acts as a Faraday cage. The table is equipped with a microscope mounted on its top. The wafer to be tested is placed on a special conductive support or "chuck", to which vacuum is applied so as to prevent the wafer from moving. Electrical contacts on the wafer are established via coaxial cables, terminating in special probes that consist of fine tungsten needles. The needles can be accurately positioned under the microscope manually, by means of micrometric screws. The only points at which electrical

contact could be made on the detectors are the bias traces, the guard ring pads, the DC pads and the bonding pads on the AC strips.

During the experimental tests, the coaxial probes could be connected to the following electrical instruments in different configurations, depending on the type of measurements to be performed: a Keithley 487 Picoammeter/Voltage Source, a Keithley 617 Programmable Electrometer, a Keithley 485 Autoranging Picoammeter and a Keithley 590 C-V Analyser. All instruments were controlled by a Macintosh computer via an IEEE 488 interface, making use of the MultiTest instrument control/data analysis software developed at Imperial College.

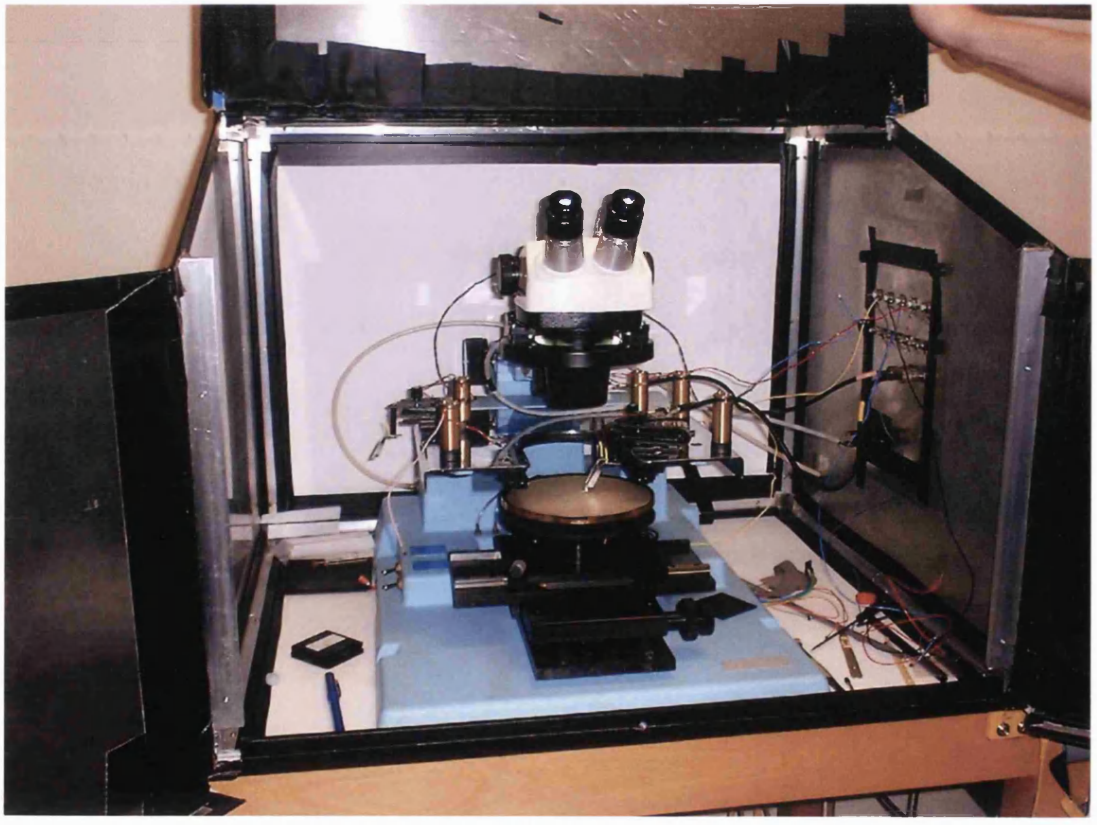

Fig. 3.6: Image showing the probe station that was used to perform the measurements of the electrical properties of the detectors.

3.3 Visual inspection

All silicon wafers were first visually inspected with the microscope for any important physical defects, such as cracks, severe misalignment of strips, etc. that would justify the rejection of the detector. Each wafer was carefully scanned strip by strip using the microscope, on both sides. No serious defects were observed on any detector. Limited surface contamination was identified on some areas of the detectors. Scratches on a few of the metal strips were also found, although their appearance suggested that the damage was only superficial. It was felt that the observed imperfections should not affect the detector performance, although this could be confirmed only by subsequent experimental measurements. Figures 3.7 to 3.12 show some examples of the pictures that were taken during the detector inspection.

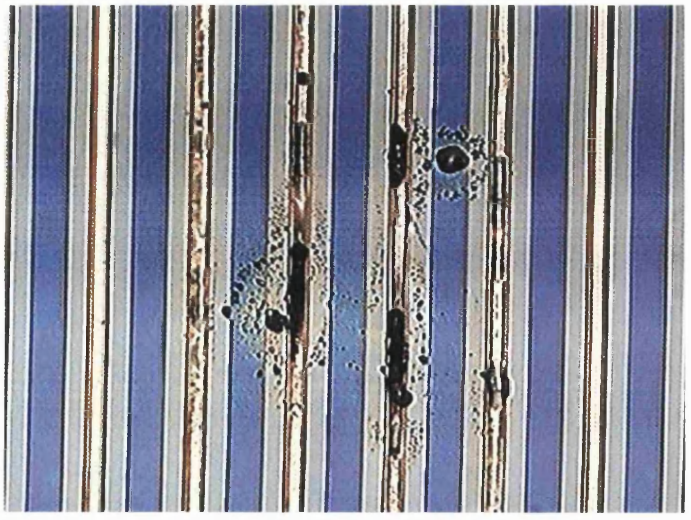

Fig. 3.7: Photograph taken during inspection of detector B2578-1 (strips 43-48, *p*-side).

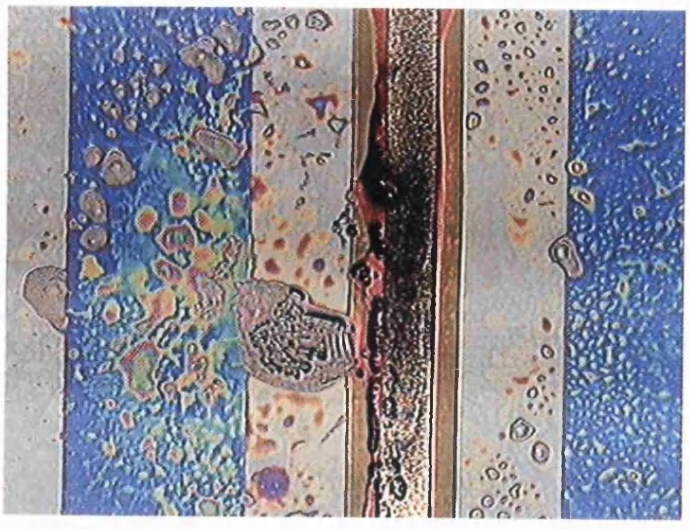

Fig. 3.8: Photograph taken during inspection of detector B2578-1 (detail of strip 45, *p*-side).

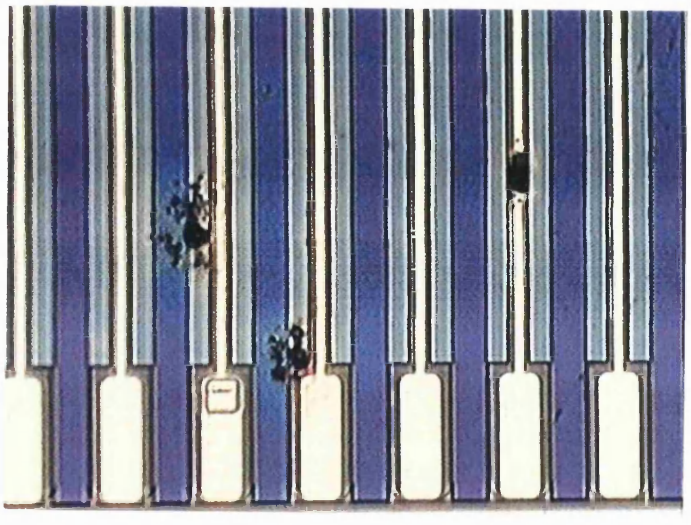

Fig. 3.9: Photograph taken during inspection of detector B2578-1 (strips 22-28, *p*-side).

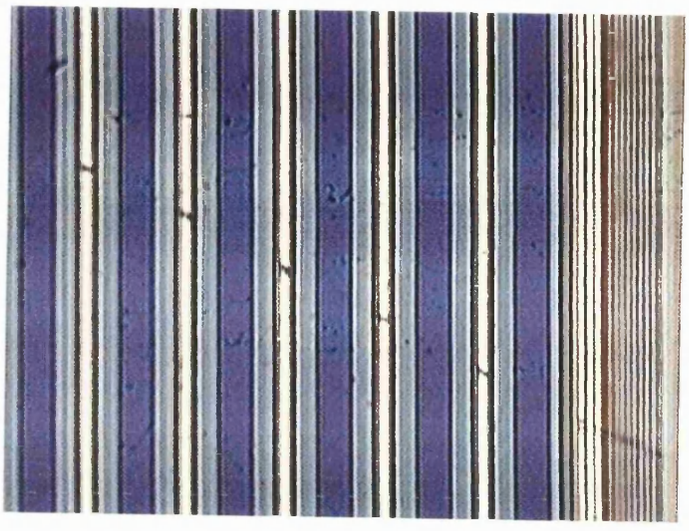

Fig. 3.10: Photograph taken during inspection of detector B2578-1 (strips 124-120, *p*-side).

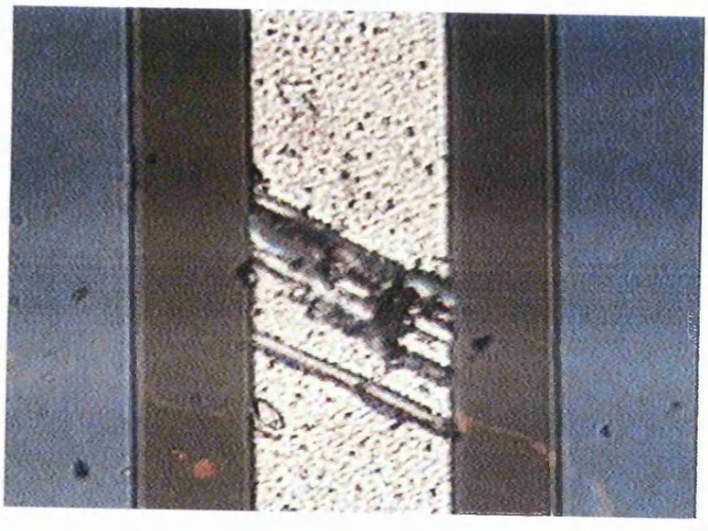

Fig. 3.11: Photograph taken during inspection of detector B2578-1 (detail of strip 126, *p*-side).

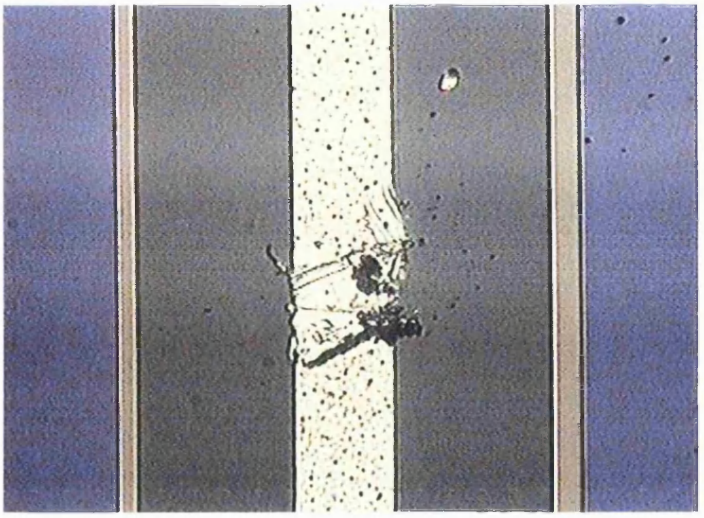

Fig. 3.12: Photograph taken during inspection of detector B2578-1 (strip 65, *n*-side).

3.4 Measurements of leakage current

The leakage current is the current that flows in a reverse-biased silicon diode when no radiation is present (apart from the background). A large leakage current is undesirable, as it broadens the FWHM energy resolution of the system. The leakage current was measured for all detectors as a function of the voltage, which was applied between the bias line and the back plane of the detector. The *n*-side was positively biased via the Keithley 487 PicoSource, with bias and guard rings held at earth potential via the two electrometers.

These measurements were performed using the instrument configuration shown in Fig. 3.13. The voltage on the back plane was increased from 0 V to 70 V in steps of 1 V. The experimental I-V curves are plotted in Fig. 3.14, 3.15, 3.16 and 3.17 for the four detectors, showing the current values that were measured on both the bias and the guard ring. All measurements were carried out at room temperature. At 50 V bias (i.e. the nominal depletion voltage) the value of the leakage current that was measured on the bias ring was in agreement with the company specifications (see

Table 3.2) for all four detectors. The maximum value reported for the leakage current at the operating voltage of 70 V was 2.4 μA for the bias ring (detector B2578-3) and 0.3 μA for the guard ring (detector B2578-2).

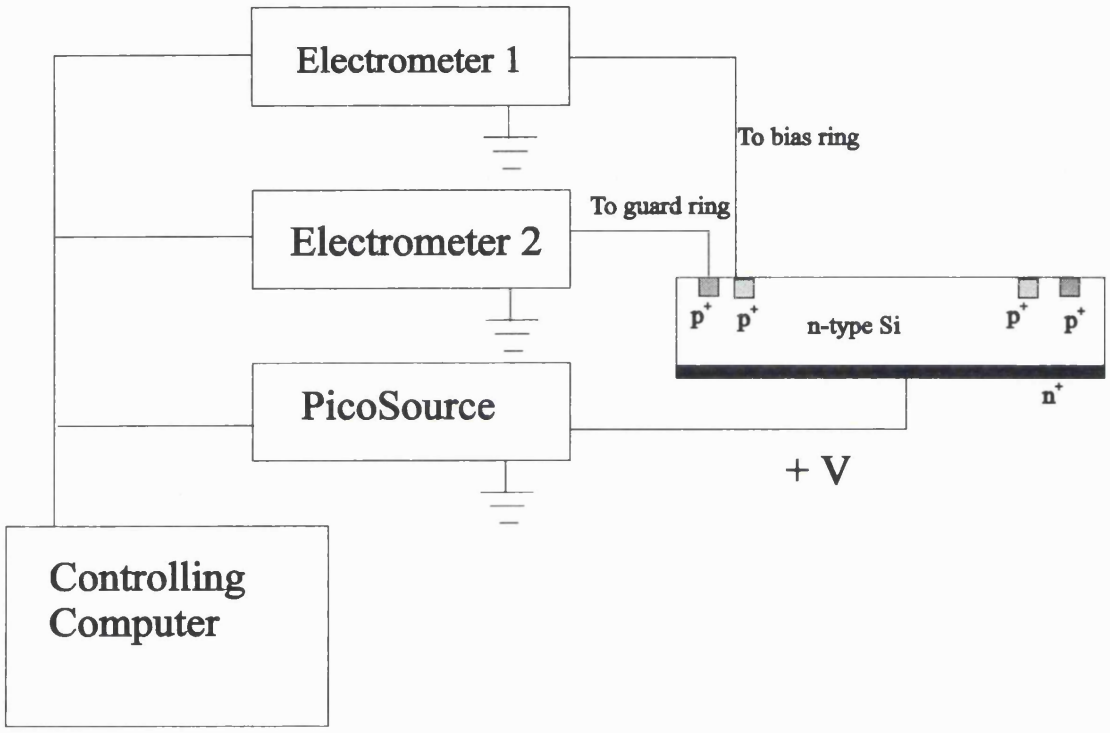

Fig. 3.13: Diagram illustrating the instrument configuration that was employed for the measurements of leakage current.

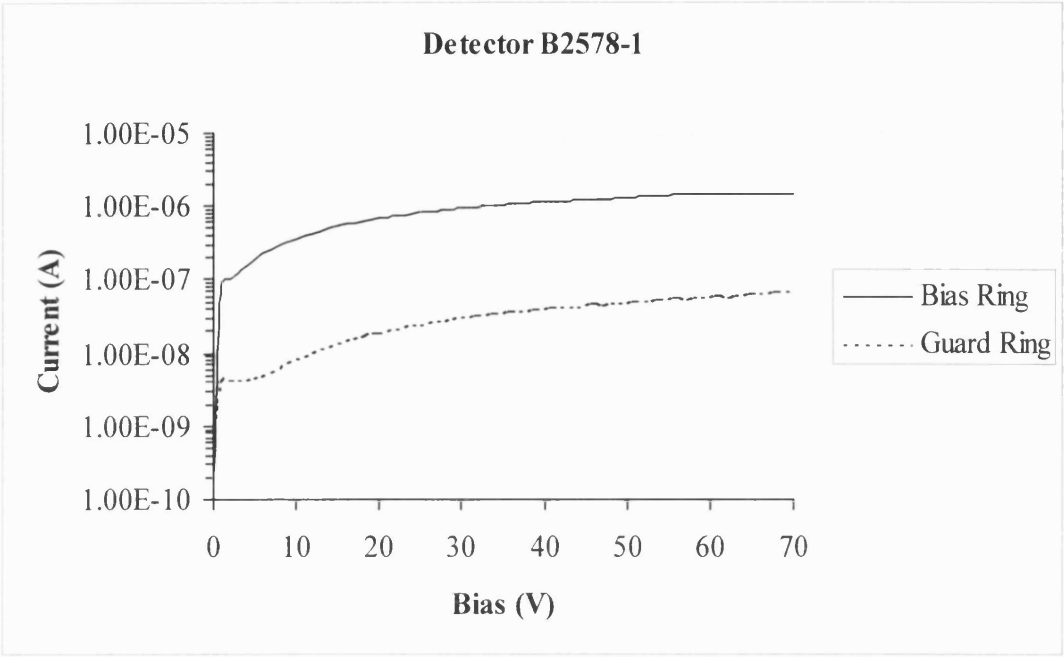

Fig. 3.14: Measurements of leakage current for detector B2578-1.

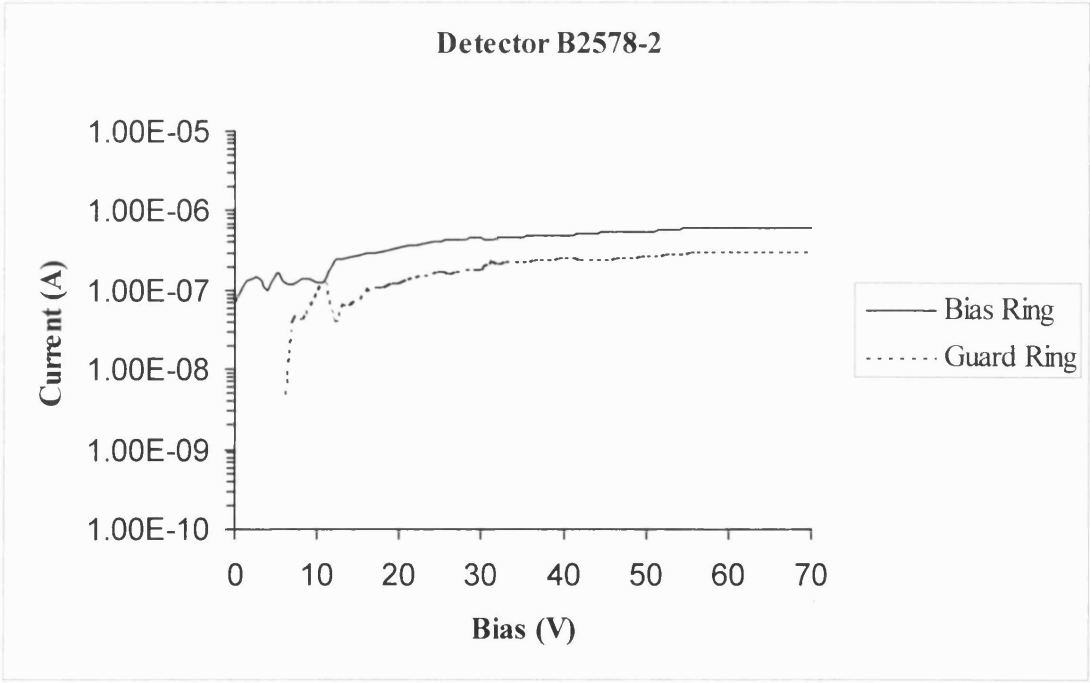

Fig. 3.15: Measurements of leakage current for detector B2578-2.

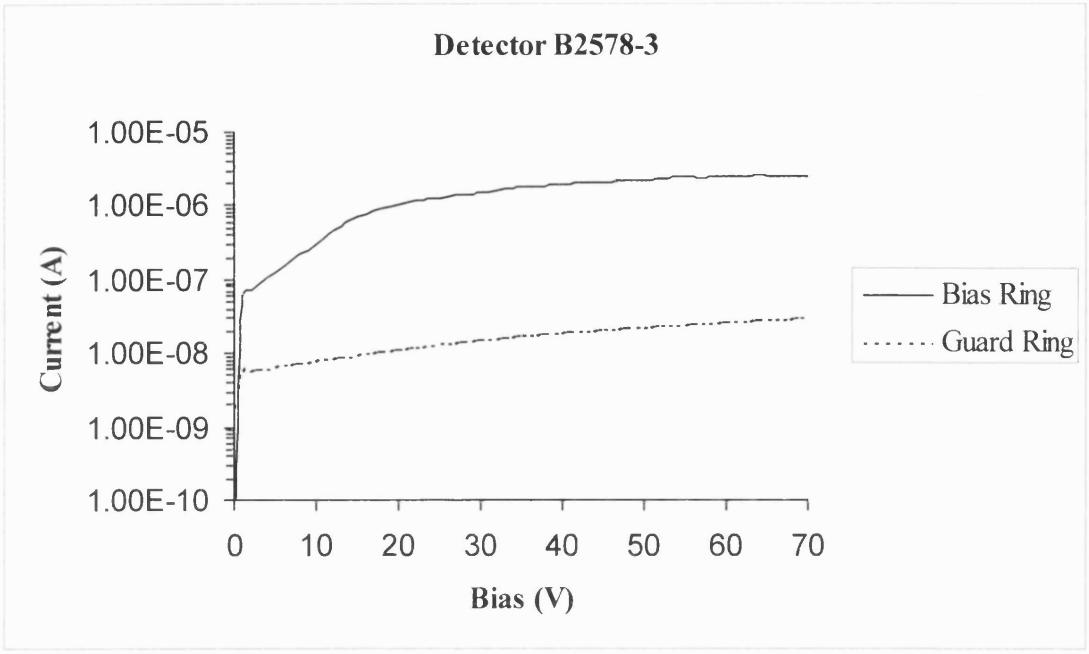

Fig. 3.16: Measurements of leakage current for detector B2578-3.

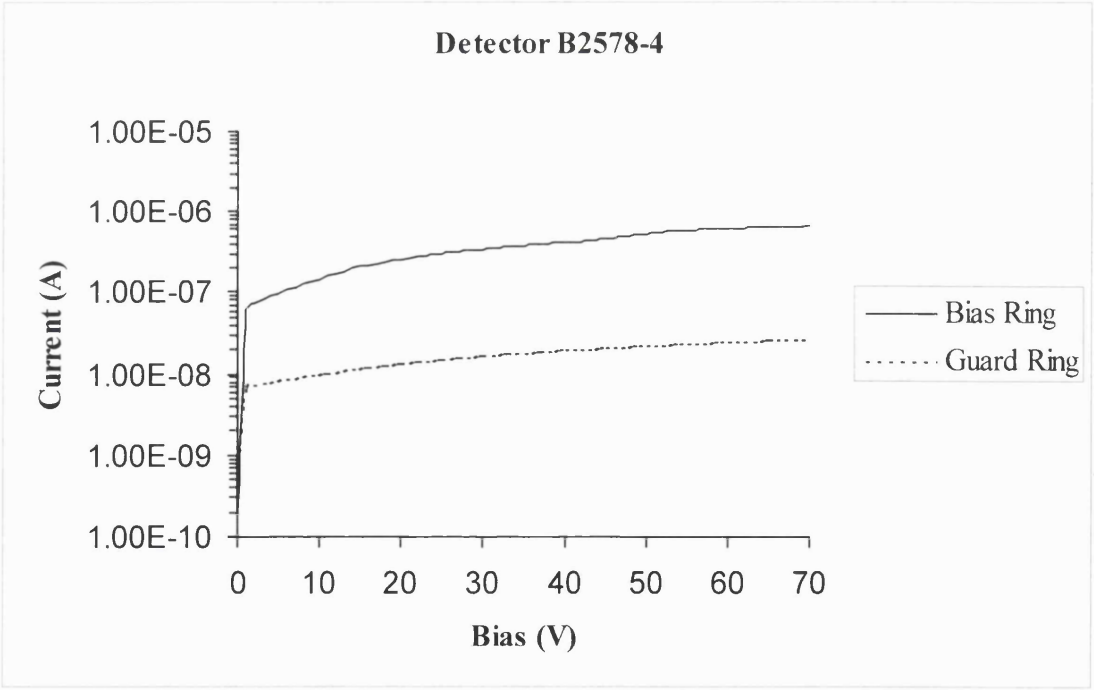

Fig. 3.17: Measurements of leakage current for detector B2578-4.

3.5 Capacitance components for a strip detector

The detector contribution to the noise performance does not only depend on its leakage current, but also on its capacitance (this aspect will be described in more detail in Chapter four). Each amplifier in the integrated readout electronics will see at its input a capacitive load associated with the bonded strip of the detector. This is given by the combination of the strip capacitance to the neighbouring strips with the strip capacitance C_B to the back plane (see Fig. 3.18). For a central strip, as the interstrip capacitance is symmetrical with respect to its neighbours on the left and the right hand-side, it will consist of two identical terms C_{IS}. The total strip capacitance C_S can therefore be expressed as follows:

$$C_S = 2C_{IS} + C_B \tag{3.1}$$

where the interstrip capacitance is often evaluated for a total of four strips, i.e. the two closest (C_{CN}) and the two outer neighbours (C_{ON}), as the contribution of farther strips tends to be negligible, especially if the strips are not closely spaced. This is the case for large pitch (~ 0.5 mm) detectors such as the IPS 60x60 – 500 NX-NY128 design:

$$C_S \approx 2(C_{CN} + C_{ON}) + C_B \tag{3.2}$$

A series of tests were carried out in order to measure the capacitance of a single strip to the back plane as well as the different components of the interstrip capacitance. Such measurements allowed the noise contribution due to the total strip capacitance to be evaluated. As the energy signal is most frequently acquired from the junction side rather than the ohmic side (the *p*-side provides better energy resolution due to its lower input capacitance), the capacitance measurements were carried out on the *p*-side of the detector.

Because of the small order of magnitude (~ pF) of the capacitance that is typically measured on microstrip detectors, the various parasitic effects (due to the cables, the contacts between the probes and the strips, etc.) had to be considered and corrected for. This was done experimentally by making use of the "open circuit correction" feature of the C-V Analyser, which allows automatic subtraction of the total parasitic capacitance. This correction was made for all experimental configurations and frequency values by performing a measurement with all probes raised from the wafer. The capacitance value that is measured with this procedure is the parasitic capacitance, which the Analyser automatically sets as the "zero" reference value for all subsequent measurements. The measured values of the total parasitic capacitance were in the order of 10^{-13} to 10^{-12} F.

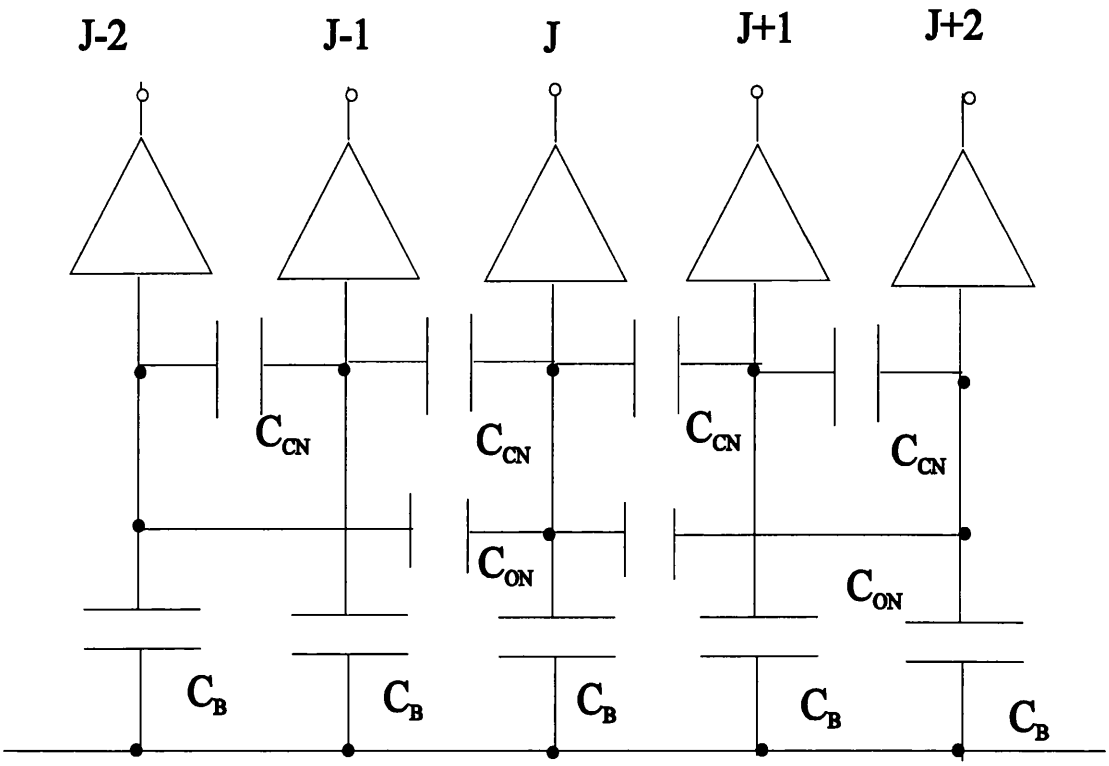

Fig. 3.18: Diagram illustrating the strip capacitance components with respect to the amplifier input.

3.6 Capacitance measurement models

3.6.1 Series and parallel models

The Keithley 590 C-V Analyser[13] allows the user to perform measurements of capacitance of an equivalent circuit connected between its input and output terminals. The measurements are made at a fixed frequency value, which can be selected as 100 kHz or 1 MHz. This equivalent circuit can be represented according to either the "series" or the "parallel" model (see Fig. 3.19 *a)* and *b)*).

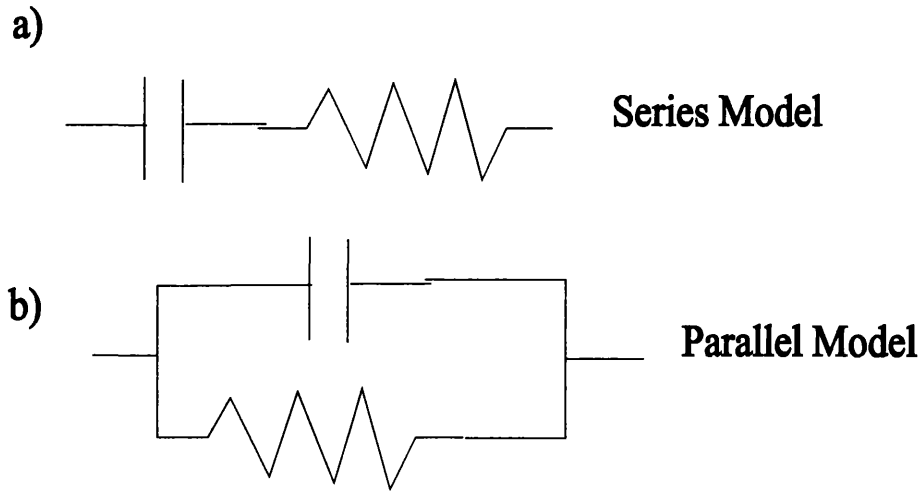

Fig. 3.19: Circuit diagrams of series and parallel models.

In both cases, the circuit is simply made up of a single resistive element and a single capacitive element, which are respectively connected in series or in parallel. The Analyser always measures the capacitance in the parallel form, but it will automatically convert the measured data into serial form (via a mathematical operation) if the relevant mode is selected. The complex impedance of the two types of circuit is expressed as follows:

[13] Keithley Model 590 CV Analyser Instruction Manual (Keithley Instruments Inc., Cleveland, Ohio, USA 1987)

$$\vec{Z} = R_s - j\frac{1}{\omega C} \qquad \textit{(series model)} \tag{3.3}$$

$$\vec{Z} = \frac{R_p}{1+\omega^2 C^2 R_p^2} - j\frac{\omega C R_p^2}{1+\omega^2 C^2 R_p^2} \qquad \textit{(parallel model)} \tag{3.4}$$

The selection of the model depends on the type of measurement that is performed. Only in the particular case of a nearly-lossless circuit (i.e. both the resistance R_s and the conductance $1/R_p$ are $\cong 0$) do the two models provide results for the capacitance measurements that are virtually identical. The user should select an equivalent circuit model that suitably approximates the structure of the device of interest. In this study, all measurements of capacitance were performed by applying the *series model*. The justification of the chosen model is given in the following sections.

3.6.2 Model of a p-n diode

The *p-n* diode can be simply described as consisting of a capacitance element C, a parallel resistance R_p and a series resistance R_s. This is represented in Fig. 3.20, where C is the capacitance between the diode planes, R_p is the resistance of the depleted region and R_s is the resistance of the undepleted silicon.

The *series model* could be used in measuring the capacitance of a *p-n* diode if the following condition was satisfied ($R_p \to \infty$) [MacEvoy, 1997]:

$$R_p >> \frac{1}{\omega C} \tag{3.5}$$

Such a relationship implies that the real part of the parallel impedance in (3.4) can be neglected with respect to the imaginary term; the parallel circuit is approximated by a purely capacitive component with impedance $\left(-\frac{1}{\omega C}\right)$.

The *parallel model* could be used if the scalar impedance in (3.4) was much greater than the series resistance ($R_s \rightarrow 0$) [MacEvoy, 1997]:

$$R_s << \sqrt{\left(\frac{R_p}{1+\omega^2 C^2 R_p^2}\right)^2 + \left(\frac{\omega C R_p^2}{1+\omega^2 C^2 R_p^2}\right)^2} = \frac{R_p}{\sqrt{1+\omega^2 C^2 R_p^2}} \tag{3.6}$$

If the condition in (3.5) is also satisfied, this relationship reduces to the following expression:

$$R_s << \frac{1}{\omega C} \tag{3.7}$$

If both (3.5) and (3.7) are true, *either the series or the parallel model* could be used to measure the diode capacitance.

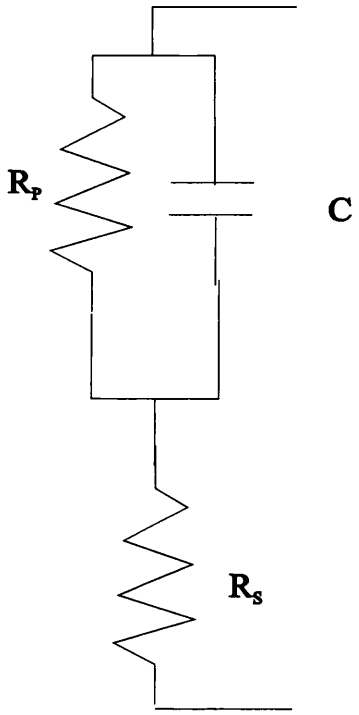

Fig. 3.20: Circuit diagram representing a *p-n* diode.

3.6.3 Model for a single strip with respect to the back plane

The *p*-side of a microstrip detector can be simply described as an array of individual, narrow and parallel diodes. The equivalent circuit of a single *p*-strip with respect to the *n*-plane can therefore be considered as the same as in Fig. 3.20, where C is the capacitance of the strip to the back plane, R_p is the resistance of the depleted region below the strip and R_s is the resistance of the thickness of silicon that has not been depleted.

The value of both resistances is clearly a function of the applied reverse bias. Even when no depletion has yet occurred, the value of the series resistance is rather small (a few kΩ), as will be shown later (see equation 3.9). The voltage drop across R_s caused by the leakage current (~ 1 μA at full depletion) is therefore always less than 1 mV and can be neglected. An approximate value of R_p may then be calculated from the I-V characteristic of the detector for a given value of the leakage current I and of the applied reverse bias V [MacEvoy, 1997]:

$$R_p = \frac{V}{I} \tag{3.8}$$

It is therefore possible to make an order of magnitude estimate of the parallel resistance of the equivalent circuit of a single strip corresponding to different experimental points of the I-V curves presented in section 3.4.

For example, in the case of detector B2578-1, for which the nominal depletion voltage is 50 V, the total leakage current is approximately 0.4 μA in the low voltage region (V = 10 V), rising to 1 μA before full depletion is reached (V = 35 V) and increasing to a maximum value of 1.5 μA at over depletion (V = 70 V). The leakage current value per strip is approximately equal to the total leakage current divided by the number N of strips (N = 128). A value in the order of a few nA is therefore obtained for the leakage current associated with a single strip before full depletion is

reached. The leakage current value per strip reaches approximately 10 nA in the detector operating voltage range (50 - 70 V). From equation (3.8) one can therefore estimate that the resistance R_p of the depleted region for a single strip varies from a few GΩ to approximately 10 GΩ in the 0-70 V range. As the capacitance of a single strip with respect to the back plane is approximately C = 6 pF (see Table 3.2), the right-hand side term of relationship (3.5) becomes $1/(\omega C) \sim 3 \times 10^5$ for a frequency of 100 kHz and $1/(\omega C) \sim 3 \times 10^4$ for a frequency of 1 MHz. The conditions for the validity of the *series model* expressed in (3.5) are therefore fully satisfied.

In order to use the *parallel model* approximation, one should verify the condition expressed in (3.6). Because we have just proved the validity of relationship (3.5), it is sufficient to satisfy relationship (3.7). An estimate of the R_s component may be obtained from the following equation:

$$R_s = \frac{\rho d}{wL} \tag{3.9}$$

where ρ is the silicon resistivity (Ωcm), d is the depth of the undepleted region (cm), w is the implant strip width (cm) and L is the strip length (cm). R_s will assume its maximum value when the detector is fully undepleted (i.e. d is equal to the detector thickness). For the detectors of the IPS 60x60 – 500 NX-NY128 type we can assume ρ = 14 kΩcm, d = 500 μm, w = 300 μm and L = 6 cm (see Table 3.1). From equation (3.9) we obtain therefore a resistance value $R_s \sim 4$ kΩ, which satisfies condition (3.7) for both values of frequency.

When measuring the C-V characteristics of a diode or of a single strip with respect to the back plane, it is normally possible to apply either the series or the parallel measurement model. The *series model* is however usually preferred, as relationship (3.5) is always satisfied. Although relationship (3.7) is normally satisfied for silicon devices that have not been irradiated, it may not be valid after irradiation. Radiation

damage may cause a variation of the doping concentration that could cause the silicon resistivity to become of the same order as the intrinsic resistivity (which is approximately 235 kΩcm) [MacEvoy, 1997]. This would then increase the value of R_S and compromise the validity of (3.7). The *series model* was employed in the measurements that are reported here.

3.6.4 Model for a single strip with respect to its neighbour

In order to represent the equivalent circuit network for the capacitance measurements of a single AC-coupled strip to one of its neighbours, a simplified diagram (Fig. 3.21) could be used: R_{ss} is the series resistance for the input and output terminals of the C-V Analyser, C_m is the capacitance between the two metal electrodes, C_c is the coupling capacitance, R_{is} is the interstrip resistance and C_{is} is the interstrip capacitance. By determining the orders of magnitudes of these parameters, it is possible to show that the *series model* is a suitable measurement model also for the interstrip circuit.

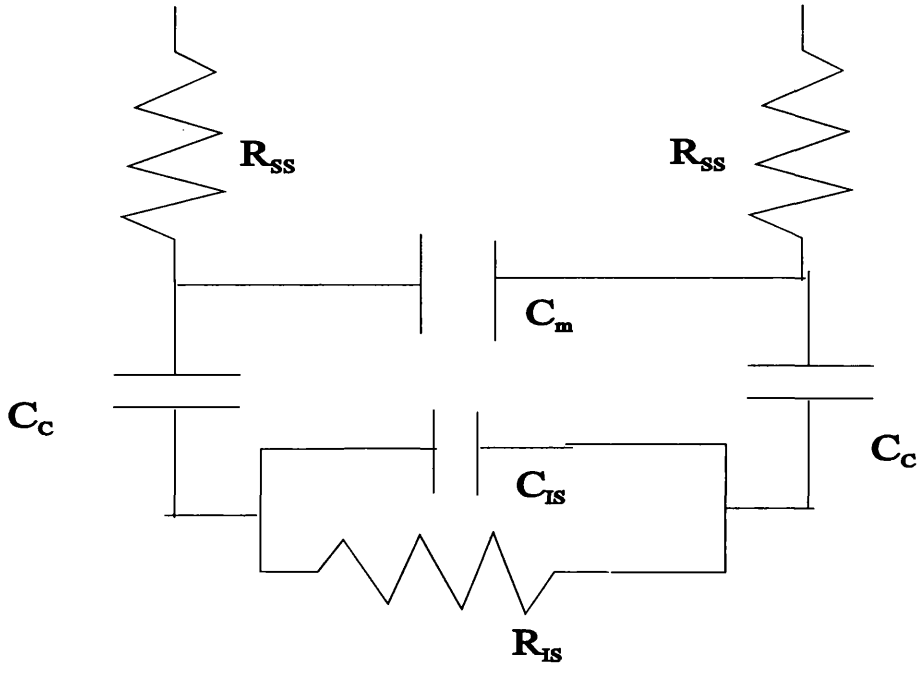

Fig. 3.21: Circuit diagram employed to describe the measurements of strip capacitance (AC contact) with respect to its first neighbour.

The interstrip capacitance is a function of the detector design and in particular of the implant strip width and the detector pitch. It is minimised by narrow strips and large readout pitch. An estimate of the *interstrip capacitance* value C_{is} of one strip with respect to its closest neighbour may be extrapolated for a specific strip geometry as a function of the ratio w/p, where w is the implanted strip width and p is the strip pitch [Bacchetta *et al.*, 1998]. From Table 3.1 (w = 300 μm and p = 470 μm) we obtain a value w/p = 0.6, which according to Bacchetta *et al.* would correspond to a capacitance value not greater than 0.6 pF/cm. A value of less than 4 pF can therefore be assumed for C_{is} (the strip length is 6 cm).

The value of the *coupling capacitance* C_c can be estimated with a simple computation. In the IPS 60x60 – 500 NX-NY128 detectors, the dielectric of the coupling capacitors consists of a first layer of SiO_2 on which a second layer of Si_3N_4 is grown (see Fig. 3.2). The total coupling capacitance per unit area can therefore be calculated from the expression:

$$\frac{1}{C_c} = \frac{1}{C(SiO_2)} + \frac{1}{C(Si_3N_4)} \; pF/mm^2 \tag{3.10}$$

where

$$C(SiO_2) = \frac{\varepsilon_0 \varepsilon(SiO_2)}{d(SiO_2)} \; pF/mm^2 \tag{3.11}$$

and

$$C(Si_3N_4) = \frac{\varepsilon_0 \varepsilon(Si_3N_4)}{d(Si_3N_4)} \; pF/mm^2 \tag{3.12}$$

where ε_0 = 8.854 x 10^{-12} Fm^{-1} is the vacuum permittivity and where the relative dielectric constants of the oxides are $\varepsilon(SiO_2)$ = 3.9, $\varepsilon(Si_3N_4)$ = 8 and their thickness values are $d(SiO_2)$ = 150 nm and $d(Si_3N_4)$ = 90 nm. From equation (3.10) one obtains a value C_c =180 pF/mm^2. As the aluminium readout strips are 50 μm wide and 6 cm long, the coupling capacitance is approximately 540 pF.

The *interelectrodic capacitance* C_m per unit area may also be obtained by means of a simple calculation:

$$C_m = \frac{\varepsilon_0 \varepsilon(air)}{p} \; pF/mm^2 \tag{3.13}$$

where the relative dielectric constant of air is $\varepsilon(air)$ = 1.00059 and p = 470 μm is the distance (equal to the strip pitch) between the central points of two metal electrodes. As the metallisation thickness is 1000 nm and the aluminium strips are 6 cm long, the capacitance between the two metal electrodes is $C_m \sim 1$ fF.

The *interstrip resistance* R_{is} is the resistance between two implant strips. Its value is always very high, typically between hundreds of MΩ and a few TΩ [Bacchetta *et al.*, 1995], [Frautschi *et al.*,1996], in order to maintain channel isolation. We can therefore assume that it is $R_{is} \geq 100$ MΩ.

The *series component of the resistance* R_{ss} results from different contributions, such as the metallisation layer of the strips, the cables connecting the probes to the instrumentation terminals, etc. These are all rather small values of resistance. The metal strip will contribute to R_{ss} with its thickness, integrated along the length of the portion of strip that is involved by the propagation of the input/output signal of the Analyser. The metal readout strip resistance R_{met} may be computed by using the following expression:

$$R_{met} = \frac{\rho_{Al}}{w_{Al}\, t_{Al}} (\Omega / cm) \tag{3.14}$$

where the aluminium resistivity is $\rho_{Al} = 2.63 \times 10^{-6}$ Ωcm, the metal strip width is w_{Al} = 50 μm and its thickness is t_{Al} = 1000 nm. From equation (3.14) a value of approximately 5 Ω/cm is obtained for the metal electrode resistivity. One may therefore assume that the overall series resistance $R_{ss} \leq 100$ Ω.

The capacitance between electrodes combines in parallel with the equivalent capacitance of the series combination of the interstrip capacitance and the two coupling capacitors. This equivalent capacitance is equal to $(C_{is}\, C_c)/(2\, C_{is} + C_c) >> C_m$ .We can therefore neglect the interelectrode capacitance and express the impedance of the circuit in Fig. 3.21 as follows:

$$Z = \left(2R_{ss} + \frac{R_{is}}{1+\omega^2 C_{is}^2 R_{is}^2} \right) - j \left(\frac{2}{\omega C_c} + \frac{\omega C_{is} R_{is}^2}{1+\omega^2 C_{is}^2 R_{is}^2} \right) \tag{3.15}$$

This is basically the serial combination of two separate subcircuits, one of the series type and one of the parallel type. The impedance of the series subcircuit can in fact be expressed in the same form as equation (3.3), with $R_s = 2\, R_{ss}$ and $C = C_c/2$, whereas the impedance of the parallel subcircuit is of the same form as (3.4), with $R_p = R_{is}$ and $C = C_{is}$. From the values estimated for the circuit parameters, it follows that $1/(\omega C_{is}) = 4 \times 10^5$ for a frequency of 100 kHz and $1/(\omega C_{is}) = 4 \times 10^4$ for a frequency of 1 MHz. This means that at both frequencies the relationship $R_{is} >> 1/(\omega C_{is})$ is satisfied and since $1/R_{is} \cong 0$ equation (3.15) reduces to:

$$Z = 2R_{ss} - j \frac{1}{\omega} \left(\frac{2}{C_c} + \frac{1}{C_{is}} \right) \tag{3.16}$$

which is an approximation of the interstrip circuit according to the *series model* (see equation (3.3)). The series resistance is equal to twice the value of the resistance associated with the readout of a single electrode; the total capacitance is given by the serial combination of the two coupling capacitors and the interstrip capacitance.

The nature of the interstrip impedance is actually almost purely capacitive. It is in fact $R_{ss} << R_{is}$, which allows us to consider the circuit series resistance $R_s \cong 0$ and the parallel resistance $R_p \cong \infty$. Therefore, the *parallel model* is also a suitable approximation of the interstrip circuit. To this regard, it can be proved that the scalar impedance of the parallel subcircuit is much greater than the impedance of the series subcircuit. The scalar impedance Z_1 of the series subcircuit ($R_s = 2R_{ss}$ and $C = C_c/2$) may be calculated as follows:

$$Z_1 = \sqrt{4R_{ss}^2 + \frac{4}{\omega^2 C_c^2}} \tag{3.17}$$

where $1/(\omega C_c) = 3 \times 10^3$ for a frequency of 100 kHz and $1/(\omega C_c) = 3 \times 10^2$ for a 1 MHz frequency. As a consequence of the relationship $R_{is} >> 1/(\omega C_{is})$ that was demonstrated, the scalar impedance Z_2 of the parallel subcircuit ($R_p = R_{is}$ and $C = C_{is}$) may be approximated as follows:

$$Z_2 \cong \frac{1}{\omega C_{is}} \tag{3.18}$$

and by substituting the relevant values for the circuit parameters in (3.17) and (3.18) one can show that $Z_1 << Z_2$ at both 100 kHz and 1 MHz of frequency. Although both models could be used, the measurements of interstrip capacitance were also performed with the *series* model, so that the same type of method would be employed for simplicity in all of the capacitance measurements.

3.7 Measurements of capacitance of a single strip to the back plane

3.7.1 Theoretical determination of value of capacitance

A simplified diagram of the capacitive network representing the capacitance components of the detector is shown in Fig. 3.22. The theoretical value for the single strip capacitance to the back plane C_B is approximately 6 pF (see the specification value given by the manufacturer in Table 3.2) and can be easily calculated on the basis of the detector geometry.

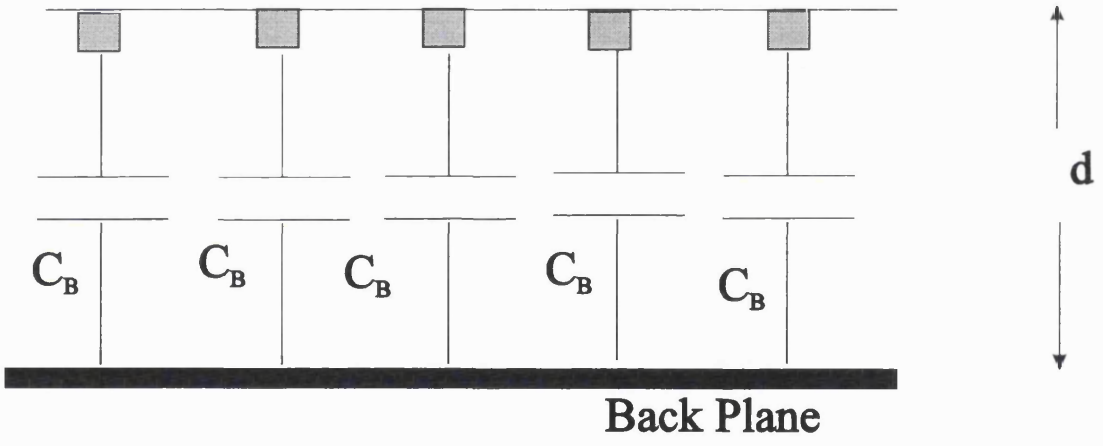

Fig. 3.22: Schematic diagram of the components forming the body capacitance of a silicon microstrip detector.

The total body capacitance at full depletion C_D can be assumed to be equal to the one of a parallel plate capacitor as follows [Sze, 1985]:

$$C_D = \frac{\varepsilon_0 \varepsilon_r S}{d} \tag{3.19}$$

where d is the thickness of the depleted region, S is the detector area, $\varepsilon_0 = 8.854 \times 10^{-12}$ Fm^{-1} is again the vacuum permittivity and $\varepsilon_r = 11.9$ is the relative dielectric constant for silicon. Considering the geometry of the detectors of the IPS 60x60 – 500 NX-NY128 type ($w = 500$ μm, $S = 36$ cm^2), this results in $C_D \cong 760$ pF. Looking at the diagram in Fig. 3.22, we can express the total body capacitance of a detector with N strips as the combination of N 'strip to back plane' capacitors in parallel:

$$C_D = NC_B \tag{3.20}$$

If $C_D = 760$ pF and N=128, one obtains from this relationship that $C_B = 6$ pF.

3.7.2 Experimental results

The capacitance measurements for a single strip to the back plane were performed on detector B2578-3 with the instrument configuration shown in Fig. 3.23. The voltage on the back plane was increased from 0 to 70 V in steps of 2 V, with the bias line held at earth potential. The closest two neighbouring strips and the outer two neighbouring strips were also held at earth potential during the measurements. This was done to prevent the capacitive coupling of neighbouring floating strips from contributing to the measured capacitance.

The measurements were performed on both the AC and DC pads of a central strip on the p-side of the detector (strip n. 65) and were repeated at frequencies of 100 kHz and 1 MHz. The results of these four measurements are plotted in Fig. 3.24. The capacitance values that were measured at over depletion (70 V) for both frequencies and for both type of connections were found to agree within 3 to 5 % with the value that was estimated theoretically.

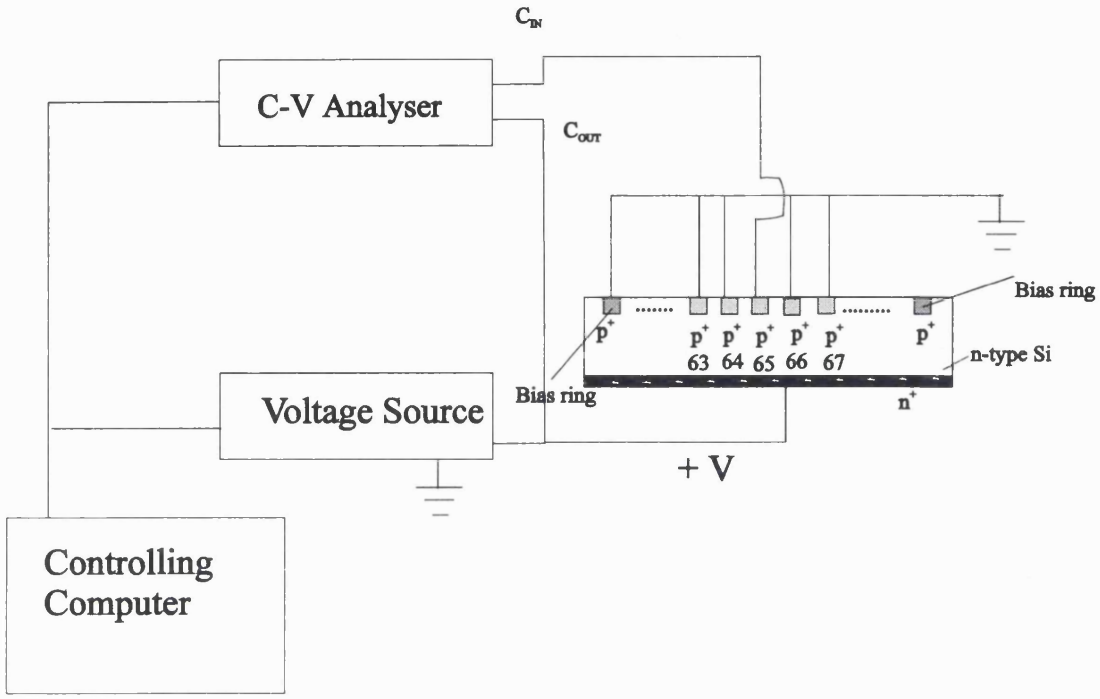

Fig. 3.23: Diagram illustrating the instrument configuration that was employed for the measurements of capacitance of a single *p*-strip (n. 65) with respect to the back plane.

With a more rigorous approach, one should note that the measurements performed with the AC connection included the presence of the coupling capacitors, as the total capacitance C_{Tot} of a single strip to the back plane can be expressed as follows:

$$\frac{1}{C_{Tot}} = \frac{1}{C_C} + \frac{1}{C_B} \tag{3.21}$$

However, the coupling capacitors C_C are normally quite large with respect to the body capacitance C_B of the strip (see Table 3.2). They are in fact designed to be sufficiently greater than the interstrip capacitance so as to avoid signal spreading over the neighbouring strips. We can therefore use the following approximation:

$$C_C >> C_B \Rightarrow \frac{1}{C_{Tot}} \cong \frac{1}{C_B} \tag{3.22}$$

which explains why no significant differences were observed between the capacitance values obtained at over depletion (70 V) using the DC or the AC connection on the strip pad.

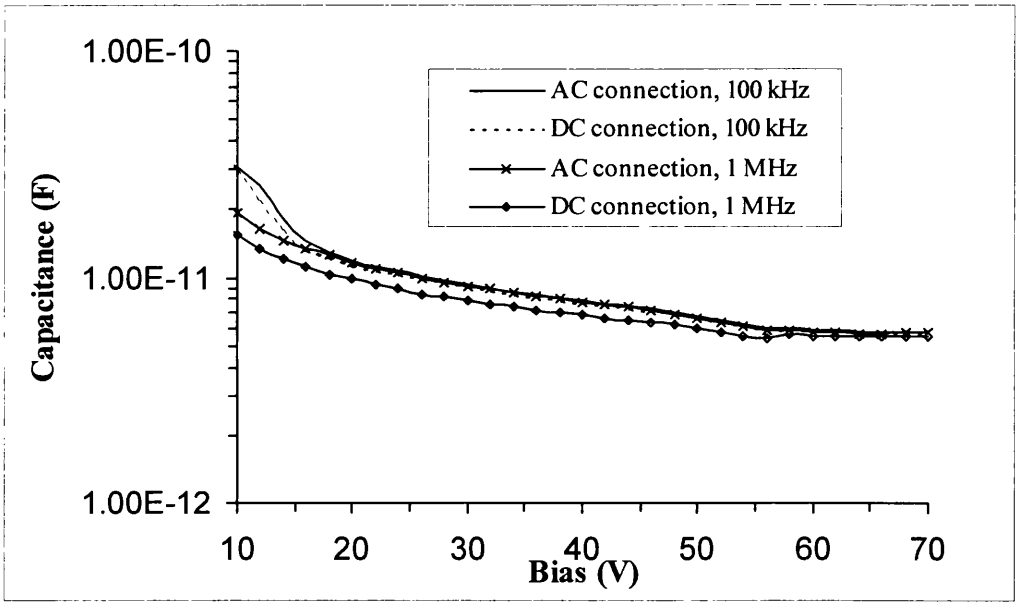

Fig. 3.24: Capacitance to the back plane of strip 65 on the *p*-side of detector B2578-3. Strips n. 63, n. 64, n. 66, n. 67 were held at earth potential.

3.7.3 Estimate of depletion voltage

The C-V characteristics of the detector were also used in order to extrapolate an estimate of the depletion voltage, so as to compare it with its nominal value (i.e. 50 V, see Table 3.1). This extrapolation procedure relies on the fact that a p^+- n junction capacitance decreases with the square root of the increasing applied bias and it maintains a constant value once the detector is fully depleted [Sze, 1985]:

$$C(V) = \frac{\varepsilon_0 \varepsilon_r}{w} = \sqrt{\frac{\varepsilon_0 \varepsilon_r q_e N_D}{2(\phi_B + V_{RB})}} \quad \text{for} \quad V_{RB} \leq V_{depl} \quad \textit{(per unit area)} \tag{3.23}$$

$$C(V) = \frac{\varepsilon_0 \varepsilon_r}{d} \quad \text{for} \quad V_{RB} > V_{depl} \quad \textit{(per unit area)} \tag{3.24}$$

where the parameters d, ε_0 and ε_r have the same meaning as in equation (3.19), and where V_{RB} is the positive voltage applied to the n-type contact (reverse bias), V_{depl} is the voltage at total depletion, Φ_B is the built-in potential of the junction, q_e is the electronic charge, N_D is the number of donors (i.e. the concentration in the lightly doped n-type bulk) and w is the thickness of the depleted region. Below V_{depl} the function $C(V)$ obeys a power-law, but the capacitance becomes a constant for $V_{RB} > V_{depl}$, since there is no additional region to deplete of carriers remaining in the bulk silicon.

An estimate of the depletion voltage can be extracted from a plot of *Log(C)* versus *Log(V)* (see Fig. 3.25). The estimated value of depletion voltage can be found at the intersection of two straight lines, obtained by fitting the C-V data (plotted in logarithmic scale) in the linearly decreasing region and in the plateau region. The shape of the experimental characteristic curve made the actual value of depletion voltage rather difficult to determine. A depletion voltage of approximately 55 V was extrapolated from the data in Fig. 3.25.

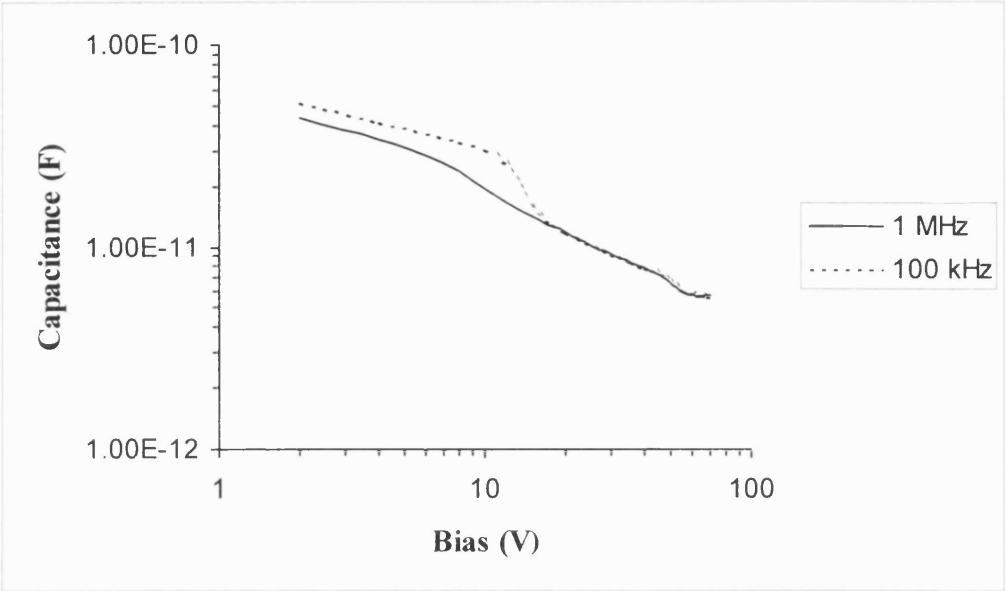

Fig. 3.25: Measurement of strip to back plane capacitance as a function of detector bias. The measurement was performed on the AC connection of strip 65. Closest and outer neighbours (i.e. strips 63, 64, 66 and 67) are held at earth potential.

3.8 Measurements of interstrip capacitance

These measurements were performed on the AC pads of one central strip and its four neighbours on the detector *p*-side. In all measurements the bias ring was held at earth potential whilst the voltage on the back plane was increased from 0 to 70 V in steps of 2 V. In the first configuration of the experimental set-up (see Fig. 3.26) the two outer neighbouring strips were grounded, so as to measure the capacitance of the central strip to its two closest neighbours. In the second configuration (see Fig. 3.27) the two closest neighbours were grounded, and the capacitance of the central strip was measured with respect to its two outer neighbours. Finally, in the third configuration (see Fig. 3.28) the total interstrip capacitance was evaluated for the central strip, by measuring its capacitance with respect to all four neighbours.

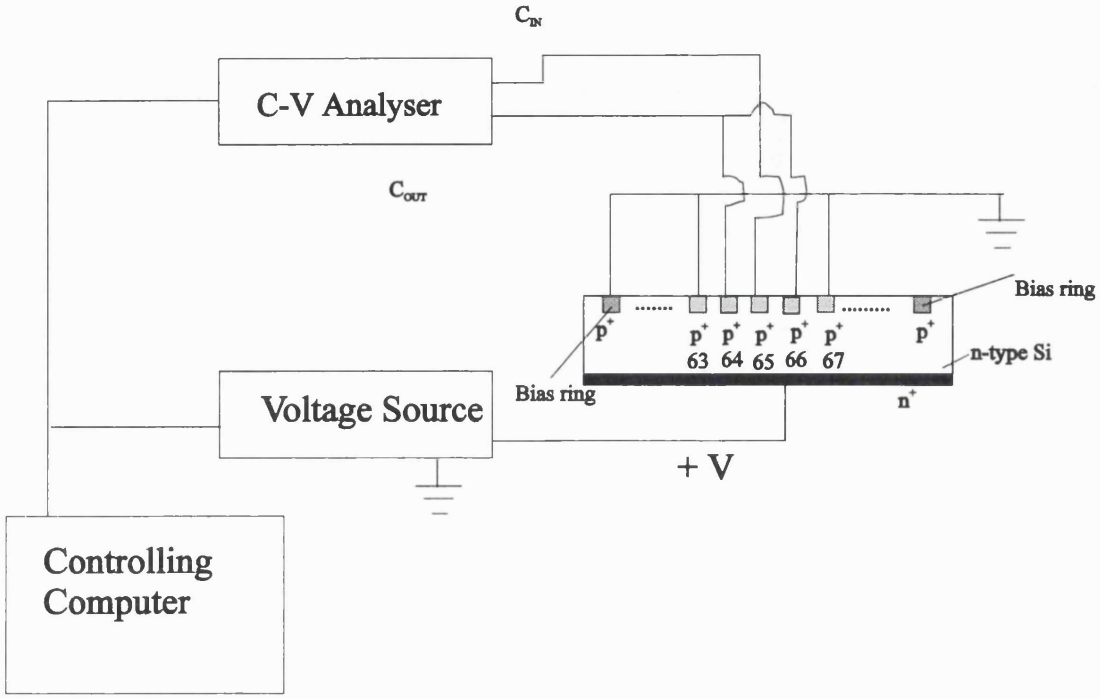

Fig. 3.26: Diagram illustrating the instrument configuration that was employed for the measurements of capacitance of a single *p*-strip (65) with respect to its closest two neighbours (i.e. strips 64 and 66).

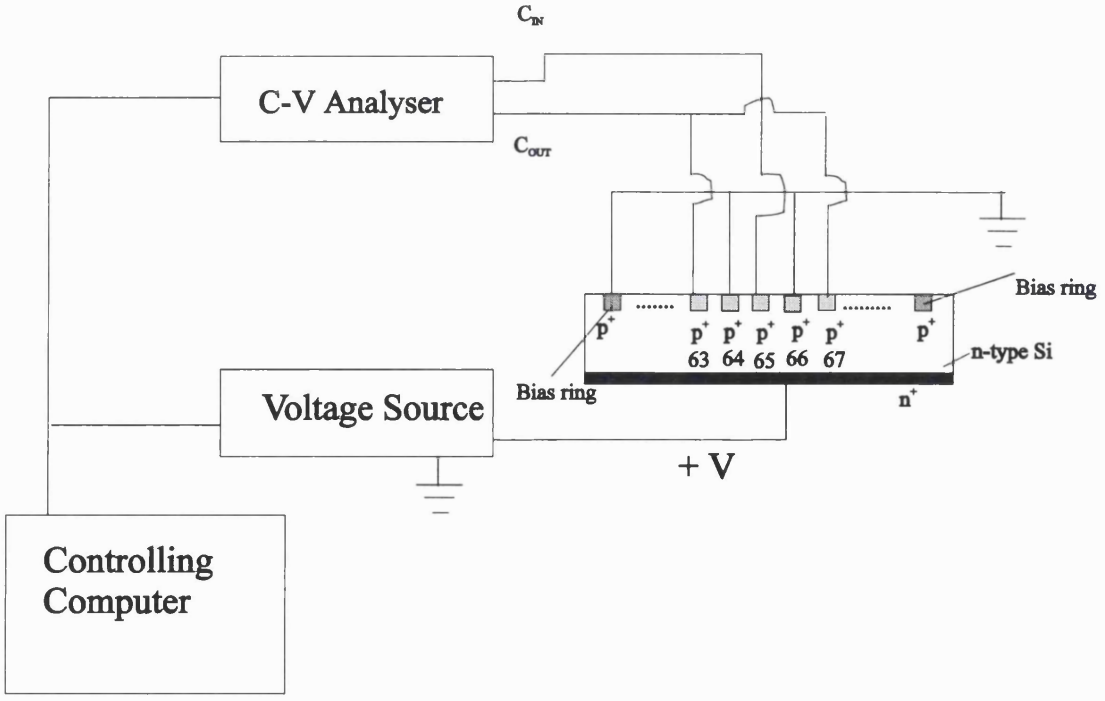

Fig. 3.27: Diagram illustrating the instrument configuration that was employed for the measurements of capacitance of a single *p*-strip (65) with respect to its two outer neighbours (i.e. strips 63 and 67).

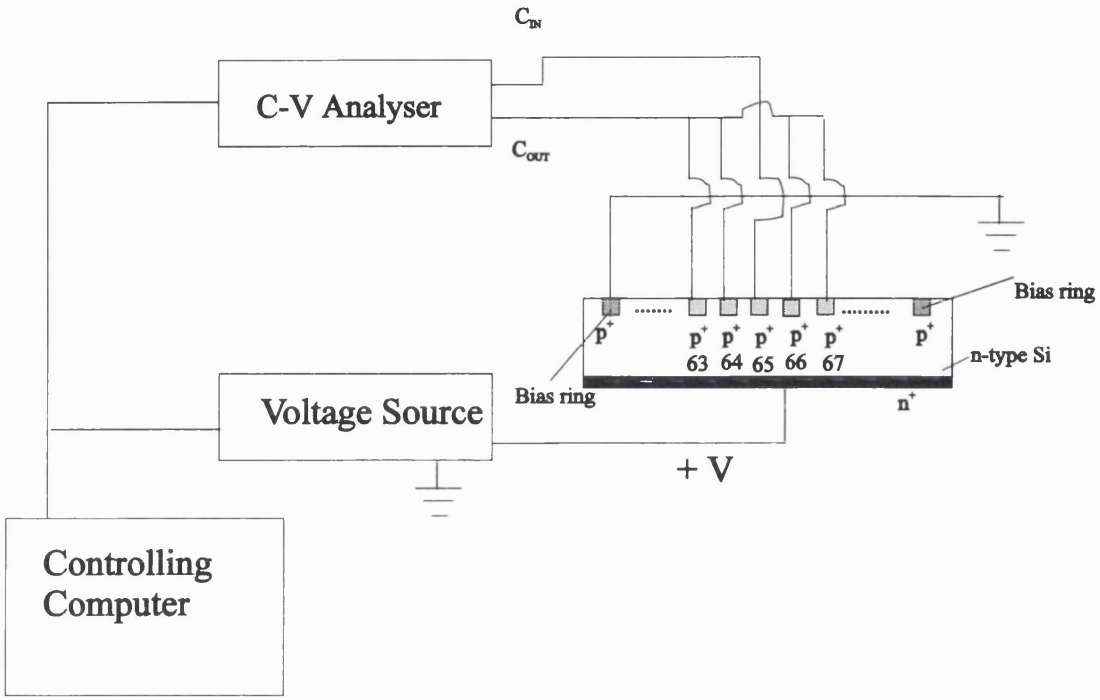

Fig. 3.28: Diagram illustrating the instrument configuration that was employed for the measurements of total interstrip capacitance for a central strip (65).

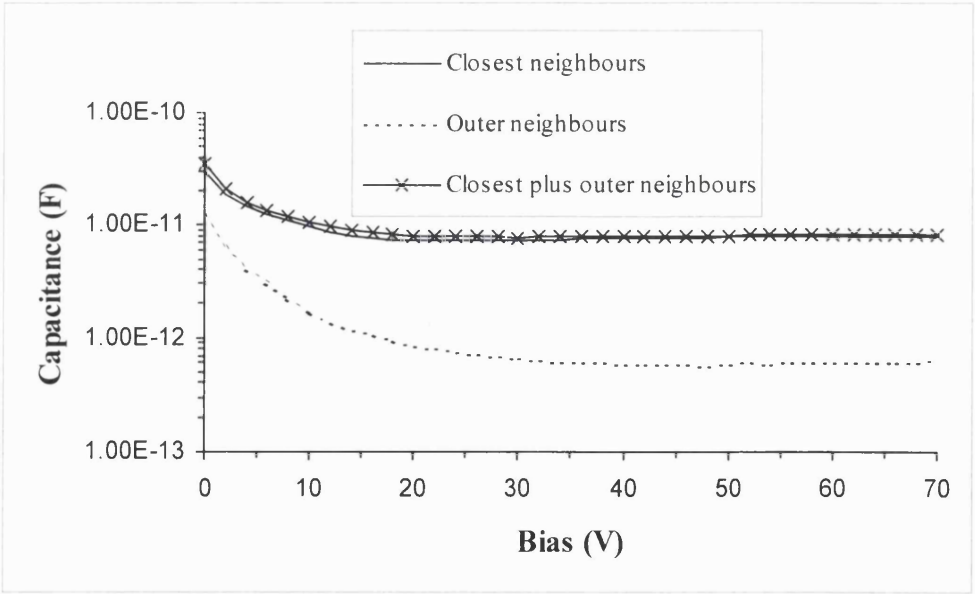

Fig. 3.29: Experimental measurements of interstrip capacitance with respect to the two closest neighbours, the two outer neighbours and all four neighbours. The measurements were performed on the AC connection of strip 65 at a frequency of 1 MHz.

The total interstrip capacitance value measured at over depletion (70 V) for the central strip (considering its four neighbours) is approximately 8 pF. This value is given mainly by the coupling of the two closest neighbours, as the contribution of the outer neighbours is only of the order of 3%.

The results reported in Fig. 3.29 were obtained at a frequency of 1 MHz, which has been used in the literature as a reference frequency for measurements of interstrip capacitance on AC coupled detectors [Barberis *et al.*, 1994]. Different authors have in fact observed that such measurements exhibit a strong frequency dependence.

Circuit simulation programs designed for the analysis of electronic circuits have been employed in order to study the electrical characteristics of AC coupled strip detectors. Their application has shown that the phenomenon of the frequency dependence of the measured interstrip capacitance should be interpreted in terms of the detector behaving as an extended network of capacitors and resistors (see Fig. 3.30) [Bacchetta *et al.*, 1995]. Using such circuit models, every detector strip is divided into hundreds or even thousands of elementary cells, each consisting of discrete circuit components. A computer programme is then employed to solve the equations that describe the circuit voltages and currents, thus allowing the user to predict the electrical behaviour of the detector. It was shown that the capacitance value increases with frequency until it reaches a plateau at the high frequency limit of approximately 1 MHz [Barberis *et al.*, 1994]. This frequency dependence effect was also observed in the experimental data obtained from the IPS 60x60–500 NX-NY128 detectors. The effect can be seen in Fig. 3.31, where the measurements of the AC interstrip capacitance between one metal strip and its closest four neighbours are plotted for both 100 kHz and 1 MHz frequency.

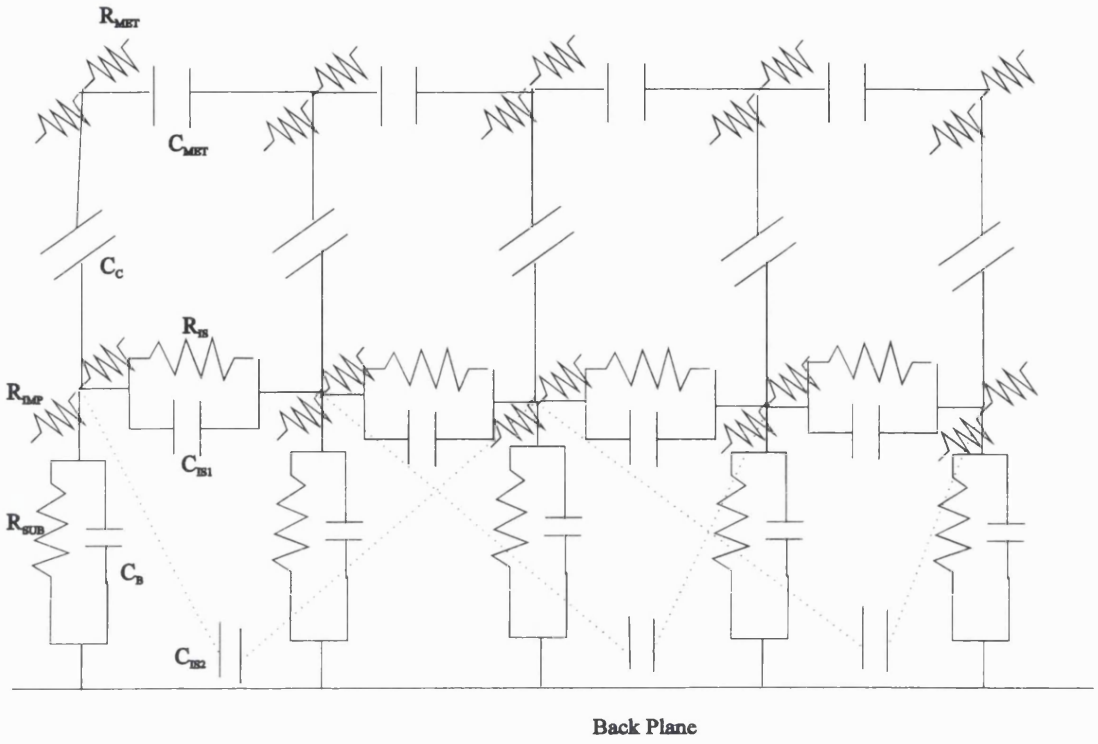

Fig. 3.30: The structure of the electrical network used for the simulation model of the AC-coupled strip detectors in [Bacchetta *et al.*, 1998], [Bacchetta *et al.*, 1995]. Only one central strip and its four neighbours are considered in this figure. Every strip is divided across its length into hundreds of elementary cells. Looking at the cross section plane along the strips, each cell consists of a pair of resistors R_{MET} representing the metal strip, a pair of resistors R_{IMP} representing the implant strip and a coupling capacitor C_C bridging both pairs. All these unit cells are connected in series into a network. In the cross section plane perpendicular to the strips, the network is made up by the inter-electrode capacitance C_{MET}, the interstrip capacitors to first (C_{IS1}) and second neighbours (C_{IS2})and the interstrip resistors R_{IS}. The p^+-n diodes are also part of the network. They are here represented as the parallel combination of R_{SUB} (substrate resistance between the p+ implant and the back side) with C_B (strip capacitance to the back plane), which are present in both cross sectional planes.

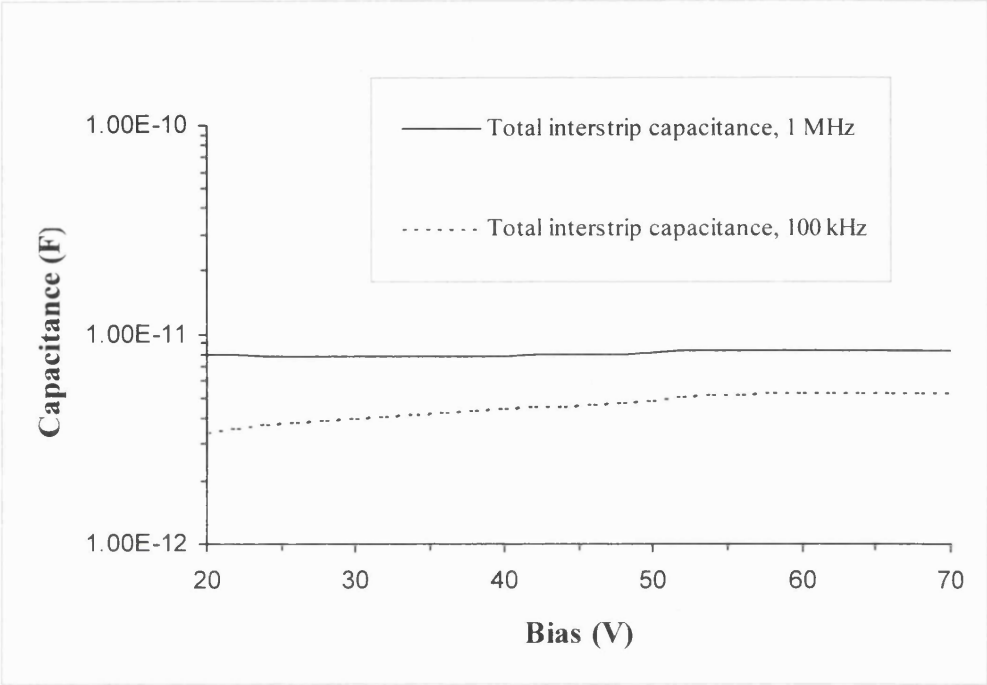

Fig. 3.31: Measurements of interstrip capacitance (with respect to the four closest neighbours) that were performed on strip 65 (p-side of detector B2578-3) at both 1 MHz and 100 kHz frequencies.

As the detectors are AC coupled, the measurements do not strictly provide us with the "true" value of the interstrip capacitance. In the measurements obtained with the instrument configuration of Fig. 3.26 (measurements to the two closest neighbours), the measured quantity C_{AC} results from a combination of the coupling capacitors C_c of the three strips with the "true" interstrip capacitance values C_{is} of the two neighbouring strips, plus a very small contribution C_m (~ 1 Ff, see section 3.6.4) from the coupling of the metal electrodes. The measured value of capacitance is actually more important for real applications, as it is the AC interstrip capacitance that contributes to the amplifier noise in experimental conditions. However, by constructing an adequate equivalent circuit of the capacitor network that describes our measurements (see Fig. 3.32), it is possible to estimate the "true" value of the interstrip capacitance.

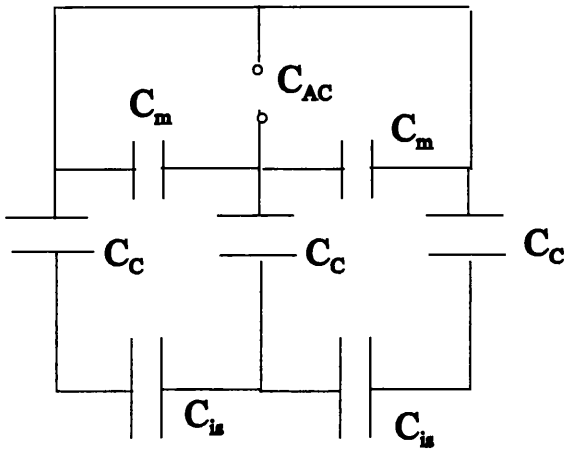

Fig. 3.32: Schematic of the capacitor network involved in the experimental measurements of interstrip capacitance.

If we neglect the parallel contribution of the intermetal capacitance (as $C_m << C_{AC}$ it is $C_{AC} + 2C_m \cong C_{AC}$) we will obtain:

$$C_{is} = \frac{C_{AC} C_c}{2C_c + C_{AC}} \tag{3.25}$$

which can be approximated as follows (since $C_c >> C_{AC}$):

$$C_{is} \cong \frac{C_{AC}}{2} \tag{3.26}$$

From equation (3.26) we obtain that the AC interstrip capacitance value C_{AC} measured with respect to the first two neighbours can be approximated as the sum of the "true" interstrip values C_{is} of the two strips. From the experimental measurements the value of the interstrip capacitance with respect to its two closest neighbours is ~ 8 pF; therefore, the capacitance C_{is} of one strip with respect to one of its closest neighbours is ~ 4 pF. This value is in agreement with the estimate given in section 3.6.4, which was obtained from fitted data in the literature that predict the interstrip

capacitance value C_{is} as a function of the strip width/pitch ratio [Bacchetta *et al.*, 1998].

In most commercially available microstrip silicon detectors, the typical readout pitch is 50 μm and the standard detector thickness is 300 μm. The pitch is therefore quite small with respect to the depletion thickness, resulting in interstrip capacitance values that are typically one order of magnitude larger than the capacitance between the strip and the back plane. The interstrip capacitance in most silicon detectors is therefore the dominant capacitive component at the input of the readout electronics. As can be seen from these measurements, as well as from the theoretical considerations previously presented, this is no longer the case for detectors such as the IPS 60x60 – 500 NX-NY128 type. The strip pitch (470 μm) is almost equal to the detector active gap (500 μm), and the interstrip capacitance is of the same order of magnitude as the capacitance of the strip to the back plane. On one hand, this has the positive effect of reducing the noise of the readout strip that is caused by the interstrip coupling. On the other hand, however, it may pose a critical issue when this kind of detectors is used in capacitive charge division readout mode, due to the charge loss to the back plane capacitance [Dabrowski *et al.*, 1994].

3.9 Tests on coupling capacitors

The capacitors that couple the charge between the metal readout strips and their implant strips have the function of isolating the bias voltage and the leakage current from the front-end of the readout chip. If "pinholes", i.e. pierces in the coupling oxide, are present in some capacitors, a short will be created between the corresponding implant and metal strip, thus allowing the leakage current to flow through. Tests were carried out so as to identify the presence of such pinholes and hence preventing the bonding of the associated strips to the electronics. The manufacturing company provided us with the number of defective strips in each

detector (see Table 3.2), but no information had been recorded regarding the strip position or the detector side where the pinholes had been found. The tests on the coupling capacitors were carried out on three detectors (B2578-1, B2578-2, B2578-3).

The experiments searching for pinholes in the capacitors were performed on the bare wafers by measuring the current flowing between the bias ring and the AC pad of each readout strip, when a given potential was applied across the coupling capacitors. This potential was made similar to the one that the capacitors would experience during the operation of the detector.

One way of biasing the detector is to ground one side whilst applying the high voltage on the other side. However, as the metal strips connected to the APV6 are at a potential of less than 1 V, biasing the detector with this method would subject the coupling capacitors to a large difference of potential on the high voltage side, and to a very small difference of potential on the grounded side. In order to avoid this imbalance and minimise the stress produced on the capacitor dielectric, it was decided that during operation the total bias V_{op} across the detector would be obtained by applying a symmetrical potential on the two sides, i.e. $+(V_{op}/2)$ on the *n*-side and $-(V_{op}/2)$ on the *p*-side. Assuming an operational voltage of 70-80 V (see Table 3.1), one obtains that during operation a maximum voltage of approximately 40 V will be applied on each side across the coupling capacitors. These tests were thus performed with a conservative value of 45 V applied to the coupling capacitors.

In Fig. 3.33 and Fig. 3.34 the experimental set-up employed for such tests is shown for the detector *p*- and *n*-side respectively. A protection resistor of 1 MΩ was used to limit the maximum current flowing between the detector and the Voltage Source. The measurements were performed by examining the 128 strips one by one on each side of the detector. If no pinhole was present, the measured current was of the order of 0.1 pA, rising to hundreds of pA when a failing coupling capacitor was found. The

capacitors were tested on the bare wafers for detector B2578-2 and B2578-3. No pinholes were found in the coupling capacitors of detector B2578-2, whereas three failing coupling capacitors were identified on detector B2578-3. Such experimental results did not agree with the information provided by the company (see Table 3.2).

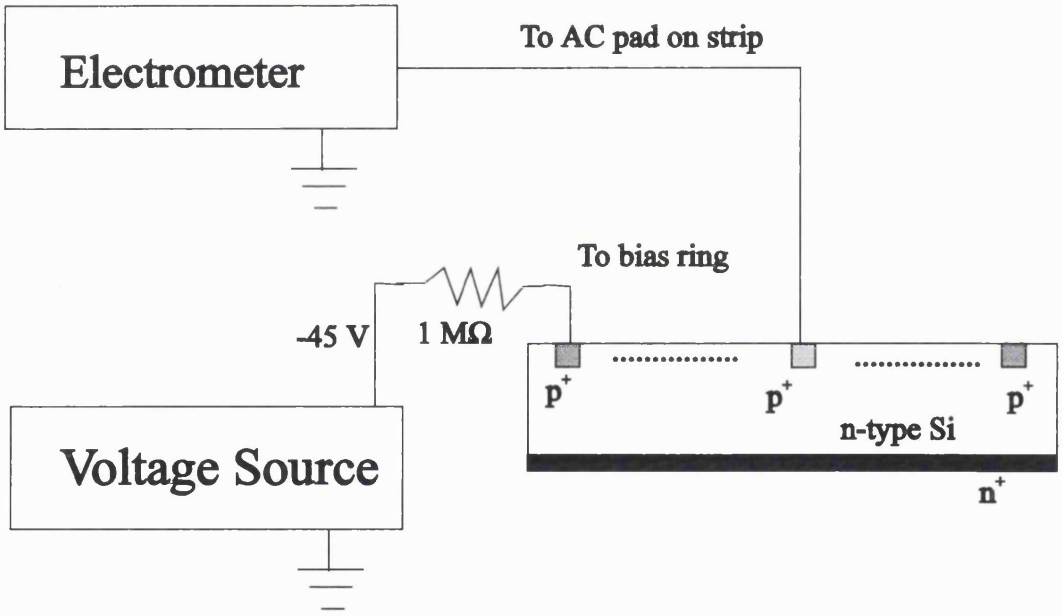

Fig. 3.33: Diagram illustrating the instrument configuration that was employed for testing the coupling capacitors on the *p*-side of the detector.

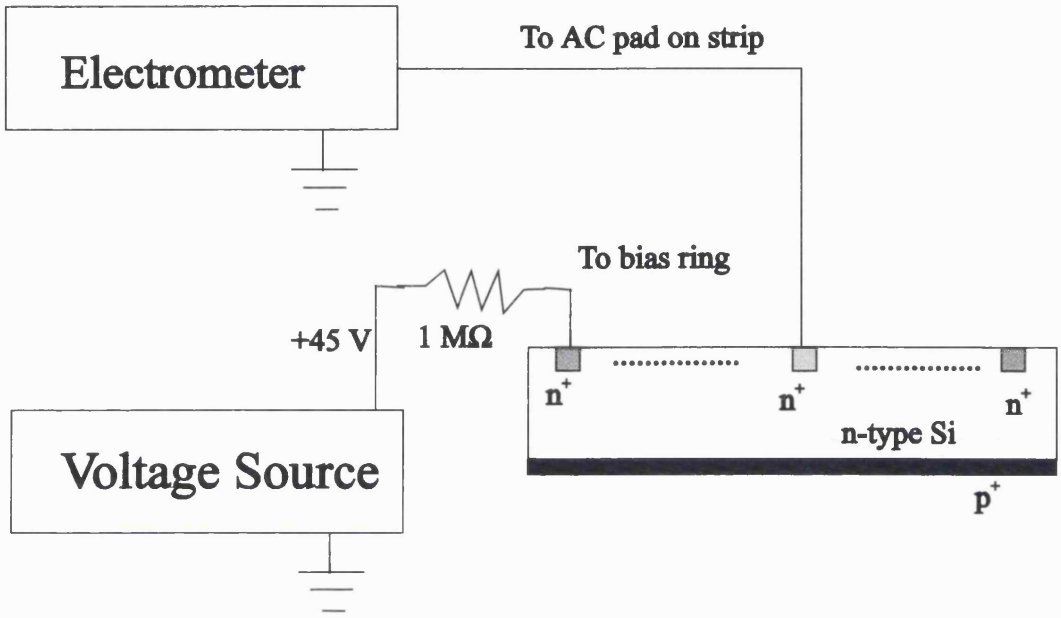

Fig. 3.34: Diagram illustrating the instrument configuration that was employed for testing the coupling capacitors on the *n*-side of the detector.

Chapter 4

Performance Measurements of Bonded Silicon Strip Detectors

4.1 Introduction

Following the characterisation of their electrical properties, two of the microstrip detectors were bonded to the electronics and assembled into scatter modules. These were then tested using the experimental set-up at Imperial College, which is described in this chapter. This system is routinely employed to test silicon strip detectors and their integrated readout electronics. The reason for testing the modules on a standard acquisition system for strip detectors is twofold. Firstly it allowed us to test the sensors on a general-purpose and fully operational set-up; the acquired data will serve as a benchmark for the readout system developed at UCL for the Compton camera (which is described in the next chapter). Furthermore, the study of the performance of the scatter modules as standard detectors for charged particles (β^-) provided a simple method for the energy calibration of the strips, thus making it possible to estimate the typical FWHM noise (keV) of a detector channel. Such a result not only made it possible to correlate the detector noise performance with the previous measurements of current and voltage characteristics, but it also allowed us to make a prediction on the spatial resolution of the designed camera, as will be discussed in the next chapter.

4.2 The integrated readout electronics

4.2.1 Overview of the APV6 readout chip

The APV6 is one of the latest prototypes of front end readout chips that have been developed for the CMS silicon tracker at LHC. A detailed description of the chip can be found in [French, 1997], [Raymond *et al.*, 1997]. The APV6 is a 128-channel analogue pipeline implemented on a 12 mm x 6.3 mm silicon area, fabricated in radiation-hardened technology (Harris AVLSIRA process). The chip has a power consumption of 2.4 mW/channel.

In the APV6, detector signals are amplified, shaped and stored at a sample rate of 40 MHz, which is the operation frequency of the LHC. Each pipeline channel contains 160 capacitor cells, where data are stored for up to 4 μs and read out when externally triggered. The APV6 can be operated in two different ways: *deconvolution* or *peak* mode. In the first case a weighted sum of three samples of the stored pulse is multiplexed out, whereas in the second case only a single sample (which can be timed to be at the peak of the shaped pulse) is read and output. The peak mode was selected for this application. The position of the pipeline cell to be read out is the same for all 128 channels and is determined by the trigger timing, which is defined by a user supplied 'latency' value (see Fig. 4.1). The latency is the time interval (in units of clock cycles) that occurs between storing a point to the pipeline and sending a trigger.

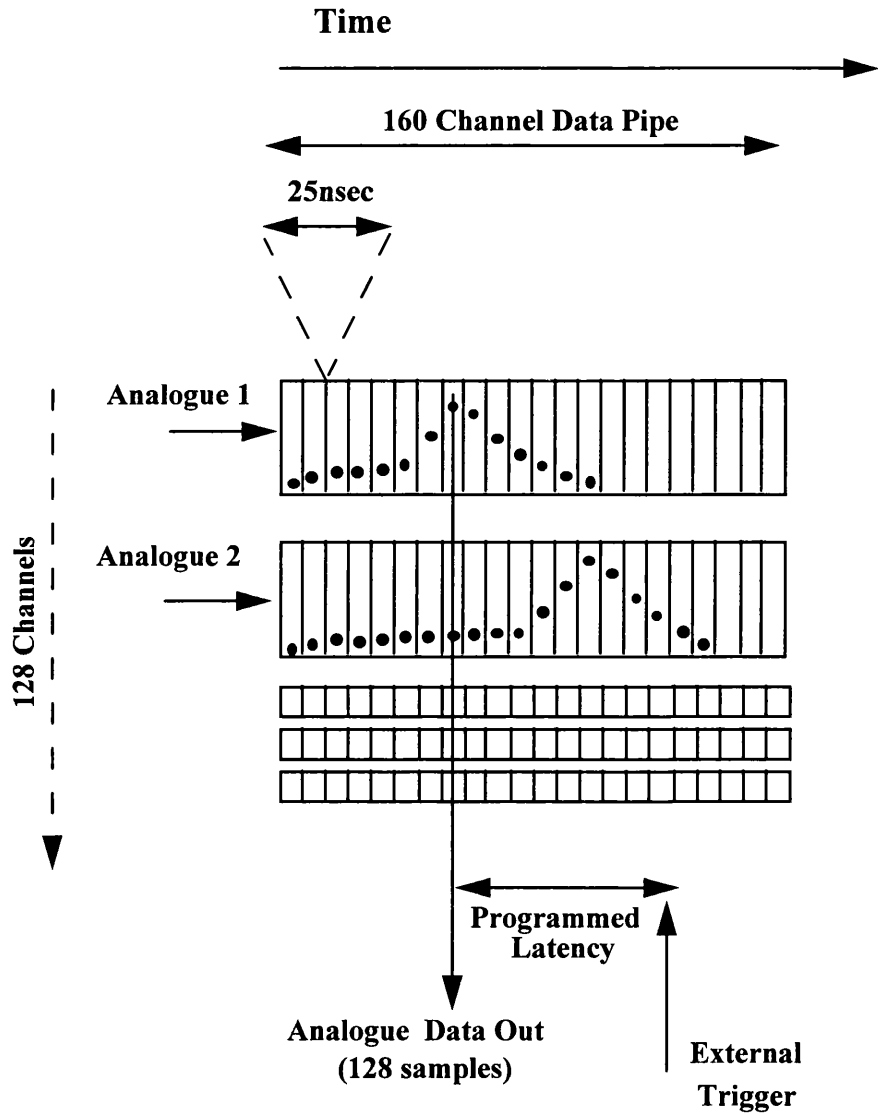

Fig. 4.1: Schematic of the pipeline [Cullum, 2000].

4.2.2 Output data format

A 128:1 analogue multiplexer operating at 20 MHz (i.e. half the clock frequency) is used to serially transmit the data from the channels in current mode. The output data stream is 7 μs long and consists of a 12-bit digital section followed by 128 analogue levels (see Fig. 4.2). The digital section comprises a 4-bit header (where a low bit in the third position indicates an error condition) and an 8-bit digital value that identifies the pipeline address from which the data have been read out. An independent digital output synchronised with the data stream is also available and can be used as a trigger for external digitisation. Because of the architecture of the multiplexer, the output of the analogue data follows a non-consecutive order and shows a characteristic pedestal pattern. The channels are output in 8 groups of 16 channels. In the j-th group (j=0,7) the channel order is as follows: 0+j, 32+j, 64+j, 96+j, 8+j, 40+j, 72+j,104+j, 16+j, 48+j, 80+j, 112+j, 24+j, 56+j, 88+j, 120+j. In Fig. 4.3 the same data as plotted in Fig. 4.2 are shown, after restoring the data to consecutive order. It can be seen that a pattern is present in the pedestals, consisting of four batches of channels with similar pedestal levels.

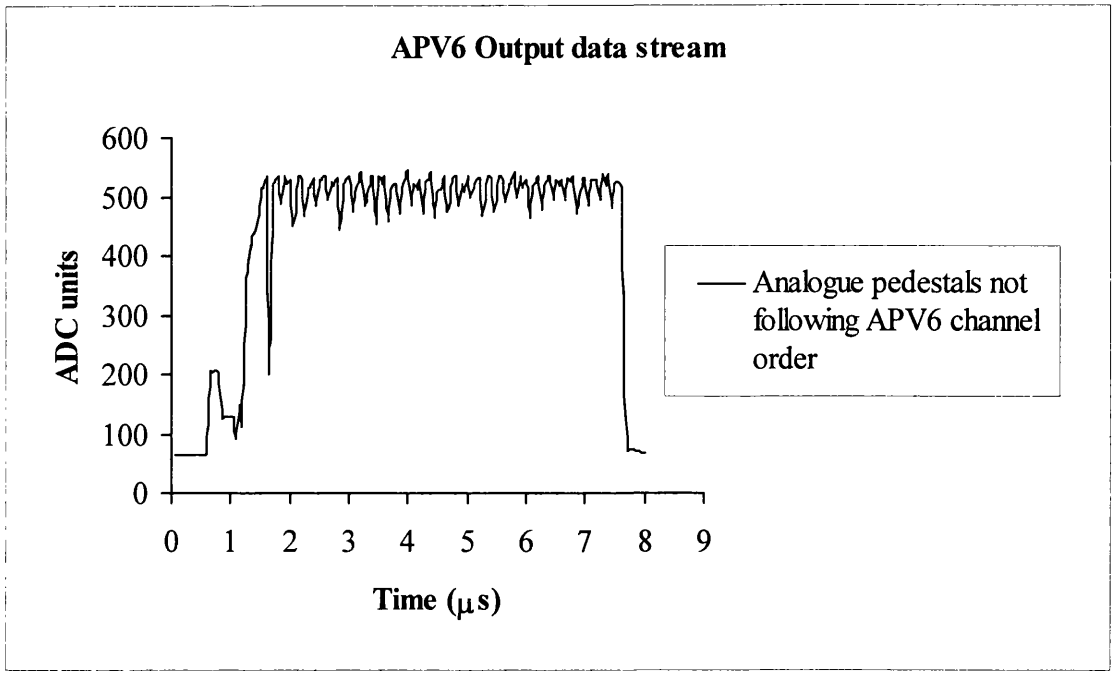

Fig. 4.2: Example of data output from the APV6 (detector B2578-3, p-side). The detector bias is 70 V. The data shown here are the 'pedestal' values, averaged over 1,000 events.

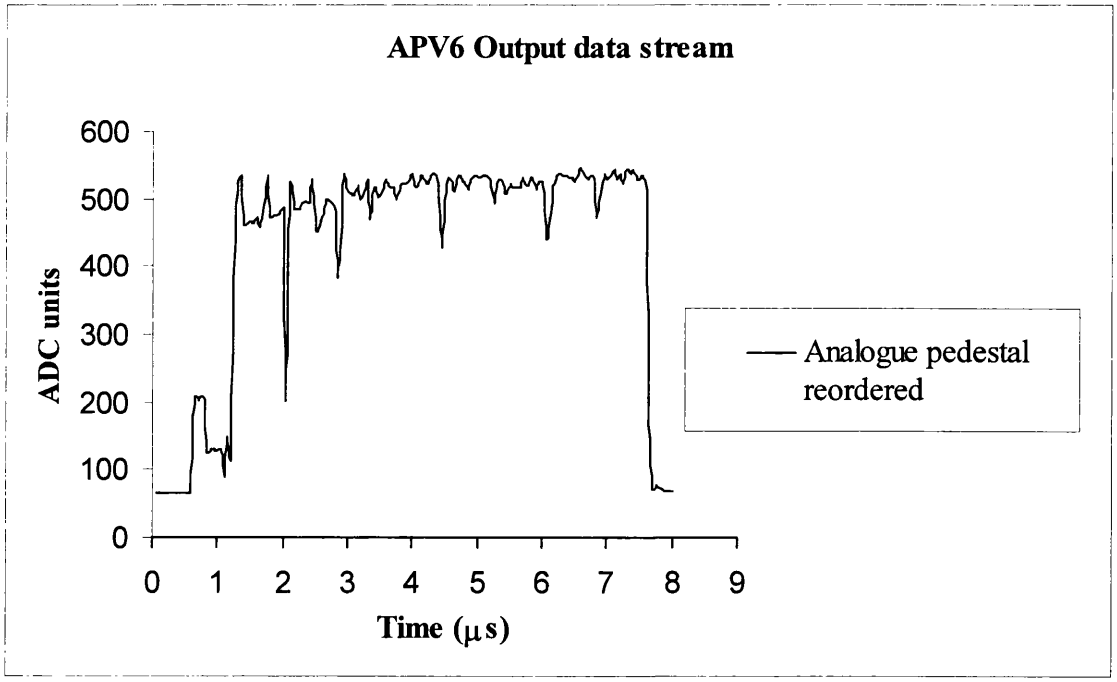

Fig. 4.3: Same data as above, but reordered.

4.2.3 Noise performance of the APV6

In the experiments for applications at CERN, the amplifier in the APV6 chip is normally operated so as to produce a symmetrical pulse shape with a shaping time (i.e. the pulse peaking time) of 50 ns. As will be discussed in section 4.4, the noise level of a readout chip for a given value of shaping time τ can be expressed in terms of its *Equivalent Noise Charge* or *ENC*.

The APV6 has a much lower noise contribution than the previous prototypes. Typical *ENC* measurements in peak mode with τ = 50 ns give approximately 510+36/pF electrons as a function of input capacitance [Raymond *et al.*, 1997]. Assuming an input capacitance of 10 pF from the detector strip, one obtains a FWHM noise level of approximately 7.4 keV in silicon[14]. However, for this application a lower noise level was desirable. Moreover, such a short pulse shape (τ = 50 ns) was not suitable for the Compton camera application, as explained in the next paragraph.

In peak mode operation, it is necessary to programme the latency value so as to sample the peak value of the pulse. This is a particularly important requirement in the Compton camera application, where energy resolution is of paramount importance. In most HEP applications, the timing of events is known and synchronised to the clock cycle; the latency value can thus be suitably calculated for peak sampling. In this project, on the other hand, the external trigger will be provided by an additional detector, as will be described in chapter five. The trigger signal will occur randomly with respect to the APV6 clock and must be synchronised to it by means of special electronics. If the delay between the event in the trigger detector and the collimator detector is constant, then a fixed latency value determined experimentally will be appropriate even with a sharply peaked pulse. However, the energy signal will not enable a trigger request unless it is above a given threshold. This process of signal

[14]FWHM noise (keV silicon) = *ENC* (electrons) x 2.35 x w, where w is the ionisation energy in silicon (w = 3.26 x 10^{-3} keV). The factor 2.35 is introduced as the *ENC* is the standard deviation of the Gaussian curve that represents the noise broadening of an ideal line spectrum (see section 4.4.1).

discrimination could therefore introduce a time dependence of the trigger request on the height of the shaped pulse.

A flat-top pulse with a long falling time in the APV6 would help overcoming this problem, as it would ensure that the pulse-height information is retained when the trigger request occurs. To investigate this, a study was carried out at Imperial College in order to tune the shaping time of the pulse, aiming at lowering the noise figure as well as achieving a flat-top pulse shape. It was suggested that an asymmetric pulse shape should be used, with a 'short' rising time (~ 150 ns) and a 'long' falling time (~ 9 μs). For this pulse shape, the measurement of the *ENC* lowered to approximately 413+23/pF electrons [Raymond, 1997]. This expression corresponds to 5.5 keV FWHM in silicon, assuming 10 pF of external input capacitance. These noise measurements, however, were carried out on the bare chip. It was concluded that the noise level and the effects of the suggested pulse shape should be re-assessed once the APV6 channels were bonded to the detector. The results of this evaluation are reported in section 4.7.3.

4.3 Bonding of the detectors to the readout electronics

In order to read out each strip detector, two APV6s would require bonding onto opposite planes, in orthogonal direction one with respect to the other. The mount board had to be sufficiently compact so as to be placed inside the wire bonding station as well as to allow geometrical flexibility of the camera configuration. A "sandwich" structure (metal-PCB-metal) was specifically designed at Imperial College in order to support the detector and the associated integrated readout electronics. A technical drawing showing the dimensions of the metal frames sandwiching the PCB layer is given in Fig. 4.4. A photograph of a constructed module hosting a detector bonded to the two readout chips is also shown (see Fig. 4.5). As the input pitch on the APV6 was much smaller (50 μm) than the silicon detector pitch (470 μm), 50 μm to 200 μm pitch adapters (consisting of fine metal

lines on a glass substrate) were used in a two-stage fanout so as to gradually accommodate the pitch difference (Fig. 4.6).

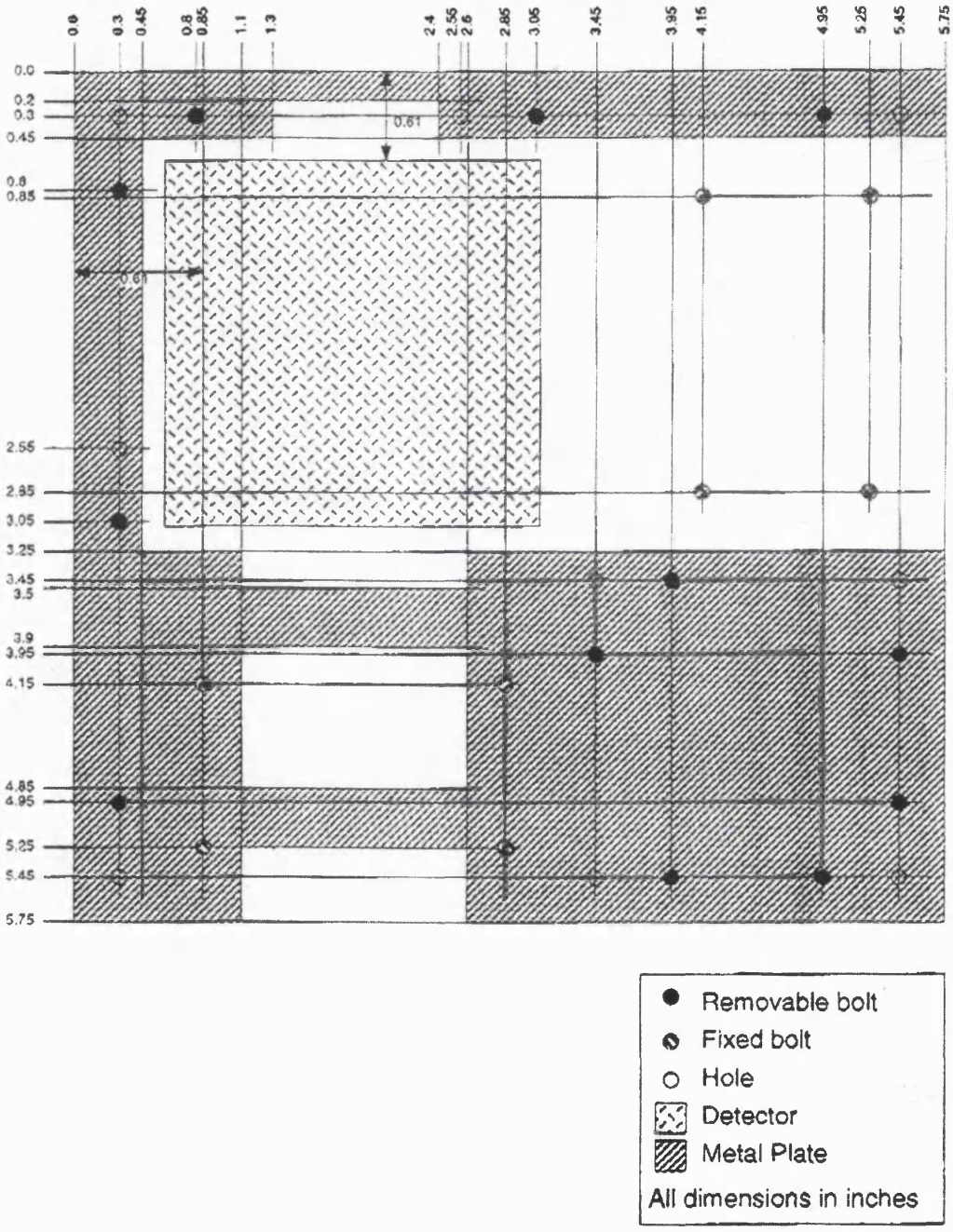

Fig. 4.4: Metal support for the board hosting a detector with two APV6s (technical drawing supplied by Imperial College).

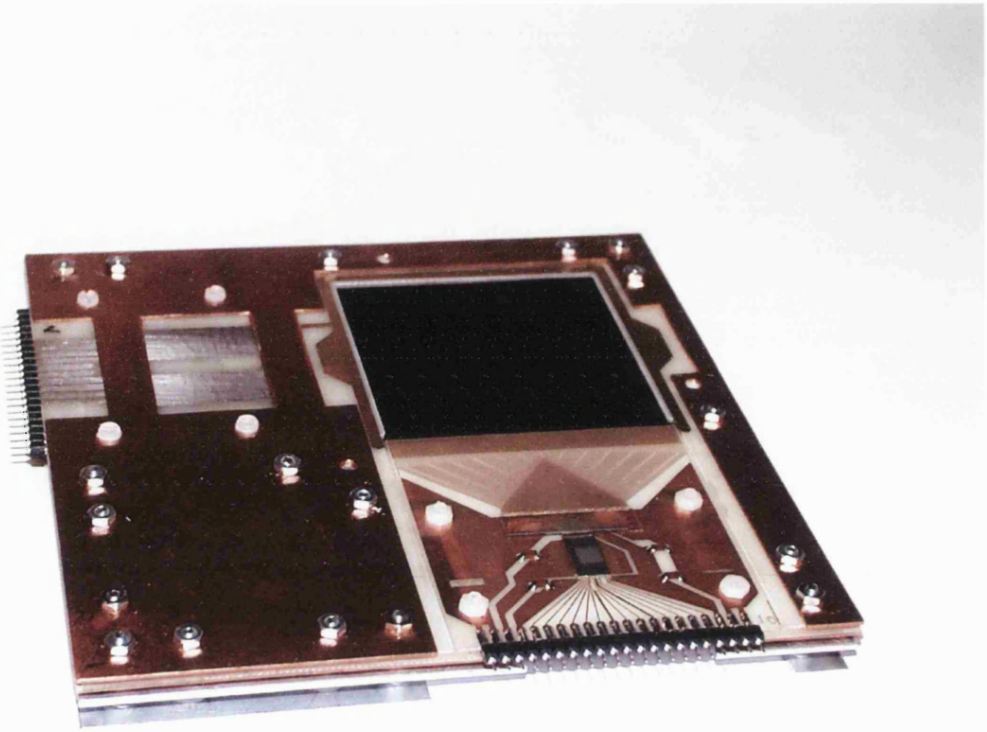

Fig. 4.5: Mount board for a double sided strip detector (*n*-side facing up) and integrated readout electronics.

Two detectors (B2578-1 and B2578-2) were mounted and bonded to the electronics. Visual inspection tests were also performed on these detectors after bonding. The bonding pattern was carefully inspected, in order to identify possible unbonded strips and to ensure a correct correlation between the APV6 channels and the detector strips. The bonding scheme was in fact rather complex, due to the large number of strips and to the presence of many intermediate stages (detector-PCB-pitch adapter-APV6).

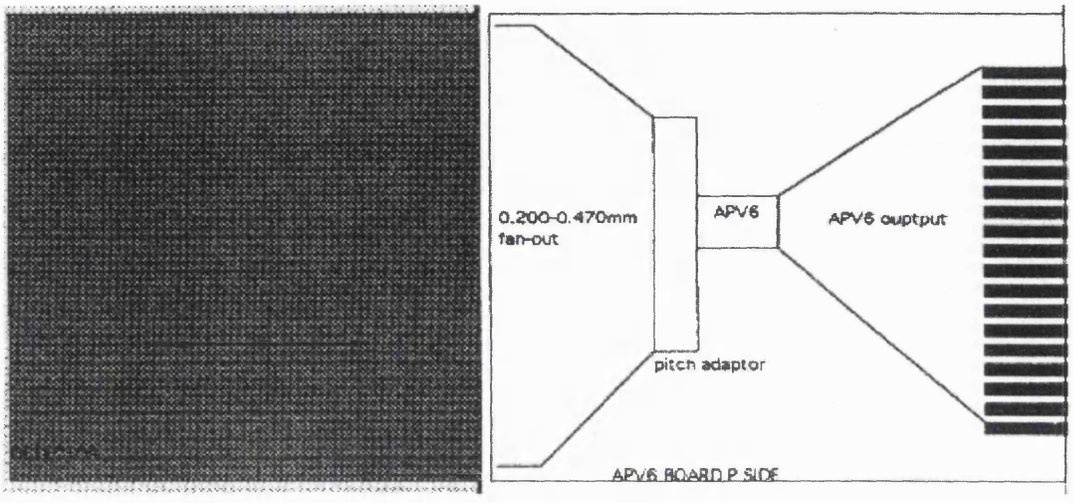

Fig. 4.6: Diagram showing the detector-APV6 bonding scheme, including the 200 μm to 50 μm pitch adaptor (drawing supplied by Imperial College).

A very thorough inspection was required in particular for detector B2578-2, as once bonded this detector showed unacceptable values of leakage current (up to a few hundreds of μA). These current values were much higher than the ones measured prior to bonding (i.e. in the order of 1 μA). Unfortunately, the microscope examination found that a crack was now present on the wafer, short-circuiting the two sides and making the detector unusable. This finding was unforeseen and difficult to explain, as the detector had not been subjected to obvious mechanical damage; cracks do not normally occur as a consequence of mere ultrasonic bonding. Detector B2578-2 was rejected and subsequently replaced with detector B2578-3. Visual inspection of this detector showed no damage following the bonding process.

4.3.1 Tests of coupling capacitors on bonded detectors

Testing of the coupling capacitors was performed not only on the bare wafers but also on the bonded detectors, in order to check that no damage had occurred during the wire bonding of the readout electronics to the AC pads. If a strip bonded to the amplifier has a defective coupling capacitor, not only will an unwanted path be created for the leakage current, but the potential of that strip will also be brought down to the voltage level of the electronics, causing severe distortion of the electric

field in that region of the detector. If a pinhole is found, it will then be necessary to detach that strip from the electronics and leave it at the bias potential.

The tests on the coupling capacitors were performed on the bonded strips by measuring the voltage of every single metal strip, after powering up the readout electronics. The experimental set-ups that were used for the measurements on the detector *p*- and *n*- sides are shown respectively in Fig. 4.7 and Fig. 4.8.

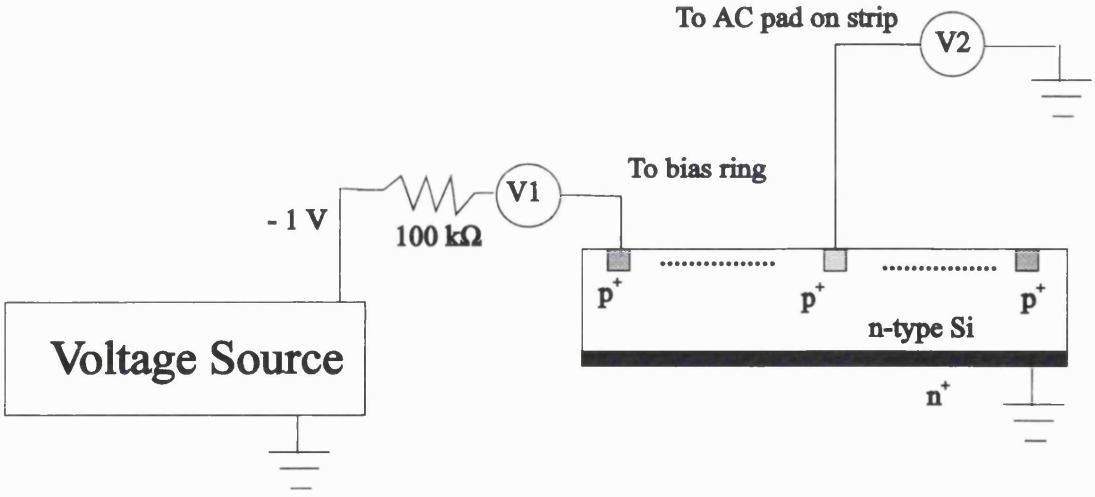

Fig. 4.7: Diagram illustrating the instrument configuration that was employed for testing the coupling capacitors on the *p*-side of the bonded detectors.

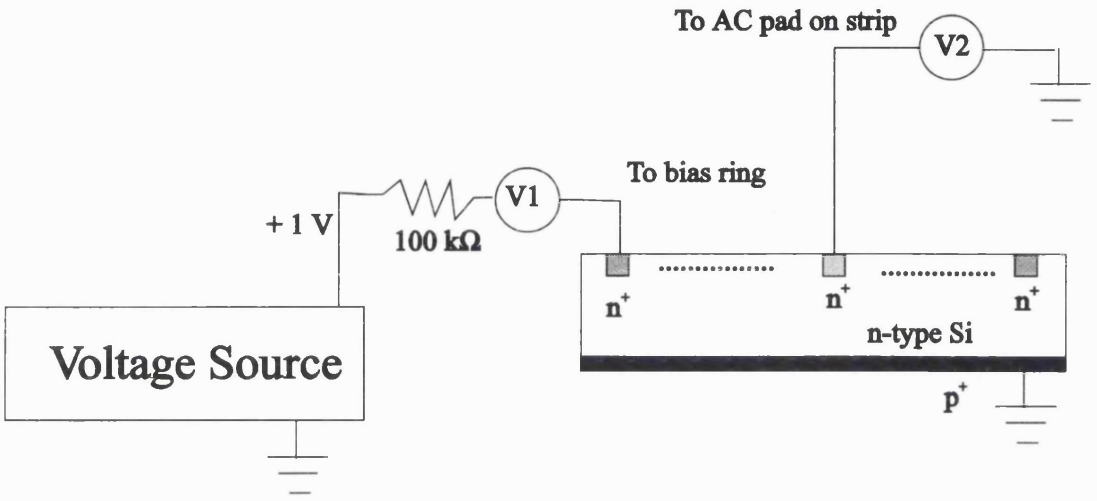

Fig. 4.8: Diagram illustrating the instrument configuration that was employed for testing the coupling capacitors on the *n*-side of the bonded detectors.

A bias of only 1 V was applied to the detector, in order to prevent the amplifier input from sinking a high leakage current if a pinhole in the oxide was found. A protection resistor (100 kΩ) was put between the voltage source and the connection to the bias ring during the measurements on both detector sides. When the detector is biased, the implant strips are brought to the potential of the bias ring via the punch-through effect. If no pinholes are present, the metal readout strips (which are bonded to the readout electronics) are isolated from the implant strips by the coupling oxide. The measured potential of the metal strips should therefore be the same as the one of the APV6 input (0.6 V). However, if a coupling capacitor is damaged and the implant strip is shorted to its readout metal layer, a DC current will flow across the capacitor. The measured potential on the metal strip will no longer be at the same level as the electronics, but it will now increase towards the value of the bias voltage applied to the implant strip.

These measurements were performed by examining the 128 strips one by one on each side of the detector. The strips associated with failing coupling capacitors were disconnected from the electronics by cutting the corresponding metal trace on the PCB that allows the detector to be joined to the pitch adapter on the detector mount board. These measurements on the coupling capacitors of the bonded detectors were performed on detectors B2578-1, B2578-2 and B2578-3, of which only the latter two had been tested for pinholes also prior to bonding. The results of these tests showed an increased number of defective coupling capacitors following the bonding of the electronics (new pinholes in the dielectric appeared in three capacitors on the *p*-side of detector B2578-2 and in one capacitor on the *n*-side of detector B2578-3).

4.3.2 Identification of "defective" strips

The total number and the position of the "defective" strips found on the three detectors B2578-1, B2578-2 and B2578-3 are reported in Tables 4.1, 4.2 and 4.3. These include not only the strips affected by the presence of pinholes and that were subsequently disconnected from the readout electronics, but also the strips that showed accidentally broken or missing bonds during the visual inspection tests. The tables also report the corresponding APV6 channel number. It is important to remark, however, that 'missing strips' are not a major problem in the Compton camera application. Inactive areas in the detector in fact do not produce image defects as in conventional systems, but they simply affect the overall system sensitivity.

Table 4.1: Summary of 'defective' strips in detector B2578-1.

	DETECTOR B2578-1	
	p-side	
Strip number:	*APV channel:*	*Type of defect:*
4, 7, 102, 106, 117, 120, 128	2, 7, 100, 104, 117, 118, 126	Pinholes in coupling capacitors
8	6	Accidentally broken trace on the PCB joining the detector to the pitch adapter
	***n*-side**	
Strip number:	*APV channel:*	*Type of defect:*
2,13, 128	127, 114, 1	Pinholes in coupling capacitors
92	37	Broken bond between the detector and the PCB

Table 4.2: Summary of 'defective' strips in detector B2578-2.

	DETECTOR B2578-2	
	p-side	
Strip number:	*APV channel:*	*Type of defect:*
33, 65, 66	32, 64, 65	Pinholes in coupling capacitors
126	125	Broken trace on the PCB joining the detector to the pitch adapter
17, 29, 127, 128	16, 28, 126, 127	Missing or broken bonds between the detector and the PCB
	***n*-side**	
Strip number:	*APV channel:*	*Type of defect:*
1	127	Missing bond between the detector and the PCB
2	126	Broken trace on the pitch adapter

Table 4.3: Summary of 'defective' strips in detector B2578-3.

	DETECTOR B2578-3	
	p-side	
Strip number:	*APV channel:*	*Type of defect:*
1	"Skipped strip". No associated channel on the APV6. As a consequence channel 127 on the APV6 is not bonded to any strip on the detector.	The strip is connected up to the pitch adaptor but this has no connection to any channel on the APV6
71, 72, 119	69, 70, 117	pinholes in coupling capacitors
127	125	PCB trace disconnected from pitch adaptor
128	126	Missing connection from the detector to the PCB
	***n*-side**	
Strip number:	*APV channel:*	*Type of defect:*
1	"Skipped strip". No associated channel on the APV6. As a consequence channel 0 on the APV6 is not bonded to any strip on the detector.	Missing connection from the detector to the PCB
2	127	PCB trace disconnected from pitch adaptor
46	83	Pinhole in coupling capacitor

4.4 Theoretical estimate of strip noise

4.4.1 The Equivalent Noise Charge

The electronic noise is one of the factors that affect the energy resolution in a silicon detector. The signal fluctuations due to the electronic noise are recorded by an analyser even in the absence of an external radiation source. These noise pulses show as a Gaussian spectrum, centred around the "zero energy" channel (see Fig. 4.9). The standard deviation (σ) of such a Gaussian curve is the root mean square (*RMS*) voltage of the noise and can also be represented in terms of the *Equivalent Noise Charge* (*ENC*). The *ENC* is the genuine charge signal (produced from the detector on the input capacity of the preamplifier) that would generate the same output as the RMS noise V_n [Nicholson, 1982].

Let us define the *signal to noise ratio* η as the ratio of the mean signal pulse height V to the RMS noise voltage V_n:

$$\eta = \frac{V}{V_n} \tag{4.1}$$

If the signal is obtained from a charge Q produced in a radiation detector, we can then write:

$$\frac{ENC}{Q} = \frac{V_n}{V} = \frac{1}{\eta} \tag{4.2}$$

The *ENC* is the amount of charge at the input for which the signal-to-noise ratio at the output is equal to unity. The units for the *ENC* are normally Coulombs, but it can also be expressed in terms of the corresponding number of electrons (*ENC/e*, where $e = 1.6\text{x}10^{-19}$ C).

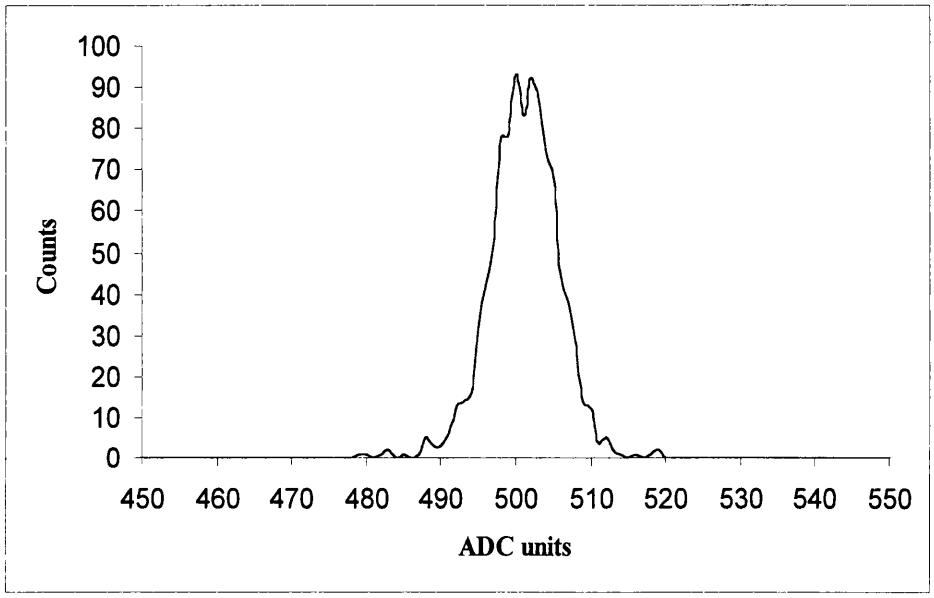

Fig. 4.9: Noise peak (arbitrary offset of 500 ADC units), as measured over 1,000 events for a central strip on the *p*-side of detector B2578-3.

The general expression for the ENC (or σ) in a detector - readout chip system will include the contribution of the pre-amplifying and shaping integrated electronics plus the additional components associated with the detector itself. The noise of a single strip of an AC coupled silicon detector may in fact be parameterised in terms of several contributions [Dubbs *et al.*, 1996], [Nygård *et al.*, 1991]:

$$\sigma^2 = \sigma_{chip}^2 + \sigma_{Rmet}^2 + \sigma_I^2 + \sigma_{Rbias}^2 \qquad (4.3)$$

where

σ_{chip} = noise associated with the readout chip

σ_{Rmet} = thermal noise due to the metal strip resistance

σ_I = shot noise due to the detector leakage current

σ_{Rbias} = thermal noise in the detector bias resistor

Some of the terms in equation (4.3) represent noise sources in series with the input and will therefore depend on the input capacitance. The terms associated with parallel noise sources will not be a function of the input capacitance, as a variation of capacitance will affect both signal and noise together, thus not affecting the *ENC*. In the following sections, the contribution of each term is evaluated in order to obtain an estimate of the noise level that results from the silicon scatter detectors using the APV6 readout chip.

4.4.2 Noise components from the readout chip

There are four main individual noise sources in the integrated readout electronics and they are associated with the input field effect transistor (FET) of the preamplifier: thermal noise in the gate resistor, shot noise from the gate current, thermal noise and Flicker (*1/f*) noise in the FET channel [Delaney, 1980], [Nicholson, 1982]. The current *thermal noise* (or *Johnson noise*) is thermally generated in any resistor and is associated with the random Brownian motion of the electrons: the fluctuations in the carrier velocities result in small fluctuating voltages across the resistor. The current *shot noise* is due to the discrete nature of the carriers: it originates from the fluctuations of the number of individual charged particles that are available for conduction. The *Flicker noise* (or *1/f noise*) predominates at lower frequencies and it appears to be dependent on crystal imperfections and surface effects in semiconductors. Its origin however is not completely understood.

The general expression of the *ENC* may be computed for various practical shaping systems. In the APV6, the output pulse shape closely approximates simple *CR-RC* shaping. It can be shown [Nicholson, 1982] (see Appendix I) that for a *CR-RC* shaping amplifier with time constants τ_1 and τ_2 ($\lambda = \tau_2/\tau_1$) and with input capacitance C_{in} one obtains:

$$(ENC)^2 = \frac{k_1}{\frac{2\lambda}{\lambda^{1-\lambda}}\,2\lambda(\lambda+1)\tau_1} C_{in}^2 + \frac{k_2\tau_1}{\frac{2\lambda}{\lambda^{1-\lambda}}\,2(\lambda+1)} + \frac{k_3 \ln\lambda}{\frac{2\lambda}{\lambda^{1-\lambda}}\,(\lambda^2-1)} C_{in}^2 \quad [Coulomb]^2 \qquad (4.4)$$

where the coefficients k_1, k_2 and k_3 depend on the geometrical and physical characteristics of the transistor as well as on the temperature.

In the above equation, the first term expresses the contribution of the FET channel thermal noise, which is a series noise source. The second term includes the contribution of the gate resistor thermal noise and the gate current shot noise. These are both parallel noise sources, as they do not depend on the input capacitance. Finally, the last term expresses the contribution of the Flicker noise, which is a series noise source and in good quality amplifiers is usually negligible with respect to the other two terms.

All the terms in (4.4) give their minimum contribution for $\lambda = 1$, i.e. when the rise and fall times of the amplifier are made equal ($\tau_1 = \tau_2 = \tau$). The expression for the *ENC* in this particular case is given by [Nicholson, 1982]:

$$(ENC)^2 = \exp(1)^2\left(\frac{k_1}{4\tau}C_{in}^2 + \frac{k_2\tau}{4} + \frac{k_3}{2}C_{in}^2\right) \quad [\text{Coulomb}^2] \tag{4.5}$$

The noise at the output of a preamplifier and CR-RC shaper chip is usually quoted by most manufacturers in a simpler form. It is expressed as the number of electrons corresponding to the equivalent noise charge, as a function of the external capacitance C_{in} applied at the chip input and for a stated value of the peaking time τ (or the time constants τ_1 and τ_2 if they are different):

$$\sigma_{chip} = \sigma_0 + \beta_C C_{in} \qquad [\text{electrons}] \tag{4.6}$$

where σ_0 is the noise of the bare amplifier (expressed in electrons) and β_C is the amplifier slope (expressed in electrons/pF).

For the APV6, assuming a shaped pulse with time constants $\tau_1 = 150$ ns and $\tau_2 = 9$ μs, $\sigma_0 = 413$ e^- and $\beta_C = 23$ e^-/pF [Raymond, 1997]. If we assume that the total

parasitic capacitance is given by the total strip capacitance as expressed by equation (3.1) in Chapter three, we obtain from our capacitance measurements that C_{in} ~14 pF and therefore from equation (4.6) that σ_{chip} ~ 735 electrons.

4.4.3 Noise components from the detector

The detector contributes to the total strip noise both in the series noise (via its capacitance and the metal strip resistance) and in the parallel noise (via its leakage current and its bias resistor). For an explanation on how the noise equations included in this section were obtained, please refer to Appendix I.

The aluminium strip resistance contributes to the series thermal noise with the following term:

$$\sigma^2_{Rmet} = \frac{kTR_{met}C_{in}^{\ 2}}{e\lambda^{\frac{\lambda+1}{1-\lambda}}(\lambda+1)\tau_1} \quad [\text{electrons}]^2 \tag{4.7}$$

where τ_1 = 150 ns, $\lambda = \tau_2 / \tau_1 = 60$ (τ_2= 9 μs), e = 1.6x10^{-19} C is the elementary electronic charge, k = 1.38 x10^{-23} J/(mol K) is the Boltzmann constant, T=300 K is the room temperature and R_{met} = 30 Ω is the metal strip resistance (see eq. (3.14) in Chapter three). Using these values for the parameters in equation (4.7) one obtains that $\sigma^2_{Rmet} \cong 7160$ [electrons]^2.

The parallel source of thermal noise comes from the detector bias resistor and may be computed as follows:

$$\sigma^2_{Rbias} = \frac{kT\tau_1}{e\lambda^{\frac{2\lambda}{1-\lambda}}(\lambda+1)R_{bias}} \quad [\text{electrons}]^2 \tag{4.8}$$

where $R_{bias} > 100$ MΩ (see Table 3.1 in Chapter three), resulting in a maximum value $\sigma^2_{Rbias} \cong 16400$ [electrons]^2.

Finally, another source of parallel noise is the shot noise from the detector leakage current, which can be estimated using the relationship:

$$\sigma_I^2 = \frac{I\tau_1}{\lambda^{\frac{2\lambda}{1-\lambda}} 2(\lambda+1)} \quad \text{[electrons]}^2 \tag{4.9}$$

where we can assume that the detector leakage current per strip is I = 20 nA. This estimate is obtained by averaging the leakage current measured on the whole face of the detector (i.e. 2.5 μA for 128 strips in total). From equation (4.9) one obtains that $\sigma_I^2 \cong 621000$ [electrons]^2.

By combining all contributions we can finally calculate the total noise (sigma in electrons) associated with a single detector channel:

$$\sigma = \sqrt{\sigma^2_{chip} + \sigma^2_{Rmet} + \sigma^2_I + \sigma^2_{Rbias}} \cong 1090 \qquad \text{[electrons]} \tag{4.10}$$

This estimate corresponds to approximately 9.2 keV FWHM for silicon.

The values of the physical parameters employed in the noise calculations and the estimates obtained for each component are summarised in Tables 4.4 and 4.5. It can be seen that the largest contributions to the noise are produced by the readout chip (via the input capacitance) and by the detector leakage current. The evaluation of the total strip noise given in (4.10) is obviously an approximation of the noise level experimentally observed in the strips, as various simplifying assumptions were made. For example, the total parasitic capacitance was here evaluated in terms of the strip capacitance with respect to its nearest four neighbours and to the back plane. Other

parasitic effects of second order due to additional sources of input stray capacitance (pitch adaptor, connectors, cables, etc.) have been neglected. The value of the leakage current per strip employed in equation (4.9) is also a reference estimate. Monitoring of the detectors during hours of operation has shown current variations of the order of several μA. The leakage current may increase because of temperature rise, surface contamination with detector use or because the detector is not perfectly isolated from light. For example, it was observed that in detector B2578-3 the leakage current reached a peak value of 5 μA. This would correspond to approximately 40 nA per strip and would increase the estimated FWHM noise level to 12 keV.

Table 4.4. Parameters employed in the estimate of the components of the strip noise.

Temperature	300 K
Leakage current per strip	20 nA
Shaped pulse time constants	τ_1 = 150 ns, τ_2 = 9 μs
Input capacitance	14 pF
Bias resistor	100 MΩ
Metal strip resistance	30 Ω

Table 4.5. Estimated values for the different components of strip noise.

σ_{chip} (e^-)	σ_{Rmet} (e^-)	σ_{Rbias} (e^-)	σ_I (e^-)	**Total noise** (σ in e^-)	**Total FWHM noise** (keV in Si)
735	85	128	788	1090	9.2

4.5 Detection of charged particles

4.5.1 Description of experimental set-up

The data acquisition system employed for the detection of charged particles and for the noise measurements, which are both described in this chapter, was developed by the High Energy Physics group at the Blackett Laboratory, Imperial College. The system is based on a VME crate (see Fig. 4.10) controlled by a Power Macintosh computer running Labview software. The APV6 slow control is implemented via a VME to I^2C interface. The clock and trigger lines are supplied by a SEQSI[15] programmable pulse generator. The APV6 analogue data are digitised by a Front End Driver (FED) ADC module[16].

[15] Sequencer, designed at the Rutherford Laboratories by M. Morrissey.
[16] Digitiser (10-bit, single-channel prototype), custom Rutherford design for the CMS.

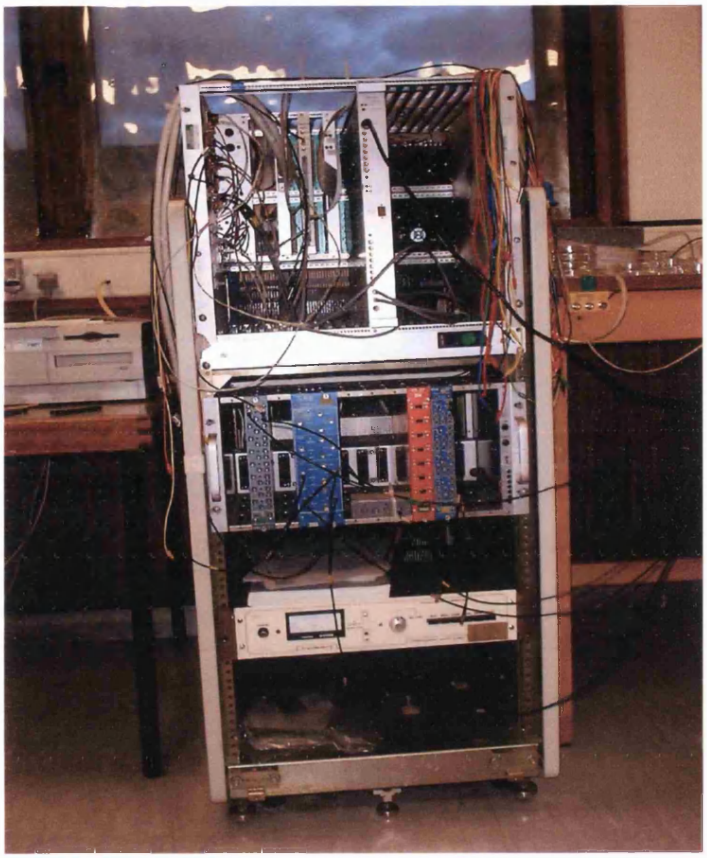

Fig. 4.10: The VME crate of the data acquisition system that was employed in the experiments for the detection of charged particles at Imperial College.

The β-particle pulse height spectra were acquired using a collimated ^{90}Sr source located approximately at the centre of the detector. The detector and radiation source were enclosed in a light-tight aluminium box. A plastic scintillator was placed behind the silicon detector in order to provide a trigger. The scintillator was located behind a small exit window that had been created in the box, so as to allow the transmission of low penetrating radiation (see Fig. 4.11). As the system is designed for the readout of a single-sided strip detector, the *p*- and *n*-side in each detector module were tested in separate experiments.

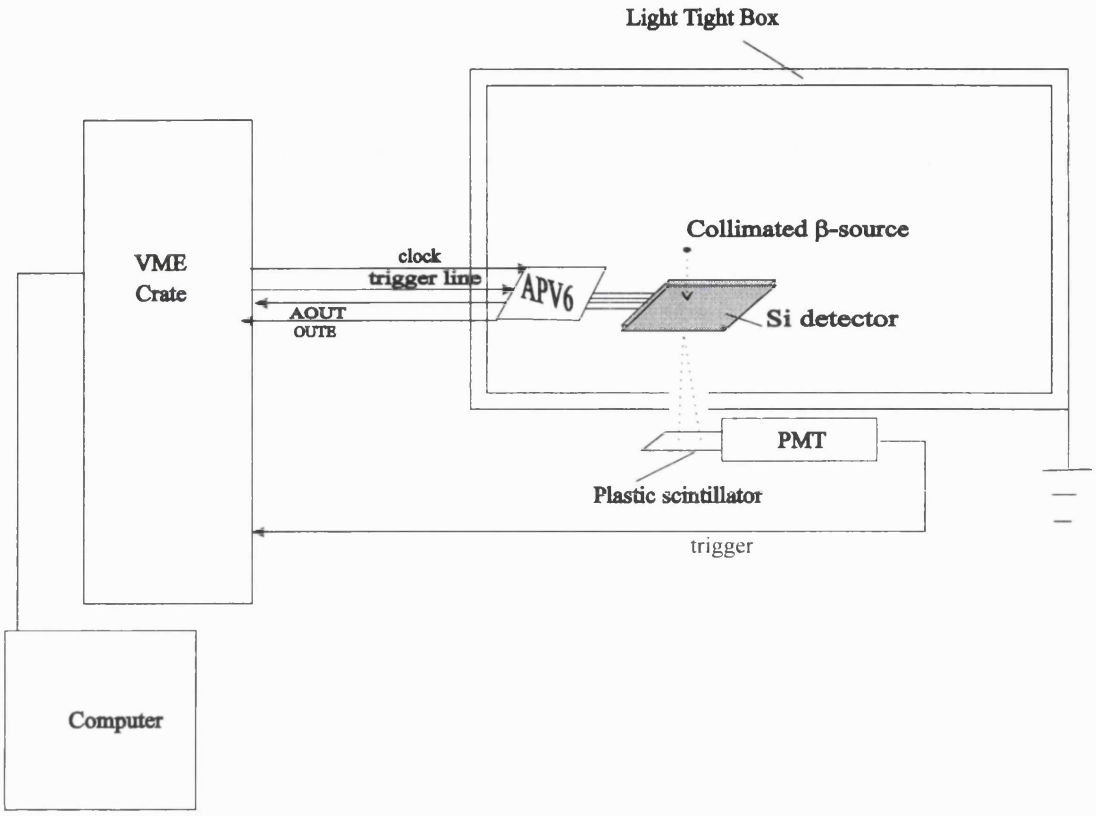

Fig. 4.11: Schematic diagram of the experimental set-up that was employed for the particle detection and noise measurements at Imperial College. AOUT and OUTE are the analogue and digital outputs of the APV6.

The data acquisition software of this system allows the user to perform a series of operations on the digitised data. Due to the method implemented for channel multiplexing, the output data of the APV6 follow a non-consecutive order (see section 4.2.2). The first operation simply consists of *re-ordering* the analogue levels into the 0,1....127 channel sequence. The re-ordered data obtained from the *p*-side of the detector by triggering with the ^{90}Sr source are shown in Fig. 4.12. Another operation (*Pedestal Subtraction*) is subsequently applied in order to eliminate the typical pattern exhibited by the raw data frame obtained from the APV6. In the absence of a signal from external radiation, the output data stream consists of a 12-bit digital header, followed by 128 analogue levels that represent the "pedestals" of the APV6 channels. The pedestal pattern is removed from the analogue data by

subtracting the average pedestal (i.e. the average acquired over 1,000 events) on a channel by channel basis. Finally, a third operation (*Common Mode Subtraction or CMS*) is performed so as to remove the common mode contribution to the noise. This is calculated for every event as the average readout value across all channels, and is also subtracted from the analogue data. The channels that show particularly high levels of noise and those that collect pulses from the radiation source are excluded from the CMS procedure. The effect of pedestal and common mode subtraction is shown in Fig. 4.13.

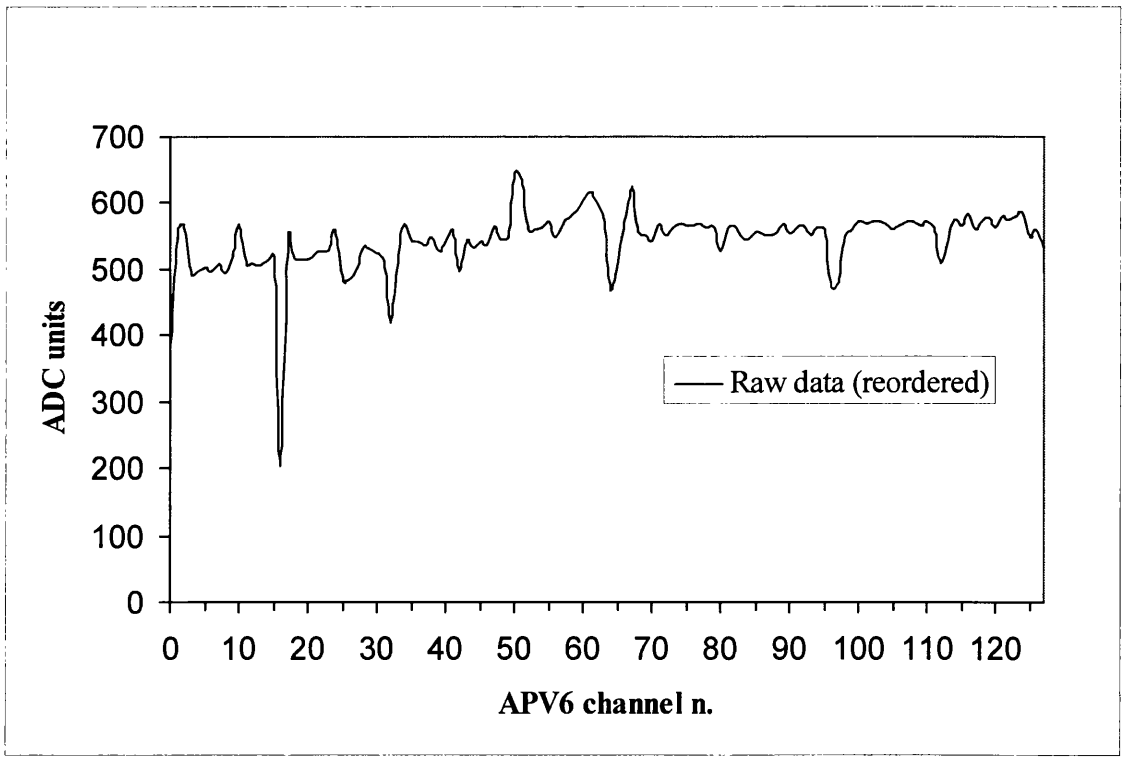

Fig. 4.12: Example of data acquired from the APV6 (128 digitised values) and subsequently reordered.

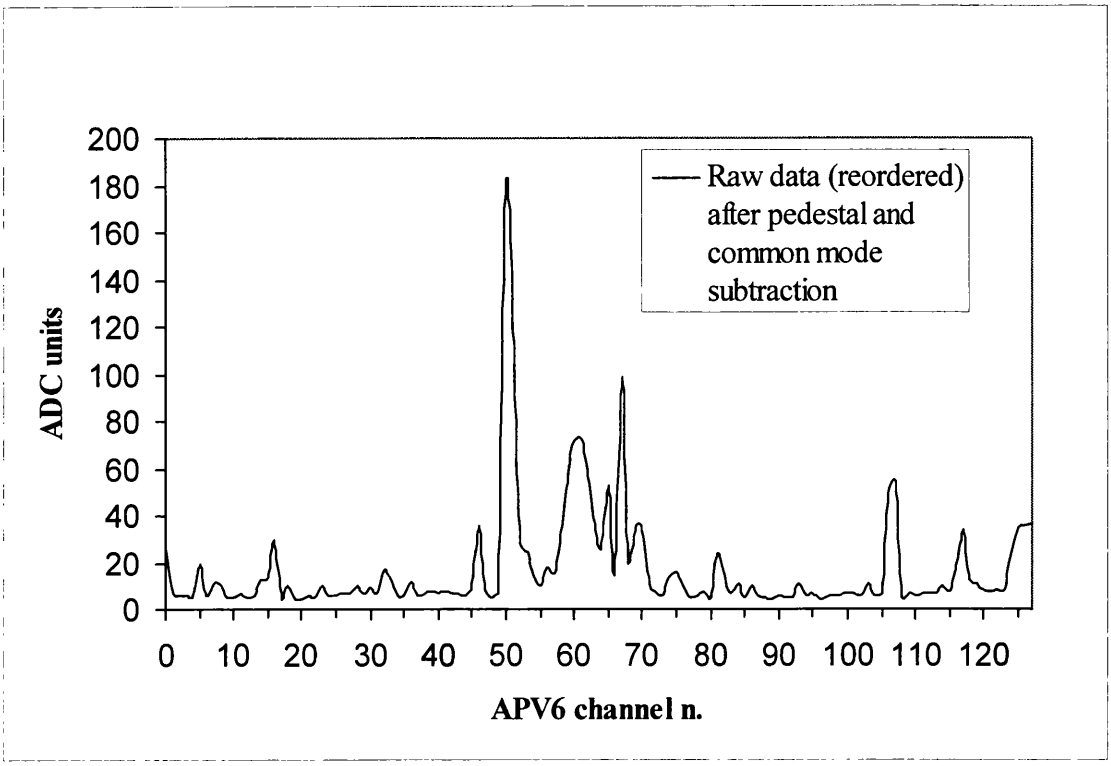

Fig. 4.13: Same data as in Fig. 4.12, after pedestal and CM subtraction.

4.5.2 Determination of the APV6 settings for pulse peak sampling

The "peak mode" operation of the APV6 makes it possible to read out a single sample of the shaped pulse, as described in section 4.2.1. In order to read out the peak value of the analogue pulse shape stored in the pipeline, it is necessary to suitably adjust the timing between a sample being written to and being read from the pipeline. The sample that is read out is the one that was stored a programmed interval of time before the trigger. This time interval is defined by the value programmed in the "latency" register, which contains the separation (in clock cycles) between the write and trigger pointers to the pipeline.

The 'peak mode' operation of the APV6 requires searching for the optimum value of the APV6 'latency' register. This may be done experimentally by observing the position (in ADC channels) of the ^{90}Sr 'Landau peak' as a function of the programmed latency value. The Landau peak is a characteristic peak in the energy

deposition spectrum of the β-particles that traverse a given thickness of silicon, as described in more detail later in this chapter. The latency value was varied from 6 to 20 in steps of 1 clock cycle. The optimum latency value (11 clock cycles) was found at the maximum channel number that defines the Landau peak (see Fig. 4.14).

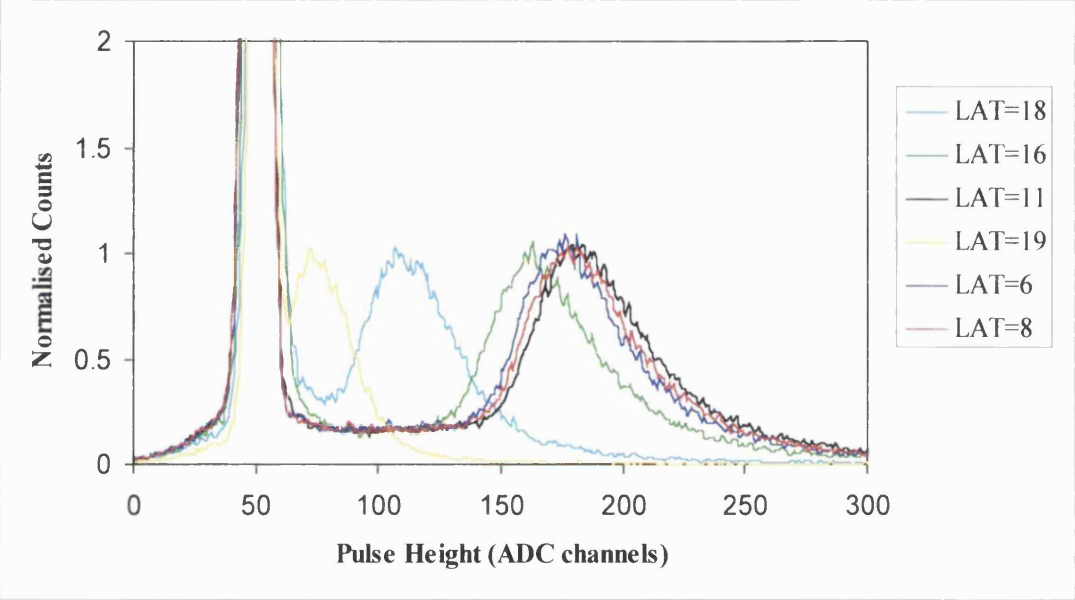

Fig. 4.14: ^{90}Sr β-spectra acquired from one strip on the p-side of detector B2578-1, by programming different values of 'latency' in the APV6. The detector was biased at 60 V. The counts in the spectra are normalised to the maximum. The 'zero energy' channel was arbitrarily set to ADC channel 50.

In Fig. 4.15, the position of the Landau peak is plotted as a function of the programmed latency value (in reverse order). Such a plot provides a coarse reconstruction of the stored pulse shape. The graph shows that for a trigger latency equal to 11 the sample reserved for readout is a peak value from the flat top of the pulse.

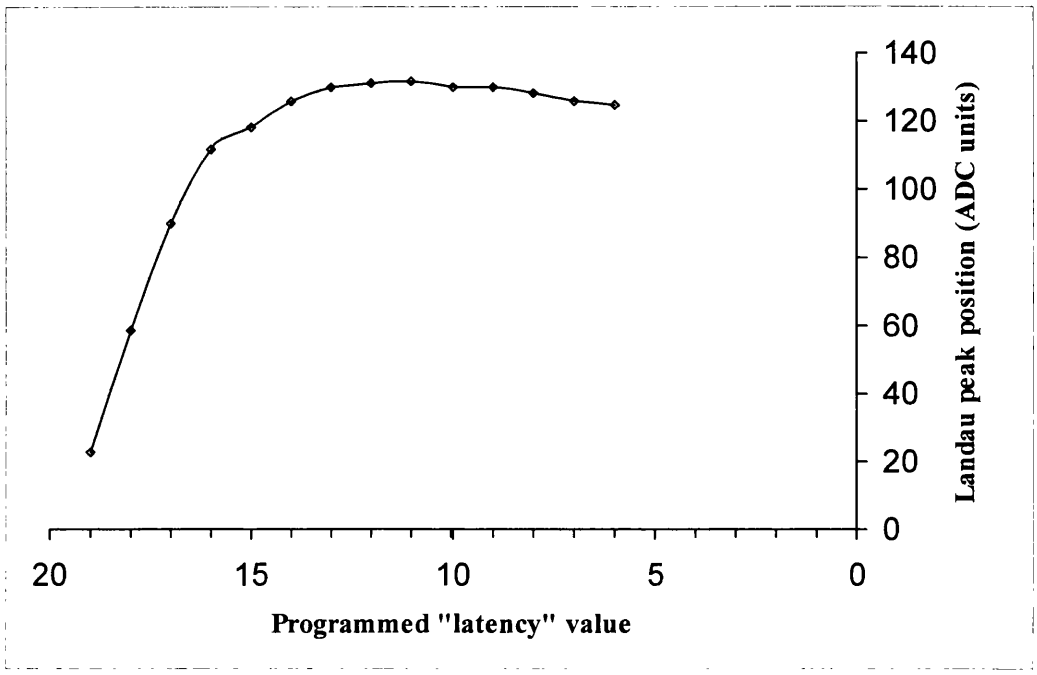

Fig. 4.15: Position of the Landau peak (in ADC channels) as a function of the value programmed in the latency register. The plot was obtained from the spectra shown above. The arbitrary offset (50 ADC units) has been subtracted.

4.5.3 Determination of operating voltage

Silicon detectors are operated by applying an external reverse bias that ensures full depletion of the device. In complex devices such as silicon microstrip detectors, the extrapolation of the full depletion voltage from the C-V characteristic presents difficulties, due to the non-ideal shape of the experimental curves (see section 3.7.3 in chapter three).

The operating voltage may thus be determined once again with spectroscopic measurements, by observing the position of the Landau peak as a function of the applied bias. When the operating voltage is such that the device is fully depleted and all the charge produced by the radiation is collected at the electrodes, the pulse height corresponding to the Landau peak will be recorded with its maximum value in ADC units. During these measurements the bias applied to the detector was varied from 40

V to 80 V in steps of 10 V. The latency register value was kept constant at its optimum value (11 clock cycles). The experiments showed that for both detectors (B2578-1 and B2578-3) the pulse height magnitude would not increase once a bias greater than 70 V was applied (see Fig. 4.16). This bias voltage (70 V) was therefore established as the optimum operating value for the silicon detector modules.

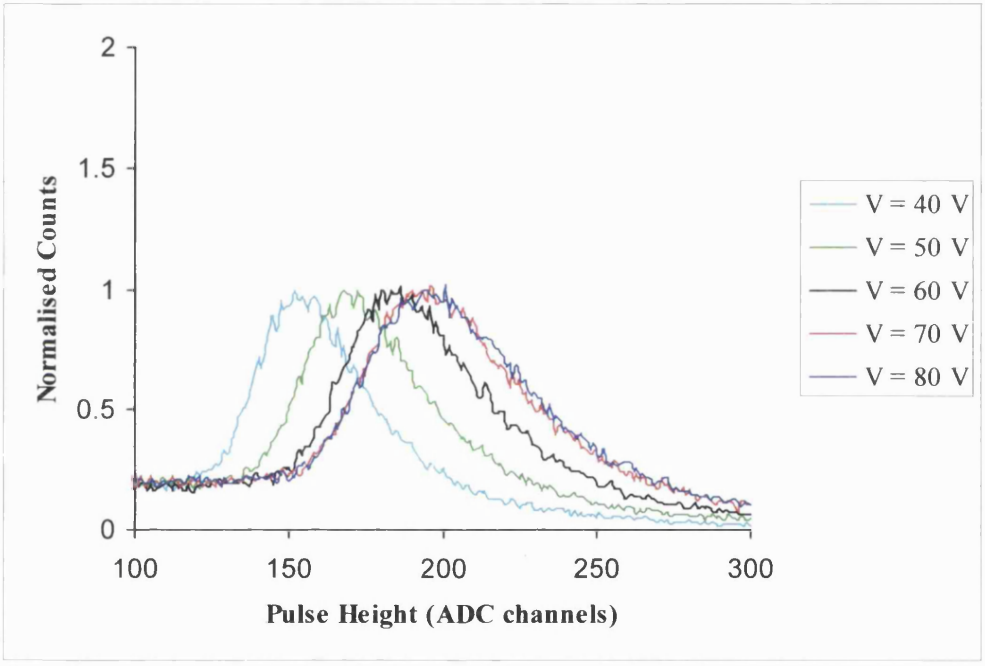

Fig. 4.16: ^{90}Sr β-spectra acquired from strip 67 on the p-side of detector B2578-1, by applying increasing bias voltages to the detector. The counts in the spectra are normalised to the maximum. The 'zero energy' channel was arbitrarily set to ADC channel 50. The noise peaks (which are centred at zero energy) are therefore not visible in this figure.

4.6 Detector calibration using ^{90}Sr

4.6.1 Energy loss of charged particles in silicon

When a charged particle traverses a medium, it interacts with the electrons and the nuclei of the atoms of the surrounding material. In the case of heavy charged particles, these interactions are almost exclusively collisions, which may simply excite the atom ("soft" collisions) or cause the ejection of secondary electrons with

considerable kinetic energy (δ-rays from "hard" collisions). The mean rate of energy loss per unit path length due to collision interactions is the linear *collision stopping power*. In the case of mono-energetic particles, this is approximated by the Bethe-Bloch equation as follows[17] [Attix, 1986]:

$$\left(\frac{dE}{dx}\right)_{col} = \frac{4\pi z^2 Ze^4 N}{\beta^2 m_0^2 c^2}\left[\ln\left(\frac{2m_0c^2\beta^2}{(1-\beta^2)I}\right)-\beta^2\right] \quad [\mathrm{MeVcm^{-1}}] \tag{4.11}$$

where

ze = charge of the primary particle (with e = electronic charge)

Z = Atomic number of the medium

N = number of atoms/cm^3 of the medium = $\rho N_A/A$, being ρ the medium density (g/cm^3), A the medium atomic weight and N_A the Avogadro number

m_0c^2 = electron rest mass (= 0.511 MeV)

β = velocity of the primary particle in units of c

I = mean ionisation and excitation potential of the absorber (MeV)

In the form of (4.11), the Bethe-Bloch equation is valid for heavy particles only (e.g. protons or pions) and is almost independent of particle type. In the case of light charged particles (such as electrons) the collision stopping power is a similar expression, where modifications must be included as the incident electrons and the atomic electrons in the medium are indistinguishable particles. In order to show the typical behaviour of the energy loss rate curves, the collision stopping powers for electrons and protons in silicon (for which I = 173 eV) are plotted as an example in Fig. 4.17 as a function of the product $\beta\gamma$ (where β = v/c and $\gamma = (1-\beta^2)^{-1/2}$). As can be seen from the graph, the energy loss due to the passage of an electron is reduced with respect to the energy loss due to the passage of a heavy particle. This is caused by the

[17] For simplicity the terms for density and shell correction have not been included in equation (4.11). The complete expression of the Bethe-Bloch approximation can be found for example in [Skyrme, 1967], [Attix, 1986].

identical nature of the interacting electrons, which affects the maximum allowed energy transfer.

In practical cases, most relativistic particles have stopping powers close to the minimum of the Bethe-Bloch curve and for this reason are said to be "minimum ionising particles" (or "*mips*"). The average energy deposit of 1 *mip* in 100 μm of silicon is approximately 39 keV [Physics Letters, 1990].

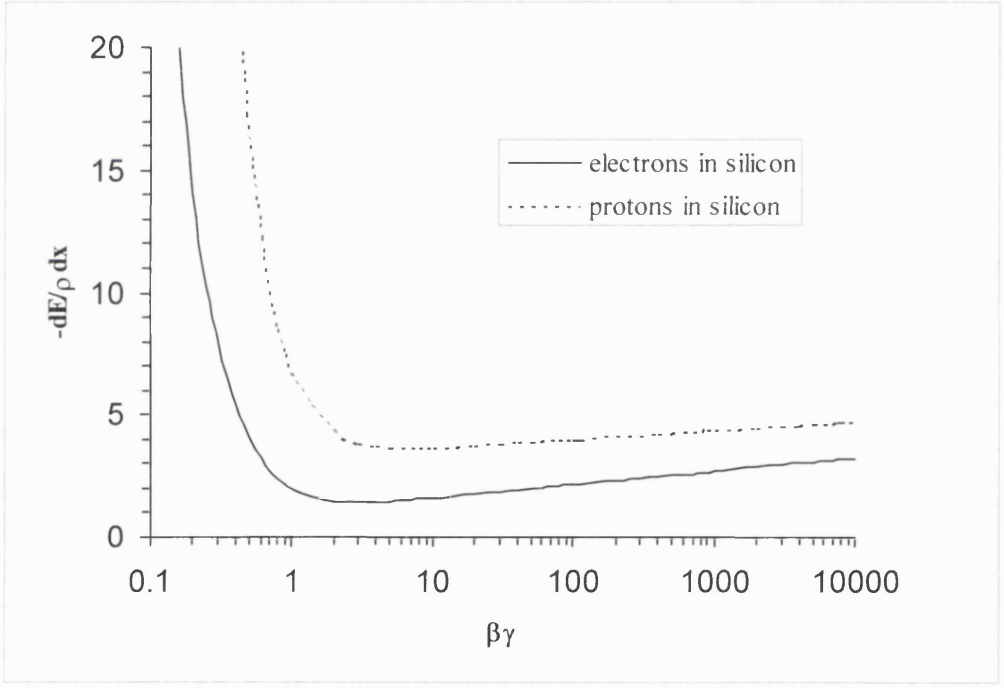

Fig. 4.17: Mass stopping power in silicon (i.e. the stopping power dE/dx divided by the medium density ρ in $MeVcm^2/g$), plotted for both electrons and protons as a function of the product βγ.

Energetic electrons may also be subject to energy loss by production of bremsstrahlung radiation. The total linear stopping power is the sum of the collision and radiation terms:

$$\frac{dE}{dx} = \left(\frac{dE}{dx}\right)_{col} + \left(\frac{dE}{dx}\right)_{rad} \tag{4.12}$$

The ratio of the two terms is often expressed by the following relationship [Attix, 1986]:

$$\frac{(dE/dx)_{rad}}{(deE/dx)_{col}} \cong \frac{EZ}{700} \tag{4.13}$$

The energy loss mechanism by radiation production gains importance with increasing electron energy and atomic number of the medium, as can be seen from relationship (4.13). For electrons such as beta particles (the maximum energy of which is typically in the order of a few MeV) the fraction of energy loss due to bremsstrahlung production is relatively low in a material like silicon. Furthermore, most of the bremmstrahlung photons are very energetic and they are likely to escape the silicon detector without interacting. Therefore, the energy loss by emission of radiation does not contribute significantly to the energy deposition recorded by the passage of beta particles in a silicon detector.

4.6.2 The "Landau peak"

If we assume that the thickness of the material is small so that the stopping power does not change along the path, the mean energy lost by a particle in the absorber will be the rate of loss of energy (given by the Bethe-Bloch approximation) multiplied by the thickness of the absorber. However, large fluctuations of the energy loss will occur with respect to this average value. These are not simply associated with the statistical nature of the collision process, but also with the probability of δ-ray production, which may cause energy losses that are considerably larger than the average value. The ionisation produced by a charged particle results in an energy-loss distribution, which is characteristic of the passage of the particle in a given thickness of a specific medium.

A discussion of the energy loss distributions associated with the passage of charged particles through silicon can be found for example in [Skyrme, 1967], [Hall, 1984].

The first theoretical study of the energy loss fluctuations was performed by Landau. The description of the energy loss straggling was subsequently made more accurate by Vavilov, who introduced a limit to the maximum energy transfer in a single collision (which is assumed to be infinite in the original Landau theory). The Landau-Vavilov distribution is asymmetric and skewed towards high energies. The average value of the distribution is therefore larger than the most probable value, which occurs at the so called 'Landau peak'. If the medium is particularly thick (~ cm) the number of collisions becomes large and by the Central Limit Theorem the distribution approximates a Gaussian function. The average value of energy loss in this case approaches the most probable value.

The pulse height spectrum recorded by a charged particle detector is described in its general features by the Landau-Vavilov distribution. However, some important differences need highlighting. Firstly, the distribution of the energy *lost* by a particle does not necessarily correspond to the distribution of the energy *deposited* by the particle in the absorber. A large number of δ-rays may in fact escape from the sensitive volume of the detector. This is particularly the case for the passage of relativistic particles in thin and relatively light media, such as silicon detectors. Therefore, due to the finite geometry and the finite absorption efficiency of the detector, the distribution of the energy deposited will not exhibit such an extreme tail at high energies as a pure Landau-Vavilov distribution. Moreover, experimental studies have observed that the measured distributions tend to be broader than expected on a theoretical basis. The energy loss spectrum that is measured experimentally is in fact a convolution of a Landau-type curve with a Gaussian distribution. This phenomenon is not simply due to the noise produced by the readout electronics. The discrepancy in the width of the distribution is also caused by electron binding effects, as the Landau-Vavilov theory is based upon free electron scattering [G. Hall, 1984], [Hancock *et al.*, 1983].

Despite these differences, the Landau-Vavilov theoretical distribution still provides us with a suitable qualitative description of a measured distribution. Therefore, even if the 'Landau peak' is strictly the modal value of a pure Landau-Vavilov distribution, this denomination is usually also applied to the pulse height spectrum measured by a charged particle detector. The most probable value of energy deposited by a minimum ionising particle is estimated to be 26 keV in 100 μm of silicon, which scales within 10% from approximately 20 μm to 300 μm [Physics Letters, 1990]. Experimental measurements on relativistic pions are in agreement with this estimate, as they have determined that the most probable value of deposited energy for a *mip* that transverses 300 μm of silicon is 84.0±2.8 keV [Hancock *et al.*, 1983]. Hancock *et al.* have also shown (in the same reference) that the most probable energy deposited by β^- particles is approximately the same as for relativistic pions. Using a ^{106}Ru source, the Landau peak in a 300-μm thick silicon detector was measured at 86.8±2.8 keV (^{106}Ru decays to ^{106}Rh, with β^- maximum emission energy of 39 keV and 3.5 MeV respectively) [Hancock *et al.*, 1983].

During laboratory tests, the passage of *mips* through silicon detectors is frequently simulated using radio-isotopic sources of electrons, so that their 'Landau peak' can be used for energy calibration of the detector [Seller *et al.*, 1988], [Laakso *et al.*, 1993], [O'Neill *et al.*, 1995]. On the basis of the reported results, one obtains an approximate value of 24,000 electrons for the most probable signal given in 300 μm of silicon by a typical β-source. Scaling with thickness, the passage of β-particles through a 500-μm thick detector should produce an energy distribution with a Landau peak at approximately 144 keV (~ 40,000 electrons).

The silicon detectors of the Compton collimator were tested using a ^{90}Sr β-source. The decay scheme for ^{90}Sr is shown in Fig. 4.18. The emission spectrum is a combination of the father and daughter β-decays, with a maximum energy of 546 keV and 2.28 MeV respectively (see Fig. 4.19). In order to confirm the position of the Landau peak, the extrapolated value of 144 keV was checked against simulation

results. A Monte Carlo programme, specifically developed for the study of the conversion of ^{90}Sr β-electrons to *mips* in diamond [Howard, 1998] was applied to the case of silicon. Assuming a silicon detector of 500 μm in thickness, the simulation programme produces a most probable value of deposited energy of (140 ± 1) keV [Howard, 2000]. A simulated Landau distribution from ^{90}Sr betas in 500 μm of silicon is shown in Fig. 4.20.

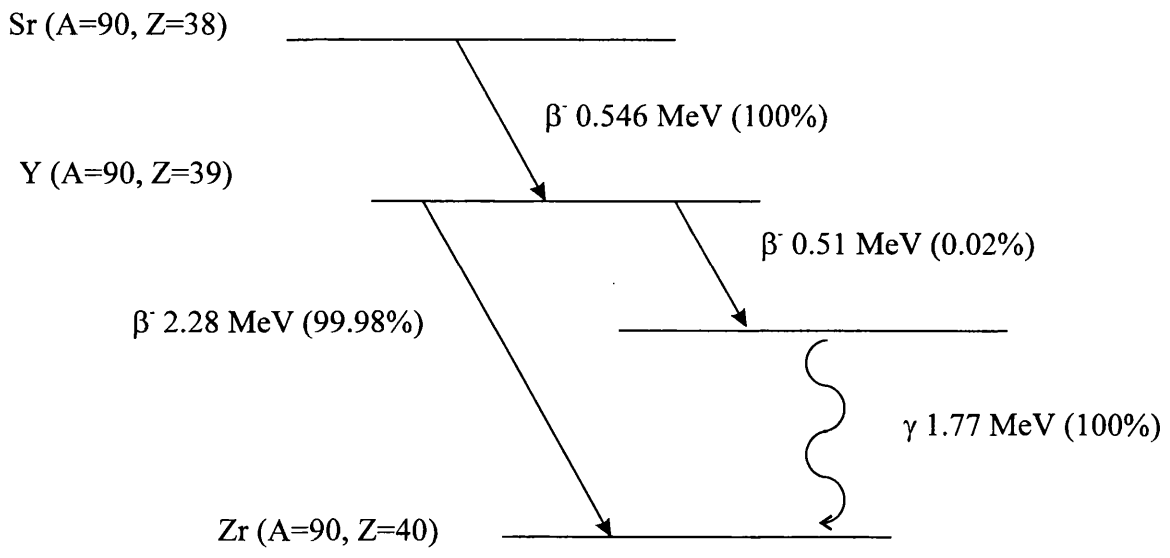

Fig. 4.18: Decay scheme of ^{90}Sr. The half-lives of ^{90}Sr and ^{90}Y are 27.7 y and 64 h respectively.

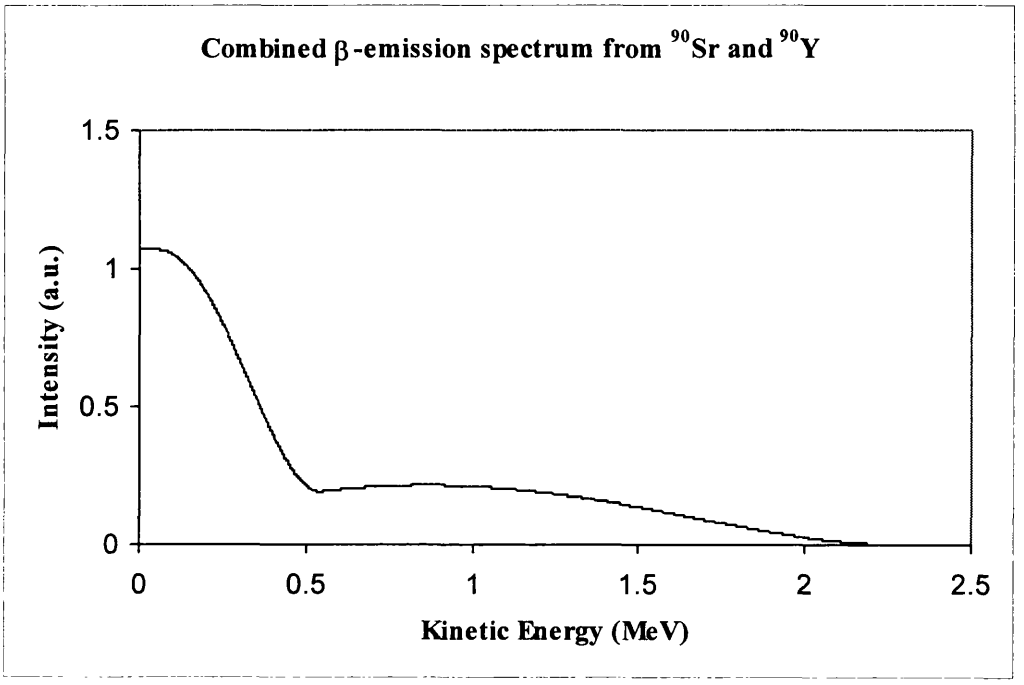

Fig. 4.19: Simulated β- spectrum emitted from the decay of ^{90}Sr into ^{90}Y.

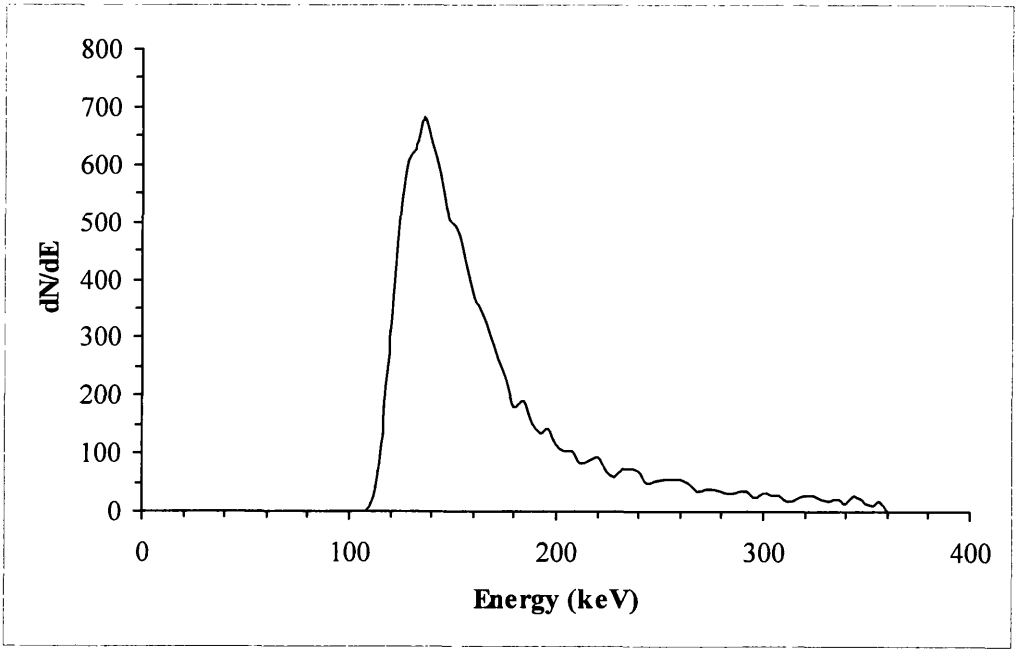

Fig. 4.20: Simulated Landau spectrum for a ^{90}Sr source in a 500-μm thick silicon detector [Howard, 2000].

The conversion from ADC units to keV in silicon may be obtained experimentally by fitting the Landau peak to the β-spectra acquired from a strip (see Fig. 4.22). Assuming that the most probable energy value of the spectrum is located at approximately (140±1) keV, the channel separation between the noise peak and the Landau peak in Fig. 4.21 shows that 1 ADC count corresponds to ~ 1 keV of deposited energy. This simple calibration procedure permits a measurement of the strip noise by converting the width (in ADC channels) of the observed noise peak to an equivalent noise charge (ENC) in keV in silicon.

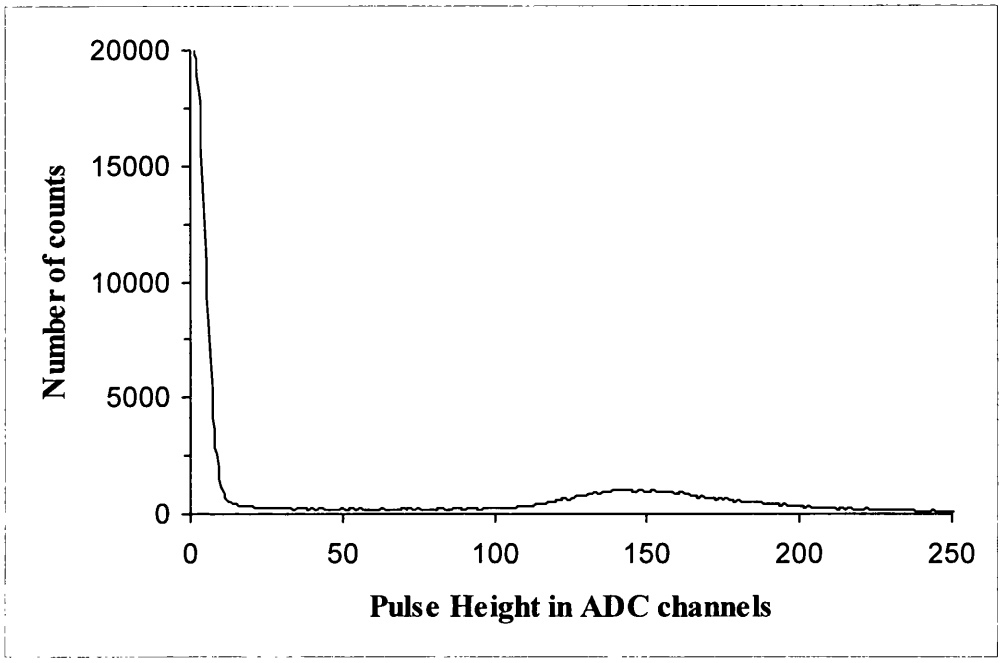

Fig. 4.21: Single strip pulse-height spectrum (experimental data) of β particles emitted from a collimated ^{90}Sr source. This spectrum was measured on the *p*-side for strip n. 67 (APV6 channel 60) of detector B2578-1. Both the noise peak (centred at channel 0) and the 'Landau peak' are visible.

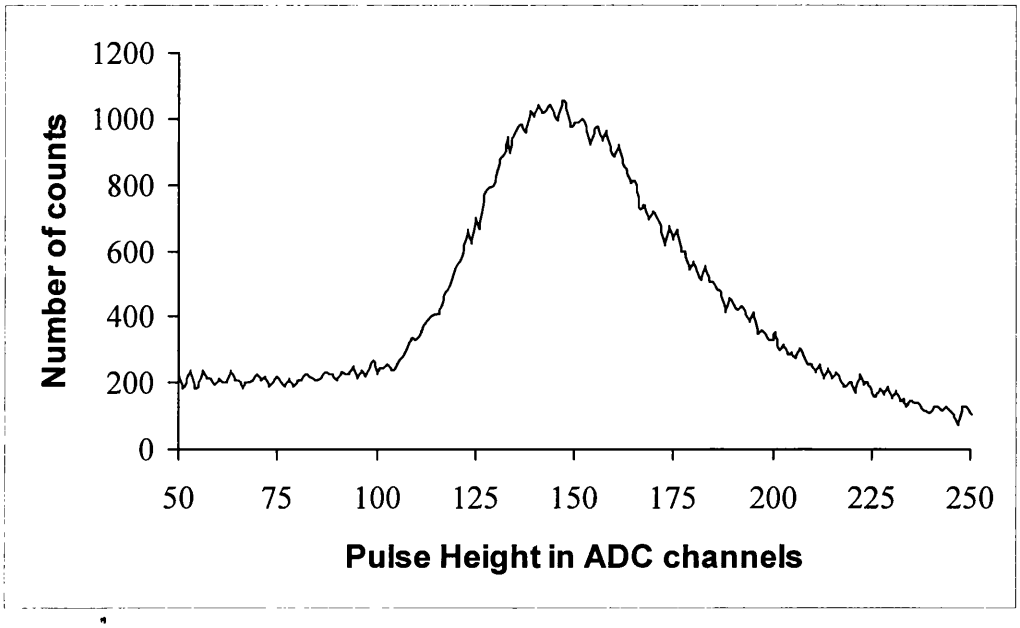

Fig. 4.22: The 'Landau peak' of the spectrum in Fig. 4.21, here plotted on a different scale (the noise peak is not shown in this graph).

4.7 Measurements of strip noise

4.7.1 Experimental results on noise distribution

The noise evaluation tests were carried out by measuring the fluctuations in the channel readout (using random triggers) over 1,000 events when no radiation source was present. The noise was evaluated as the sigma (in ADC counts) of the Gaussian noise peak in each channel, after performing pedestal and common mode subtraction. The experimental results are reported in Fig. 4.23, Fig. 4.24, Fig. 4.25 and Fig. 4.26 for both the *p*-side and the *n*-side of detectors B2578-1 and B2578-3.

An arbitrary definition of "good channels" may be obtained from the distribution of the measured noise across the detector channels. A channel is here considered "good" if its noise is less than or equal to the mean value across all channels plus one standard deviation of the distribution. The channels that were disconnected from the readout electronics were excluded in computing the noise distribution parameters, which are summarised in table 4.6.

Table 4.6: Statistical parameters (in ADC units) of the distributions of the *RMS* noise measured from the bonded channels of detectors B2578-1 and B2578-3 (the distributions are plotted in figures 4.23, 4.24, 4.25 and 4.26).

	Detector B2578-1 *p*-side	**Detector B2578-1 *n*-side**	**Detector B2578-3 *p*-side**	**Detector B2578-3 *n*-side**
Number of bonded channels	120	124	122	125
μ (all bonded channels)	5.76	15.67	6.40	8.33
σ (all bonded channels)	1.07	4.14	1.48	1.69
Number of "good channels" (i.e. for which *RMS noise* $\leq \mu + \sigma$)	110	113	110	117
μ ' ("good channels")	3.88	5.79	4.00	6.50
σ ' ("good channels")	0.05	0.23	0.07	0.07

The noise is here expressed in ADC counts. A typical detector "good channel" is strip n. 67 of detector B2578-1, from which the spectrum of Fig. 4.22 was acquired. This strip is bonded to channel 60 of the APV6 and the sigma of its noise peak is equal to approximately 4 ADC counts. On the basis of the strip calibrationprocedure described in the previous section, the estimated channel noise is 9.4 keV FWHM. This value may be considered as a reference figure representing the noise associated with a "good" central strip on the junction side. Such an experimental result is well in agreement with the theoretical estimate given in section 4.4.3.

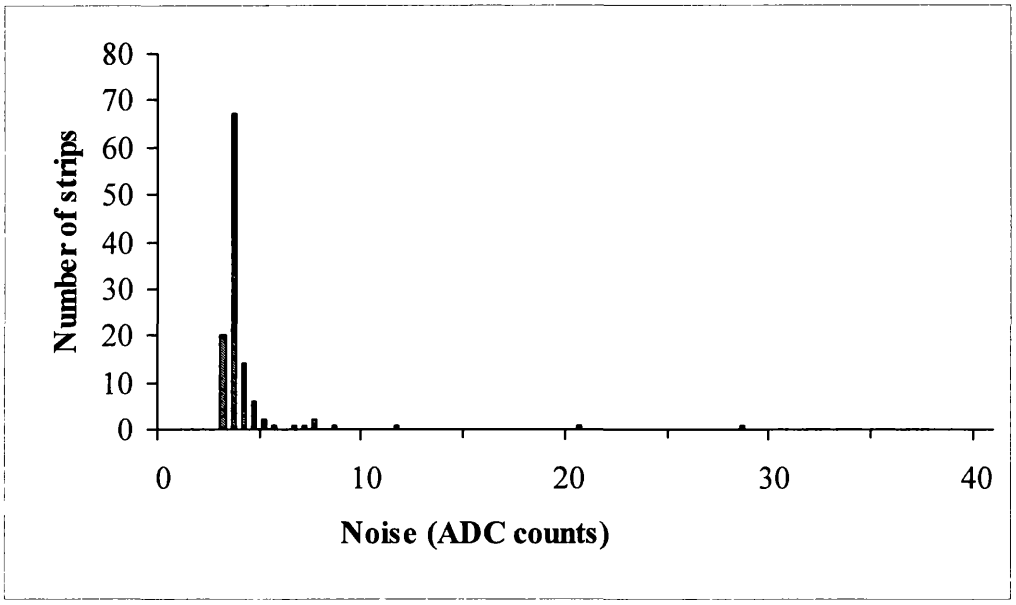

Fig. 4.23: Noise distribution for detector B2578-1, *p*-side. The noise is evaluated for each strip as the sigma (in ADC counts) of the noise peak acquired for 1,000 events.

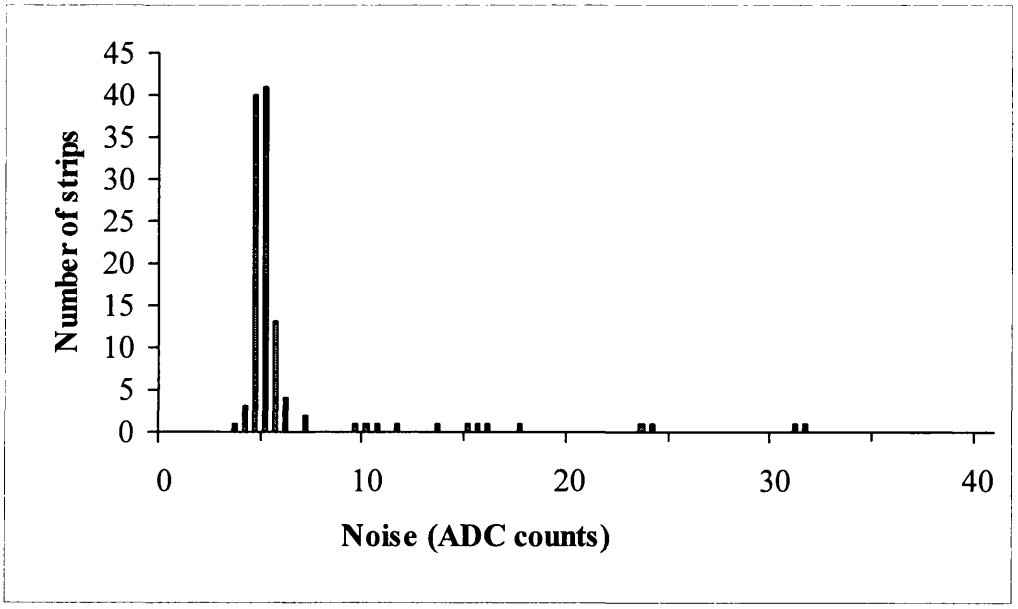

Fig. 4.24: Noise distribution for detector B2578-1, *n*-side. The noise is evaluated for each strip as the sigma (in ADC counts) of the noise peak acquired for 1,000 events.

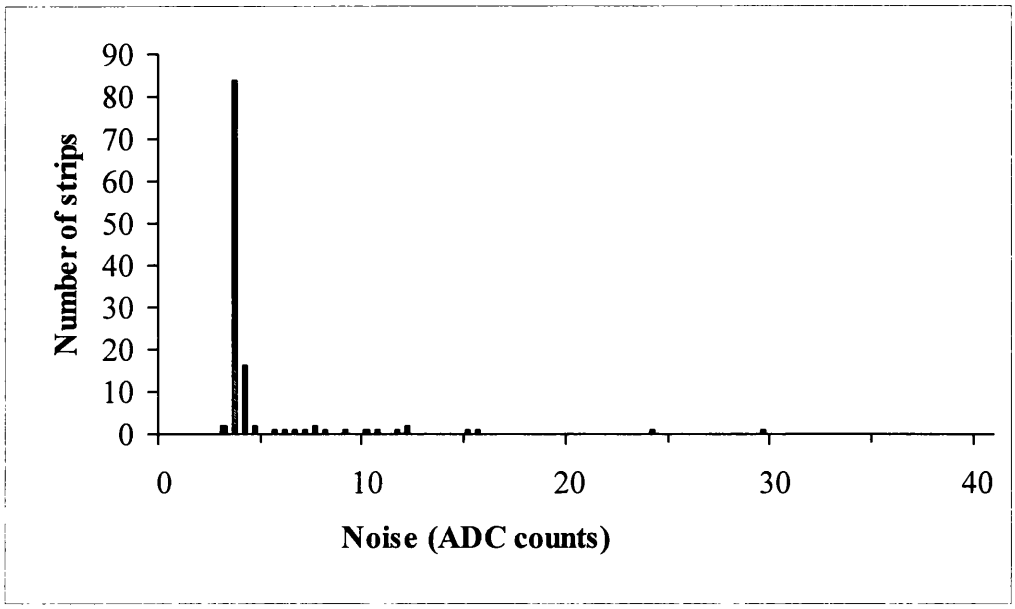

Fig. 4.25: Noise distribution for detector B2578-3, *p*-side. The noise is evaluated for each strip as the sigma (in ADC counts) of the noise peak acquired for 1,000 events.

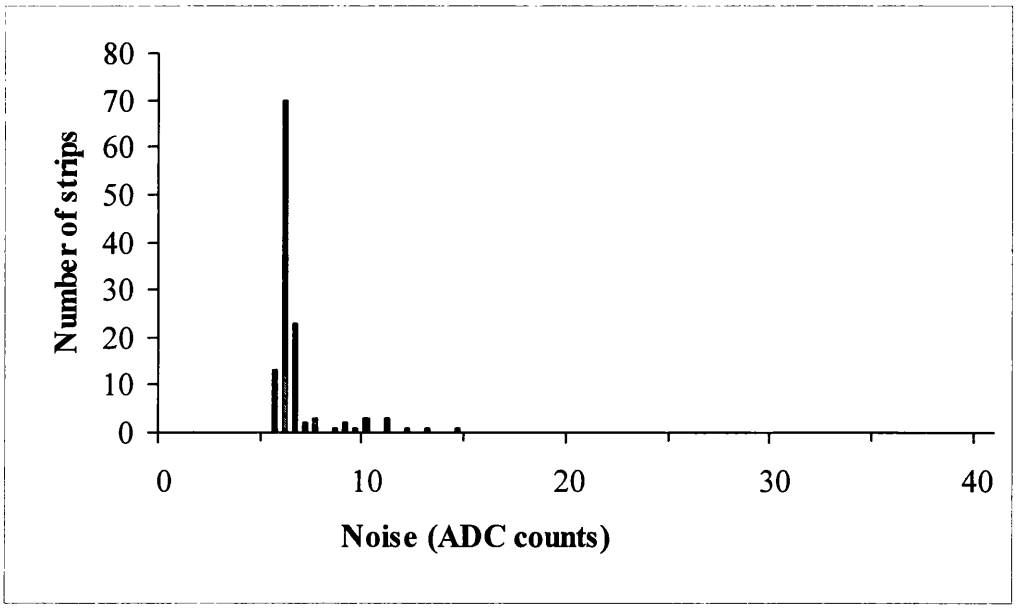

Fig. 4.26: Noise distribution for detector B2578-3, *n*-side. The noise is evaluated for each strip as the sigma (in ADC counts) of the noise peak acquired for 1,000 events.

The experimental results show that the "good channels" on a single side of the detector are between 90% and 94% of the available channels. The experimental spectra acquired from a "good channel" and from a channel of lower spectrometric quality are shown respectively in Fig. 4.27 *A)* and *B)*. Some relevant physical and electronic parameters were investigated, in order to obtain lower noise from all channels and especially in order to identify the origin of the high noise observed in some of the channels. The results of such experimental tests are presented in the following two sections.

A)

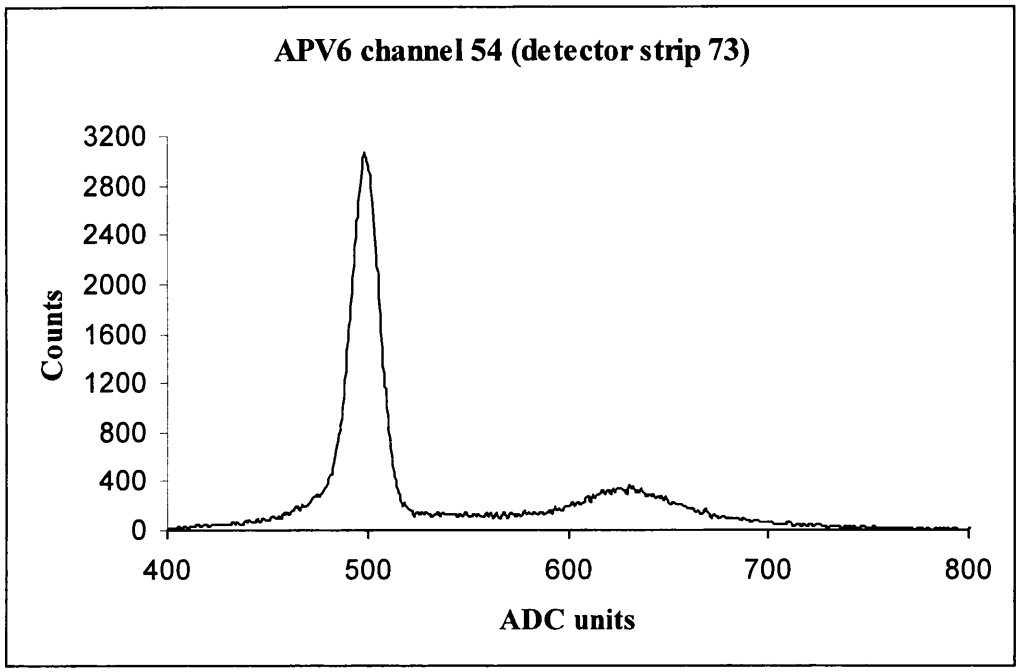

B)

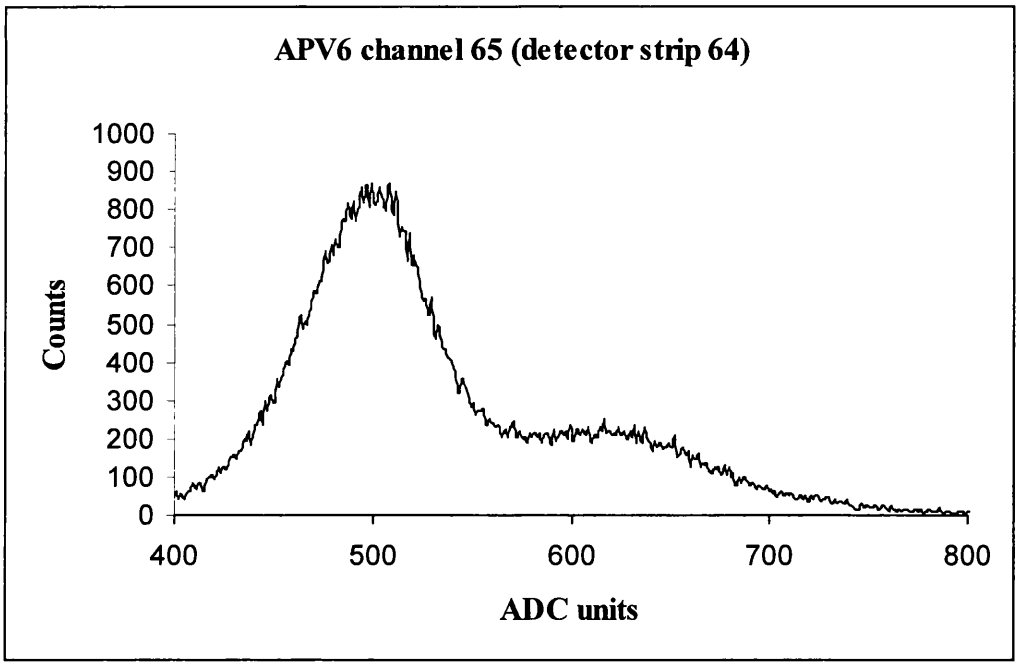

Fig. 4.27: Examples of ^{90}Sr β-spectra acquired from detector channels with different spectrometric performance (Detector B2578-1, n-side). ***A)*** The RMS noise measured in for channel 54 (i.e. detector strip n. 73) is 5.6 ADC counts. ***B)*** The noise measured for channel 65 (i.e. detector strip n. 64) is 13.8 ADC counts. One ADC count corresponds to ~ 1 keV. The noise peak is arbitrarily centred at ADC channel 500 in both graphs.

4.7.2 Effects of room temperature variation

One of the parameters that affect the noise performance in a detector is the temperature at which the device is operated. All of the experiments reported in this chapter were performed at room temperature. The effects of room temperature variation on the noise level were evaluated by comparing experimental spectra that were acquired at 19°C and 29°C, which represent the two extremes of the room temperature.

The temperature was regularly monitored during these experiments and it maintained a constant value (± 0.1°C) throughout acquisition. Fig. 4.28 shows the two noise peaks obtained from strip n. 67 of detector B2578-1 (*p*-side) at 19°C and 29° respectively. By fitting the noise peak with a Gaussian curve, it was estimated that its FWHM is approximately 8.5 keV at 19°C and 10 keV at 29°C. These results showed that a temperature increase of 10°C had increased the FWHM noise by 18%.

Such increase of the noise with temperature results from the contribution of a number of factors. From equations (4.7) and (4.8) one can see the obvious increase of the thermal noise in the resistors with temperature. The noise component associated with the bare chip is also enhanced by a temperature increase, as the coefficients k_1 and k_2 in equation (4.5) are increasing functions of temperature [Nicholson, 1982]. Finally, equation (4.9) has also an implicit dependence on temperature, as the leakage current is a function of the detector operational temperature according to the relationship:

$$I \propto T^2 e^{-\frac{E_{G0}}{2kT}} e^{-\frac{\Delta E_t}{kT}} \tag{4.14}$$

where E_{G0} is the silicon energy band gap at T = 0 K (E_{G0} = 1.12 eV) and $\Delta E_t \sim 0.04$ eV is an experimentally fitted parameter that represents the typical distance of the trap energy levels from the middle of the band gap [Walton, 1984], [Ohsugi *et al.*, 1988], [Barberis *et al.*, 1993].

From equation (4.14) it follows that given a ten centigrade increase in temperature, the leakage current value is approximately doubled. At room temperature the *ENC* contribution given by the leakage current (see equation 4.9 and table 4.5) is approximately σ_I = 788 electrons, which in silicon correspond to 6.7 keV FWHM. By cooling the detector down to 0°C, the *RMS* noise contribution given by the leakage current would be reduced to approximately 226 electrons (i.e. 1.9 keV FWHM).

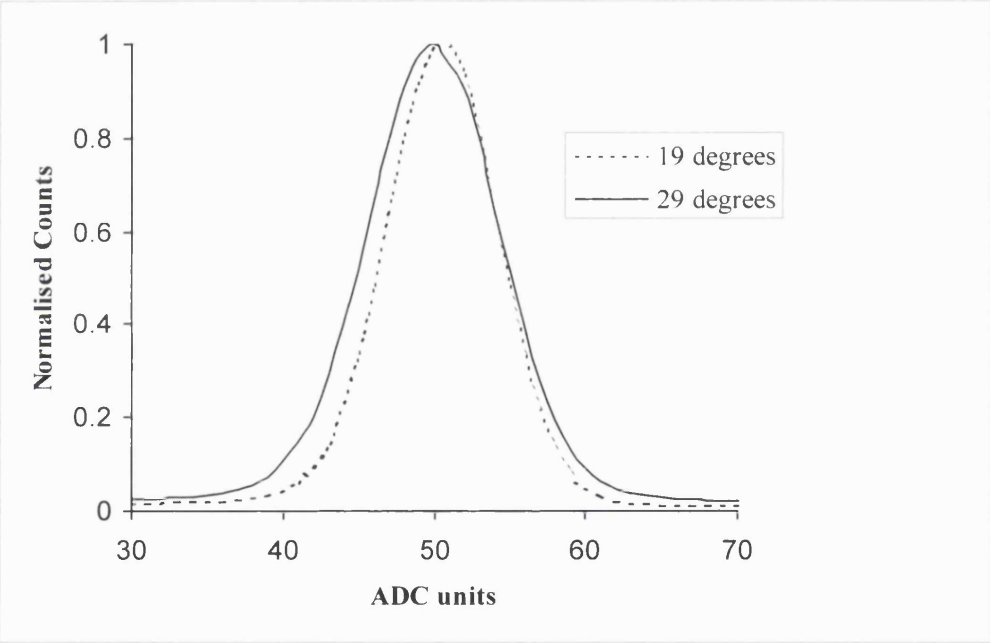

Fig. 4.28: Noise peak measured on channel 60 of the APV6 (detector strip n. 67), on the *p*-side of detector B2578-1 (bias = 70 V).

4.7.3 Effects of time constant variation

Another parameter that affects the noise level in the detector is the choice of the time constants of the shaping amplifier. All the experimental data presented in the previous sections were obtained with a relatively short rise time τ_1 (~ 150 ns) and a very long fall time τ_2 (~ 9 μs). As explained in section 4.2.3, these values of τ_1 and τ_2 were initially chosen because of the need for achieving low-noise performance of the APV6 whilst at the same time obtaining a long-lasting, flat-top pulse shape, suitable

for triggering in the Compton camera. These settings however do not optimise the noise performance of the chip-detector system. Equations (4.4), (4.7), (4.8) and (4.9) are all independent functions of the time constants τ_1 and τ_2. By combining them all together, one can express the equivalent noise charge of the system amplifier-detector as a function of the ratio $\lambda = \tau_2/\tau_1$ [Nicholson, 1982] (see Appendix I):

$$(ENC)^2 = \frac{A}{\frac{2\lambda}{\lambda^{1-\lambda}}\,2\lambda(\lambda+1)\tau_1} C_{in}^2 + \frac{B\tau_1}{\frac{2\lambda}{\lambda^{1-\lambda}}\,2(\lambda+1)} + \frac{C\ln\lambda}{\frac{2\lambda}{\lambda^{1-\lambda}}\,(\lambda^2-1)} C_{in}^2 \left[Coulombs^2\right] \qquad (4.15)$$

with:

$$A = k_1 + 2kTR_{met} \qquad (4.15\ a)$$

$$B = k_2 + \frac{2KT}{R_{Bias}} + eI \qquad (4.15\ b)$$

$$C = k_3 \qquad (4.15\ c)$$

The first term ("A term") in equation (4.15) is the series thermal noise arising from the channel in the amplifier FET and from the resistance of the metal readout strip in the detector. The second term ("B term") is the parallel noise arising from the gate resistor (thermal and shot noise in the gate resistance) and from the detector (thermal noise in the bias resistor and shot noise due to the leakage current). The third term is the Flicker noise of the FET in the amplifier. Fig. 4.29 shows a plot on an arbitrary scale of the contributions given by these three noise terms to the $(ENC)^2$ in equation (4.15), as a function of λ.

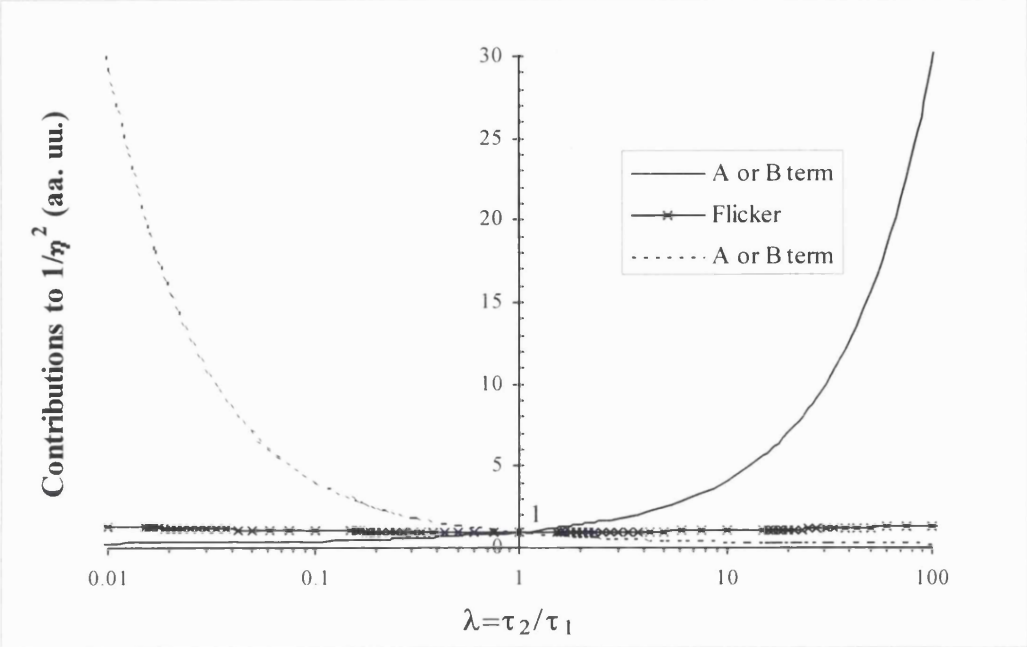

Fig. 4.29: Contributions of the different noise terms to the overall value of $1/\eta^2$ in an amplifier-detector system as a function of the ratio $\lambda = \tau_2/\tau_1$, as obtained from equation (4.15) [Nicholson, 1982]. It is assumed that the charge Q produced in the radiation detector is equal to 1 Coulomb, so that $1/\eta^2 = (ENC)^2$ (see equation (4.2) in section 4.4.1). It is also assumed that $A = B = C = 1$ in (4.15). The plotted curves are normalised to their minimum value (obtained for $\lambda = 1$). The product $\tau_1\tau_2$ is maintained constant in varying the value of λ. Mirror curves are obtained for the A and B terms, depending whether $(ENC)^2$ in equation (4.15) is expressed as an explicit function of τ_1 or τ_2.

If we assume a unitary produced charge (i.e. $Q = 1$ C in equation (4.2) of section 4.4.1), the square equivalent noise charge is also the square inverse of the signal-to-noise ratio ($1/\eta^2$). The curves in Fig. 4.29 are obtained by plotting the three terms individually, assuming the same weight for each term ($A = B = C = 1$). If the product $\tau_1\tau_2$ is kept constant while varying τ_1, the continuous line represents the A term and the dotted line represents the B term (the curves are swapped if we replace τ_1 in equation (4.15) with τ_2/λ and we express the relationship as a function of τ_2). From

these plots it can be clearly seen that amplifier, detector and Flicker noise give their minimum contribution to the overall noise when the time constants are made equal, i.e. $\lambda = 1$.

The value of the ratio of the time constants chosen for the APV6 in order to conveniently shape the pulse is $\lambda = 60$, which is not an optimum in terms of the overall noise achieved. Some simple tests were carried out, where the register values chosen as default for the APV6 were modified in order to obtain different values of the ratio λ. This was done in order to observe how varying the ratio of the time constants would affect the measured noise across all detector channels. The tests were performed on the *p*-side of detector B2578-3 by making use of three different pulse shapes (see Fig. 4.30, Fig. 4.31 and Fig. 4.32) with λ respectively equal to 60, 15 and 5. The corresponding values of the measured noise (in ADC counts) are plotted as a function of the APV6 channel number in Fig. 4.33, Fig. 4.34 and Fig. 4.35.

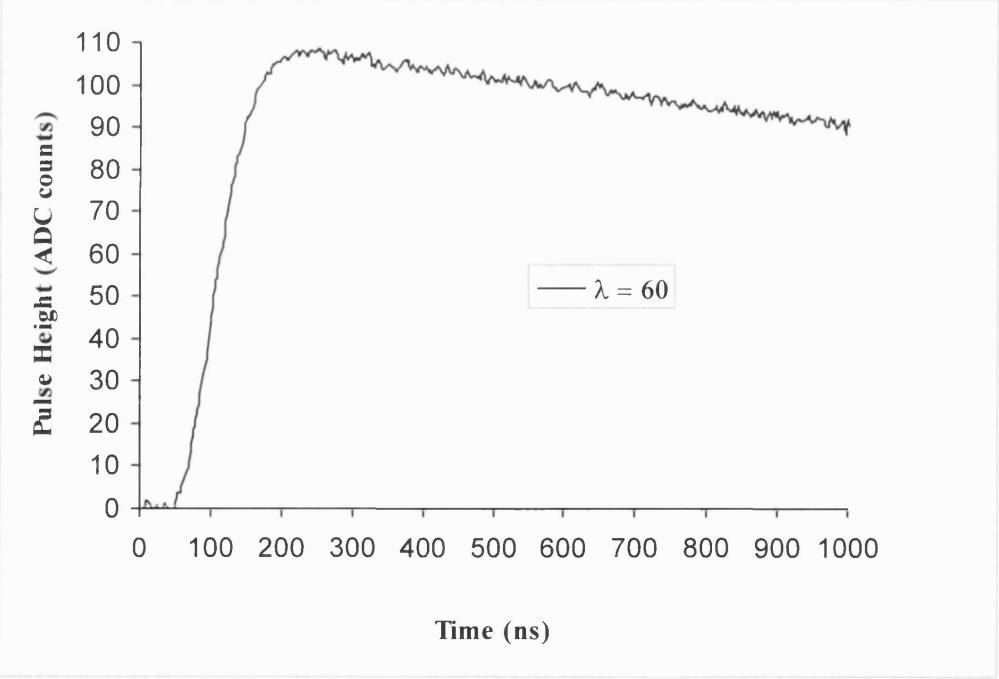

Fig. 4.30: Pulse shape that was initially selected for the Compton camera application ($\lambda = 60$). The approximate values of the time constants of the pulse are $\tau_1 = 150$ ns and $\tau_2 = 9\mu s$.

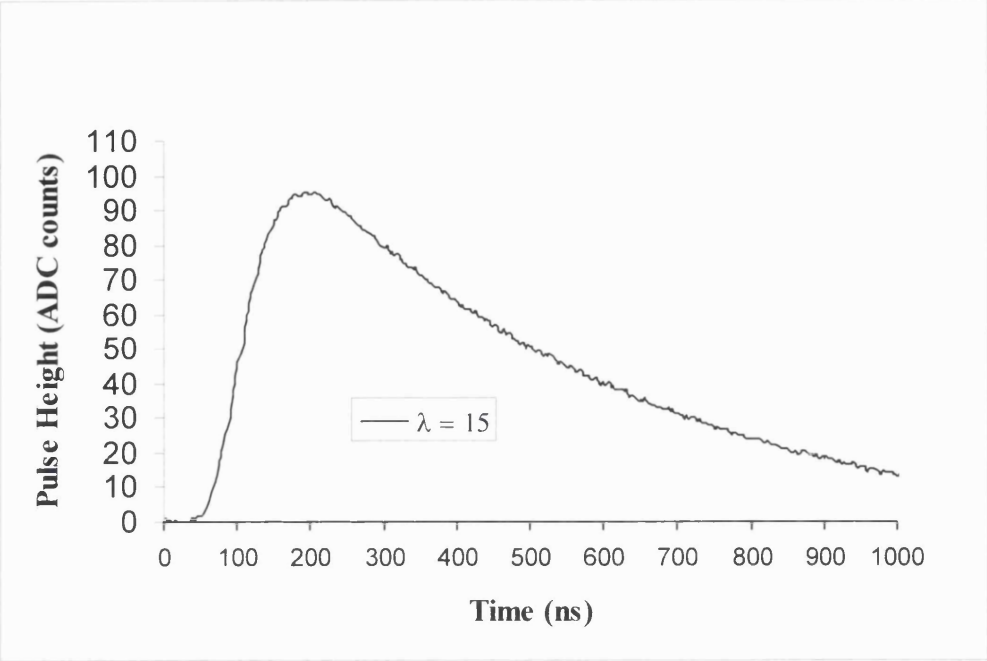

Fig. 4.31: Modified pulse shape (λ = 15). The approximate values of the time constants of the pulse are τ_1 = 100 ns and τ_2 = 1.5μs.

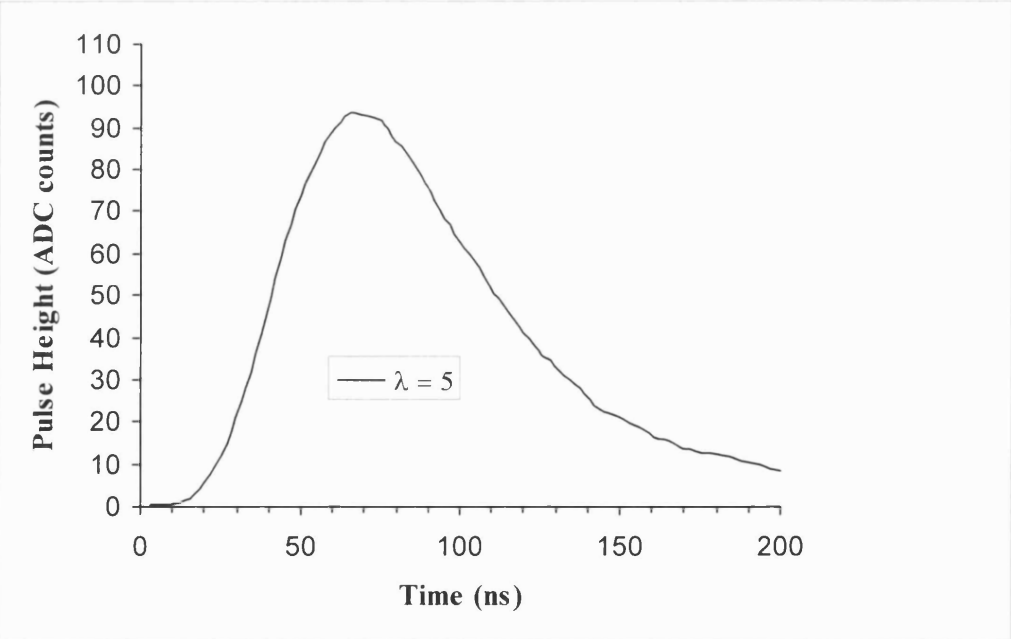

Fig. 4.32: Modified pulse shape (λ = 5). The approximate values of the time constants of the pulse are τ_1 = 50 ns and τ_2 = 250 ns.

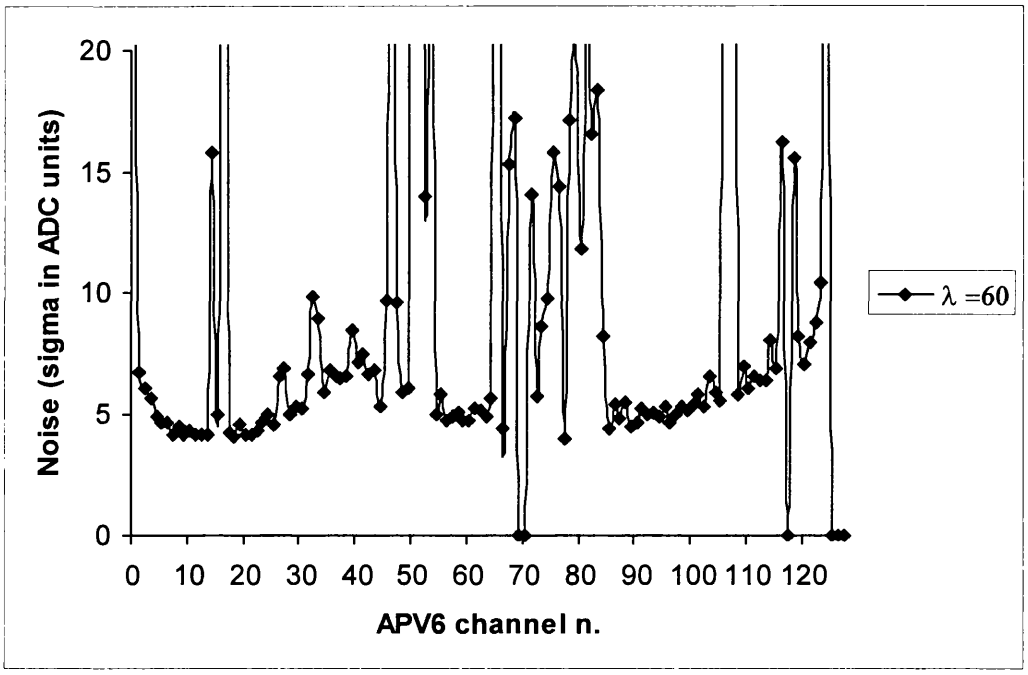

Fig. 4.33: Plot of the noise on the *p*-side of detector B2578-3 (sigma in ADC counts for 1000 events) as a function of the APV6 channel number. The pulse is shaped with time constants τ_1 = 150 ns and τ_2 = 9μs. The channels that are not connected to the detector are excluded.

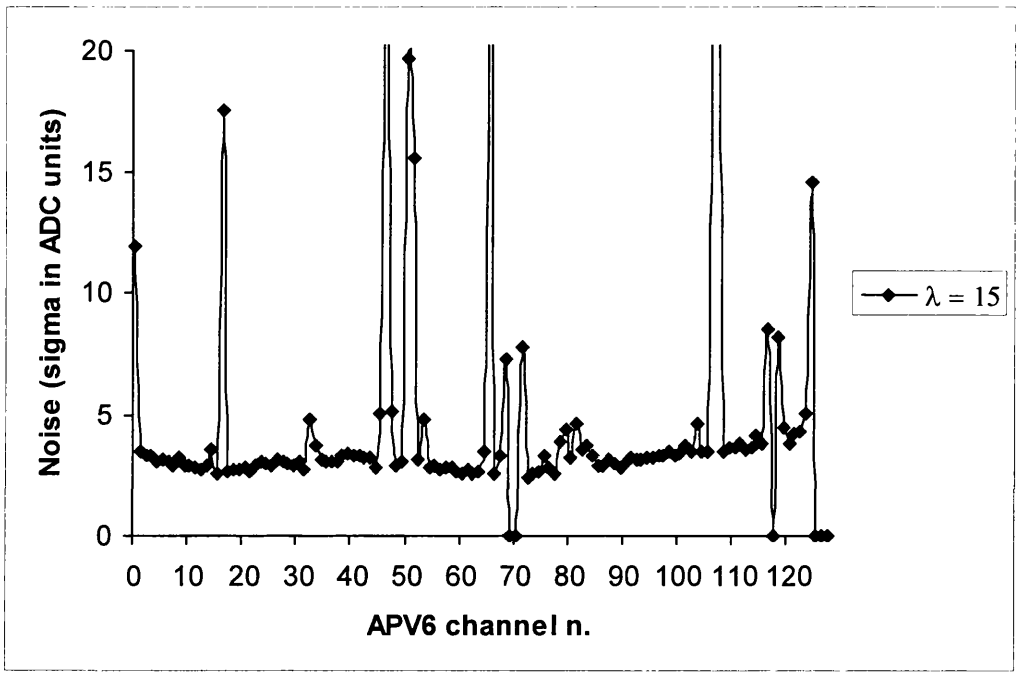

Fig. 4.34: Plot of the noise on the *p*-side of detector B2578-3 (sigma in ADC counts for 1000 events) as a function of the APV6 channel number. The pulse is shaped with time constants τ_1 = 100 ns and τ_2 = 1.5 μs. The channels that are not connected to the detector are excluded.

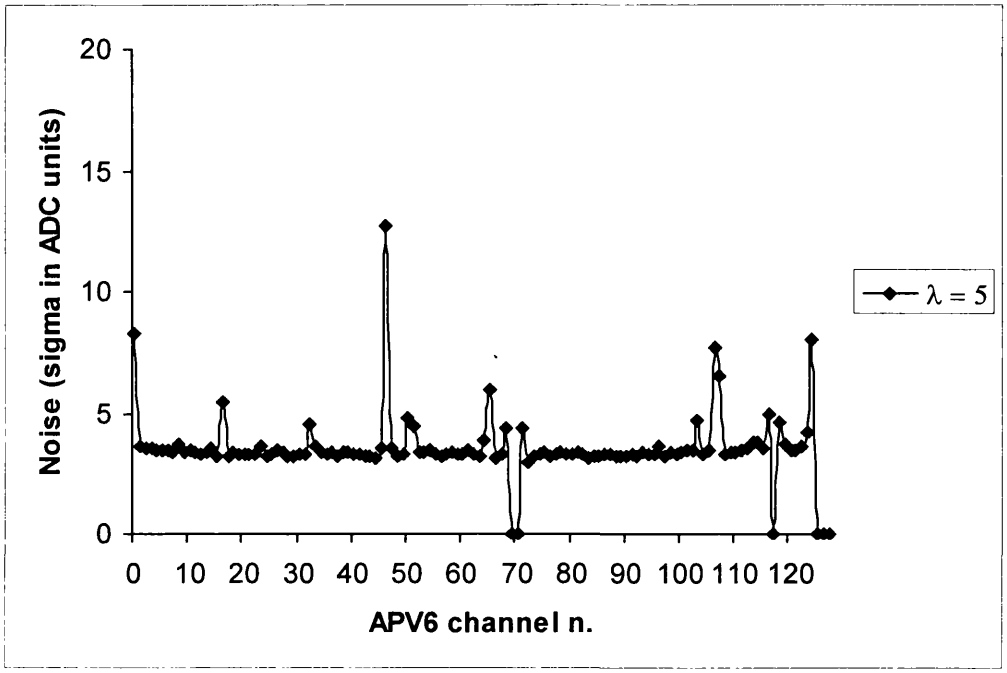

Fig. 4.35: Plot of the noise on the *p*-side of detector B2578-3 (sigma in ADC counts for 1000 events) as a function of the APV6 channel number. The pulse is shaped with time constants τ_1 = 50 ns and τ_2 = 250 ns. The channels that are not connected to the detector are excluded.

These tests showed that the number of channels with very high noise is significantly reduced if the ratio λ that characterises the pulse shape is made smaller. This can be easily seen from Fig. 4.33, 4.34 and 4.35. Although a direct comparison of the noise magnitude is not possible as the settings for the three pulse shapes do not provide exactly the same gain, one may still give an indicative estimate of this effect. The mean value of the noise μ' for the "good channels" in each set of data may be calculated as a local reference value, according to the definition given in section 4.7.1. A channel is then classified as "highly noisy" if its noise is greater than twice this reference value. Following this definition, the estimated percentage of channels with high noise is 20% for $\lambda = 60$, 11% for $\lambda = 15$ and it decreases to 3% for $\lambda = 5$.

The bare APV6 chips had been tested prior to detector bonding and no anomalies were found in the noise level across all channels (except for channel 0, the high noise of which is due to a chip fault). The source of the particularly high noise observed in

some of the readout channels should therefore be associated with the detector contribution. In order to try and identify the source of noise in these specific channels, equations (4.7), (4.8) and (4.9) were again employed. They allowed the detector contribution to the noise to be calculated for the separate components and for the three different λ values. The results are reported in table 4.7.

Table 4.7: Noise contributions computed for different pulse shapes.

τ_1	τ_2	$\lambda = \tau_2/\tau_1$	σ_{Rmet} (e^-)	σ_{Rbias} (e^-)	σ_I (e^-)	**Detector contribution to the noise** (σ in e^-) $\sqrt{\sigma_{Rmet}^2+\sigma_{Rbias}^2+\sigma_I^2}$	**Detector contribution to the FWHM noise** (keV in Si)
150 ns	9 µs	60	85	128	788	803	6.8
100 ns	1.5 µs	15	114	58	355	378	3.2
50 ns	250 ns	5	188	27	168	254	2.1

These estimates show that the physical parameters of the detector are such that for the chosen default values of the time constants (λ = 60) the dominant component in the detector noise is associated with the leakage current. As the value of λ is made smaller by modifying the values of both τ_1 and τ_2, the parallel noise (σ_{Rbias} combined with σ_I) is decreased whilst the series noise (σ_{Rmet}) is increased. The overall effect is, as expected, a reduction of the detector total contribution to the noise.

This simple analysis shows that the high noise observed in some of the channels is due to the parallel component. The dramatic reduction of the noise level observed in these channels when reducing the time constant ratio suggests that the most likely cause of localised high noise is the strip leakage current, which is the largest contribution to the parallel noise. In previous calculations, we estimated the leakage current of a single strip as the total current measured in the detector bulk, averaged over the number of strips. This is of course an approximation, as the leakage current is not perfectly uniform across all strips. Its value may in fact be considerably higher for specific strip positions, due to the presence of preferential paths caused by small defects or surface contamination.

Chapter 5

Development of a Laboratory Compton Camera prototype

In this chapter, a laboratory set-up configuration is proposed so as to operate the silicon microstrip detectors in a Compton camera prototype. The chapter includes the experimental work on the Compton camera prototype under construction at UCL. The control signals for the APV6 chip, which was employed for detector readout, are described. The use of this chip in the Compton camera application required the development of a special-purpose interface unit, which was designed for this project at the Institute of Nuclear Medicine, Middlesex Hospital [Cullum, 2000]. The development and testing of such electronics at UCL are described in this chapter, along with an overview of the data acquisition system. The computer model of Compton camera is applied in order to estimate the angular resolution of the system for various levels of strip noise in the silicon detectors. Predictions of the imaging performance of the scatter collimator are made, assuming both the case of a point source in air and of a point source imbedded in tissue-like phantoms of different size.

5.1 A proposed laboratory prototype of Compton camera

5.1.1 An externally triggered configuration based on double Compton scatter

The design of the initial camera prototype was aimed to test the scatter detectors in Compton mode. In order to read out the detector signals, the latest version of the APV chip series (APV6) [Raymond *et al.*, 1997] was made available for this project (see Chapter 4, section 4.2). The APV6 chip was originally developed at Imperial College and the Rutherford Appleton Laboratory for the Compact Muon Solenoid (CMS) tracker experiments at the CERN Large Hadron Collider (LHC). The properties of high reliability and low-noise, along with the number of readout

channels matching the number of strips on each side of the selected detector (128), made the APV6 an attractive option for this application, in combination with the willingness of the High Energy Physics Group at Imperial College to collaborate in the project.

The APV6 chip requires an external trigger for data readout. In HEP applications, the timing of the particle interactions in the detector is known and is given by the frequency of beam collisions in the accelerators. By contrast, in γ-ray imaging the photon emissions and interactions in the detector occur at random times. The camera prototype had therefore to be designed around the requirement for an external trigger of the readout electronics. As a consequence, the system configuration was devised so as to allow the detection of three separate events. The operation of the proposed camera is based on a double Compton interaction occurring in any two elements of a stack of silicon strip detectors. An additional detector is placed behind the stack, so as to absorb the double scattered photon and provide a trigger for the readout of the hit position and energy information in the silicon detectors. A High-Purity Germanium (HPGe) planar detector with a diameter of 32 mm and a thickness of 10 mm will initially act as the triggering component. This configuration, which is illustrated in Fig. 5.1, relies on the principle of multiple Compton imaging (for the simple case of double scatter) that has been proposed by various authors (see section 1.4.4 *IV*).

Although the camera design provides for four silicon layers, the set-up will be initially operated with two scatter elements. During experimental operation an energy window will be set on the basis of Compton kinematics, in order to send the trigger signal only after a potential double scatter interaction. Such a window should be defined by the camera geometry and by the source primary energy, which determine the possible energy values of those photons that Compton scatter in two silicon layers. The energy selection for the trigger events is best performed with a high-resolution detector. HPGe detectors are excellent γ–ray spectrometers, with an energy resolution of less than 600 eV FWHM for 122 keV γ-rays. The signals of the three

detectors will also be added together in order to ensure that the total energy deposition matches the source energy. The analogue data will then be sent as input to a DAQ board connected to a computer for data analysis and storage.

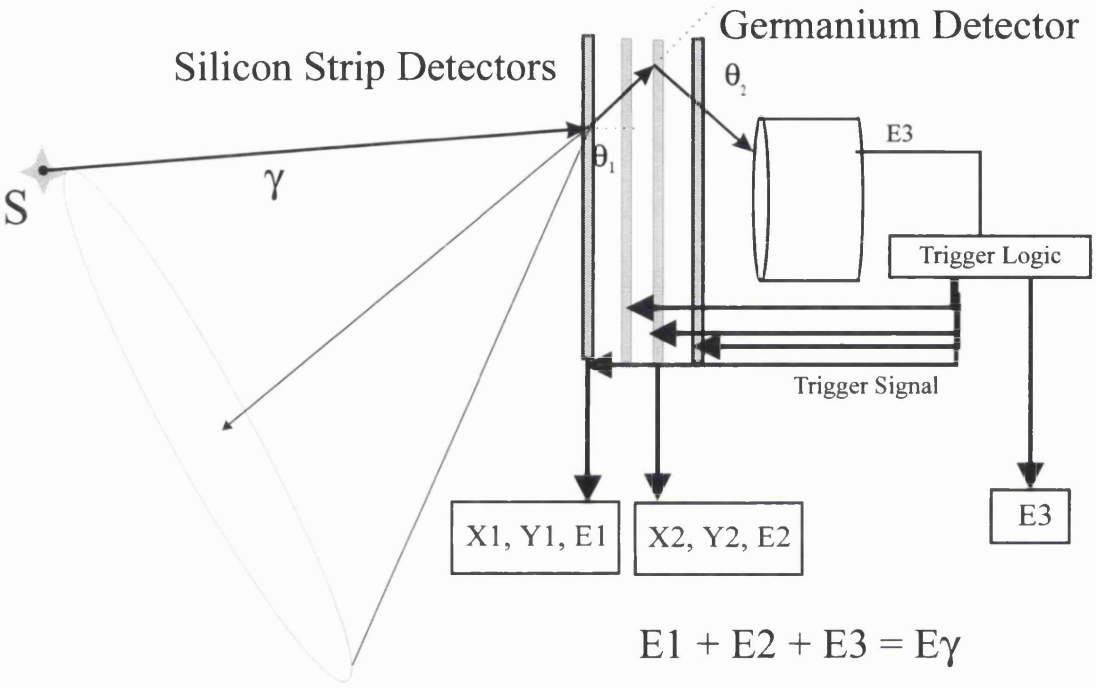

Fig. 5.1: Configuration of the proposed camera. The scattered photon is single Compton scattered in each one of the silicon detectors and is then intercepted by the HPGe trigger detector.

5.1.2 Assembly of scatter collimator

Once a board comprising one silicon strip detector and two APV6s had been assembled and fully tested at Imperial College (see sections 4.3, 4.5, 4.6 and 4.7 of the previous chapter), it was then mounted at UCL on a PCB plane. This was hosted in a metal rack that can accommodate in sequence up to four planes on separate rails. The PCB planes were designed so that different detectors could be located simply on axis, one behind the other, as well as off axis, in order to allow the selection of a preferential range of scatter angles. A photo of a detector plane is shown in Fig. 5.2, where one can also see the two readout cards that plug into each of the two APV6s on

the opposite sides of the detector. Each PCB plane (31.5 cm x 23 cm in size) was sealed on both sides with a removable cover made of a 0.5-mm-thick carbon fibre sheet, in order to ensure light tightness, as shown in Fig. 5.3. The thickness of the sheet was suitably chosen so that it would allow transmission of beta particles from a ^{90}Sr source; these particles are often used for tests on strip detectors, as was discussed in Chapter 4. An image of the mount rack is shown in Fig. 5.4. The rack, which is made of aluminium, was built as a 26.5-cm high, 36-cm wide and 8-cm deep unit, thus making the collimator light and compact.

Simulation work indicated that in a two-element camera increasing the separation distance from 1 cm to 10 cm diminishes the system efficiency by approximately a factor of 20. However, as was observed in section 2.3.1 of Chapter 2, higher spatial resolution can be achieved by increasing the separation between the camera elements. In order to maximise the collimator compactness and efficiency, the distance between two silicon detectors in adjacent rails was kept to the minimum value (approximately 1 cm) allowed by the supporting structures. As it is reported in the next section, the prediction of the computer model was that, due to the good spatial and energy resolutions of these strip detectors, a separation of 1 cm was sufficient to provide an acceptable spatial resolution in the image.

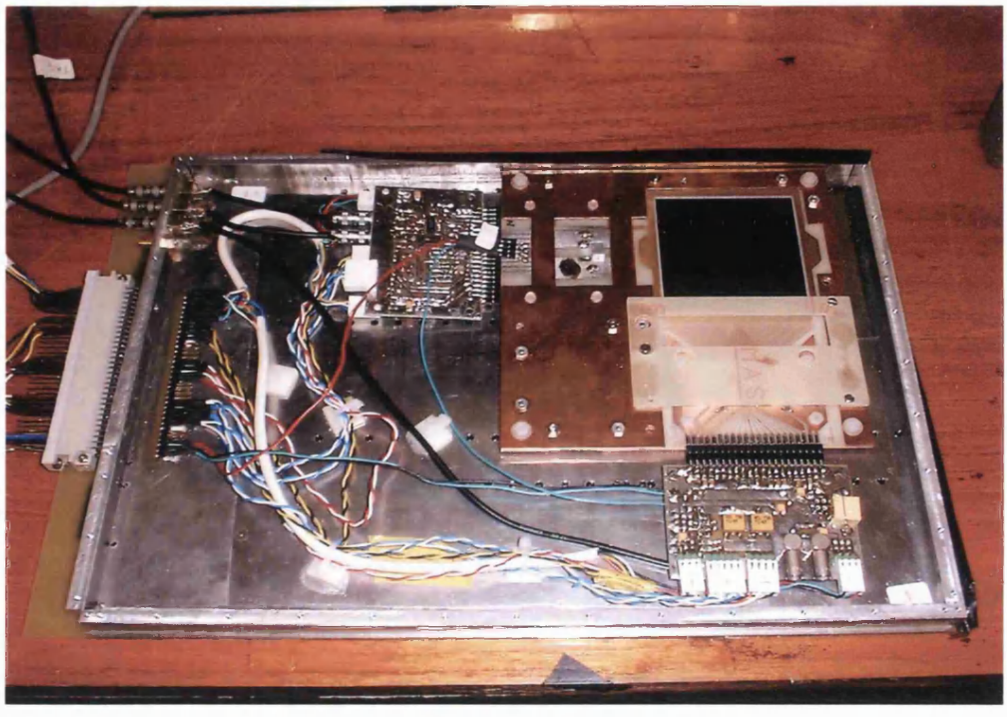

Fig. 5.2: Photograph of a detector plane (the carbon fibre cover was here removed).

Fig. 5.3: Photograph of a detector plane with its carbon fibre cover.

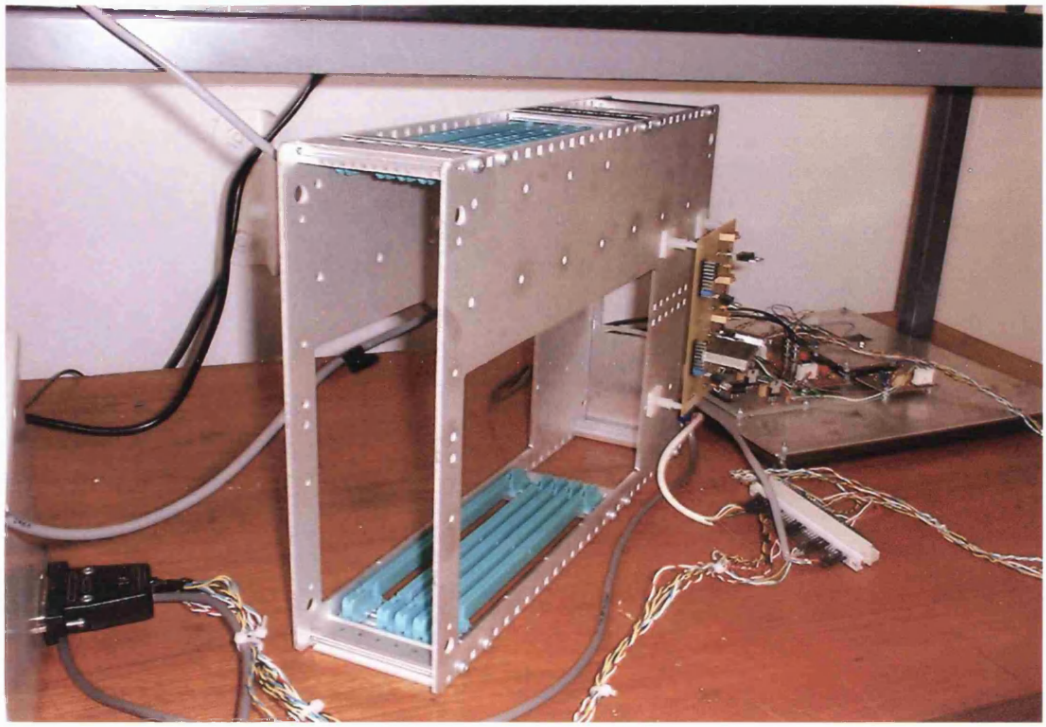

Fig. 5.4: The detector mount rack. In the background, to the right of the rack, is the APV6 stand-alone set-up employed for preliminary testing (see section 5.4).

5.2 Control sequences for the APV6 readout chip

The APV6 operation mode (i.e. *peak* or *deconvolution* mode, see section 4.2.1) and other configuration parameters (bias settings for pulse shaping, amplification, latency value, etc.) can be programmed via a two-wire serial bus that conforms to the Phillips I^2C standard. It is possible to address up to 15 APV6s on the same bus, with the binary address 1111 being reserved for global addressing of all APVs. On the APV6s bonded to the strip detectors, the addresses are set by logic voltages and are 'hard-wired' on the board housing the chip.

In addition to the I^2C slow-control signals and 40-MHz clock, the operation of each chip also requires a separate trigger line for sending the fast-control signals in

order to trigger, reset and 'calibrate' the chip. The *trigger* signal is in the form of a single pulse ('1') lasting the duration of a clock cycle (i.e. 25 ns). The *reset* signal, which re-initialise the pipeline and clears possible error states, consists of two 25-ns pulses separated by one clock cycle ('101'). Finally, the *calibration* signal is a sequence of two consecutive 25-ns pulses ('11'); this signal sends a request for on-chip generation of test pulses. This feature allows the measurement of the pulse shape in all the APV channels. All the described sequences (trigger, reset and calibrate) must be synchronised to the 40MHz clock, which controls data storage to the pipeline. A schematic of the APV6 chip and its required control signals are shown in Fig. 5.5.

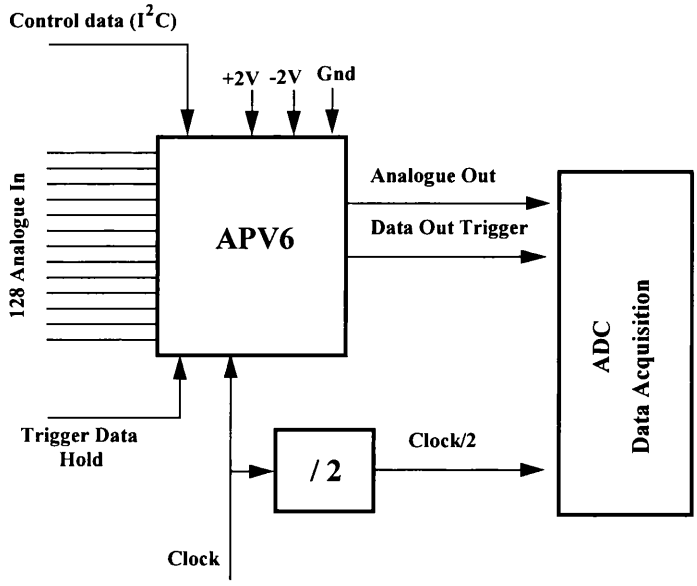

Fig. 5.5: Diagram showing the APV6 and its slow- and fast-control signals [Cullum, 2000].

5.3 Development of special interface electronics

5.3.1 Overview of the UCL data acquisition system

At Imperial College and CERN the APV6 is controlled and read out by a rather complex VME-based system, the size (and cost) of which was not suitable for a portable instrument. A dedicated acquisition/control system was therefore designed for this project at the Institute of Nuclear Medicine of the Middlesex Hospital [Cullum, 2000].

The system, which has been built in the Radiation Physics laboratory of UCL, is based around a PC and a small electronic interface unit. The control of the APV6 is carried out by the interface unit, which was specifically developed for the Compton camera, and data collection is performed by a fast digitiser card commercially available for the PC. Figure 5.6 is a schematic showing the electronics for one microstrip detector.

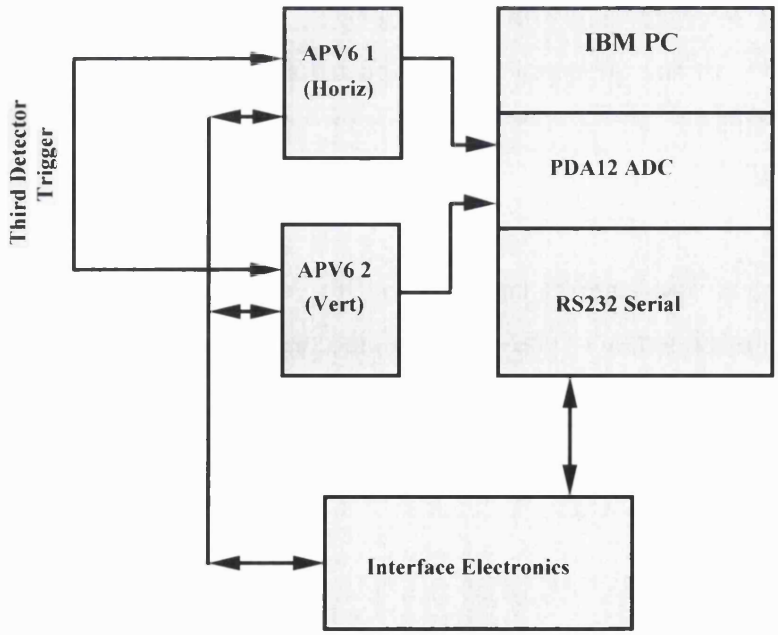

Fig. 5.6: Overview of the UCL acquisition system for the Compton camera [Cullum, 2000].

As each detector makes use of two APV6 chips (one for each side) and the PDA12A[18]digitiser card has two analogue inputs, a single card is sufficient for the readout of one detector. The whole system can be controlled running a Borland C^{++} program in a DOS environment.

5.3.2 The interface unit

This unit is based around a single board microcontroller (TDS2020[19]) which incorporates an Hitachi H8/532 processor running at 19.8MHz. The board was chosen due to its small size, relatively low cost, ability to easily interface keypads and liquid crystal displays (LCDs), and the built-in I^2C bus controller. The processor is programmed in a combination of Forth and assembler. During development the code was written on and downloaded from a PC, after debugging it was stored in EPROM on the microprocessor sub-assembly board.

The APV6 parameters are defined using an integral keypad and liquid crystal display (see Fig. 5.7) or remotely via an RS232 serial link. In either case the values are shown on the attached LCD. This allows the flexibility of using the interface unit either in stand-alone form or under control of a PC. In addition to the microcontroller and electronics associated with the integral keypad and display, the unit contains a dedicated interface board, which supplies the chip clock and provides suitable synchronisation of the various sequences on the trigger line. The clock and control signals are provided at differential ECL levels, as required for the APV6 input. The board also buffers the I^2C bus between the microcontroller and the APV6, so as to allow level shifting from 0-5 V on the TDS2020 to +/-2 V on the APV6. Finally, the board produces a 20 MHz clock signal for the PC-based ADC cards and allows it to be synchronised to the analogue data output stream from the APV6s. A detailed description of the interface electronics including circuit diagrams is given in Appendix II.

[18] PDA12A card manufactured by Signatec Inc., California USA

[19] TDS2020 manufactured by Triangle Digital Services Ltd, London UK

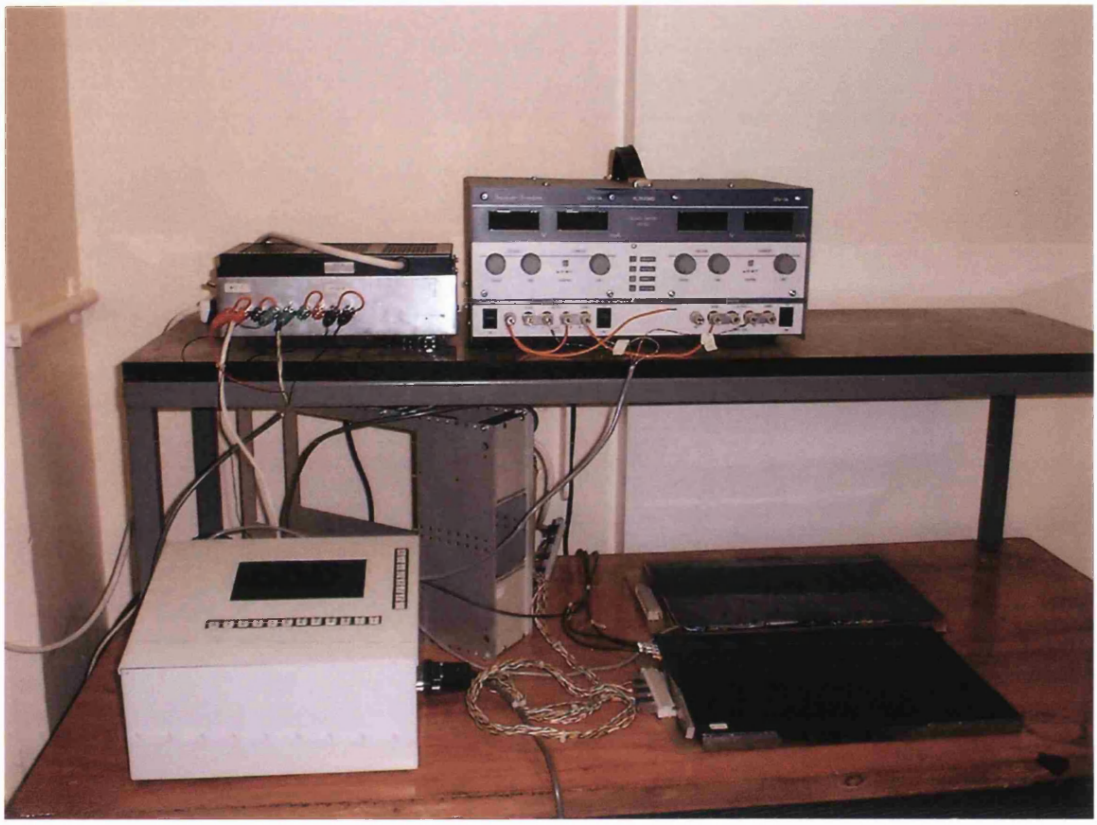

Fig. 5.7: Image showing the components of the UCL silicon Compton camera. The two detector planes are to the right of their mount rack; to the left is the control box (equipped with a keypad and a liquid crystal display), which contains the interface board with the TDS2020 microcontroller. Above are the power supply units for biasing the detector and powering the control box.

5.4 Tests on the operation of the interface electronics

In order to verify the correct operation of the dedicated interface electronics and DAQ system developed at UCL, a single APV6 and three auxiliary boards were provided by Imperial College for test purposes. These components were assembled in the stand-alone test set-up at UCL shown in Fig. 5.8. The system consisted of a board hosting the APV6 chip, accompanied by three peripheral boards that provided power supplies and interfaced the input/output signals for the chip.

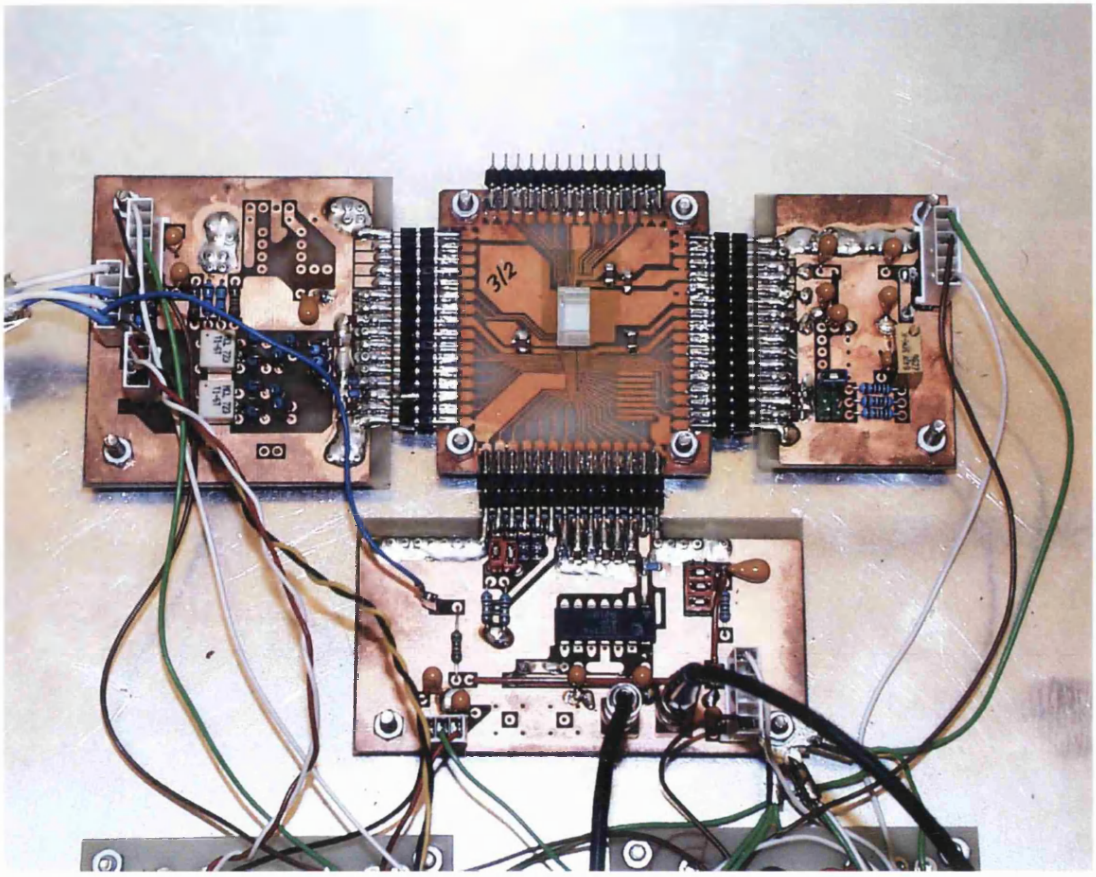

Fig. 5.8: Test set-up for the APV6.

5.4.1 Tests on the APV6 'slow control'

Tests were carried out so as to verify that the microcontroller could 'communicate' correctly with the APV6 via the I^2C bus. To this regard, some template sequences (as recorded by a digital scope) for data transmission to and from the APV6 were provided by Imperial College. These sequences showed an example of 'writing to' and 'reading from' an APV6 register. The format of the template data was correctly reproduced on the UCL stand-alone system (see Fig. 5.9 and Fig. 5.10). In both the 'read' and 'write' template sequences the signal from the I^2C data line (which is bi-directional between the interface unit and the APV6) is plotted together with the I^2C clock (the pulses of which last approximately 5 μs).

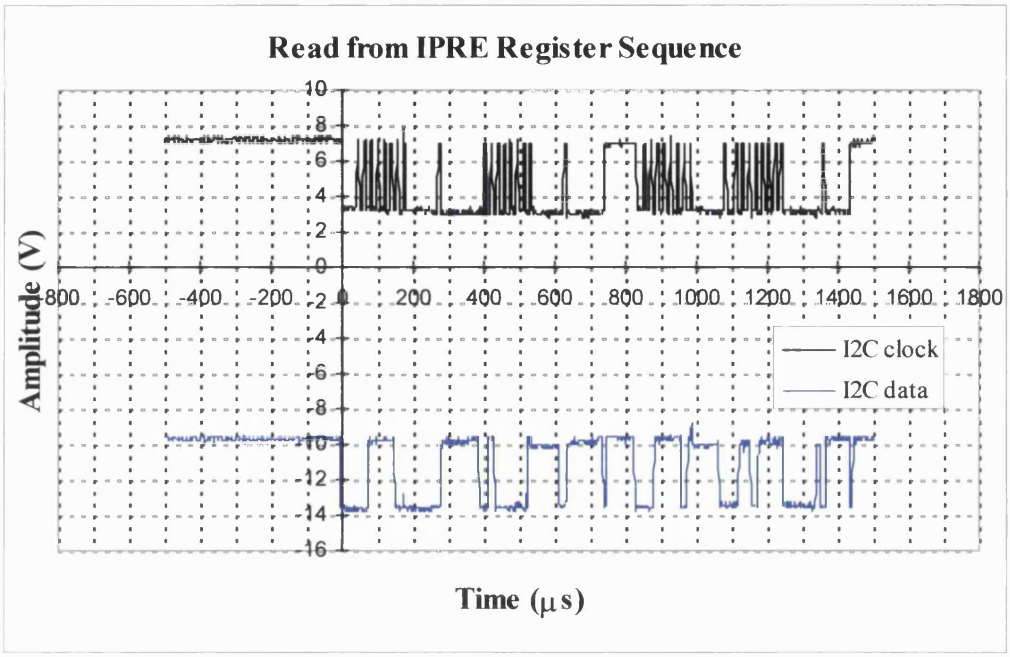

Fig. 5.9: Correct I^2C sequence for reading a value from the APV6 register IPRE (which contains the settings for the preamplifier bias current).

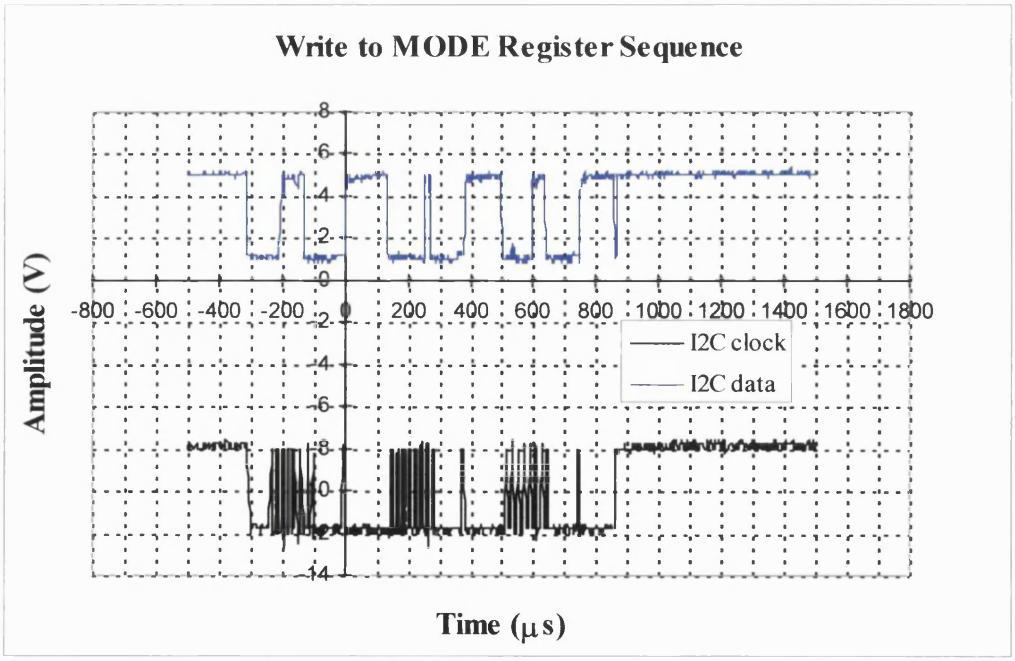

Fig. 5.10: Correct I^2C sequence for writing a value to the APV6 register MODE (which defines the operation mode of the APV6, i.e. peak or deconvolution, and enables or inhibits the calibration test pulses).

5.4.2 Tests on the APV6 'fast control'

A series of tests was also successfully carried out in order to ensure that the control sequences on the trigger line (trigger, reset and calibrate) were produced in the correct form (differential ECL levels) by the interface board and were correctly timed with respect to the pulses from the 40-MHz clock. The signals were monitored between the APV6 input pads and the ground; the signals sensed on the positive input pad of the trigger line (TRGP) and the clock (CLKP) are shown in Fig. 5.11, Fig. 5.12 and Fig. 5.13 in the case of the trigger ('1'), reset ('101') and calibrate ('11') sequences respectively. The trigger line is always sampled on rising edges of the clock signal.

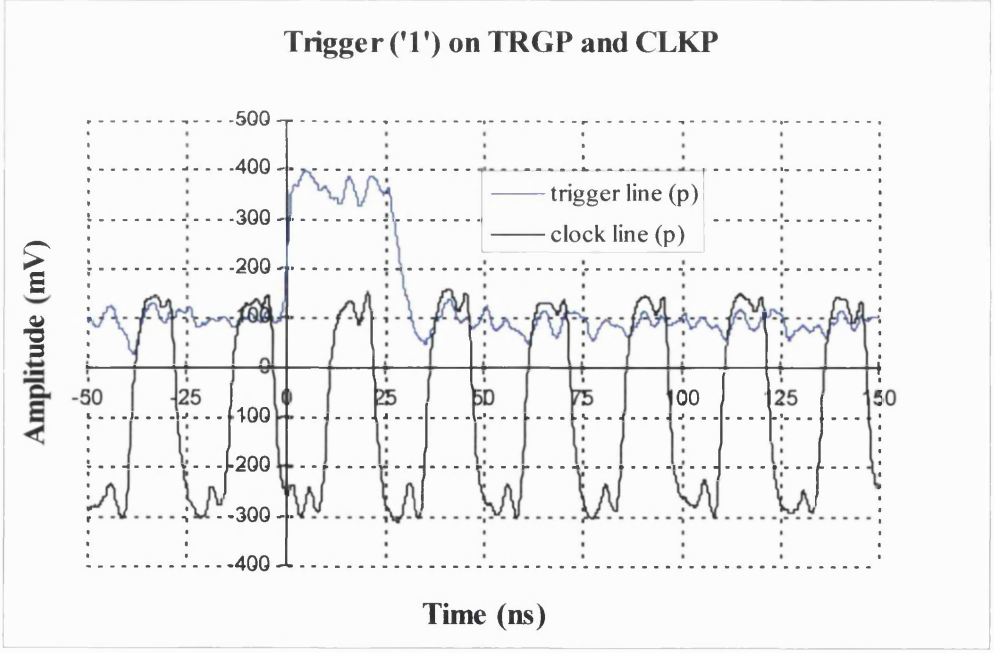

Fig. 5.11: Trigger signal ('1') plotted above the APV6 40-MHz clock. The trigger line is sampled on rising edges of the clock.

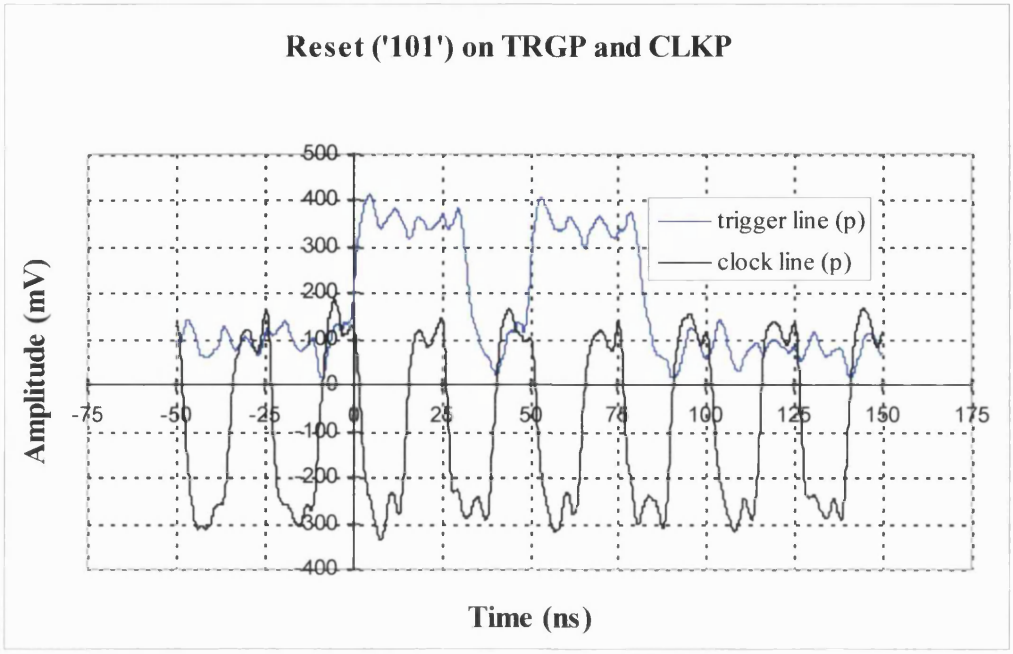

Fig. 5.12: Reset signal ('101') plotted above the APV6 40-MHz clock. The trigger line is sampled on rising edges of the clock.

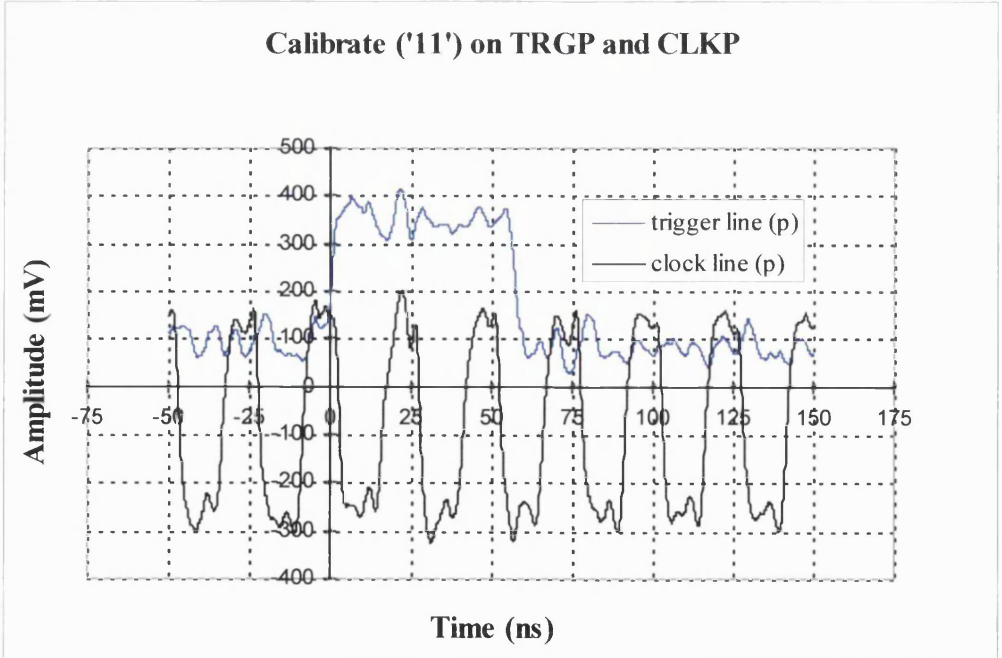

Fig. 5.13: Calibrate signal ('11') plotted above the APV6 40-MHz clock. The trigger line is sampled on rising edges of the clock.

Once the calibrate sequence had been correctly timed to the clock, it was used to produce internal pulses, so as to test the system developed for the APV6 readout. The magnitude of the pulses is defined by the user and programmed into a specific register of the APV6. The charge injected to produce a voltage step can be written to the CLVL register as an integer number between 0 and 255; this corresponds to a value of charge that can be varied between 0 and 15.3 fC in steps of 0.06 fC.

The timing of the pulse can also be programmed (using register CSKW) in steps of 1/8th clock cycle. By sampling the pulse at a fixed time (i.e. with a constant value of the latency) and progressively shifting the pulse timing one can thus reconstruct an image of the pulse for the measurement of the pulse shape.

The calibration pulses can be applied to 8 groups of 16 channels. The channels belonging to the same calibration group do not follow consecutive numbering, but they appear in output as consecutive channels. It is possible to 'fire' only selected groups, according to the value programmed into the 8-bit Calibrate Mask Register (CDRV) of the APV6. Each bit represents a group of channels, with LSB referring to the first group of output channels and MSB to the last one. A bit set to 1/0 enables/disables calibration of the corresponding group of channels. For example, setting CDRV = 5 (i.e. '00000101' binary) will enable injection of test pulses in the first and third group of channels. This situation is shown in Fig. 5.14, where the analogue output of the APV6 (AOUT) is shown in synchronisation with the digital output of the chip (OUTE), indicating correct chip operation and readout. Preceding and following the data stream (which is approximately 7 μs long) one can also see the so-called 'ticks' of the APV6; these are single pulses (logic '1s') that occur every 1.75 μs and are always present, except during the readout interval, even when no event has been triggered.

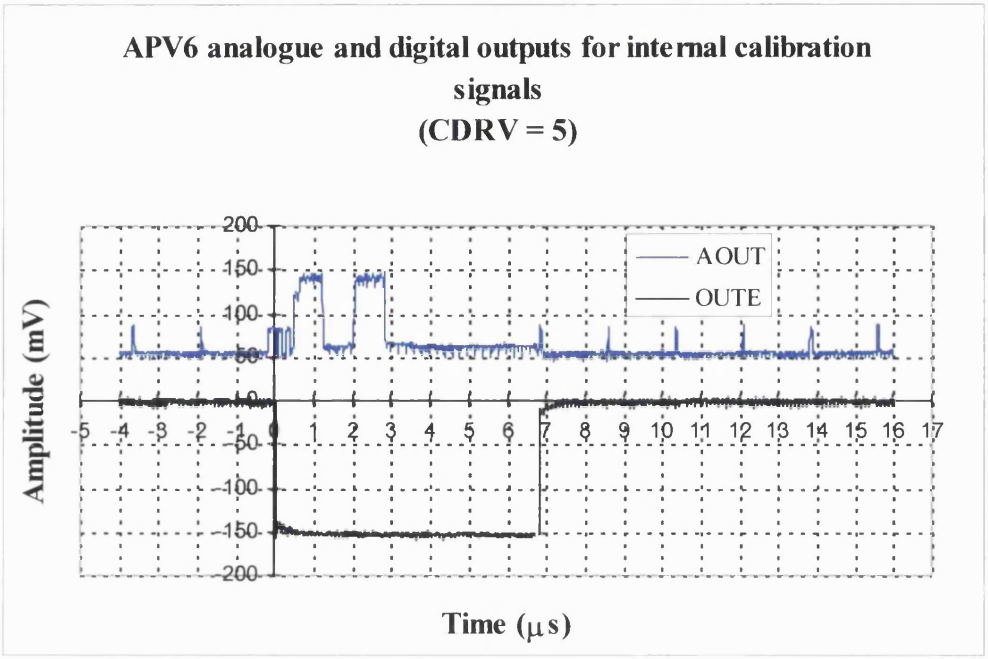

Fig. 5.14: Analogue (AOUT) and digital (OUTE) outputs for internal calibration signals produced in the APV6.

After evaluation of the stand-alone set-up of a single APV6, all the tests described were successfully repeated by connecting the system to the two APV6s bonded to a detector plane. On the detector plane, the three peripheral boards of the stand-alone set-up have been 'merged' and replaced with a single readout card for each chip (the two readout cards for the two APV6s that are bonded to one detector plane can be seen in Fig. 5.2). At present, two detector planes have been built, and the operation of both APV6s at the UCL set-up has been fully tested in one of the two planes.

5.5 Simulation of the imaging performance of the proposed scatter collimator

The computer model described in Chapter Two (see section 2.4.1) was initially developed for the simulation of a silicon scatter detector operating in coincidence with an absorption scintillation detector. The Monte Carlo code was then adapted so as to track double Compton interactions occurring in two separate silicon strip detectors (see Fig. 5.15). The model was applied to the design of the silicon collimator in the UCL Compton camera prototype, so as to simulate the imaging performance of the system.

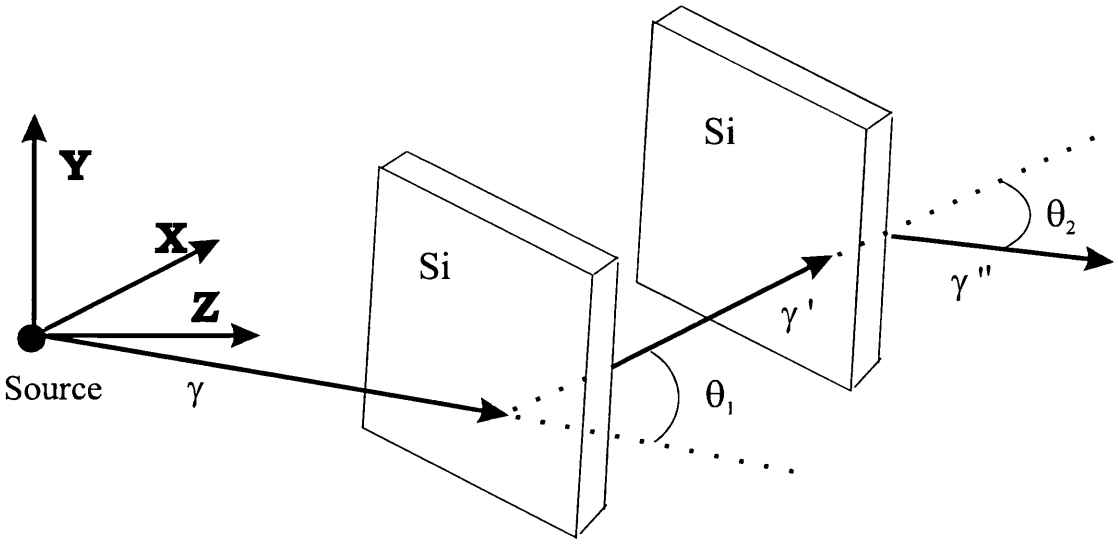

Fig. 5.15: Diagram showing the operation of two elements of the silicon scatter collimator, based on a double Compton scatter interaction. The events that were tracked in the simulation consisted of a single Compton scatter interaction in one of the detectors, followed by another single Compton scatter event in the other. For each event of interest, the positions of interaction in the two detectors and the energy deposited in the first detector were recorded.

5.5.1 Effects of strip noise on angular resolution

The Monte Carlo model was applied in order to simulate how the point spread function of the Compton scatter collimator is affected by the electronic noise in the strip detectors. Predictions were made for the first set-up of the collimator, which will consist of two silicon layers with 1 cm spacing. The modelling of the two silicon scatter elements was performed with the EGS4-based computer model previously described, assuming for each element a 500 μm-thick silicon detector, with a 6 x 6 cm^2 sensitive area and a strip pitch of 500 μm. The simulations were performed assuming uniformly distributed noise across all channels. The FWHM spatial resolution obtained for a point source in air at 10 cm distance is plotted in Fig. 5.16 as a function of the FWHM noise in silicon expressed in keV. The corresponding FWHM angular resolution should range from approximately 3 to 6 degrees as the FWHM noise of the readout channels varies from 2 to 10 keV.

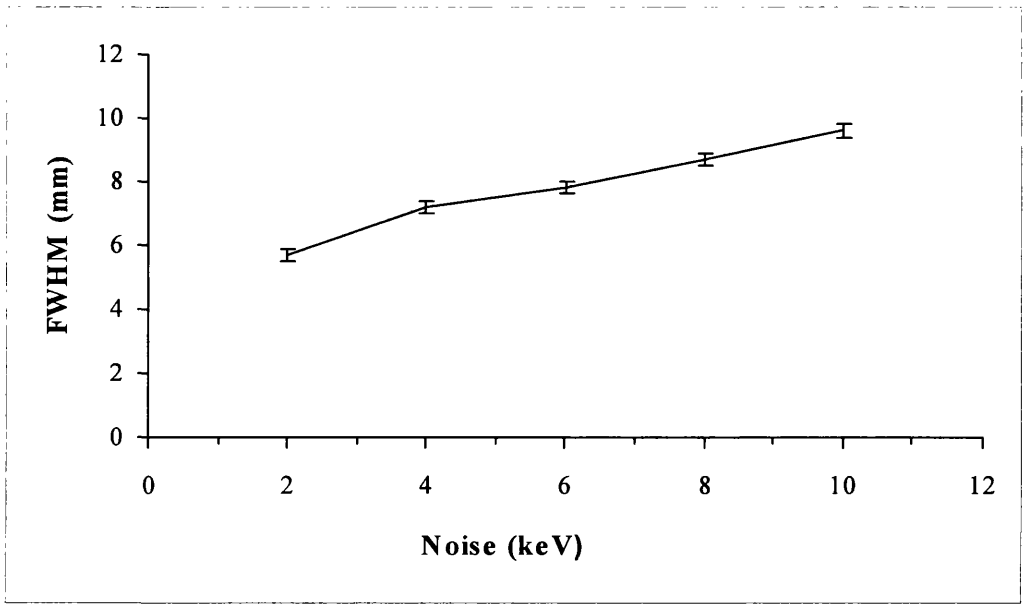

Fig. 5.16: The simulated FWHM of the Point Spread Function of a 511 keV gamma-ray source is plotted as a function of electronic noise in the silicon detectors. The point source is isotropic and located at 10 cm from the Compton collimator. The noise is expressed as the FWHM in keV in silicon.

The experimental measurements and theoretical considerations presented in Chapter Four (sections 4.4 and 4.7) allowed us to determine that the chip-detector configuration chosen for the scatter modules would produce a noise level of approximately 9 keV FWHM for a typical readout channel. On the basis of the results presented in section 4.7, it is reasonable to conclude that this value could be reduced to at least 6 keV FWHM by cooling the detector and/or by adjusting the APV6 settings for the pulse shape. Both operations would in fact reduce the contribution to the noise produced by the leakage current, which was shown to have a major effect on the system spectrometric performance. The level of electronic noise (FWHM in keV) in the simulations that follow was therefore assumed to be of 5.5 keV, giving a detector FWHM energy resolution of approximately 6% at 100 keV of energy deposition. This level of noise also defined the minimum scatter angle that could be detected in both layers (~ 9°).

5.5.2 Collimator performance for a point source in air

The imaging performance of the scatter collimator was first evaluated assuming the simple case of an isotropic point source in air. Figure 5.17 shows the simulated image of a 511 keV point source placed in air at a 10-cm distance from the face of a two-element collimator (1 mm total silicon thickness) with 1 cm spacing between detectors. The FWHM of the PSF was estimated to be equal to (7.7 $\pm$ 0.3) mm, which corresponds to an angular resolution of approximately 4°. The collimator absolute efficiency (number of detected double Compton events per photon emitted by the source) was estimated to be approximately 1.7 x 10^{-5}. This value is reduced to approximately 1 x 10^{-5} if the analysis is limited to those events that are potentially useful for external triggering, i.e. where the double scattered photons emerge from the second detector with positive direction.

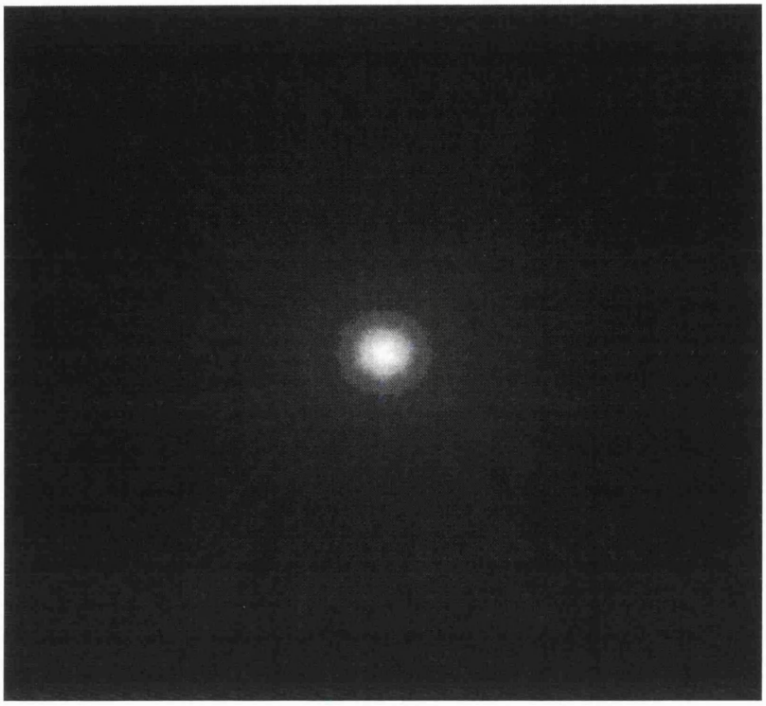

Fig. 5.17: Simulated image of a point source of 511 keV of energy, located in air at 10 cm from the face of the electronic collimator. Image obtained with approximately 28,000 double Compton events in silicon.

The summed spectrum of the coincident energy signals from the two silicon layers was obtained for all double Compton events that were transmitted by the collimator in forward direction (see Fig.5.18); it was found that following a double Compton scatter interaction, a photon with an initial energy of 511 keV was not likely to have lost more than approximately 350 keV; this implies that a minimum threshold of 160 keV could be established for a third detector in order to enable the trigger for the silicon sensor readout. If we assumed that in each silicon element no events could be detected below a noise threshold of ~ 5-6 keV, the energy window in the trigger detector would then be set between 160 and 500 keV.

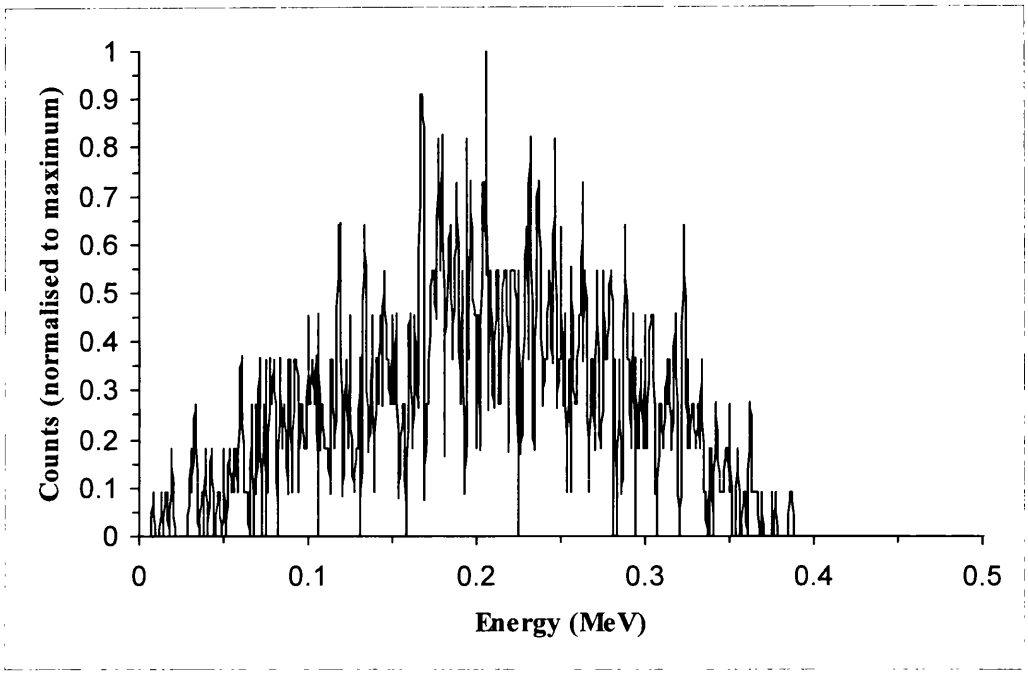

Fig. 5.18: Summed spectrum of coincident energy signals, produced by double Compton scatter photons in a two-element silicon collimator.

The model was also applied in order to evaluate the raw sensitivity of a scatter collimator consisting of a stack of silicon detectors: the collimator absolute efficiency for a stack of four strip detectors (each 6 x 6 cm^2 x 500 μm in size) was estimated to be approximately 7.6×10^{-5}, with a 10-cm distance between the collimator surface and the point source. Simulations were also carried out for a ten-element stack, which was estimated to provide a collimator absolute efficiency of 2.8×10^{-4}. This figure would increase to an approximate value of 10^{-3} if 1-mm thick silicon detectors were used.

A computer simulation was also carried out in order to determine the distribution of scatter angles for single Compton events at 511 keV. The impinging photons were simulated as a central pencil beam, perpendicular to the surface of the silicon strip detector. The Monte Carlo code was employed to record the flight direction of the emerging photons undergoing a single Compton interaction. The angular distribution of such photons is plotted in Fig. 5.19. It has a peak at approximately 33°. The 'ditch'

in the curve is due to the partial absorption of the photons scattered at 90°. The detector thickness (500 μm) is in fact much smaller than its dimensions in the plane perpendicular to the beam (6 cm x 6 cm).

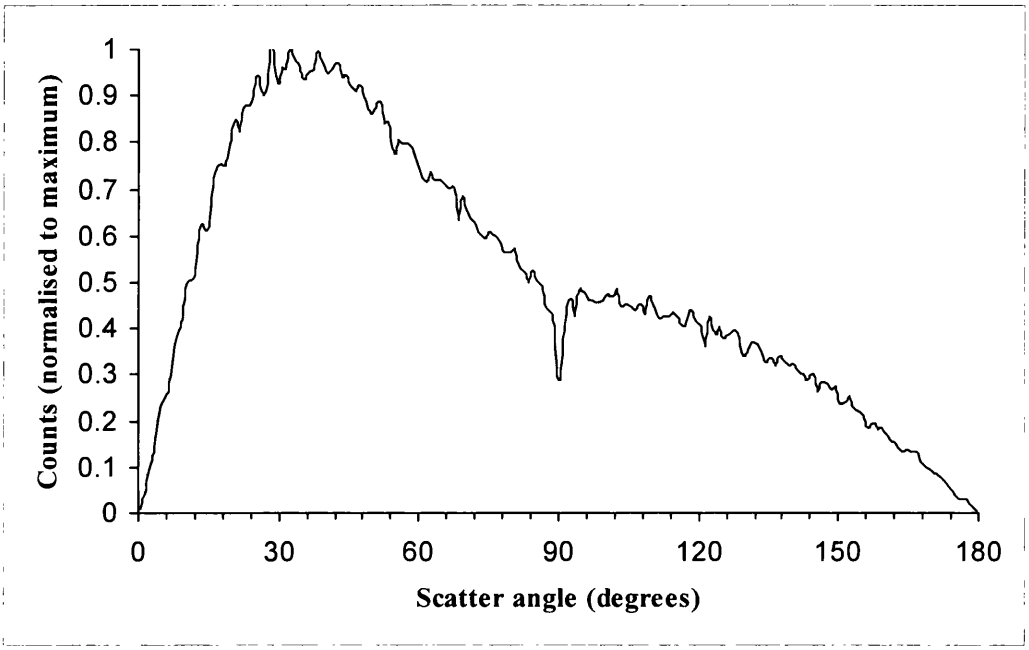

Fig. 5.19: Distribution of scatter angles for all 511 keV photons that emerge from a silicon strip detector following a single Compton scatter event. The 'ditch' in the curve is due to the partial absorption of the photons scattered at 90°.

Finally, a simulation test was carried out in order to estimate the effects of Doppler broadening on the angular resolution of the silicon collimator at 511 keV. The relevant LSCAT option in EGS4 was "switched off" in a simulation run and the corresponding results were compared to the simulated data that included the effects of Doppler broadening. The observed degradation in angular resolution was approximately 16%.

5.5.3 Considerations of scatter effects in tissue

Simulation work was also carried out so as to obtain information on the effects of photon scatter in tissue in Compton imaging at 511 keV. The computer model was employed in order to produce the image of an isotropic point source in the same geometrical conditions as described in the previous section; in this application, however, the 10-cm gap set between the source and the silicon collimator was filled with soft tissue instead of air.

The image was reconstructed for two different cases. In the first case, it was assumed that all detected photons contributed to the image; in other words, the energy window used for scatter rejection was infinitely wide. In the second case, events were rejected if their energy prior to the first detector interaction was less than 10 keV below the source energy. The image profiles are plotted for both cases in Fig. 5.20, where they are also compared to the image profile of a point source in air.

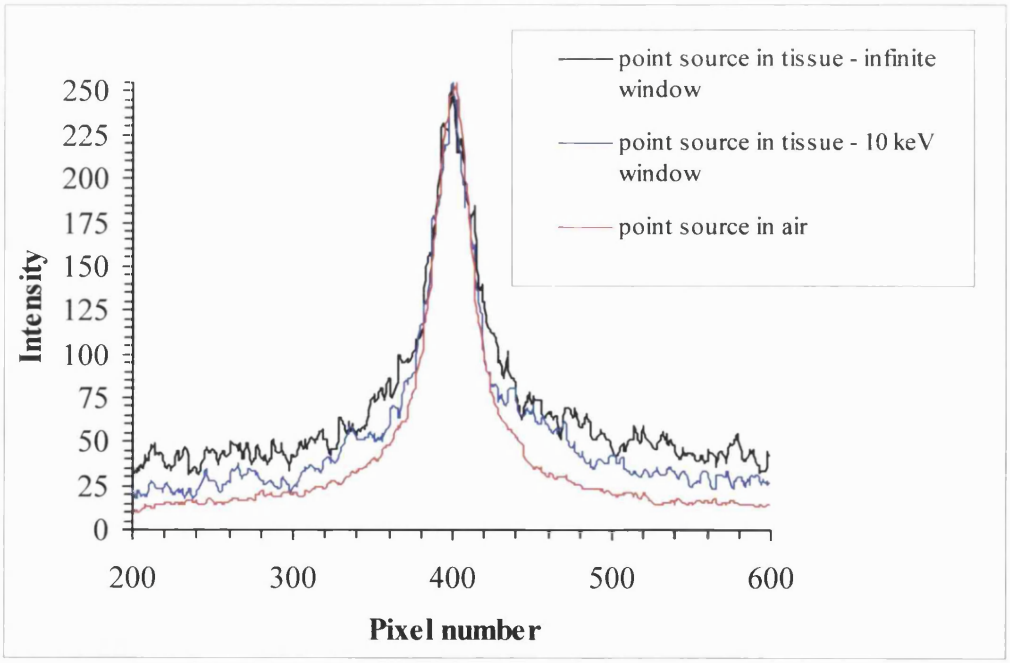

Fig. 5.20: Point source at 10 cm – in air and tissue, with and without scatter correction.

The effects of scatter in a 10-cm layer of tissue were observed as a degradation of the signal/noise ratio (or "peak-to-valley") in the image; however, they did not affect significantly the FWHM of the profile. An angular resolution of approximately 4° (the same as in the case of a point source in air) was obtained even when considering the maximum effect of scatter (infinite energy window). With the discrimination at 10 keV below the source energy, a change in the angular resolution could not be appreciated as the scatter correction improved only the "tails" of the profiles.

In order to obtain a better approximation to a clinical imaging situation, as well as to compare the effects of different amounts of tissue, simulations were also carried out for the case of radiation sources inside 3-D objects. In these investigations, the source simulated a point-like tumour imbedded at the centre of a uniform cylinder of soft tissue. The photon emission was isotropic and covered the entire solid angle. The number of simulated photon histories was 2×10^8 for each case. This number was based on the typical conditions of a clinical examination; we assumed the administered activity to be in the order of 100 MBq, the acquisition time to be in the order of a few minutes (e. g. 200 s) and the ^{18}F-FDG uptake to be equal to 1 %. The distance between the centre of the phantom and the face of the electronic collimator was maintained constant (15.5 cm) for all cases. Three simple cases were modelled: a breast-size object (cylinder of 10 cm in diameter, 10 cm in length), a head-size object (cylinder of 20 cm in diameter, 20 cm in length) and an abdomen-size object (cylinder of 30 cm in diameter, 30 cm in length). The images obtained for these three cases are shown in Fig. 5.21 *a)*, Fig. 5.21 *b)* and Fig 5.21 *c)*.

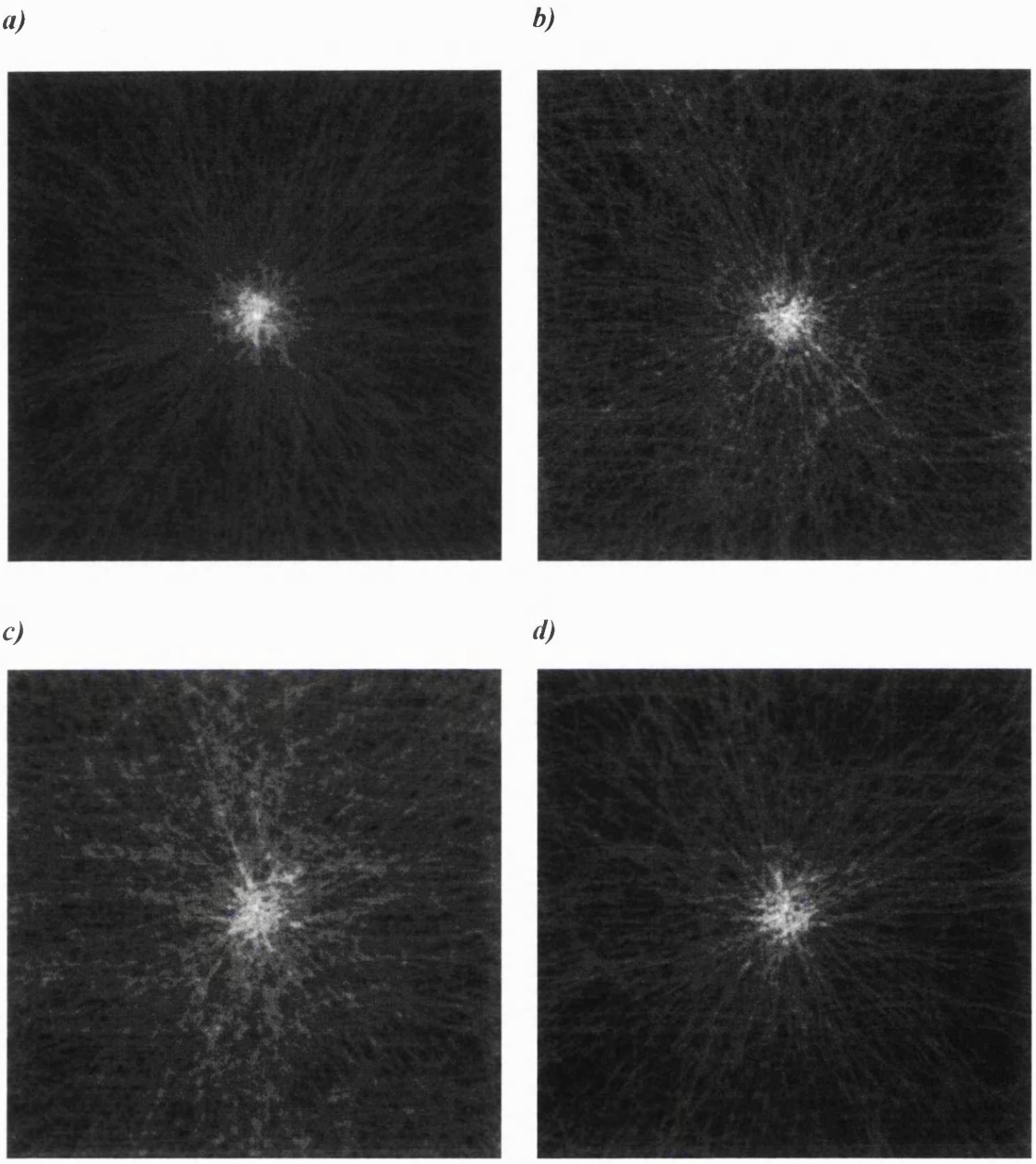

Fig. 5.21: Simulated images of 511 keV point sources imbedded in cylindrical phantoms of tissue equivalent material: ***a)*** breast-size phantom; ***b)*** head-size phantom; ***c)*** abdomen-size phantom; ***d)*** again abdomen-size phantom, but with scatter rejection (applied within a 10 keV window below the source energy).

Analysis of the images showed that the scatter in tissue did not alter the value of the FWHM of the image profiles of the breast and head-size objects. Some degradation of the profile was found in the case of the abdomen-size object, for which however it was estimated that the angular resolution was worsened only by approximately half a degree. Again, the application of scatter correction did not improve the FWHM angular resolution, but it diminished the background noise (see Fig 5.21 *d)* and Fig. 5.22).

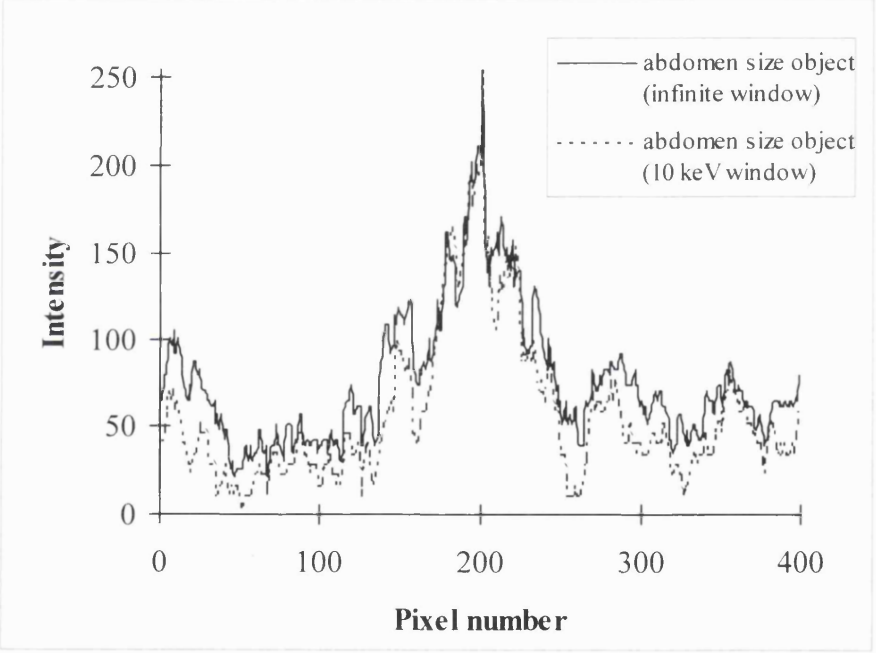

Fig. 5.22: Horizontal profiles of a point source in a tissue object of size comparable to an abdomen, with scatter correction (10 keV window) and without scatter correction (infinite window).

Chapter 6

Conclusions

6.1 Summary of results

The principle of γ–ray collimation based on Compton scatter de-couples the inverse relationship between spatial resolution and detection sensitivity, which characterises conventional SPECT systems. The principle of Compton imaging favours medical applications with high-energy radioisotopes. In this work, Compton cameras were suggested as a potentially advantageous technique for imaging long-lived positron emitters. Results were presented on the design and experimental development of a Compton collimator, based on the use of semiconductor detectors.

A Monte Carlo simulation study was carried out in order to evaluate the use of elemental and compound semiconductors as scatter elements for a high-energy (511 keV) Compton collimator. The Compton scatter efficiency of all materials was related to the performance of a conventional, parallel-hole collimator. It was estimated that a sensitivity gain between 10^2 and 10^3 could be achieved in the 140-511 keV energy range, depending on the size and the material of the collimator. The study concluded that silicon is at present the most suitable scatter material for the construction of a clinical Compton camera.

A computer model was developed in order to optimise the characteristics of a silicon detector for the electronic collimation of annihilation photons. The model simulated the functioning of a two-element Compton camera and included all the physical and geometrical factors that affect its angular resolution. The fundamental requirements of a silicon scatter detector were determined for its use in a desktop prototype system. The detector should be approximately 1 mm thick, have a

minimum sensitive area of 2.4 x 2.4 cm^2, have a spatial resolution in the order of 300 μm and have an energy resolution of 6 % or better for 100 keV of energy deposition.

The results on the detector design were applied to the experimental development of a prototype collimator, based on the use of silicon microstrip detectors. The simulation tool was employed to evaluate the use of commercially available strip detectors and readout electronics. Effects associated with strip pitch and wafer thickness were investigated. The results showed that the optimum strip pitch should be approximately 500 μm. It was also proved that a wafer thickness of 0.5 mm would improve the spatial resolution of the system, whilst maintaining acceptable scatter efficiency and containment of recoil electrons. A double-sided microstrip detector with a thickness of 500 μm and a strip pitch of 470 μm was eventually selected for this project. The detector sensitive area was 6 x 6 cm^2, hosting 128 strips on each side. The detector was to be used in conjunction with the APV6 readout chip, for which a noise level of 5.5 keV FHWM was estimated.

Tests were carried out for the electrical characterisation of the unbonded silicon strip detectors. Experiments were performed to measure the detector current-voltage and capacitance-voltage characteristics. The measured values of leakage current at full depletion were in the order of 1 – 2 μA. Circuit models were developed so as to perform and interpret the measurements of strip capacitance. The capacitance of a single strip was measured to be 6 pF with respect to the back plane, and 8 pF with respect to its four neighbours. The measurements of the electrical parameters of the detectors were applied to produce a theoretical estimate of the strip noise of ~ 9.2 keV.

The silicon detectors were bonded to the readout electronics and tested for defective strips. Two detection modules were assembled and employed for the detection of minimum ionising electrons, using a fully operational acquisition system developed at Imperial College. Strip calibration was performed making use of the ^{90}Sr 'Landau peak'. The noise distribution was measured across all strips. The noise

level of a typical detector channel was found to be approximately 9.4 keV (FWHM), in excellent agreement with the theoretical estimate based on the measured values of leakage current and strip capacitance. Experimental results on temperature effects and pulse shape variation indicated that the leakage current was the most probable cause of high noise. It was suggested that the noise level could be reduced by cooling the detector and/or by modifying the time constant values of the shaping amplifier.

A small laboratory prototype Compton camera was proposed, consisting of a stack of four silicon microstrip detectors, operating in a double Compton configuration and externally triggered readout mode. The experimental development of the camera was initiated by assembling two silicon modules for the first set-up of the collimator. A germanium detector, placed behind the stack, would provide the external trigger. Custom electronics were developed in order to enable the use of the APV6 in this application. Results were presented on the successful testing of a dedicated interface unit, which was constructed to synchronise trigger sequences, supply the chip clock and set the APV6 parameters.

A specific-purpose Monte Carlo code was employed, so as to correlate different levels of strip noise to the imaging performance of the Compton collimator. Modelling of the proposed two-element collimator at 511 keV (assuming a channel noise of ~ 6 keV) predicted an angular resolution of approximately 4°, which surpasses by 3° the typical performance of ultra-high-energy mechanical collimators. The collimator sensitivity to double Compton scatter was estimated to be 1.7×10^{-5}, which is of the same order of magnitude as the geometric efficiency of a high-energy lead collimator. The estimated value of sensitivity increased to 7.6×10^{-5} for a four-element collimator and to 2.8×10^{-4} for a ten-element stack. Simulation work was also presented for the case of point sources imbedded in tissue. Preliminary results suggested that patient scatter at 511 keV should not significantly affect the quality of the image profile. However, the use of a clinical Compton camera may be most suited to the imaging of small objects. The small size of the camera would in fact allow its use as a close field imager, thus increasing sensitivity with respect to the

performance evaluated at a standard distance of 10 cm between source object and electronic collimator.

6.2 Future work

This thesis presented the first results on the design and experimental development of a Compton collimator for positron emitter imaging. The construction of a laboratory prototype Compton camera is currently under way at UCL. Substantial progress has been made on the system development and the completion of the experimental prototype is the aim for the immediate future. Although the emphasis of future work should be put on the experimental aspects of the project, the simulation and computing contents of this work could also be extended.

The first experimental tasks to be performed using the dedicated DAQ system at UCL should repeat the same strip calibration procedure that was carried out at the silicon laboratory of Imperial College. Such tests will assess the reliability of the readout system and the reproducibility of the measurements of strip noise. The operation of the existing two silicon modules in conjunction with the germanium detector will have to be tested in a simple set-up of the designed Compton camera, using a 511-keV point source (^{22}Na) in air. Experimental tests need to be carried out to determine the optimum pulse shaping performed by the APV6 in order to minimise channel noise.

The angular resolution of the camera should be evaluated experimentally and compared with the predicted performance, so as to assess the robustness of the computer model. In order to verify the results on the system sensitivity, however, the simulation tool should be extended so as to include the presence of an additional detector to provide the external trigger. The detection of three interactions will diminish the efficiency advantage that was predicted for the scatter collimator, which in this work was evaluated for its intrinsic performance.

The developed computer model aimed to select the optimum parameters of the collimator and to assess the potential of the design, as a separate issue from the mode of triggering. The configuration of the proposed camera prototype, however, was dictated by the characteristics of the readout electronics, which required an external trigger. Future developments of the system may consider the use of self-triggering readout electronics, such as chips from the Viking series [Overdick *et al.*, 1997] or the RENA chip [Kravis *et al.*, 1999].

Another interesting area for future work is the study of calibration methods other than the detection of minimum ionising particles, as the evaluation of the Landau peak may not provide sufficient accuracy for this application. The choice of the optimum calibration procedure will depend on the characteristics of the readout electronics. In the case of externally triggered readout chips, such as the APV6, alternative calibration methods could be based on the use of unsealed ^{241}Am sources [O'Neill *et al.*, 1995] or Compton scatter of high-energy photons [Zych *et al.*, 1996].

The optimum geometrical configuration of the camera elements should also be studied. Such experimental results would provide valuable information for more sophisticated and efficient designs. More efficient camera configurations could be researched; a stack of silicon scatter detectors could be employed in combination with a solid-state, position sensitive calorimeter. This thesis has concentrated on the optimisation of the scatter detector; future work could address the design criteria for the back detector.

Further investigations are also required on the effects of Doppler broadening in Compton imaging for photon energies of clinical interest (140 – 511 keV). On the basis of simulation results, it was recently suggested [Ordonez *et al.*, 1997], [Wilderman *et al.*, 1998] that this phenomenon considerably affects the operation of Compton cameras. Experimental evidence is needed so as to quantify this effect on the angular resolution of Compton collimators.

Finally, one of the most challenging aspects in the medical application of scatter-based collimation is image reconstruction, the study of which was outside the scope of this thesis. Imaging of complex three-dimensional sources will require the development of more sophisticated reconstruction methods. As the number of sensitive elements of the prototype camera will eventually be extended, opportunities will exist to investigate algorithms based on polarisation effects of multiple Compton interactions. Such methods have been proposed in the literature [Dogan *et al.*, 1992], but never actually applied to an experimental device.

Appendix I

Electronic Noise in Strip Detectors

AI.1 General noise model for a detector-preamplifier system

For any detector-preamplifier system, the noise can be expressed in terms of an equivalent input noise source of spectral density [Nicholson, 1982], [Delaney, 1980] (see Fig. AI.1):

$$\overline{dv^2} = F(\omega)d\omega \tag{AI.1}$$

where

$$F(\omega) = a^2 + \frac{b^2}{\omega^2} + \frac{c^2}{\omega} \tag{AI.2}$$

In the above expression, a^2 is the series noise term (mainly from the preamplifier plus a small contribution from the detector), b^2/ω^2 is the parallel noise term (from both preamplifier and detector), and c^2/ω is the Flicker noise term (from the preamplifier).

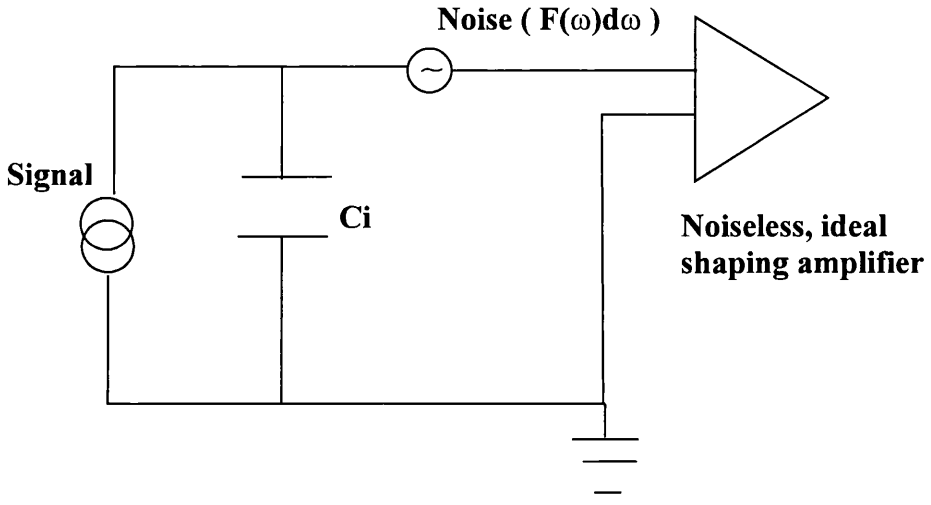

Fig. AI.1: General model for a detector-shaping amplifier system. C_i is the total input capacitance.

AI.2 Expression of Equivalent Noise Charge for a CR-RC shaper

If the amplifier gain has a frequency dependence of the type $H(j\omega)$, the mean square voltage at the output will be given by [Nicholson, 1982]:

$$V_n^2 = \int_0^\infty F(\omega)\left|H(j\omega)\right|^2 d\omega \qquad \text{(AI.3)}$$

For a *CR-RC* shaper of time constants τ_1 and τ_2, the frequency function $H(j\omega)$ is as follows:

$$H(j\omega) = \frac{j\omega\tau_1}{(1+j\omega\tau_1)(1+j\omega\tau_2)} \qquad \text{(AI.4)}$$

By substituting expressions (AI.2) and (AI.4) in (AI.3) and by solving the integral, one obtains the following relationship:

$$V_n^2 = \frac{\pi a^2}{2\lambda(\lambda+1)\tau_1} + \frac{\pi b^2\tau_1}{2(\lambda+1)} + \frac{c^2}{\lambda^2-1}\ln\lambda \qquad \text{(AI.5)}$$

where $\lambda = \tau_2/\tau_1$.

The output pulse of the *CR-RC* shaper is:

$$V(t) = \frac{Q}{C_i}\frac{\tau_1}{\tau_1-\tau_2}\left(e^{-\frac{t}{\tau_1}} - e^{-\frac{t}{\tau_2}}\right) \qquad for\ t \geq 0 \qquad \text{(AI.6)}$$

where Q is the charge associated with the detector signal and C_i is the input capacitance.

It can be shown that the function $V(t)$ in (AI.6) has the following peak amplitude:

$$V = \frac{Q}{C_i}\lambda^{\frac{\lambda}{1-\lambda}} \tag{AI.7}$$

By definition of *Equivalent Noise Charge* (or *ENC*, see section 4.4.1 of Chapter Four), it is:

$$\frac{ENC}{Q} = \frac{V_n}{V} \tag{AI.8}$$

Therefore, by combining equations (AI.7) and (AI.8):

$$ENC^2 = \frac{V_n^2 C_i^2}{\lambda^{2\lambda/(1-\lambda)}} \tag{AI.9}$$

And by substituting V_n^2 with expression (AI.5) one obtains the following expression for the Equivalent Noise Charge for a CR-RC shaper:

$$(ENC)^2 = \frac{C_i^2}{\lambda^{\frac{2\lambda}{1-\lambda}}}\left(\frac{\pi a^2}{2\lambda(\lambda+1)\tau_1} + \frac{\pi b^2 \tau_1}{2(\lambda+1)} + \frac{c^2 \ln\lambda}{(\lambda^2-1)}\right)\left[Coulombs^2\right] \tag{AI.10}$$

AI.3 Noise contributions in a strip detector system

The individual noise sources in a strip detector-readout chip system are discussed in sections 4.4 and 4.7 of Chapter Four, where the total strip noise is computed for the system of interest as a function of various physical parameters. The aim of the following sections is to provide the reader with an explanation of the equations that appear in those sections, which were employed for the theoretical evaluation of the strip noise. The global contribution of all noise sources to the equivalent noise charge is expressed in section 4.7.3 by equation (4.15), which is derived in this appendix with the help of some fundamental references ([[Nicholson, 1982], [Delaney, 1980], [Dubbs *et al.*, 1996], [Nygård *et al.*, 1991]).

AI.3.1 Contribution of integrated readout electronics

In the readout electronics employed for strip detectors, the preamplifier is integrated in an electronic chip. The preamplifier contributes to the noise with a power density spectrum $F(\omega)_{chip}$, which can be expressed as follows [Nicholson, 1982], [Delaney, 1980]:

$$F(\omega)_{chip}\, d\omega = \left(\frac{k_1}{\pi} + \frac{k_2}{\pi \omega^2 C_i^2} + \frac{k_3}{\omega} \right) d\omega \qquad \text{(AI.11)}$$

where the first term is the thermal noise in the channel FET, the second term is due to the shot noise and the thermal noise in the gate resistor, and the third term is the Flicker noise. The coefficients k_1, k_2 and k_3 depend on the geometrical and physical characteristics of the transistor and on the temperature. This expression includes the dependence of the chip noise from the detector, as the input capacitance C_i is the total strip capacitance.

AI.3.2 Detector contributions

Additional noise sources in a detector channel are associated with the resistance of the metal strip, the strip bias resistor and the strip leakage current. The following sections examine such contributions in more detail.

I) Metal strip resistance

The mean square voltage developed by a resistor in any frequency interval df at a temperature T is given by Nyquist's law:

$$\overline{v^2} = 4kTRdf \qquad \text{(AI.12)}$$

Since $df = d\omega / (2\pi)$, then, assuming $R = R_{met}$, where R_{met} is the metal strip resistance, one obtains:

$$\overline{v^2} = \frac{2kTR_{met}\, d\omega}{\pi} \qquad \text{(AI.13)}$$

II) Bias resistor

Equation (AI.12) can be also applied to the case of the bias resistor R_{Bias}. In terms of an equivalent current source, the relationship becomes:

$$\overline{i^2} = \frac{\overline{v^2}}{R_{Bias}^2} = \frac{4kTdf}{R_{Bias}} = \frac{2kTd\omega}{\pi R_{Bias}} \qquad \text{(AI.14)}$$

This current will flow across the input capacitance C_i. The corresponding mean square voltage appearing at the amplifier input will be given by the value of $\overline{i^2}$ multiplied by the square of the impedance of C_i:

$$\overline{v^2} = |Z|^2 \overline{i^2} = \frac{1}{\omega^2 C_i^2} \frac{2kTd\omega}{\pi R_{Bias}} \qquad \text{(AI.15)}$$

III) Leakage current

The detector leakage current I is a source of shot noise, which is associated with the fluctuations of number of carriers in the current. If dN is the average number of carriers in a time dt, then the corresponding average current is ($I = dQ/dt$):

$$I = \frac{edN}{dt} \qquad \text{(AI.16)}$$

where e is the electron charge.

The number dN will fluctuate statistically with a standard deviation equal to $(dN)^{1/2}$. From equation (AI.16), the corresponding current fluctuation i is:

$$i = \frac{e\sqrt{dN}}{dt} \qquad \text{(AI.17)}$$

From equation (AI.16), it is $dN = Idt/e$, thus:

$$i = \frac{e\sqrt{Idt}}{dt\sqrt{e}} \tag{AI.18}$$

Squaring up equation (AI.18) we obtain for the mean square fluctuation:

$$\overline{i^2} = \frac{eI}{dt} = eIdf = \frac{eId\omega}{2\pi} \tag{AI.19}$$

A detailed analysis [Schottky, 1918] shows that this quantity should actually be twice the relationship in (AI.19). The mean square current fluctuation is therefore:

$$\overline{i^2} = \frac{eId\omega}{\pi} \tag{AI.20}$$

Again, this current will flow across the input capacitance C_i. The corresponding mean square voltage appearing at the amplifier input will be given by the value of $\overline{i^2}$ multiplied by the square of the impedance of C_i:

$$\overline{v^2} = |Z|^2 \overline{i^2} = \frac{1}{\omega^2 C_i^2} \frac{eId\omega}{\pi} \tag{AI.21}$$

AI.3.3 Equation for the Equivalent Noise Charge

The detector contribution $F(\omega)_{detector}$ to the noise power density spectrum for a single strip will be given by the sum of the terms expressed by equations (AI.13), (AI.15) and (AI.21), which are respectively associated with the resistance of the metal strip, the strip bias resistor and the strip leakage current:

$$F(\omega)_{\det ector}\, d\omega = \left(\frac{2kTR_{met}}{\pi} + \frac{2kT}{\pi R_{Bias}\omega^2 C_i^2} + \frac{eI}{\pi\omega^2 C_i^2} \right) d\omega \tag{AI.22}$$

Let us now write explicitly the spectral power density $F(\omega)$ for a chip-detector system, by combining equations (AI.11) and (AI.22):

$$F(\omega) = \frac{k_1 + 2kTR_{met}}{\pi} + \frac{k_2 + \frac{2kT}{R_{Bias}} + eI}{\pi\omega^2 C_i^2} + \frac{k_3}{\omega} \qquad \text{(AI.23)}$$

This is of the same form as equation (AI.2), with

$$a^2 = \frac{k_1 + 2kTR_{met}}{\pi} \qquad \text{(AI.23 } a\text{)}$$

$$b^2 = \frac{k_2 + \frac{2kT}{R_{Bias}} + eI}{\pi C_i^2} \qquad \text{(AI.23 } b\text{)}$$

$$c^2 = k_3 \qquad \text{(AI.23 } c\text{)}$$

Finally, by substituting (AI.23 *a*), (AI.23 *b*) and (AI.23 *c*) in equation (AI.10), we obtain the following expression for the Equivalent Noise Charge in the case of a system comprising a strip detector and a readout chip with CR-RC shaping:

$$(ENC)^2 = \frac{A}{\lambda^{\frac{2\lambda}{1-\lambda}} 2\lambda(\lambda+1)\tau_1} C_{in}^2 + \frac{B\tau_1}{\lambda^{\frac{2\lambda}{1-\lambda}} 2(\lambda+1)} + \frac{C\ln\lambda}{\lambda^{\frac{2\lambda}{1-\lambda}} (\lambda^2-1)} C_{in}^2 \left[Coulombs^2\right] \qquad \text{(AI.24)}$$

where:

$$A = k_1 + 2kTR_{met} \qquad \text{(AI.24 } a\text{)}$$

$$B = k_2 + \frac{2KT}{R_{Bias}} + eI \qquad \text{(AI.24 } b\text{)}$$

$$C = k_3 \qquad \text{(AI.24 } c\text{)}$$

Equations (AI.24), (AI.24 *a*), (AI.24 *b*) and (AI.24 *c*) are the same as equations (4.15), (4.15 *a*), (4.15 *b*) and (4.15 *c*) in Chapter Four, *Q.E.D.*

By isolating the six addition terms in (AI.24), it is thus also possible to identify equations (4.7), (4.8) and (4.9) of section 4.4.3; they can be related to the second, the fourth and the fifth term respectively. These equations were employed in Chapter Four for the computation of the detector noise contribution from the resistance of the metal strip, the strip bias resistor and the strip leakage current. However, in equations (4.7), (4.8) and (4.9) the *ENC* is expressed in electrons rather than Coulombs; such equations should therefore be multiplied by a factor e=1.6 x 10^{-19} C in order to match the corresponding terms in equation (AI.24) of this Appendix.

Appendix II

The Interface Electronics

The interface electronics for the UCL Compton camera DAQ system was developed as a compact unit (see section 5.3.2 of Chapter Five). This comprises the TDS2020 microcontroller, the electronics associated with the integral keypad and liquid crystal display and the interface board, which is dedicated to the formation of the fast-control signals for the APV6. In addition, the board performs voltage level shifting for the slow-control (I^2C) signals between the microcontroller and the APV6. The board also produces a clock signal for the PC-based ADC cards and allows it to be synchronised to the data output stream from the APV6s. This appendix, the content of which was extracted and/or adapted from [Cullum, 2000], is a technical description of the interface board.

AII.1 Basic description of the interface board and its functions

The fast-control signals on the APV6 trigger line are generated by the interface board in response to a simple rising edge on one of its four inputs. These input signals can be either supplied as test sequences by the microcontroller or as a trigger by an external detector. The interface board plugs onto the motherboard of the interface unit. The timing and duration of the input control signals to the interface board are non critical and are at TTL levels. The board uses mainly high speed CMOS (74HCT series) logic. A second smaller assembly ('piggy-back' board) plugs onto the interface board. This additional board was not included in the original design but became necessary to properly condition the ECL clock and trigger signals when multiple APV6s are used.

The functions of the interface board can be summarised as follows:

1) To provide a reset sequence ('101') to the APV6 in response to a manual request from integral keypad or PC. The sequence has to be suitably timed to the chip clock.

2) To provide a calibrate sequence to the APV6 in response to a manual request from integral keypad or PC. This calibrate sequence must be followed by a trigger to allow readout of the calibrate data. The calibrate signal is a ('11'), again suitably synchronised with the system clock. The subsequent trigger is a single 1 which must follow a set time after the calibrate request. The actual value of the delay can be programmed into the APV6 via the 'latency' register.

3) To provide a trigger signal ('1') in response to a trigger event from an external detector or a manual request from the integral keypad or PC. The system must be insensitive to subsequent trigger events during the readout time. The system responds in an identical manner to manual requests or to those from an external detector. The requests from the external detector can be disabled on the board within the controlling software.

4) To shift all fast-control signals (i.e. clock, calibrate, reset or trigger) on the APV6 trigger and clock inputs from TTL to differential ECL voltage levels.

5) To provide voltage level shifting (between 0-5 V and +/- 2V) for the bi-directional I^2C data slow-control signal and uni-directional clock signal between the microcontroller and the APV6. The clock is always supplied by the microcontroller irrespective of whether data is being written to or read from the APV6.

AII.2 Method of operation

For the operation of the interface electronics it is necessary to refer to the circuit diagram in Fig. AII.1 *a)* and *b)*.

AII.2.1 System Clock

The basic system clock is supplied by IC1 and is subsequently divided down by two (pin 14) and 4 (pin 13) of IC2. These signals are termed Clk, Clk/2 and Clk/4. Throughout this description the system clock is assumed to be at a frequency of 40MHz, i.e. a cycle duration of 25 ns (12.5 ns 'high' and 12.5 ns 'low'), which is the

standard operation frequency of the APV6. The functioning of the board is actually independent of clock frequency except that the various timings and delays will need to be scaled accordingly.

AII.2.2 Manual Reset

The manual reset ('101') clears the APV6 pipeline and resets internal pointers. It is needed before using the APV6 following power-up or after changing the values stored in any of the APV6 registers. The reset sequence is instigated by a high level on pin 13 of IC9, which is then also present on IC9 pin 11 and IC11 pin 1. Its duration is not critical and it can occur at any part of the clock cycle.

The high level on IC11 pin 1 allows Clk/2 signal (which is always present on IC11 pin 2) to eventually appear on IC12 pin 6 and hence IC11 pin 9. The high level on IC9 pin 11 produces a high level on IC10 pin 2. The next rising edge of the Clk/4 signal on pin 3 of IC10 causes pin5 of IC10 to go high. The rising edge of this signal therefore signifies a reset request, but importantly it is synchronised with the rising edge of Clk/4 and hence the rising edge of Clk. This signal is applied to pin2 of IC13 after passing through variable delay unit Delay4, causing a positive going pulse on pin 13 of IC3. This pulse enables the reset sequence.

The pulse length can be varied by using the capacitor C12 and the variable resistor VR6; it should be set between 75 and 125 nsec (nominally 100nsec, 4 clk pulses). This pulse length is sufficient to span the 101 reset sequence (and not to obtain further high data or '1's) as long as the synchronisation of this pulse with clk/2 is correct. The enable pulse from IC13 pin 13 is 'anded' with the clk/2 sequence (or clk/4 sequence in the case of the calibrate - see next section) on pins 9 and 10 of IC11. To obtain the correct sequence from IC11 pin8, pin 9 of IC11 must be low when pin10 goes high. This is the use of Delay4.

The output from IC11 pin 8 and hence IC12 pin 11 is the reset sequence, except that it needs to be suitably re-synchronised with the Clk signal. This is the use of

Delay3. Finally the TTL sequence is applied to IC4 pin 7, producing a differential ECL level sequence on pins 1 and 3.

AII.2.3 Calibrate Sequence

The calibrate sequence ('110') is achieved in much the same way as the reset sequence, except by using the clk/4 sequence. With the calibrate line high on IC11 pin 4, the clk/4 sequence (which is continuously present on IC11 pin 5) will appear on IC11 pin 6 and hence IC12 pin 6 and IC11 pin 9. The high calibrate signal also appears on IC12 pin 1 and hence IC10 pin 2, causing the same set of processes to occur as described for the reset sequence.

AII.2.4 Calibrate Trigger

The calibrate sequence causes the production of an internal 'event', i.e. a 'dummy' analogue pulse in the APV6. To read out this event a trigger ('1') must follow the calibrate sequence after a fixed time. The actual value of this delay can be programmed into the APV6.

The trigger for the calibrate sequence is produced in the following way. At the same time that IC12 pin12 goes high so does IC11 pin13. To ensure that this is a calibrate and not a reset request this signal is 'anded' with the calibrate signal (IC11 pin12) to produce a rising edge on IC11 pin11. This rising edge will have a fixed time relationship to the start of the calibration sequence. The rising edge on IC13 pin 10 produces an output pulse on IC13 pin 5, the duration of which is set by C8 and VR5. This should be set between 2800 and 6000 ns (14-30 times clock/8), nominally set to 4400 ns, the length is not critical. This pulse is applied to pin 1 of IC3, bringing the counter out of reset, and counting at the rate of clock/8 (IC3 is clocked on pin 2 by the signal from pin 12 of IC18, which is brought out of reset at the same time of IC3). At the start of the 14^{th} clock/8 pulse (i.e. after 13 x 25 x 8 = 2600 ns) pins 11,12 and 13 of IC3 are high, and hence so are pins 3, 4, 5 and 6 of IC5, pin 6 remains high for 50ns. This produces a rising edge on IC12 pin 9 and hence IC12 pin 8 and IC14 pin 2. IC14 produces a positive output pulse on pin 13 of length determined by C14

and VR8. This pulse length is set to be longer than the readout period (which is approximately 7μs). On the next rising edge of Clk (on IC10 pin 11), IC10 pin 9 goes high (i.e. the trigger information is now synchronised with the system clock).

The rising edge of this signal is applied to IC14 pin10 (after passing through variable delay line Delay1) which produces a positive output pulse on IC14 pin5 of duration 25-75ns (nominal 50ns), set by C13 and VR7. Delay1 is used to ensure that the rising edge of this signal occurs whilst Clk/2 is low. The duration of the pulse is such to ensure that under these circumstances one and only one (i.e. 25ns) high pulse of clk/2 appears on IC5 pin12. Delay2 is used to resynchronise this pulse to Clk, it then passes through IC12 pins 13 and 11 to IC4 pin 7 to be converted to ECL levels on IC4 pins 1 and 3.

AII.2.5 Normal Trigger

This is produced in response to a rising edge on IC5 pins 9 and 10 from an external trigger detector (or some other TTL trigger source). The system is sensitive to the rising edge of this pulse and its length is therefore not critical. As there may be pulses on this input which need to be ignored when carrying out acquisitions using internal trigger source (calibrate or trigger only) it is necessary to disable this input when not in use. This is done by 'anding' the signals with a control signal present on IC5 pin 11. When enabled, the external trigger event causes a rising edge on IC9 pins 9 and 8 and then on IC12 pins 10 and 8. The same sequence of events as described above for the calibrate trigger is hence instigated.

AII.2.6 Manual Trigger

This produces the same sequence of events as the normal trigger except it is initiated by a rising edge on IC9 pin 10.

AII.2.7 Multiple Triggers

The system has to be made insensitive to multiple events. Very fast multiple triggers could be misinterpreted as a reset sequence. This is achieved by the system being

basically edge triggered. A second trigger whilst the first is being processed (i.e. the pulses from IC14 pin13 and IC15 pin13 are still high) will only result in the length of these pulses being increased. As the rest of the trigger circuit responds only to level changes of these signals the system is insensitive to the second trigger.

AII.2.8 I^2C Bus

This is basically a two-wire bus, one carrying a clock signal which is always supplied by the master device (TDS2020) and one carrying data. The 'data in' and 'data out' lines on the APV6 are in fact separate, but during operation are tied together.

The I^2C clock signal on pin 2 of IC16, which runs between 0 V and 5 V, is shifted by IC16 to run between +/- 2.0 V on pin 6. The data line is common (i.e. in and out on the same wire) on the TDS2020 side. This is achieved by using the output enable function of IC17 and IC7. When not enabled, the output line goes into a high impedance state. IC17 and IC7 also perform voltage level shifting (from 0/5 V to +/- 2 V or vice versa) of the I^2C in and out data signals.

In order to write data to the APV6, the Enable APV6 data in line is set high. So IC17 pin 7 goes high and IC17 pin 6 goes into a high impedance state. At the same time IC6 pin 6 goes low and hence IC8 pin6 drops to –2 V, enabling IC7 (via IC7 pin 7). This allows data to be sent from the TDS2020 on IC7 pin2 to the APV6 on IC7 pin6.

In order to read data from the APV6, the enable APV6 data in line is set low. This causes IC6 pin 6 (and hence IC8 pin 2 and IC8 pin 6) to go high (+2 V). IC7 pin7 therefore goes high disabling the output from IC7 (i.e. IC7 pin 6 goes into a high impedance state). Subsequently, data sent from the APV6 on IC17 pin 2 are presented at TTL levels on IC17 pin6 for reading by the TDS2020.

AII.2.9 Control of multiple APV6s

As mentioned earlier, an additional board was introduced for the fast-control (clock

and trigger line) signal conversion from TTL to ECL levels when multiple APV6s have to be controlled. Due to the termination resistance on the APV6s, it is only possible to drive one APV6 per output of the chip that performs the conversion (i.e. IC4 in Fig. AII.1 *a*). In order to allow four APV6s (i.e. two detector planes) to be controlled at the same time, a sub-board ('piggy back' board) was specifically designed (see Fig. AII.2). The signals on IC4 of the main interface card (Fig. AII.1 *a*) are guided via a connector onto the piggy back board at IC1 (Fig. AII.2). There are two converter (MC10124) chips on the piggy back board: IC2 is used to produce four differential ECL clock outputs and IC3 to produce four differential ECL trigger outputs. Their function and wiring is as described earlier for the original board. IC4 (a 74HCT04 in Fig. AII.2, not to be confused with IC4 of Fig. AII.1 *a*) is used simply to buffer the TTL clock and trigger signals from IC1 so as to allow them to drive the four inputs on each of the MC10124 converters. IC4 also buffers the 40-MHz clock signal before it is passed to the PDA12A ADC cards via a coaxial cable.

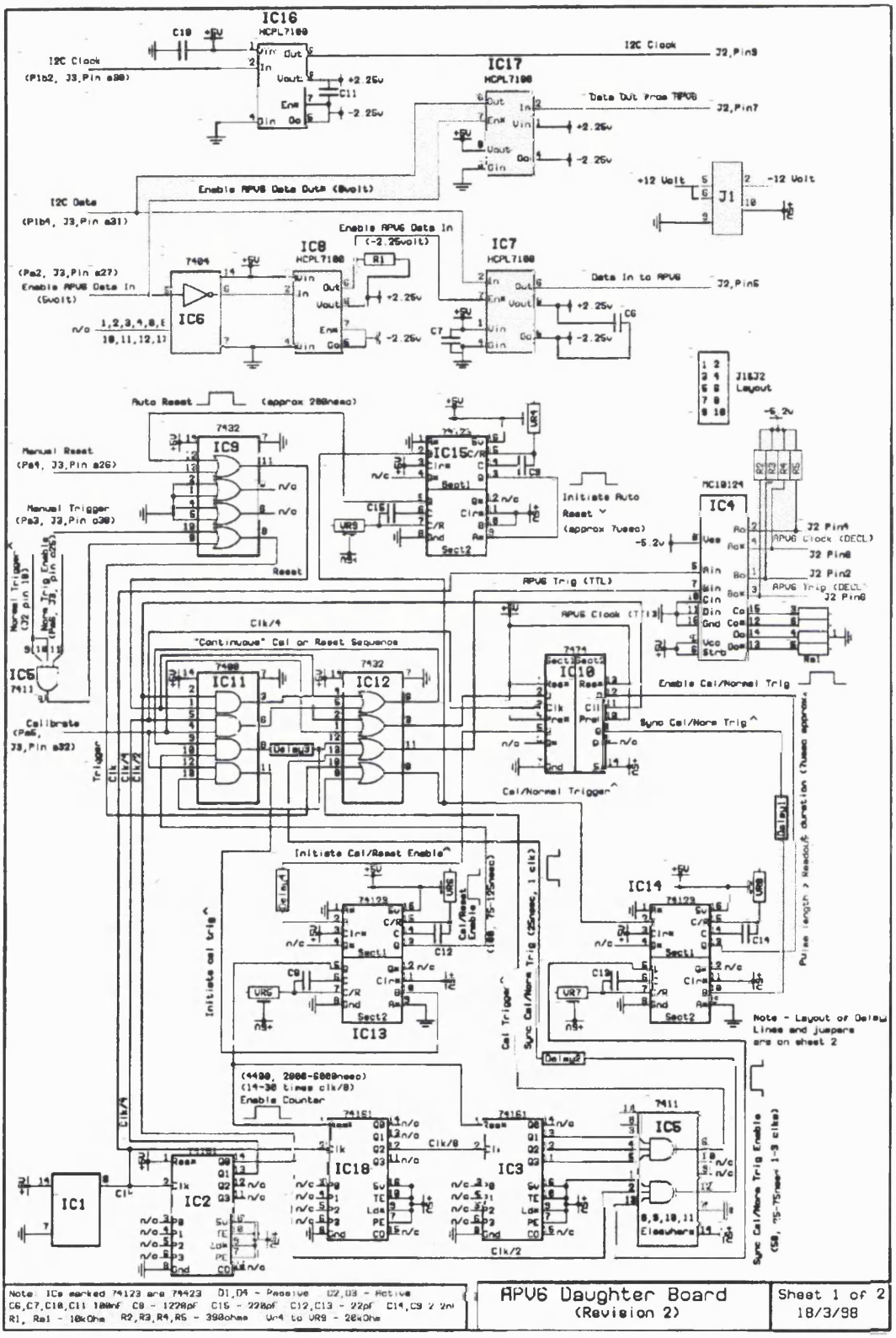

Fig. AII.1: a) Circuit diagram of the interface board (Part 1).

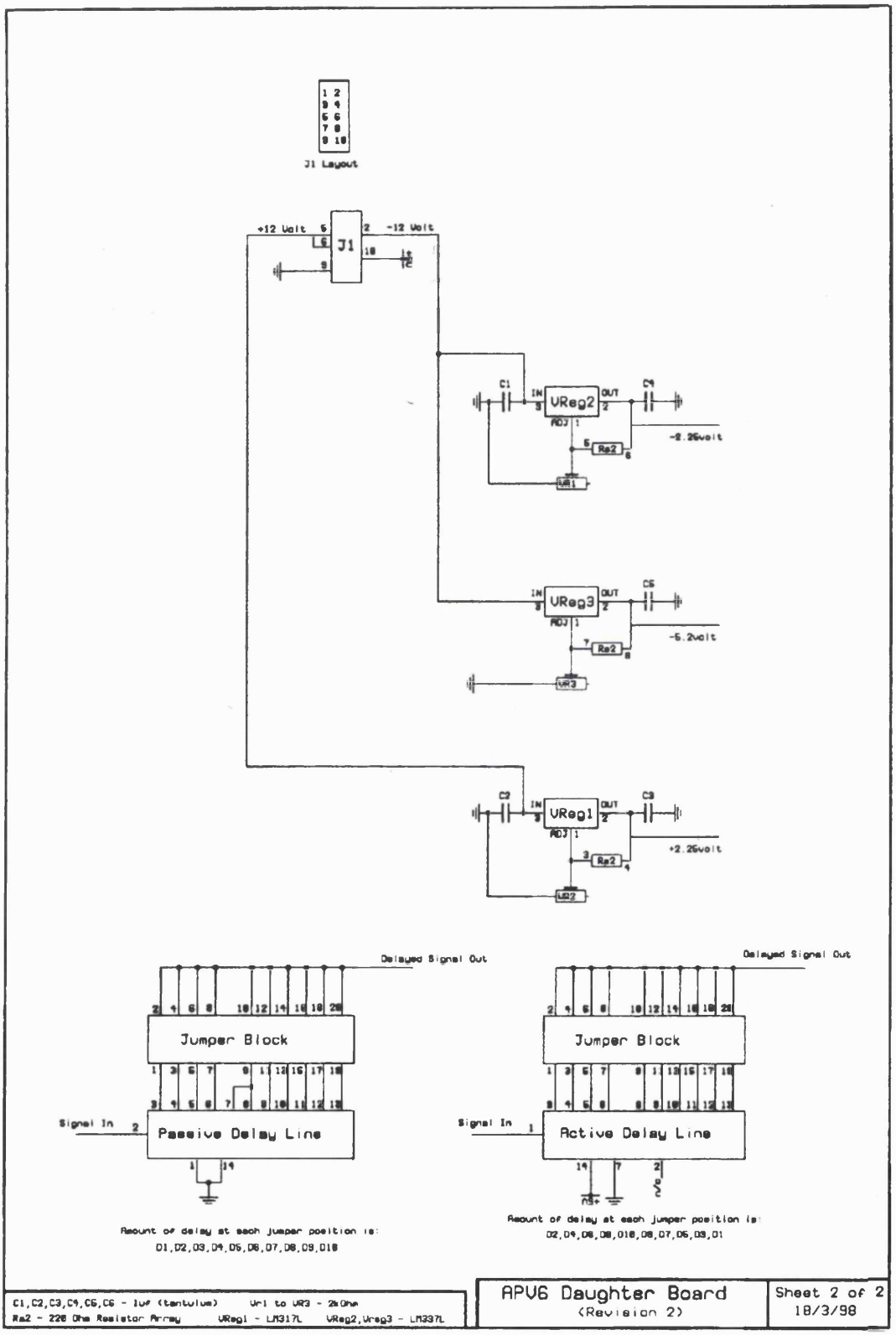

Fig. AII.1: b) Circuit diagram of the interface board (Part 2).

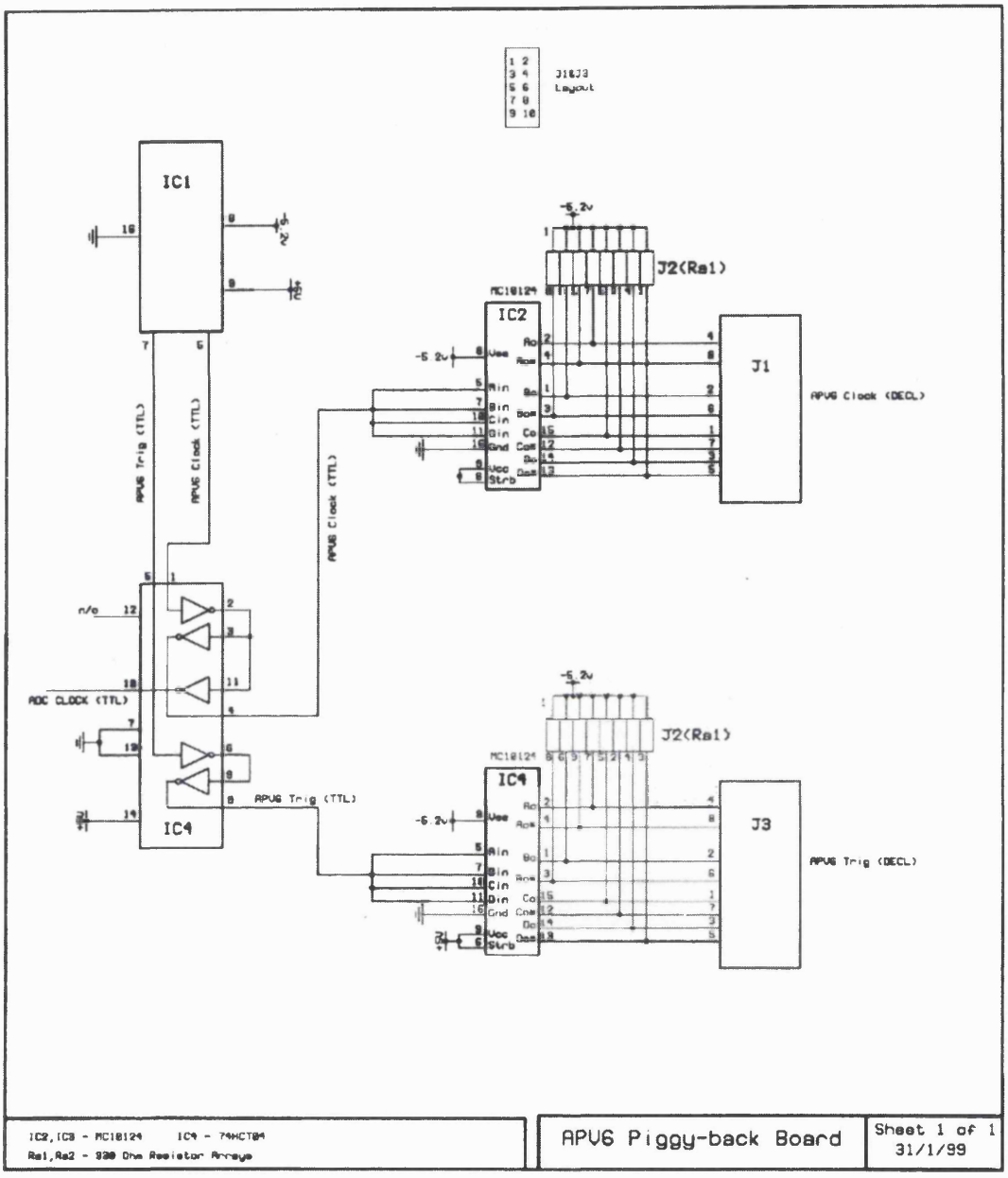

Fig. AII.2: Circuit diagram of the 'piggy-back' board.

References

[Ait-Ouamer *et al.*, 1990] Ait-Ouamer F A, Kerrick A D, Sarmouk A, O'Neill T J, Sweeney W E, Tümer T O, Zych A D and White R S:Calibration and performance of the UCR double Compton gamma ray telescope, 1990 *IEEE Trans. Nucl. Sci.* **37** (2) 535-540

[Allport *et al.*, 1991]: Allport P P, Carter J R, Gibson V, Goodrick M J, Hill J C, Katvars S G, Bullough M A, Greenwood N M, Lucas A D, Wilburn C D, Carter A A, Pritchard T W, Nardini L, Seller P and Thomas S L: FOXFET biassed microstrip detectors, 1991 *Nucl. Instr. and Meth. Phys. Res.* **A310** 155-159

[Anger, 1958] Anger H O: Scintillation camera 1958 *Rev. Sci. Instr.* **29** (1) 27-33

[Aprile *et al.*, 1996] Aprile E, Egorov V, Xu F, Chupp E L, Dunphy P P, Doke T, Kikuchi J, Fishman G J, Pendleton G, Masuda K and Kashiwagi T: The Liquid Xenon Gamma-Ray Imaging Telescope (LXeGRIT) for medium energy astrophysics, 1996 *SPIE Proc. Int. Soc. Opt. Eng.* **2806** 337-348

[Aprile *et al.*, 1998] Aprile E, Egorov V, Giboni K L, Kozu T, Xu F, Doke T, Kikuchi J, Kashiwagi T, Fishman G J, Rehage R and Trice D: The electronics read out and data acquisition system for a liquid xenon time projection chamber as a balloon-borne Compton telescope, 1998 *Nucl. Instr. and Meth. Phys. Res.* **A412** 425-436

[Attix, 1986]: Attix F H: *Introduction to Radiological Physics and Radiation Dosimetry* (J. Wiley & Sons, 1986) 160-177

[Bacchetta *et al.*, 1995] Bacchetta N, Bisello D, Candelori A, Paccagnella A, Spada M and Vanzi M: SPICE analysis of signal propagation in Si microstrip detectors, 1995 *IEEE Trans. Nucl. Sci.* **42** (4) 459-466

[Bacchetta *et al.*, 1998] Bacchetta N, Bisello D, Candelori A, Da Rold M, Nardi F and Paccagnella A: HSPICE simulations of Si microstrip detectors, 1998 *Nucl. Instr. and Meth. Phys. Res.* **A409** 142-146

[Barberis *et al.*, 1993] Barberis E, Boisevain J G, Cartiglia N, Ellison J A, Ferguson P, Fleming J K, Holzscheiter K, Jerger S, Joyce D, Kapustinsky J S, Leslie J, Lietzke C, Matthews J A J, Palounek A P T, Pitzl D, Rowe W A, Sadrozinski H F – W, Skinner D, Sommer W F, Sondheim W E, Wimpenny S J and Ziock H J: Temperature effects on radiation damage to silicon detectors, 1993 *Nucl. Instr. and Meth. Phys. Res.* **A326** 373-380

[Barberis *et al.*, 1994] Barberis E, Cartiglia N, LeVier C, Rahn J, Rinaldi P, Sadrozinski H F-W, Wichmann R, Ohsugi T, Unno Y, Miyata H, Tamura N and Yamamoto K: Capciatnces in silicon microstrip detectors, 1994 *Nucl. Instr. and Meth. Phys. Res.* **A342** 90-95

[Batignani *et al.*, 1991] Batignani G, Bosisio L, Focardi E, Forti F, Giorgi M A, Moneta L, Parrini G, Tonelli G and Triggiani G: Development and performance of double sided silicon strip detectors, 1991 *Nucl. Instr. and Meth. Phys. Res.* **A310** 160-164

[Bax *et al.*, 1995] Bax J J, Visser F C, Van Lingen A, Visser C A and G J J Teule: Myocardial F-18 Fluorodeoxyglucose imaging by SPECT, 1995 *Clin. Nucl. Med.* **20** (6) 486-490

[Bolozdynya *et al.*, 1996] Bolozdynya A, Egorov V, Koutchenkov A, Safronov G, Smirnov G, Medved S and Morgunov V: High pressure xenon electronically collimated camera for low energy gamma ray imaging, 1996 *IEEE Nuclear Science Symposium Conference Record* **2** 1157-1161

[Bolozdynya *et al*,.1997] Bolozdynya A, Ordonez C E and Chang W: A concept of cylindrical Compton camear for SPECT, 1997 *IEEE Nuclear Science Symposium Conference Record* **2** 1047-1051

[Bolozdynya and Morgunov, 1998] Bolozdynya A I and Morgunov V L: Multilayer electroluminescence camera: concept and Monte Carlo study, 1998 *IEEE Trans. Nucl. Sci.* **45** (3) 1646-1655

[Brunsden, 1975] Brunsden B, Harper P V and Beck R N : Elimination of collimator-hole pattern by double displacement of a hexagonal array, 1975 *J. Nucl. Med.* **16** 517

[Caccia *et al.*, 1987] Caccia M, Evensen L, Hansen T E, Horisberger R, Hubbeling L, Peisert A, Tuuva T and Weilhammer P: A Si strip detector with integrated coupling capacitors, 1987 *Nucl. Instr. and Meth. Phys. Res.* **A260** 124-131

[Chen et al., 1992] Chen W, Kraner H, Li Z, Rehak P, Gatti E, Longoni A, Sampietro M, Holl P, Kemmer J, Faschingbauer U, Scmitt B, Wörner A and Wurm J P: Large area cylindrical silicon drift detector, 1992 *IEEE Trans. Nucl. Sci.* **39** (4) 619-628

[Cook and Maisey, 1996] Cook G J R and Maisey M N: The current status of clinical PET imaging, 1996 *Clinical Radiology* **51** 603-613

[Cullum, 2000] Cullum I*: Microstrip Detector Data Acquisition using APV6s and a PC Controller*, internal document (July 2000, University College London)

[Dabrowski *et al.*, 1994] Dabrowski W, Grybos P, Krammer M, Pernegger H and Rakoczy D: Charge division in silicon strip detectors with a large strip pitch, 1994 *Nucl. Instr. and Meth. Phys. Res.* **A349** 424-430

[Damerell, 1995] Damerell C J S: *Vertex detectors: the state of the art and future prospects*, 1995 Council for the Central Laboratory of the Research Councils Preprint RAL-P-95-008

[Delaney, 1980] Delaney C F G: *Electronics for the Physicist with applications* (Elis Horwood, 1980) 253-266

[Dogan *et al.*, 1990] Dogan N, Wehe D K and Knoll G F: Multiple Compton scattering gamma ray imaging camera, 1990 *Nucl. Instr. and Meth. Phys. Res.* **A299** 501-506

[Dogan *et al.*, 1992] Dogan N, Wehe D K and Akcasu A Z: A source reconstruction method for multiple scatter Compton cameras, 1992 *IEEE Trans. Nucl. Sci.* **39** (5) 1427-1430

[Dogan and Wehe, 1994] Dogan N and Wehe D K: Efficiency and angular resolution calculations for a prototype multiple Compton scatter camera, 1994 *Nucl. Instr. and Meth. Phys. Res.* **A345** 296-302

[Drane *et al.*, 1994] Drane W E, Abbott F D, Nicole M W, Mastin S T and Kuperus J H: Technology for FDG SPECT with a relatively inexpensive gamma camera, 1994 *Radiology* **191** 461-465

[Du *et al.*, 1999] Du Y F, He Z, Knoll G F, Wehe D K and Li W: Evaluation of a Compton scattering camera using 3D position-sensitive CdZnTe detectors, 1999 *SPIE Proc. Int. Soc. Opt. Eng.* **3768** 228-238

[Dubbs *et al.*, 1996] Dubbs T, Kashigin S, Kratzer M, Kroeger W, Pulliam T, Sadrozinski H F W, Spencer E, Wichmann R, Wilder M, Bialas W, Dabrowski W, Unno I, Oshugi T: Noise determination in silicon micro strips, 1996 *IEEE Trans. Nucl. Sci.* **43** (3) 1119-1122

[England *et al.*, 1981] England J B A, Hyams B D, Hubbeling L, Vermeulen J C and Weilhammer P: Capacitative charge division read-out with a silicon strip detector, 1981 *Nucl. Instr. and Meth.* **185** 43-47

[Erlandsson and Ohlsson, 1998] Erlandsson K and Ohlsson T: Positron emission tomography – basic principles, *Monte Carlo calculations in nuclear medicine* edited by Ljungberg M L, Strand S-E and King M A (Institute of Physics Publishing, 1998) 221-231

[Evans and Martin, 1996] Evans B L and Martin J B: Modeling and design of portable Compton gamma-ray cameras, 1996 *IEEE Nuclear Science Symposium Conference Record* **2** 793-797

[Everett *et al.*, 1977] Everett D B, Fleming J S, Todd R W and Nightingale J M: Gamma-radiation imaging system based on the Compton effect, 1977 *Proc. Inst. Electr. Eng.* **124** (11) 995-1000

[Fahey and Harkness, 1996] Fahey F F and Harkness B A: SPECT imaging with rotating gamma camera systems, *Nuclear Medicine* edited by Henkin R E, Boles M A, Dillehay G L, Halama J R, Karesh S M, Wagner R H and Zimmer A M (Mosby, 1996) **I** 232-246

[Frautschi *et al.*,1996] Frautschi M A, Hoeferkamp M R and Seidel S C: Capacitance measurements of double-sided silicon microstrip detectors, 1996 *Nucl. Instr. and Meth. Phys. Res.* **A378** 284-296

[French, 1997] French M: *APV6 User Manual*, Rutherford Appleton Laboratory internal document, April 1997.

[Fujieda and Perez-Mendez, 1986] Fujieda I and Perez-Mendez V: Theoretical considerations of a new electronically collimated gamma camera utilizing gas scintillation, 1986 *Jap. J. Appl. Phys.* **25** (12) 1925-1931

[Gatley, 1996] Gatley S J: Positron radiopharmaceutical agents and their chemistry, *Nuclear Medicine* edited by Henkin R E, Boles M A, Dillehay G L, Halama J R, Karesh S M, Wagner R H and Zimmer A M (Mosby, 1996) **I** 429-440

[Gatti and Rehak, 1984] Gatti E and Rehak P: Semicondcutor drift chamber – an application of a novel charge transport scheme, 1984 *Nucl. Instr. and Meth. Phys. Res.* **A225** 608-614

[Gunter, 1996] Gunter D L: Collimator characteristics and design, *Nuclear Medicine* edited by Henkin R E, Boles M A, Dillehay G L, Halama J R, Karesh S M, Wagner R H and Zimmer A M (Mosby, 1996) **I** 96-124

[Halblieb et al., 1984] Halblieb J A, Kensek R P, Mehlhorn T A, Valdez G D, Seltzer S M and Berger M J: *ITS Version 3.0: The Integrated TIGER Series of coupled electron/photon Monte Carlo transport codes*, 1984 SANDIA National Laboratories, Livermore, CA Report SAND-84-0573

[Hall, 1984] Hall G: Ionisation energy losses of highly relativistic charged particles in thin silicon layers, 1984 *Nucl. Instr. and Meth. Phys. Res.* **220** 356-362

[Hancock *et al.*, 1983] Hancock S, James F, Movchet J, Rancoita P G and VanRossum L: Energy loss and energy straggling of protons and pions in the momentum range 0.7 to 115 GeV/c, 1983 *Phys. Rev. A* **28** (2) 615-620

[Hasegawa *et al.*, 1999] Hasegawa S, Uehara T, Yamaguchi H, Fujino K, Kusoka H , Hori M and Nishimura T: Validity of ^{18}F-Fluorodeoxyglucose imaging with a dual-

head coincidence gamma camera for detection of myocardial viability, 1999 *J. Nucl. Med.* **40** (11) 1884-1892

[Hichwa, 1996] Hichwa R D:Production of PET radioisotopes and principles of PET imaging, *Nuclear Medicine* edited by Henkin R E, Boles M A, Dillehay G L, Halama J R, Karesh S M, Wagner R H and Zimmer A M (Mosby, 1996) **I** 279-291

[Hoffman *et al.*, 1976] Hoffman E J, Phelps M E, Mullani N A, Higgins C S and Ter-Pogossian M M: Design and performance characteristics of a whole-body positron transaxial tomograph, 1976 *J. Nucl. Med.* **17** (6) 493-502

[Howard, 1998] Howard A S: *Diamond Detectors for Particle Physics*, PhD Thesis, Imperial College, February 1998.

[Howard, 2000] Alex Howard, *private communication* (Imperial College, May 2000).

[Holl *et al.*, 1989] Holl P, Kemmer J, Prechtel U, Ziemann T, Hauff D, Lutz G, Schwarz A S and Strüder L: A double-sided silicon strip detector with capacitive readout and a new method of integrated bias coupling, 1989 *IEEE Trans. Nucl. Sci.* **36** (1) 251-255

[Ivanov *et al.*, 1998] Ivanov V I, Aleksejava L A, Gagliardi M A, Gagliardi T and Nenonen S: The influence of the M-pi-n structure on CdTe X-ray detector performance, 1998 *IEEE Trans. Nucl. Sci.* **45** (3) 390-393

[Jarritt and Acton, 1996] Jarritt P H and Acton P D: PET imaging using gamma camera systems: a review, 1996 *Nucl. Med. Comm.* **17** 758-766

[Johnson *et al.*, 1995] Johnson W N, Dermer C, Kroeger R A, Kurfess J D, Gehrels N, Grindlay J, Leising M D, Prince T, Purcell W, Ryan J and Tümer T: Advanced

Telescope for High Energy Nuclear Astrophysics (*ATHENA*), 1995 *SPIE Proc. Int. Soc. Opt. Eng.* **2518** 74-84

[Kamae *et al.*, 1987] Kamae T, Enomoto R and Hanada N: A new method to measure energy, direction and polarization of gamma rays, 1987 *Nucl. Instr. and Meth. Phys. Res.* **A260** 254-257

[Kamae *et al.*, 1988] Kamae T, Hanada N and Enomoto R: Prototype design of multiple Compton gamma-ray camera, 1988 *IEEE Trans. Nucl. Sci.* **35** (1) 352-355

[Kemmer and Lutz, 1988] Kemmer J and Lutz G: New structures for position sensitive semiconductor detectors, 1988 *Nucl. Instr. and Meth. Phys. Res.* **A273** 588-598

[King *et al.*, 1994] King S E, Phillips G W, Haskins P S, McKisson J E, Piercey R B and Mania R C: A solid-state Compton camera for three-dimensional imaging, 1994 *Nucl. Instr. and Meth. Phys. Res.* **A353** 320-323

[Knoll, 1989] Knoll G F: *Radiation Detection and Measurement* (J. Wiley & Sons, 1989) 114-117

[Kramer *et al.*, 1998] Kramer P H, Kind P and Gaspers S: Preliminary study for the design of a gamma camera based upon compound semiconductors, 1998 *Physica Medica*, **XIV** (2) 31-33

[Kravis *et al.*, 1999] Kravis S D, Tümer T O, Visser G, Meeding D G and Yin-Shi: A multichannel readout electronics for nuclear application (RENA) chip developed for position sensitive solid state detectors, 1999 *Nucl. Instr. and Meth. Phys. Res.* **A422** 352-356

[Kurfess, 1998] Kurfess J D: Compton scatter imaging in astrophysics, 1998 *IEEE Trans. Nucl. Sci.* **45** (3) 936-942

[Kuykens and Audet, 1988] Kuykens H J P and Audet S A: A 3x3 silicon drift chamber array for application in an electronic collimator, 1988 *Nucl. Instr. and Meth. Phys. Res.* **A273** 570-574

[Laakso *et al.*, 1993]: Laasko M, Singh P, Engels E Jr and Shepard P F: Operation and radiation resistance of a FOXFET biasing structure for silicon strip detectors, 1993 *Nucl. Instr. and Meth. Phys. Res.* **A326** 214-221

[LeBlanc *et al.*, 1998] LeBlanc J W, Clinthorne N H, Hua C H, Nygård E, Rogers W L, Wehe D K, Weilhammer P and Wilderman S J: C-SPRINT: a prototype Compton camera system for low energy gamma ray imaging, 1998 *IEEE Trans. Nucl. Sci.* **45** (3) 943-949

[LeBlanc *et al.*, IEEE 1999] LeBlanc J W, Clinthorne N H, Hua C H, Nygård E, Rogers W L, Wehe D K, Weilhammer P and Wilderman S J: Experimental results from the C-SPRINT prototype Compton camera, 1999 *IEEE Trans. Nucl. Sci.* **46** (3) 201-204

[Le Blanc *et al.*, NIM 1999] LeBlanc J W, Clinthorne N H, Hua C H, Rogers W L, Wehe D K, and Wilderman S J: A Compton camera for nuclear medicine applications using ^{113m}In, 1999 *Nucl. Instr. and Meth. Phys. Res.* **A422** 735-739

[Lewellen *et al.*, 1997] Lewellen T K, Miyaoka R S, Jansen F and Kaplan M S: A data acquisition system for coincidence imaging using a conventional dual head gamma camera, 1997 *IEEE Trans. Nucl. Sci.* **44** (3) 1214-1218

[Lewellen *et al.*, 1999] Lewellen T K, Miyaoka R S and Swan W L: PET imaging using dual-head gamma cameras: an update, 1999 *Nucl. Med. Comm.* **20** 5-12

[MacEvoy, 1997] MacEvoy B C: *Defect kinetics in silicon detector material for applications in the large hadron collider*, 1997 PhD thesis, Imperial College. Rutherford Appleton Laboratory RAL-TH-97-003, 113-124

[Martin *et al.*, 1993] Martin J B, Knoll G F, Wehe D K, Dogan N, Jordanov V, Petrick N and Singh M: A ring Compton scatter camera for imaging medium energy gamma rays, 1993 *IEEE Trans. Nucl. Sci.* **40** (4) 972-978

[Martin *et al.*, 1994] Martin J B, Dogan N, Gormley J E, Knoll G F, O'Donnell M and Wehe D K: Imaging multi-energy gamma-ray fields with a Compton scatter camera,1994 *IEEE Trans. Nucl. Sci.* **41** (4) 1019-1025

[McKisson *et al.*, 1994] McKisson J E, Haskins P S, Phillips G W, King S E, August R A, Piercey R B and Mania R C: Demonstration of three-dimensional imaging with a germanium Compton camera, 1994 *IEEE Trans. Nucl. Sci.* **41** (4) 1221-1224

[Miyaoka *et al.*, 1995] Miyaoka R S, Lewellen T K, Kim J S, Kaplan M S, Kohlmyer S K, Costa W and Jansen F: Performance of a dual headed SPECT system modified for coincidence detection, 1995 *IEEE Nuclear Science Symposium Conference Record* **3** 1348-1352

[Miyaoka *et al.*, 1996] Miyaoka R S, Costa W L S, Lewellen T K, Kohlmyer S K, Kaplan M S, Jansen F and Stearns C W: Coincidence imaging using a standard dual head gamma camera, 1996 *IEEE Nuclear Science Symposium Conference Record* **2** 1127-1131

[Moore *et al.*, 1992] Moore S C, Kouris K and Cullum I: Collimator design for single photon emission tomography, 1992 *Eur. J. Nucl. Med.* **19** 138-150

[Namito *et al.*, 1994] Namito Y, Ban S and Hirayama H: Implementation of the Doppler broadening of a Compton-scattered photon into the EGS4 code, 1994 *Nucl. Instr. and Meth. Phys. Res.* **A349** 489-494

[Nelson *et al.*, 1985] Nelson W R, Hirayama H and Rogers D W O: *The EGS4 code system*, 1985 Stanford Linear Accelerator Center Report SLAC-265

[Nicholson, 1982] Nicholson P W: *Nuclear Electronics* (J. Wiley & Sons, 1982) 122-165

[Niemela *et al.*, 1996] Niemela A, Sipila H and Ivanov VI: High-resolution p-I-n CdTe and CdZnTe X-ray detectors with cooling and rise-time discrimination, 1996 *IEEE Trans. Nucl. Sci.* **43** (3) 1476-1480

[Nygård *et al.*, 1991] Nygård E, Aspell P, Jarron P, Weilhammer P and Yoshioka K: CMOS low noise amplifier for microstrip readout - design and results, 1991 *Nucl. Instr. and Meth. Phys. Res.* **A301** 506-516

[Ohsugi *et al.*, 1988] Ohsugi T, Taketani A, Noda M, Chiba Y, Asai M, Kondo T, Sato T, Takasaki M, Tanaka K H, Kondo K, Hirayama H, Yamamoto K and Tanaka H: Radiation damage in silicon microstrip detectors, 1988 *Nucl. Instr. and Meth. Phys. Res.* **A265** 105-111

[O'Neill *et al.*, 1992] O'Neill T J, Ait-Ouamer F, Scwatrz I, Tümer T O, White R S and Zych A D: Compton recoil electron tracking with silicon strip detectors, 1992 *IEEE Trans. Nucl. Sci.* **39** (4) 629-634

[O'Neill *et al.*, 1995] O'Neill T J, Bhattacharya D, Blair S, Case G, Tümer T O, White R S and Zych A D: The TIGRE desktop prototype results for 511 and 900 keV gamma rays, 1995 *IEEE Trans. Nucl. Sci.* **42** (4) 933-939

[Ordonez *et al.*, 1997] Ordonez C E, Bolozdynya A and Chang W: Doppler broadening of energy spectra in Compton cameras, 1997 *IEEE Nuclear Science Symposium Conference Record* **2** 1361-1365

[Overdick *et al.*, 1997] Overdick M, Czermak A, Fischer P, Herzog V, Kjensmo A, Kugelmeier T, Ljunggren K, Nygård E, Pietrizk C, Schwan T, Strand S.-E, Straver J, Weilhammer P, Wermes n and Yoshioka K: A "Bioscope" system using double-sided silicon strip detectors and self-triggering read-out chips, 1997 *Nucl. Instr. and Meth. Phys. Res.* **A392** 173-177

[Patton *et al.*, 1996] Patton J A, Sandler M P, Ohana I and Weinfeld Z: High-energy (511-keV) imaging with the scintillation camera, 1996 *Radiographics* **16** 1183-1194

[Peisert, 1993] Peisert A: Silicon microstrip detectors, *Instrumentation in High Energy Physics*, edited by Fabio Sauli, *Advanced Series on Directions in High Energy Physics* **9** (World Scientific, 1993) 1-79

[Phlips *et al.*, 1996] Phlips B F, Inderhees S E, Kroeger R A, Johnson W N, Kinzer R L, Kurfess J D, Graham B L and Gehrels N: Performance of a Compton telescope using position-sensitive germanium detectors, 1996 *IEEE Trans. Nucl. Sci.* **43** (3) 1472-1475

[Physics Letters, 1990] Review of Particle Physics, 1990 *Physics Letters* **B239**.

[Raymond, 1997] Mark Raymond, *private communication* (Imperial College, August 1997).

[Raymond *et al.*, 1997] Raymond M, Hall G, Millmore M, French M, Jones L L and Murray P: The APV6 readout chip for CMS microstrip detectors, 1997 *Proceedings of the Third Workshop on Electronics for LHC Experiments* CERN/LHCC/97-60 158-162

[Robert and Milne, 1999] Robert G and Milne R: A Delphi study to establish national cost-effectiveness research priorities for positron emission tomography, 1999 *Eur. J. Rad.* **30** 54-60

[Rohe and Valentine, 1996] Rohe R C and Valentine J D: An energy-subtraction Compton scatter camera design for *in vivo* medical imaging of radiopharmaceuticals, 1996 *IEEE Trans. Nucl. Sci.* **43** (6) 3256-3263

[Rönnqvist *et al.*, 1994] Rönnqvist C, Santos F, Toker O, Weilhammer P, Yoshioka K, Nygård E, Czermak A, Jalocha P, Dulinski W and Hu Y: Double-sided silicon microstrip detectors and low noise self triggering multichannel readout chips for imaging applications, 1994 *Nucl. Instr. and Meth. Phys. Res.* **A348** 440-443

[Royle and Speller, 1994] Royle G J and Speller R D: Design of a Compton camera for imaging 662 keV radionuclide distributions, 1994 *Nucl. Instr. and Meth. Phys. Res.* **A348** 623-626

[Royle and Speller, 1996] Royle G J and Speller R D:A flexible geometry Compton camera for industrial gamma ray imaging, 1996 *IEEE Nuclear Science Symposium Conference Record* **2** 821-824

[Royle and Speller, 1997] Royle G J and Speller R D: Compton scatter imaging of a nuclear industrial site, 1997 *IEEE Nuclear Science Symposium Conference Record* **1** 365-368

[Schönfelder *et al.*, 1984] Schönfelder , Diehl R, Lichti G G, Steinle H, Swanenburg B N, Deerenberg A J M, Aarts H, Lockwood J, Webber W, Macri J, Ryan J, Simpson G, Taylor B G, Bennett K and Snelling M: The imaging telescope COMPTEL on the Gamma Ray Observatory, 1984 *IEEE Trans. Nucl. Sci.* **31** (1) 766-770

[Schönfelder *et al.*, 1993] Schönfelder V, Aarts H, Bennett K, de Boer H, Clear J, Collmar W *et al*: Instrument Description and performance of the imaging gamma-ray telescope COMPTEL aboard the Compton Gamma-Ray Observatory, 1993 *Astrophys. J. Suppl.* **86** 657-692

[Schopper *et al.*, 1999] Schopper F, Andritschke R, Shaw H, Nefzger C, Zoglauer A, Diehl R and Schönfelder V: MEGA - Medium Energy Gamma Astronomy telescope, poster presented at the 5^{th} *Compton Symposium on Gamma-Ray Astrophysics*, September 1999, Portsmouth, New Hampshire U.S.A.

[Schopper *et al.*, 2000] Schopper F, Andritschke R, Shaw H, Nefzger C, Zoglauer A, Schönfelder V and Kanbach G: CsI calorimeter with 3-D position resolution, 2000 *Nucl. Instr. and Meth. Phys. Res.* **A442** 394-399

[Schottky, 1918] Schottky W: Über spontane Stromschwankungen in verschiedenen Elektrizitätsleitern, 1918 *Annalen der Physik* **57**, 541-567

[Schwarz, 1994] Schwarz A S: Silicon strip vertex detectors at LEP, 1994 *Nucl. Instr. and Meth. Phys. Res.* **A342** 218-232

[Seller *et al.*, 1988]: Seller P, Allport P P, Tyndel M: Results of silicon strip detector readout using a CMOS low power microplex (MX1), 1988 *IEEE Trans. Nucl. Sci.* **35** (1) 176-180

[Singh, 1983] Singh M: An electronically collimated gamma camera for single photon emission computed tomography. Part I: Theoretical considerations and design criteria, 1983 *Med. Phys.* **10** (4) 421-427

[Singh and Doria, 1983] Singh M and Doria D: An electronically collimated gamma camera for single photon emission computed tomography. Part II: Image

reconstruction and preliminary experimental measurements, 1983 *Med. Phys.* **10** (4) 428-435

[Singh and Doria, 1985] Singh M and Doria D: Single photon imaging with electronic collimation, 1985 *IEEE Trans. Nucl. Sci.* **32** (1) 843-847

[Singh *et al.*, 1988] Singh M, Leahy R, Brechner R and Hebert T: Noise propagation in electronically collimated single photon imaging, 1988 *IEEE Trans. Nucl. Sci.* **35** (1) 772-777

[Singh and Brechner, 1990] Singh M and Brechner R R: Experimental test-object study of electronically collimated SPECT, 1990 *J. Nucl. Med.* **31** (2) 178-186

[Singh *et al.*, 1995] Singh M, Doty F P, Friesenhahn S J and Butler J F:Feasibility of using Cadmium-Zinc-Telluride detectors in electronically colliamted SPECT, 1995 *IEEE Trans. Nucl. Sci.* **42** (4) 1139-1146

[Skyrme, 1967] Skyrme D J: The passage of charged particles through silicon, 1967 *Nucl. Instr. and Meth.* **57** 61-73

[Smith *et al.*, 1998] Smith L E, He Z, Wehe D K, Knoll G F and Wilderman S J: Design and modeling of the hybrid portable gamma camera system, 1998 *IEEE Trans. Nucl. Sci.* **45** (3) 963-969

[Solomon and Ott, 1988] Solomon C J and Ott R J: Gamma ray imaging with silicon detectors – a Compton camera for radionuclide imaging in medicine, 1988 *Nucl. Instr. and Meth. Phys. Res.* **A273** 787-792

[Sorenson and Phelps, 1987] Sorenson J A and Phelps M E: *Physics in Nuclear Medicine* (W. B. Saunders, 1987) 298-345

[Squillante and Shah, 1995] Squillante M R and Shah K S: Other materials: status and prospects, *Semiconductors for Room Temperature Nuclear Detector Applications* edited by Schlesinger T E and James R B, Semiconductor and Semimetals **43** (Academic Press, 1995) 470-471

[Stuewer and Cooper, 1977] Stuewer R H and Cooper M J: History, *Compton scattering: the investigation of electron momentum distributions* edited by B Williams (McGraw-Hill, 1977) 1-27

[Sze, 1985] Sze S M: *Semiconductor devices – Physics and Technology* (John Wiley and Sons, 1985) 70-87

[Todd *et al.*, 1974] Todd R W, Nightingale J M and Everett D B: A proposed γ camera, 1974 *Nature* **251** 132-134

[Toker, 1994] Toker O, Masciocchi S, Nygård E, Rudge A and Weilhammer P: VIKING, a CMOS low noise monolithic 128 channel frontend for Si-strip detector readout, 1994 *Nucl. Instr. and Meth. Phys. Res.* **A340** 572-579

[Tümer *et al.*, 1997] Tümer T O, Yin S and Kravis S: A high sensitivity, electronically collimated gamma camera, 1997 *IEEE Trans. Nucl. Sci.* **44** (3) 899-904

[Van Lingen *et al.*, 1992] Van Lingen A, Huijgens P C, Visser F C, Ossenkoppele G J, Hoekstra O S, Martens H J M, Huitink H, Herscheid K D M, Green M V and G J J Teule: Performance characteristics of a 511-keV collimator for imaging positron emitters with a standard gamma-camera, 1992 *Eur. J. Nucl. Med.* **19** (5) 315-321

[Walton, 1984] Walton J T: Silicon detectors: new challenges, 1984 *Nucl. Instr. and Meth. Phys. Res.* **226** 1-11

[Weilhammer, 1994] Weilhammer P: Double-sided Si strip sensors for LEP vertex detectors, 1994 *Nucl. Instr. and Meth. Phys. Res.* **A342** 1-15

[Weilhammer *et al.*, 1996] Weilhammer P, Nygård E, Dulinski W, Czermak A, Djama F, gadomski S, Roe S, Rudge A, Schopper F and Strobel J: Si pad detectors, 1996 *Nucl. Instr. and Meth. Phys. Res.* **A383** 89-97

[Wilderman *et al.*, 1998] Wilderman S J, Les Rogers W, Knoll G F and Engdahl J C: Fast algorithm for list mode back projection of Compton scatter camera data, 1998 *IEEE Trans. Nucl. Sci.* **45** (3) 957-962

[Wollenweber *et al.*, 1998] Wollenweber S D, Tsui B M W, Lalush D S, Frey E C, McCartney W H, Tocharoenchai C, Rempel T D and Simcic V: Initial characterization of the Siemens E.CAM$^+$: a dual-detector camera with coincidence imaging capability, 1998 *IEEE Nuclear Science Symposium Conference Record* **3** 1470-1476

[Zhang *et al.*, 1998] Zhang L, Lanza R C, Horn B K P and Zimmerman R E: High energy 3-D nuclear medicine imaging using coded apertures with a conventional gamma camera, 1998 *IEEE Nuclear Science Symposium Conference Record* **3** 1532-1534

[Zych *et al.*, 1979] Zych A D, Wislon R B, Zanrosso E, White R S, Dayton B and Simone J: Double scatter telescope for medium energy gamma ray astronomy from a satellite, 1979 *IEEE Trans. Nucl. Sci.* **26** (1) 506-512

[Zych *et al.*, 1996] Zych A, Bhattacharya D, Dixon D, O'Neill T, Tümer T, White R S, Macri J, McConnell M, Ryan J, Ögelman H, Paulos R, Wheaton W, Akyüz A, Samimi J and Özel M: An Advanced TIGRE Instrument for Intermediate-Energy Gamma-Ray Astronomy, presented at the *Workshop on the Applications and*

Methods of Compton Scatter Imaging, IEEE Nuclear Science Symposium and Medical Imaging Conference, Anaheim November 1996.